

Solid-state Deposition of Bulk Metallic Glass and High-entropy Alloy via Cold Spray

Ningsong Fan

Department of Mechanical, Manufacturing, and Biomedical Engineering

Trinity College Dublin, the University of Dublin

January 2024

A thesis submitted to the Trinity College Dublin, the University of Dublin

in partial fulfillment of the requirements for the degree of

Doctor of Philosophy



Supervisor: Dr. Shuo Yin

Internal Examiner: Prof. Garret O'Donnell

External Examiner: Prof. Wei Zhou

Declaration

I hereby declare that this thesis represents my own work which has been done after registration at Trinity College Dublin, the University of Dublin, for the degree of the postgraduate programme, named Doctor in Philosophy in the Department of Mechanical, Manufacturing, and Biomechanical Engineering, and has not been previously included in a thesis or dissertation submitted to this or any other institution for a degree, diploma, or other qualifications.

I agree to deposit this thesis in the University's open access institutional repository or allow the library to do so on my behalf, subject to Irish Copyright Legislation and Trinity College Library conditions of use and acknowledgement.

Signed: Ningsong Fan

Date: September 30, 2023

Abstract

Metallic glasses (MGs) and high-entropy alloys (HEAs) are both emerging multi-component alloys with unique microstructures and extraordinary properties. Cold spray, as a burgeoning solid-state material deposition process, plays an active role in manufacturing high-performance coatings and restoring damaged metal parts and has been moved into solid-state additive manufacturing in recent years, which provides an alternative to allow the fabrication of MGs and HEAs. The low processing temperature involved in cold spray helps to minimize metallurgical defects, such as phase transformation, oxidation, and crystallization (for MGs), in the deposits and retain an original structure as feedstock powder. For MGs, although the study on cold-sprayed BMGs has been carried out in the past two decades, the interparticle bonding mechanism and dynamic evolution of crystallization are both unclear and need further clarification. While for HEAs, the study on microstructure evolution and mechanical properties of cold-sprayed HEAs is quite limited, and systematic research on cold spraying HEA coatings or deposits is imperative to widen their potential application. The equiatomic CoCrFeNi HEA, serving as a basic system in the HEA family, was selected as the research object and fabricated by cold spraying. Considering the high deformation resistance of CoCrFeNi HEA, which may lead to the formation of pores and poor interparticle bonding even under high processing parameters, various strengthening strategies (i.e., post heat-treatment, in-process densification, and microalloying) were carefully combined with the cold spray process to intentionally modify the microstructure and improve the mechanical properties (e.g., tensile properties, compressive properties, and wear resistance) of the cold-sprayed CoCrFeNi HEA. The main research content and results of this study are as follows:

Amorphous $Zr_{55}Cu_{30}Ni_{15}Al_{10}$ bulk metallic glass deposit was produced by cold spray. The bonding mechanism of metallic glass particles was systematically investigated

by studying the deformation behavior of individual particles after deposition. In addition, the dynamic evolution mechanism of the amorphous phase into nanocrystal structures at severely deformed interfacial regions during cold spray was also carefully investigated. The results showed that two collective particle bonding mechanisms contributed to the formation of metallic glass deposits, i.e., high-velocity impact induced localized metallurgical bonding at the fringe of the interface and high particle temperature induced viscosity reduction and the resultant annular metallurgical bonding band. Moreover, the different amorphous/nanocrystal structures in cold-sprayed metallic glass deposits, which can represent different evolution stages in the nanocrystallization process, were observed for the first time. The nanocrystallization process can be divided into the following three stages: composition segregation, the formation of ordered 1D and 2D transition structures, and 3D nanocrystals.

The CoCrFeNi high-entropy alloy (HEA) was fabricated by cold spray and then post-spray annealed at the temperature range of 500-1000 °C for 2 hours. By adjusting the annealing temperature, four types of deposits (i.e., as-sprayed, recovered (500 °C), partially recrystallized (700 °C), and fully recrystallized (1000 °C) deposits) were obtained, and their microstructure, compressive and tensile properties were systematically explored. The results showed that the as-sprayed deposit exhibited high compressive yield strength but fractured within the elastic deformation regime in the tensile test. Only recover annealing hardly influenced the microstructure and mechanical properties of the deposits. While recrystallization annealing could trigger enhanced interface diffusion and the resultant metallurgical bonding. The partially recrystallized and fully recrystallized deposits exhibited an excellent combination of compressive strength and ductility. While the fully recrystallized deposit exhibited almost equal tensile and compressive yield strength and the best recovery of tensile ductility.

The CoCrFeNi HEA deposits were fabricated using different combinations of particle size ranges and gas parameters. The microstructure evolution, deformation behavior, and mechanical properties of the deposits under different combinations were investigated. The results showed that a combination of a wide particle size range of the feedstock powder and low gas parameters could trigger in-process densification of the deposits. At such conditions, a proportion of the particles (particularly those with large sizes) fail to deposit and rebound after their impact instead. The rebound particles result in accumulative plastic deformation of the deposited particles and further reduction in porosity. With this novel strategy, the detrimental thermal effects encountered in cold spraying using high-temperature processing gas (such as oxidation, nitridation, and phase changes) can be effectively minimized. However, the strategy comes at the expense of the large-sized particles, implying low deposition efficiency. Moreover, the mismatch between the particle size ranges and the gas parameters will lead to the inclusion of less deformed large-sized particles, leading to the formation of large pores and deteriorated mechanical performance.

Microalloying strategy was applied to CoCrFeNi HEA feedstock powder, and the CoCrFeNiMo_x (x=0, 0.2, 0.5, and 1) deposits were fabricated by cold spray to improve the wear resistance of CoCrFeNi deposits. The microstructure evolution, mechanical properties, and tribological properties were systematically investigated. The results showed that Mo₀, Mo_{0.2}, and Mo_{0.5} deposits have a face-centered-cubic (FCC) single structure, while Mo_{1.0} deposits were composed of FCC matrix and hard brittle phases. The doping of Mo element into CoCrFeNi HEA deposits significantly increased the hardness due to the enhanced solid solution strengthening and precipitation strengthening. As a result, the anti-wear properties of Mo-doped CoCrFeNi HEA deposits were gradually improved with the increase in Mo ratios. The Mo_{1.0} deposit exhibited the lowest specific wear rate of $0.51 \times 10^{-4} \text{ mm}^3/\text{N}\cdot\text{m}$, which was reduced by 94.9% in comparison to the Mo₀ deposit.

Keywords: Cold spray, Additive manufacturing, Bulk metallic glass (BMG), High-entropy alloy (HEA), Plastic deformation, Microstructure, Mechanical properties.

Acknowledgements

First and foremost, I would like to express my sincere gratitude to my supervisor, Dr. Shuo Yin, for his invaluable guidance, unlimited support, and outstanding feedback throughout my entire doctoral research program over the past four years. I have been extremely lucky to have a supervisor who is willing to share his broad knowledge of cold spray with me and offer valuable opportunities to me to participate in academic collaboration. I would also like to thank Dr. Rocco Lupoi for co-leading the STAM research group and making global impacts, particularly in the cold spray community.

I would like to extend my deepest gratitude to Dr. Yingchun Xie (Institute of New Materials, Guangdong Academy of Sciences, China) for his assistance in sample preparation. This dissertation would have never been accomplished without his assistance and support. I would like to acknowledge the assistance from Dr. Chunjie Huang (Universität der Bundeswehr, Germany), Dr. Jan Cizek (The Czech Academy of Sciences, Czech Republic), Dr. Aran Rafferty (Trinity College Dublin, Ireland) and Mr. Tao Chen (South China University of Technology, China) for their help in material characterization. A special thanks to the lab technician, Mr. Robert Dunbar, for equipment training and technical support. In addition, I would like to mention the Advanced Microscopy Laboratory (AML) of Trinity College Dublin for its support in data acquisition.

I would like to recognize the efforts of Dr. Wenya Li (Northwestern Polytechnical University, China), Dr. Wen Chen (University of Massachusetts, US), and Dr. Lin Liu (Huazhong University of Science and Technology, China) for the fruitful discussions and valuable suggestions on the published journal articles involved in this dissertation.

I would like to thank my colleagues in the research group for their time and

willingness to share their experiences and views. Thanks to all the members of staff from Trinity College, who offered me help and opportunities during this long journey.

I would like to acknowledge the support from the China Scholarship Council (CSC) -Trinity College Dublin Joint Scholarship Programme (201906460020), which offers me a precious opportunity to pursue the doctorate degree in Ireland. Thanks to Trinity College for providing a breathtakingly beautiful campus and a positive research environment. The experience of studying at Trinity College will be the most memorable memory of my life.

Lastly and most importantly, I would like to thank my family and friends for their love, support, and trust throughout my years of study and through the process of research. Thank you very much.

This journey is long and full of difficulties, but now it is finally coming to an end. Thanks again to those who have helped me to achieve this goal.

List of Publication

Journal Articles

1. **Ningsong Fan**, Chunjie Huang, Zhongyu Wang, Pengfei Yu, Wen Chen, Rocco Lupoi, Qingge Xie[✉], Lin Liu[✉], Shuo Yin[✉]. Interparticle bonding and interfacial nanocrystallization mechanisms in additively manufactured bulk metallic glass fabricated by cold spray, *Additive Manufacturing*, 58, 2022, 101626. (JCR Q1, IF 11.632) – [Chapter 3](#)
2. **Ningsong Fan**, Aran Rafferty, Rocco Lupoi, Wenya Li, Yingchun Xie, Shuo Yin[✉]. Microstructure evolution and mechanical behavior of additively manufactured CoCrFeNi high-entropy alloy fabricated via cold spraying and post-annealing *Materials Science and Engineering A*, 873, 2023, 144748. (JCR Q1, IF 6.4) – [Chapter 4](#)
3. **Ningsong Fan**, Jan Cizek, Chunjie Huang, Xinliang Xie, Zdenek Chlup, Richard Jenkins, Rocco Lupoi, Shuo Yin[✉]. A new strategy for strengthening additively manufactured cold spray deposits through in-process densification, *Additive Manufacturing*, 36, 2020, 101626. (JCR Q1, IF 10.998)
4. Shuo Yin[✉], **Ningsong Fan**, Chunjie Huang, Yingchun Xie, Chao Zhang, Rocco Lupoi, Wenya Li[✉]. Towards high-strength cold spray additive manufactured metals: methods, mechanisms, and properties, *Journal of Materials Science & Technology*, 170, 2024, 47-64. (JCR Q1, IF 10.9) – [Chapter 2 Section 2.1](#)
5. Pengfei Yu, **Ningsong Fan**, Yongyun Zhang, Zhijun Wang, Wenya Li[✉], Rocco Lupoi[✉], Shuo Yin[✉]. Microstructure evolution and composition redistribution of FeCoNiCrMn high entropy alloy under extreme plastic deformation, *Materials Research Letters*, 10, 2022, 124-132. (JCR Q1, IF 8.3)
6. Jinguo Ge[✉], **Ningsong Fan**, Yuhong Long[✉], Jian Lin, Yongping Lei, Shuo Yin[✉]. Investigation on H13 buildups produced with wire arc additive manufacturing: deposition strategies-induced microstructural evolution and mechanical performances, *Journal of Alloys and Compounds*, 860, 2021, 157893. (JCR Q1, IF 5.316)
7. Yingchun Xie, **Ningsong Fan**, Jingwen Yang, Wenya Li, Rocco Lupoi, Xueping Guo, Renzhong Huang[✉], Shuo Yin[✉]. Improvement of tensile strength of cold sprayed Fe deposits via in-process powder preheating, *Materials Letters*, 2022. (JCR Q2, IF 3.547)
8. Bingqian Jin, Nannan Zhang[✉], Bowei Xing, **Ningsong Fan**, Sainan Nie, Xin Wang, Shuo Yin[✉], Xiaofei Zhu[✉]. Effect of annealing treatment on microstructural evolution and compressive behavior of Al_{0.5}CrFeNi_{2.5}Si_{0.25} high-entropy alloy, *Materials Characterization*,

205, 2023, 113233. (JCR Q1, IF 4.7).

9. Dong Wu, Yaxin Xu[✉], Wenya Li[✉], **Ningsong Fan**, Yang Yang, Shuo Yin. Significant improvement of mechanical properties of cold-spray-additive manufactured FeCoNiCrMn high-entropy alloy via post-annealing, *Materials Characterization*, 2023, 113350. (JCR Q1, IF 4.7).
10. D. Guo, M. Kazasidis, A. Hawkins, **N. Fan**, Z. Leclerc, D. MacDonald, A. Nastic, R. Nikbakht, R. OrtizFernandez, S. Rahmati, M. Razavipour, P. Richer, S. Yin[✉], R. Lupoi[✉], B. Jodoin[✉]. Cold spray: over 30 years of development towards a hot future, *Journal of Thermal Spray Technology*, 31(4), 866-907, 2022. (JCR Q1, IF 3.1)

Conference Presentations

1. **Ningsong Fan**, Chunjie Huang, Pengfei Yu, Wen Chen, Rocco Lupoi, Lin Liu, Shuo Yin[✉]. Interparticle bonding and interfacial nanocrystallization mechanisms in cold sprayed metallic glass. In: *International Thermal Spray Conference (ITSC)*, May 4-6, 2022, Vienna, Austria.

Book Chapters & Patents

1. **Ningsong Fan**, Xinliang Xie, Chunjie Huang, Rocco Lupoi, Shuo Yin[✉]. Applications of Laser in Cold Spray. In: *Laser Cladding of Metals*. Springer International Publishing, 2021, pp. 395-427.

Manuscripts Under Review / In Preparation

1. **Ningsong Fan**. Cold Spray Additive Manufacturing of Mo-doped CoCrFeNi High-entropy alloy with Excellent Wear Resistance. (In preparation) – [Chapter 6](#)

Contents

Declaration	I
Abstract	III
Acknowledgements	VII
List of Publication	IX
Contents	XI
List of Figures	XVII
List of Tables	XXVII
Chapter 1 Introduction	1
Chapter 2 Literature Review	5
2.1 Cold Spray Process.....	5
2.1.1 Principal, characteristics, and applications of cold spray	5
2.1.2 Cold spray processing parameters	12
2.1.3 Bonding mechanism of cold-sprayed particles	18
2.1.4 Strengthening strategies for cold-sprayed Deposits.....	27
2.2 Metallic Glass	32
2.2.1 Historical evolution	32
2.2.2 Manufacturing Processes	35
2.2.3 Plastic Deformation Behavior.....	37
2.3 Research Progress on Cold-sprayed Metallic Glasses	39
2.3.1 Feedstock Powder.....	42
2.3.2 Processing Parameters	44
2.3.3 Particle Bonding Mechanism.....	47

2.3.4	Crystallization Behavior.....	52
2.4	High-entropy Alloys	55
2.4.1	Definition	55
2.4.2	Core effects of HEAs	57
2.4.3	Manufacturing processes	62
2.5	Research Progress on Cold-sprayed High-entropy Alloys.....	63
2.5.1	Feedstock Powder	65
2.5.2	Processing Parameters.....	67
2.5.3	Microstructure Evolution and Deposit Properties	70
2.5.4	Particle Bonding Mechanism	75
2.5.5	Strengthening Cold-Sprayed High-entropy Alloy Deposits	77
2.6	Research Objectives	86
Chapter 3 Interparticle Bonding and Interfacial Nanocrystallization Mechanisms in Cold-sprayed Bulk Metallic Glass		89
3.1	Material and Methodology	90
3.1.1	Feedstock Powder	90
3.1.2	Cold Spray Deposition Process	91
3.1.3	Microstructure Characterization.....	93
3.2	Microstructure of the Cold-sprayed Zr55 deposit.....	93
3.3	Bonding Mechanism of Individual Metallic Glass Particles	95
3.3.1	Mechanism I-High-velocity Impact Induced Localized Metallurgical Bonding at the Fringe of Interface	95
3.3.2	Mechanism II- High particle temperature induced viscosity reduction and resultant annular metallurgical bonding band.....	99
3.3.3	A summary of the Bonding Mechanism of Cold-sprayed Metallic Glass Particles.....	101

3.4	Nanocrystallization of Cold-sprayed Metallic Glass Particles.....	102
3.4.1	Nanocrystallization Conditions: Thermal and Mechanical Factors	103
3.4.2	Nanocrystallization Process: From Amorphous Structure to Nanocrystals	106
3.4.3	Nanocrystallization Mechanism of Cold-sprayed Metallic Glass Particles	110
3.5	Summary.....	111
Chapter 4 Microstructure Evolution and Mechanical Behavior of Additively Manufactured CoCrFeNi High-entropy alloy Fabricated via Cold Spray and Post-annealing		
113		
4.1	Material and methodology	114
4.1.1	Feedstock Powder and Cold Spray Process.....	114
4.1.2	Microstructure Characterization	116
4.1.3	Mechanical Properties Measurement.....	117
4.2	Microstructure Evolution.....	118
4.3	Microhardness, Compressive and Tensile properties	125
4.4	Strengthening and Toughening Mechanisms	132
4.4.1	Origin of the High Strength in the Deposits	133
4.4.2	Tension-compression Asymmetry in the Deposits.....	136
4.5	Summary.....	137
Chapter 5 Strengthening Additively Manufactured CoCrFeNi High-entropy alloy by In-process		
Densification During Cold Spray		
139		
5.1	Material and Methodology.....	140
5.1.1	Feedstock Powder and Deposit Fabrication.....	140
5.1.2	Microstructure Characterization	142
5.1.3	Mechanical Properties Evaluation	143
5.2	Microstructure Evolution.....	143

5.3	Mechanical Properties	153
5.4	Strengthening Mechanisms.....	158
5.5	Advantages and Disadvantages of the in-process densification	160
5.5.1	Advantages.....	160
5.5.2	Disadvantages.....	161
5.6	Summary	162
Chapter 6 Solid-state deposition of Mo-doped CoCrFeNi High-entropy alloy with Excellent Wear Resistance via Cold Spray		
163		
6.1	Feedstock Powder and Experimental Methodology	164
6.1.1	Feedstock Powder	164
6.1.2	Cold Spray Process.....	166
6.1.3	Microstructure Characterization.....	167
6.1.4	Mechanical Properties Measurement	167
6.2	Microstructure, Deposition behavior and Phase structure	169
6.2.1	General Microstructure.....	169
6.2.2	Single Splat Deposition.....	170
6.2.3	Phase Composition.....	171
6.3	Nanohardness	173
6.4	Dry Sliding Wear Behavior	178
6.4.1	Coefficient of Friction.....	178
6.4.2	2D & 3D Wear Track Morphology and Specific Wear Rate.....	180
6.4.3	Worn Surface Morphology and Wear Mechanism.....	183
6.5	Summary	189
Chapter 7 Conclusion and Prospects.....		
191		

7.1	Conclusion.....	191
7.2	Prospects.....	194
	Reference.....	197

List of Figures

Fig. 2.1 Schematic of the working principle of cold spray.....	6
Fig. 2.2 A comparison between cold spray and thermal spray processes about gas temperature and particle velocity [20].....	7
Fig. 2.3 Different functional coatings deposited by cold spray: (a) Cold-sprayed magnetic coating on the bottom of cookware, (b) Cold-sprayed hybrid heatsinks, (c) Cold-sprayed sputtering targets, and (d) Cold-sprayed wear-resistant coating onto a brake disk [33].	8
Fig. 2.4 Repairing damaged parts via cold spray. (a) Standard repairing procedure, (b) S-92 helicopter gearbox sump, (c) Flap transmission tee box housing of an aircraft [11].	9
Fig. 2.5 Cold spray additive manufactured freestanding components. (a) Cu-alloy combustion chamber, (b) Orthogrid structures, (c) Ti-6Al-4V freestanding turbojet aircraft engine fan shaft, (d) Cu-Ni rocket nozzle. The parts from (a) to (d) are fabricated by Impact Innovation. (e) Cu hand deposited by Université de Technologie Belfort-Montbéliard, (f) Cu five-pointed star deposited by Shanxi DW automation, (g) A part fabricated by SPEE3D.	11
Fig. 2.6 (a) Schematic of the typical processing parameters used in cold spray, (b) Effect of processing parameters on the properties of cold-sprayed deposits [11].	12
Fig. 2.7 Effect of nozzle traverse speed on the single-track deposit thickness and cross-sectional profile. (a) 80 mm/s, (b) 40 mm/s, (c) 20 mm/s, (d) 10 mm/s [41].	14
Fig. 2.8 Effect of standoff distance on the deposition efficiency (a) Ref [42] (b)Ref [43].	15
Fig. 2.9 Critical velocity and impact velocity over particle size [55].	17
Fig. 2.10 Schematic correlation between particle velocity, deposition efficiency and impact effects for a constant impact temperature [60].....	19
Fig. 2.11 The time evolution of particle and the substrate shapes during impact of a 25- μm Cu particle onto the Cu substrate at 550 m/s: (a) 4.4 ns; (b) 13.2 ns; (c) 22.0 ns and (d) 30.8 ns [61].	20
Fig. 2.12 In-situ observation of the bonding moment in microparticle impact (45- μm Al particle impacts onto Al substrate at 605 m/s and 805 m/s, respectively). Material jetting is pointed with white arrows [74]. ...	23
Fig. 2.13 Schematic representation of jetting in cold spray: Stage I. Impact induces a shock wave; Stage II. Shock detaches from the leading edge; Stage III. Jet forms on the basis of pressure releases [75].	23

- Fig. 2.14** Characterization of the regions at the center of the interparticle interface of Cu deposits fabricated by cold spray at low (578 m/s, left side) and high (807 m/s, right side) particle impact velocity, respectively. (a) and (e) SEM images, (b) and (f) TEM images, (c) and (g) STEM-EDS mapping of Cu, (d) and (h) STEM-EDS mapping of oxygen [78].25
- Fig. 2.15** Schematic diagram of the bonding process of cold-sprayed particles accompanying with the breaking-up and extruding of surface oxide films and the formation of jetting [63,79].26
- Fig. 2.16** Schematic of available strengthening technologies for cold-sprayed deposits. According to the stage that these strengthening technologies are utilized in cold spray process, the strengthening technologies are classified into three categories, namely pre-process, in-process, and post-process.28
- Fig. 2.17** The size development of metallic glass since 1960s, exhibiting an evolution from film, ribbon to bulk components [125].35
- Fig. 2.18** The road of manufacturing metallic glasses towards bulk metallic glasses with complex geometries [124].36
- Fig. 2.19** Deformation map for metallic glasses in (a) stress–temperature and (b) strain rate–temperature axes [139].38
- Fig. 2.20** Research articles on cold-sprayed metallic glass deposits (Data collected from Scopus).39
- Fig. 2.21** Characteristics of the $\text{Cu}_{54}\text{Ni}_6\text{Ti}_{22}\text{Zr}_{18}$ metallic glass feedstock powder [73]. (a) Particle surface morphology, (b) High-resolution electron microscopy images with corresponding FFT insets, (c) XRD pattern, (d) DSC curve. Note the diffusion halo in FFT and broad diffraction peak in the XRD pattern indicated the feedstock powder had an amorphous structure.43
- Fig. 2.22** Effect of gas temperature, gas pressure and stand-off distance on the (a) deposition efficiency, (b) thickness, (c) porosity and (d) microhardness of the cold-sprayed $\text{Al}_{88}\text{Ni}_6\text{Y}_{4.5}\text{Co}_1\text{La}_{0.5}$ metallic glass deposit [162].45
- Fig. 2.23** Cross-sectional morphology of the as-sprayed Ni-based metallic glass coatings under different powder preheating temperature, (a) room temperature, (b) 450 °C, (c) 550 °C [89].46
- Fig. 2.24** Effects of powder preheating temperature on the (a) flattening ratio, (b) porosity, (c) bond strength, (d) microhardness and (e) amorphous phase fraction and oxygen content of the as-sprayed Ni-based metallic glass deposit [89].47
- Fig. 2.25** Individual particle deposition behavior of MG particles. (a) Deposition behavior of NiTiZrSiSn MG particles, exhibiting three characteristic regions [142], (b) A single $\text{Cu}_{50}\text{Zr}_{50}$ MG particle detached after cavitation testing and a corresponding crater on the substrate surface, both showing pronounced vain

pattern [156], (c) An incompletely detached particle by showing the vain pattern and the associated gap between the particle and the substrate [156].	48
Fig. 2.26 (a) Deposition efficiency and (b) Cross-sectional morphology of the cold-sprayed $\text{Fe}_{72.8}\text{Si}_{11.5}\text{Cr}_{2.2}\text{B}_{10.7}\text{C}_{2.9}$ metallic glass deposits or particles at different Re numbers, (c) Deposition behavior of individual $\text{Zr}_{41.2}\text{Ti}_{13.8}\text{Cu}_{12.5}\text{Ni}_{10}\text{Be}_{22.5}$ metallic glass particles at two typical Re numbers [159].	52
Fig. 2.27 Microstructure evolution at the impacting interface of the cold-sprayed Cu-based MG deposits. (a, b) The center of the interface at low gas pressure, (c, d) The center of the interface at high gas pressure, (e, f) The edge of the interface at low gas pressure, (g, h) The edge of the interface at high gas pressure. Note the nanocrystallization can be found at the edge of the impacting interface, and the increased gas pressure led to the increased nanocrystals [148].	54
Fig. 2.28 Periodic development in metals. [187,188]	56
Fig. 2.29 Excellent properties of High-entropy alloys (HEAs). (a) Hardness of HEAs compared with 17–4 PH stainless steel, Hastelloy, and 316 stainless steel [184], (b) Yield strength as a function of density for HEAs compared with other materials, particularly structural alloys [189], (c) Specific-yield strength verse Young’s modulus of HEAs compared with other materials, particularly structural alloys [189], (d) Fracture toughness as a function of yield strength for HEAs in relation to a wide range of material systems [190].	57
Fig. 2.30 (a) Schematic illustration of intrinsic lattice distortion effect on Bragg diffraction. A comparison between a perfect lattice with the same atoms and a distorted lattice with a solid solution of different-sized atoms which are expected to randomly distribute in the crystal lattice [191], (b) Effect of temperature and distortion on XRD intensity [191], (c) XRD patterns of Cu–Ni–Al–Co–Cr–Fe–Si alloy series with the increasing number of incorporated principal elements [191].	59
Fig. 2.31 (a) Temperature dependence of the diffusion coefficients for Cr, Mn, Fe, Co, and Ni in different matrices [192], (b) Normalized activation energies of diffusion for Cr, Mn, Fe, Co, and Ni in different matrices [192]. Note the normalized activation energies indicate Q/T_m (or Q/T_s , where T_s is the solidus temperature for alloys), and the higher Q/T_m indicates the lower diffusion coefficient.	60
Fig. 2.32 (a) Hardness and lattice constants of $\text{CuCoNiCrAl}_x\text{Fe}$ HEA with different Al ratios [195], (b) Hardness of $\text{CoNiCrAl}_x\text{Fe}$ HEA with different Al ratios [196]. Note the A, B, and C in (a) indicate hardness and lattice constants of FCC phase and BCC phase.	62
Fig. 2.33 Summarization of current manufacturing processes for multi-scale high-entropy alloys.	63
Fig. 2.34 Different methods for the preparation of the feedstock powder used for cold spray deposition: (a) Gas-atomized FeCoNiCrMn HEA powder [16], (b) Mechanical alloyed AlNiCoFeCrTi HEA powder [214], (c) Mechanical mixed $\text{AlCrCoFe}_x\text{NiCu}$ [220].	66

- Fig. 2.35** Microstructure of the cold-sprayed FeCoNiCrMn HEA deposits under various processing parameters. A comparison of the deposits fabricated using (a) nitrogen and (b) helium, (c) Effect of gas temperature and spraying distance on the microstructure of the deposits, (d) Deposit thickness and porosity data under different gas temperatures and spraying distances..... 69
- Fig. 2.36** Representative microstructure of the cold-sprayed FeCoNiCrMn HEA coating [16]. 71
- Fig. 2.37** Electrochemical test results of the substrate with and without cold-sprayed CoCrFeNi HEA coating in 3.5 wt% NaCl solution at room temperature. (a) Open circuit potential, (b) Potentiodynamic polarization. (c) Surface morphology of the substrate with and without cold-sprayed CoCrFeNi HEA coating after immersion tests for 28 days [207]. 74
- Fig. 2.38** Oxidation mechanism of the cold-sprayed FeCoCrNiMn at 900 °C [225]..... 75
- Fig. 2.39** Cross-sectional morphologies of multi-particle impacts of CrMnCoFeNi HEA powder onto SS304 substrate (He, 3.2 MPa, 400 °C). Green and red dotted lines show bonded and not bonded areas, respectively [155]. 76
- Fig. 2.40** Microstructure and mechanical properties of the cold-sprayed FeCoNiCrMn HEA deposits before and after heat treatment. (a) OM images, EBSD IPF maps, and KAM maps [203], (b) Microhardness, and (c) Wear rate [209]. 79
- Fig. 2.41** Microstructure of the (a) as-sprayed and (b) laser-melted HEA coatings [221]. The feedstock powders used in cold spray process were composed of ~3.5 wt.% Cu, ~0.5 wt.% Al, ~21 wt.% 316L and ~75 wt.% T700. Due to the different deposition efficiency of each kind of powder, the content of each powder in the target coating was calculated to be 10.5 wt.% Cu, 1.5 wt.% Al, 47 wt.% 316L and 47 wt.% T700. The final composition of laser-melted HEA coating can be expressed as $Al_{0.1}Cr_{0.4}FeNi_{10.8}Mo_{0.2}Si_{10.05}Ti$ 81
- Fig. 2.42** Microstructure and phase structure of the cold-sprayed and laser-assisted-cold sprayed CrMnCoFeNi HEA deposits. (a) Cross-sectional microstructure of the as-sprayed CrMnCoFeNi HEA deposit, (b) Cross-sectional microstructure of the laser-assisted cold-sprayed CrMnCoFeNi HEA deposit, (c) Phase structure of the powder, CS, and LACS CrMnCoFeNi deposits [206]. Note the deposit was manufactured using nitrogen as the propelling gas under the pressure of 4.9 MPa and the temperature of 950 °C. 82
- Fig. 2.43** Microstructure and mechanical properties of the cold-sprayed Al₂O₃-reinforced FeCoNiCrMn HEA deposits. Cross-sectional microstructure of the as-sprayed (a) FeCoNiCrMn, (b) Al₂O₃-FeCoNiCrMn (1:8), (c) Al₂O₃-FeCoNiCrMn (1:4), (d) Microhardness and (e) Tribological properties [202]. 84
- Fig. 2.44** Microstructure, phase composition, and mechanical properties of the cold-sprayed AlCrCoFe_xNiCu (x=0, 0.5, 1.0, 1.5, 2.0) HEA deposits followed by induction remelting. (a) Microstructure evolution, (b) XRD pattern of the deposits before and after induction treatment, (c) Microhardness, and (d) Tribological properties [220]. Note ID refers to interdendritic and DR refers to dendritic..... 86

Fig. 3.1 Characterization of the as-atomized Zr55 amorphous powder used for deposit manufacturing. Surface morphology at (a) low magnification and (b) high magnification, (c) XRD spectrum, and (d) Particle size distribution.....	91
Fig. 3.2 In-house cold spray system in Trinity College Dublin	92
Fig. 3.3 Characterization of the cold-sprayed Zr55 deposit: (a) Cross-sectional microstructure, (b) EDS map of elements distribution, (c) Etched cross-sectional microstructure, and (d) XRD spectrum.	95
Fig. 3.4 Top view of the representative surface morphologies of (a)-(d) individual Zr55 deposited particles and (e)-(f) craters created by rebound Zr55 particles. Note the substrate used in single particle deposition is the polished cold-sprayed Zr55 deposit.	98
Fig. 3.5 FIB process of individual Zr55 deposited particle: (a) Surface morphology, (b) Cross-sectional morphology revealing particle-substrate interface, (c) Close view of metallurgical bonding at the interface.	99
Fig. 3.6 (a) Top view of the surface morphology of an individual Zr55 deposited particle with the liquid-like surface, (b)-(d) FIB process of an individual particle with the liquid-like surface: (b) Surface morphology, (c) Cross-sectional morphology revealing the particle-substrate interface, (d) Close view of metallurgical bonding at the interface.....	101
Fig. 3.7 Characterization of the nanostructure at the interparticle interface: (a) SEM image exhibiting interparticle boundary between two particles, (b) SEM and (c) TEM images of the lamella lifted out by FIB, (d)-(e) TEM micrograph with SAED pattern inset: (d) Away from the interparticle interface and (e) Near the interparticle interface, respectively.....	103
Fig. 3.8 HRTEM images and corresponding FFT diffraction patterns of localized ordered clusters near the interparticle interface: (a) Localized ordered atomic configuration, (b) Nanocrystal structure.	109
Fig. 3.9 Evolution of nanocrystals from an amorphous state.	111
Fig. 4.1 Fabrication of CoCrFeNi HEA deposits via cold spray additive manufacturing process. (a) Surface morphology of the gas-atomized powder, (b) Etched microstructure of individual powder with equiaxed grains, (c) Particle size distribution of the powder with D50 of 38.65 μm , (d) Uniform element distribution in the powder, (e) Schematic diagram of cold spray additive manufacturing, (f) Small bulk HEA (22 mm \times 10 mm \times 9 mm) machined from the deposit after cold spraying, (g) Schematic illustration of the extracted specimens from as-sprayed deposit for tension and compression tests. BD: Building direction, TD: Transverse direction.	115

- Fig. 4.2** Cross-sectional microstructure of the cold-sprayed CoCrFeNi HEA deposits under different annealing temperatures: (a) As-sprayed, (b) 500 °C, (c) 700 °C and (d) 1000 °C. The deposits exhibited gradually decreased micropores and interparticle boundaries with the increased temperatures..... 118
- Fig. 4.3** Relative density of the cold-sprayed CoCrFeNi HEA deposits under different annealing temperatures. 119
- Fig. 4.4** X-ray diffraction (XRD) analysis of the feedstock powder and the cold-sprayed CoCrFeNi HEA deposits in the as-fabricated and annealed states..... 120
- Fig. 4.5** Etched microstructure of the cold-sprayed CoCrFeNi HEA deposits under different annealing temperatures: (a, e) As-sprayed, (b, f) 500 °C, (c, g) 700 °C, and (d, h) 1000 °C. The highly deformed particles experienced remarkable recrystallization and grain growth at 1000 °C, as evidenced by the increased grain size..... 122
- Fig. 4.6** EBSD characterization of the as-sprayed CoCrFeNi HEA deposit. (a) Inverse pole figure (IPF) map, (b) Kernel average misorientation (KAM) map, (c) Grain size distribution, and (d) Misorientation angle distribution..... 124
- Fig. 4.7** EBSD characterization of the cold-sprayed CoCrFeNi HEA deposit annealed at 1000 °C (HT1000). (a) Inverse pole figure (IPF) map, (b) Kernel average misorientation (KAM) map, (c) Grain size distribution, and (d) Misorientation angle distribution. 124
- Fig. 4.8** Vickers hardness test results of the CoCrFeNi HEA feedstock powder and cold-sprayed deposits before and after annealing. (a) Feedstock powder and (b) Cold-sprayed deposits microhardness, (c) Corresponding morphology of indentations, and (d) A comparison with their counterparts fabricated through other prevailing manufacturing routes [196,268–277]. Note that the images of indents were displayed in the rainbow color scheme..... 126
- Fig. 4.9** Compressive properties of the cold-sprayed CoCrFeNi HEA deposits before and after annealing. (a) Representative engineering stress-strain curves, (b) Compressive strength and strain at failure, (c) Compressive strength at 50% stain versus yield strength of CoCrFeNi HEA parts manufactured by different techniques [271,278–288]. The yield strength of the deposits is determined by the 0.2% strain offset method..... 127
- Fig. 4.10** Tensile properties of the cold-sprayed CoCrFeNi HEA deposits before and after annealing. (a) Representative engineering stress-strain curves, (b) The ultimate tensile strength (UTS) and elongation (EL). 129
- Fig. 4.11** Fractographic analysis of the fracture surface of the cold-sprayed CoCrFeNi HEA deposits under different annealing temperatures: (a) As-sprayed, (b) 500 °C, (c) 700 °C and (d) 1000 °C. 132

- Fig. 4.12** The yield strength of the cold-sprayed CoCrFeNi deposits obtained from tensile and compression tests. Note that the as-sprayed and the HT500 deposits exhibited brittle failure without ductility under tension, and the strength at failure was taken as tensile yield strength. 136
- Fig. 5.1** Characterization of the gas-atomized CoCrFeNi HEA powders used for cold-sprayed deposits fabrication. (a, c, e) Particle surface morphology and (b, d, f) Particle size distribution. 141
- Fig. 5.2** Microstructure of the cold-sprayed CoCrFeNi HEA deposits fabricated using different combinations of particle size ranges and gas parameters in as-sprayed (left column) and vacuum heat-treated (right column) conditions. (a, b) D1, (c, d) D2, (e, f) D3, (g, h) D4, (i, j) D5. 145
- Fig. 5.3** Relative density of the cold-sprayed CoCrFeNi HEA deposits under different processing parameters in the as-fabricated and vacuum heat-treated status. 146
- Fig. 5.4** Etched microstructure and the corresponding binary images of the as-fabricated CoCrFeNi HEA deposits fabricated under different combinations of particle size ranges and gas parameters. (a) D1, (b) D2, (c) D3, (d) D4, (e) D5. 150
- Fig. 5.5** Etched microstructure (left column) and the corresponding binary images (right column) of the vacuum heat-treated CoCrFeNi HEA deposits fabricated under different combinations of particle size ranges and gas parameters. 152
- Fig. 5.6** Vickers hardness test results of the cold-sprayed CoCrFeNi HEA deposits fabricated under different combinations of particle size ranges and gas parameters in the as-fabricated and vacuum heat-treated states. (a) Microhardness and (b) Corresponding morphology of indentations. 153
- Fig. 5.7** Tensile properties of the cold-sprayed CoCrFeNi HEA deposits fabricated under different combinations of particle size ranges and gas parameters. (a) Representative engineering stress-strain curves, (b) The ultimate tensile strength (UTS) and elongation (EL), (c) A comparison of room-temperature tensile properties of CoCrFeNi HEAs fabricated by other manufacturing processes and cold spray additive manufacture [289,303–305]. 155
- Fig. 5.8** Fractographic analysis of the fracture surface of the cold-sprayed CoCrFeNi HEA deposits fabricated under different combinations of particle size ranges and gas parameters. (a, b) D1, (c, d) D2, (e, f) D3, (g, h) D4, (i, j) D5. 158
- Fig. 5.9** Schematic illustration of strengthening mechanisms occurring under typical combinations of the particle size ranges and gas parameters. (a) D1 deposit, (b) D3 deposit, and (c) D5 deposit. 160
- Fig. 6.1** Surface morphology (left side) and particle size distribution (right side) of the gas-atomized CoCrFeNiMo_x HEA feedstock for deposits fabrication. (a, b) Mo₀, (c, d) Mo_{0.2}, (e, f) Mo_{0.5}, and (g, h) Mo_{1.0}. 165

- Fig. 6.2** Cross-sectional microstructure of the cold-sprayed CoCrFeNiMo_x HEA deposits. (a) Mo₀, (b) Mo_{0.2}, (c) Mo_{0.5}, (d) Mo_{1.0}. 169
- Fig. 6.3** Representative surface morphologies of individual deposited CoCrFeNiMo_x HEA particles. (a) Mo₀, (b) Mo_{0.2}, (c) Mo_{0.5}, (d-f) Mo_{1.0}. Note the substrate used in single particle deposition is the polished cold-sprayed CoCrFeNiMo_x deposits. 171
- Fig. 6.4** X-ray diffraction (XRD) analysis of the CoCrFeNiMo_x HEA feedstock powder and the cold-sprayed deposits in the range of 20° to 100°. (a) XRD patterns, (b) Magnified patterns of main peaks. 173
- Fig. 6.5** Nanoindentation (left column) and nano-hardness (right column) mapping obtained from 10 x 6 nanoindentation grids on the polished cross-sectional CoCrFeNiMo_x HEA samples fabricated by cold spray. (a, b) Mo₀, (c, d) Mo_{0.2}, (e, f) Mo_{0.5}, (g, h) Mo_{1.0}. 175
- Fig. 6.6** Modulus mapping obtained from 10 x 6 nanoindentation grids on the polished cross-sectional CoCrFeNiMo_x HEA samples fabricated by cold spray. (a) Mo₀, (b) Mo_{0.2}, (c) Mo_{0.5}, (d) Mo_{1.0}. 175
- Fig. 6.7** (a) Nanohardness, (b) Modulus, and (c) Representative load-displacement curves of the cold-sprayed CoCrFeNiMo_x HEA deposits from the nanoindentation tests..... 177
- Fig. 6.8** Dry-sliding wear behavior of the cold-sprayed CoCrFeNiMo_x HEA deposits. (a) Schematic diagram of the reciprocating sliding friction and wear test, (b) Representative plots of COF as a function of sliding time, (c) Coefficient of friction (COF) averaged from three tests. The main parameters for the dry sliding wear test include normal load (20 N), oscillating frequency (4.0 Hz), stroke length (5.0 mm), and time of duration (30 mins). 179
- Fig. 6.9** 2D surface morphology (left side) and 3D topography (right side) of the wear tracks on the cold-sprayed CoCrFeNiMo_x HEA deposits. (a, b) Mo₀, (c, d) Mo_{0.2}, (e, f) Mo_{0.5}, (g, h) Mo_{1.0}. 181
- Fig. 6.10** (a) The maximum width and depth of the wear tracks and (b) The specific wear rate of the cold-sprayed CoCrFeNiMo_x HEA deposits..... 182
- Fig. 6.11** Representative worn surface morphology and EDS results of the cold-sprayed CoCrFeNi HEA deposit. (a) and (b) SEM images, (c) EDS mapping and points analysis..... 184
- Fig. 6.12** Representative worn surface morphology and EDS results of the cold-sprayed CoCrFeNiMo_{0.2} HEA deposit. (a) and (b) SEM images, (c) EDS mapping and points analysis. 185
- Fig. 6.13** Representative worn surface morphology and EDS results of the cold-sprayed CoCrFeNiMo_{0.5} HEA deposit. (a) and (b) SEM images, (c) EDS mapping and points analysis. 186
- Fig. 6.14** Representative worn surface morphology and EDS results of the cold-sprayed CoCrFeNiMo_{1.0} HEA deposit. (a) and (b) SEM images, (c) EDS mapping and points analysis. 188

Fig. 6.15 Cross-sectional morphology of the wear tracks of the cold-sprayed CoCrFeNiMo_x HEA deposits. (a) Mo₀, (b) Mo_{0.2}, (c) Mo_{0.5}, (d) Mo_{1.0}.189

List of Tables

Table. 2.1 Summarization of published works regarding cold-sprayed MG deposits	40
Table. 2.2 Summarization of published works about cold-sprayed HEA deposits	63
Table. 2.3 Summarization of the tribological properties of the as-sprayed high-entropy alloys.....	72
Table. 4.1 Summarization of room-temperature tensile properties of CoCrFeNi HEA fabricated by both traditional and additive manufacturing processes.	129
Table. 5.1 Cold spray processing parameters for the deposit fabrication	142
Table. 6.1 Nominal and measured element composition of CoCrFeNiMo _x HEA feedstock.....	166
Table. 6.2 Summary of Hardness (H), Modulus (E), H/E and H ³ /E ² values of the cold-sprayed CoCrFeNiMo _x HEA deposits from the nanoindentation test.....	177
Table. 6.3 Summarization of the specific wear rate of CoCrFeNiMo _x HEA samples fabricated by different manufacturing routes.	182

Chapter 1

Introduction

The exploration of new materials is an eternal pursuit in the development of human civilization. The breakthrough of any advanced technology is premised on the breakthrough of new materials in the corresponding fields, and the development of new materials, particularly advanced metal alloys, plays an irreplaceable role in the wave of Industry 4.0. The traditional strategy for developing advanced alloys is generally through adjusting the element types and contents to achieve specific properties. In recent decades, scientists and researchers attempted to develop alloys from a new perspective by adjusting the order or entropy of materials. Consequently, the two most innovative materials with high performance were invented, which were metallic glasses (MGs, also known as amorphous alloys) and high-entropy alloys (HEAs, also called multi-principal elements alloys). MGs are developed on the basis of structural disorder, exhibiting long-range disordered arrangement of atoms. They are typically manufactured by rapid solidification, and the disordered atomic structure can be frozen in a solid state. While for HEAs, they are obtained by introducing chemical disorder by multi-principal components mixing. The atoms are randomly disordered in occupation, but the alloy generally has a simple single-phase solid-solution structure. These two emerging materials exhibit extraordinary physical, mechanical, and chemical properties compared with conventional alloys due to their unique microstructures, which have received wide attention in both academia and industry and show great application potential in extreme environments.

Additive manufacturing (AM), also known as 3D printing, is a revolutionary technology that builds 3D parts by adding layer-upon-layer of raw material (i.e., resins, powders, wires, or sheets). The arrival of AM makes design-driven production a reality. It provides maximum geometric design freedom, and the manufacturing costs can be significantly reduced due to less material consumption compared with conventional manufacturing routes. Up to now, a number of different AM techniques have been successfully applied for the fabrication of MGs and HEAs, such as laser powder bed fusion [1,2], laser cladding [3,4], and thermal spray [5–10]. However, the complicated thermal history associated with these fusion-based processes usually leads to detrimental metallurgical defects (e.g., phase transformation, oxidation, and crystallization) in as-printed MGs and HEAs parts.

Cold spray is best known for a coating production technique in the past decades, and it has recently become a new member of the AM family as a solid-state material deposition process because of the unlimited size of cold-sprayed deposits. In this process, micron-sized feedstock powder is injected in a de-Laval nozzle by carrier gas and then accelerated by heated and high-pressurized propelling gas (i.e., typically N₂ and He) to supersonic velocities (up to 1200 m/s) through the nozzle before impacting toward a substrate. The particles experience rapid and extreme plastic deformation upon impact due to the high kinetic energy, inducing mechanical interlocking and metallurgical bonding at the region of interparticle interfaces. As a result, particles are stacked together, and thin coatings or bulk components can be built layer-by-layer at a temperature well below the material melting temperatures [11]. Since the feedstock powder does not involve melting in the whole process, the thermal influence on the cold-sprayed deposits can be minimized, and the deposits are expected to retain the microstructure as the original feedstock powder.

Cold spray provides a potential alternative for the fabrication of bulk MG and HEA deposits. Over the past decades, different MG systems (e.g., Fe-based, Al-based,

Cu-based, and Ni-based) have been successfully fabricated via cold spray. The research covers the optimization of processing parameters optimization, the investigation of particle bonding mechanisms, the plastic deformation behavior of particles and crystallization phenomenon, and the evaluation of coating properties. Nonetheless, there are still some issues that have not been resolved. For example, the direct evidence of interparticle bonding at interfaces and the dynamic evolution process of nanocrystalline from amorphous structure. In terms of HEAs, the feasibility of manufacturing HEAs by cold spray was first validated in 2019 by the team from Trinity College Dublin, and since then, a few relevant studies have been conducted by various research groups worldwide. However, very few of the research attempted to study the mechanical properties (e.g., strength, ductility, wear rate) of cold-sprayed HEAs and explore effective ways to enhance the properties, which is critical for their future industrial applications. Therefore, this dissertation aims to resolve the critical issues described above, and the ultimate goal is to develop novel HEA components and coatings via cold spray.

The dissertation includes seven chapters in total. In Chapter 1, the research background and the main content of the dissertation are briefly introduced. In Chapter 2, a general introduction to cold spray is first given. Then the development, material properties, prevailing manufacturing processes, and the plastic deformation of the two advanced materials (i.e., metallic glass and high-entropy alloy) involved in the dissertation are comprehensively detailed, respectively. In addition, the research progress of cold-sprayed BMGs and HEAs is comprehensively reviewed. The research objectives are proposed at the end of this chapter.

In Chapter 3, bulk Zr-based ($Zr_{55}Cu_{30}Ni_{15}Al_{10}$) BMG deposit is fabricated via the cold spray process. The deposition behavior, plastic deformation, and interparticle bonding mechanisms were systematically investigated through single splat tests. The nanostructure at the interparticle interface was carefully studied, and the

mechanistic nanocrystallization origins in the deposits were proposed.

In Chapter 4, the equiatomic CoCrFeNi HEA, serving as a basic system in the HEA family, was fabricated by cold spray additive manufacturing process, and post-spray annealing treatment was carried out at various temperatures to intentionally adjust the microstructure and balance the strength and ductility of the deposits. The microstructure, microhardness, compressive and tensile properties were systematically evaluated and compared with their counterparts which are manufactured by other prevailing conventional and additive manufacturing techniques. The origin of the high strength in deposits and the difference in mechanical response under compressive and tensile loads were discussed.

In Chapter 5, the in-process densification strategy, which is achieved by carefully matching the particle size ranges and gas parameters, was applied to strengthen the cold-sprayed CoCrFeNi HEA deposits. The microstructure evolution and tensile properties of the deposits fabricated using different combinations of particle size ranges and gas parameters were compared. The densification mechanism and the advantage of the in-process densification strategy were presented.

In Chapter 6, the Mo-doped CoCrFeNi HEA particles were used as feedstock powder for the fabrication of cold-sprayed deposits, which aims to increase the hardness and enhance the wear resistance property of the deposits. The deposition behavior and plastic deformation behavior of the CoCrFeNiMo_x (x=0, 0.2, 0.5, and 1) particle were investigated through single splat tests. The nanohardness and wear resistance properties of the CoCrFeNiMo_x deposits were evaluated. The wear mechanisms of the CoCrFeNiMo_x deposits under dry sliding friction were analyzed.

In Chapter 7, the main contribution of this dissertation is summarized. The current challenges and outlook of preparing BMGs and HEAs by solid-state cold spray deposition process are also proposed.

Chapter 2

Literature Review

2.1 Cold Spray Process

2.1.1 Principal, characteristics, and applications of cold spray

Cold spray, also referred to as supersonic particle deposition, is a solid-state material deposition process that was discovered by the research team from the Institute of Theoretical and Applied Mechanics of the Russian Academy of Science in Novosibirsk in the 1980s [12,13]. When the researchers tried to investigate the gas-solid two-phase flow in a supersonic wind tunnel, it was found that with the increase of gas velocity, the metal particles started to be stuck onto the solid surface rather than bouncing off it. In the early 1990s, the concept of cold spray was proposed and the first paper concerning cold spray was also published [13]. Subsequently, cold spray gradually attracted attention and rapidly developed as a coating preparation technology in surface engineering.

In cold spray process, metal particles are injected in the convergent section of a de-Laval nozzle by carrier gas and then accelerated by heated and high pressurized gas (i.e., N₂, He, or air) to high velocities (typically at 300 ~1200 m/s) through the nozzle before impacting toward a substrate, as schematically shown in [Fig. 2.1](#). The particles experience extreme and rapid plastic deformation upon impact due to the high kinetic energy, inducing localized mechanical interlocking and metallurgical bonding at the region of highly deformed interparticle interfaces. As a result,

particles are stacked together, and thin coatings or bulk deposits can be built layer by layer [11]. So far various metallic materials, such as pure metals [14], conventional alloys [15], high-entropy-alloys [16], metallic glasses [17], and metal matrix composites [18,19] have been successfully deposited by cold spray.

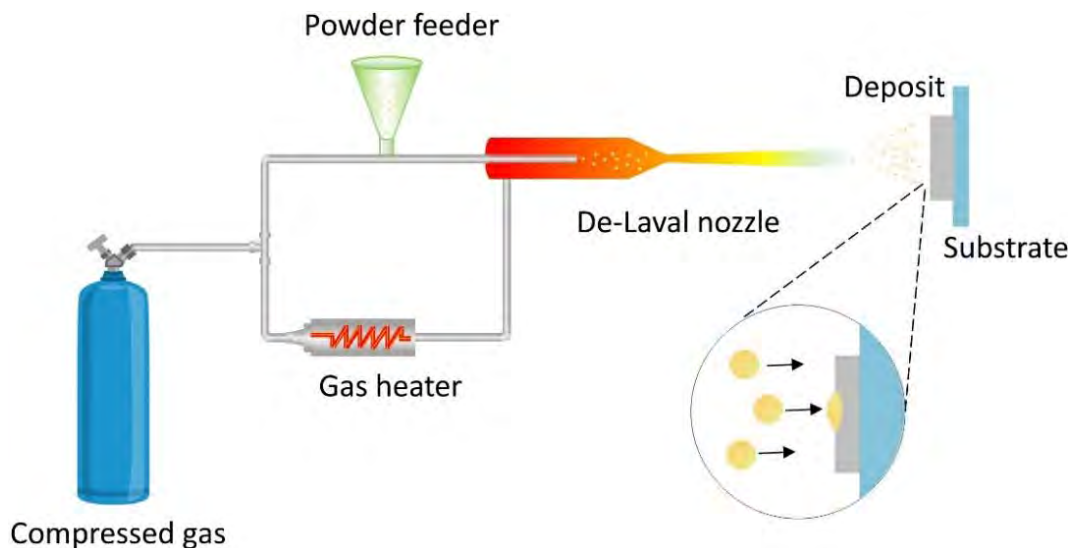


Fig. 2.1 Schematic of the working principle of cold spray.

Compared to thermal spray processes, the consolidation of powder in cold spray mainly relies on the high kinetic energy of particles rather than the thermal energy. The particles do not involve melting and remain in the solid state during the whole process. **Fig. 2.2** compares the gas temperature and particle velocity during cold spray and thermal spray processes. With the low temperature deposition characteristic, the thermal-induced defects in cold-sprayed deposits, such as oxidation, phase transformation, and thermal residual stresses, can be minimized, and the lower heat input aids in retaining the original feedstock powder structure in the deposit. In addition, the residual stress in cold-sprayed deposits is compressive stress due to the tamping effect, which enables thicker coatings (several millimeters to centimeters) or bulk components. The cold spray process is much faster than the conventional manufacturing routes of metals with deposition rates of up to a few kilograms or even a dozen kilograms per hour, which is expected to become the

fastest material deposition technology in the world.

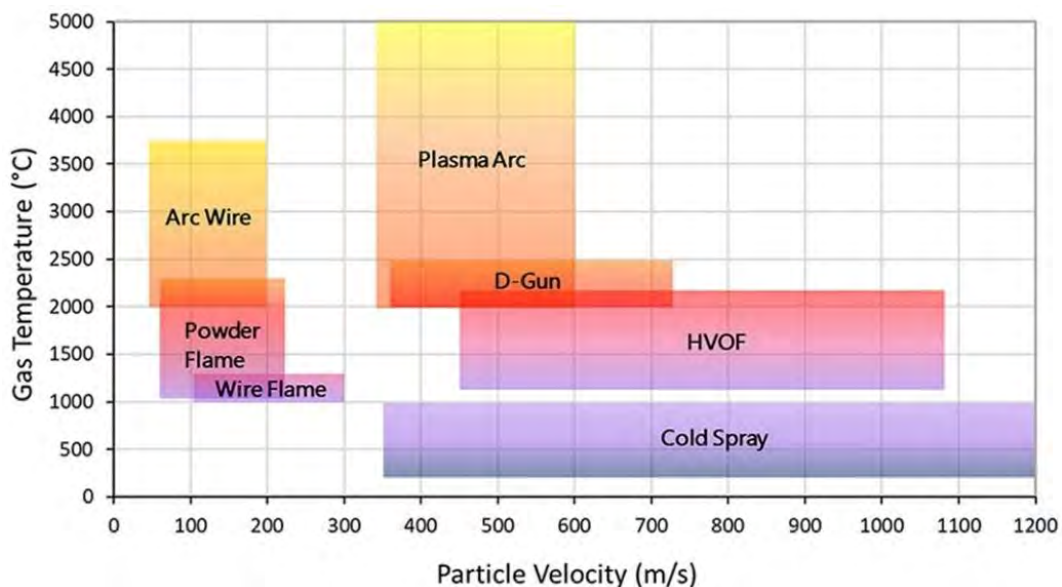
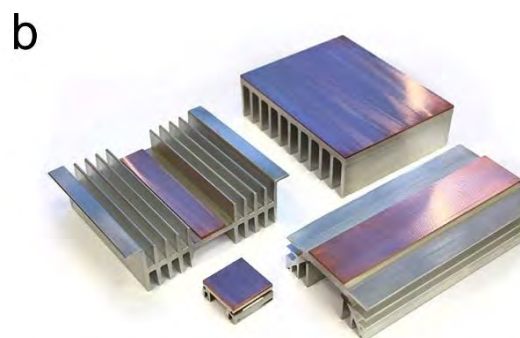


Fig. 2.2 A comparison between cold spray and thermal spray processes about gas temperature and particle velocity [20].

Cold spray is initially developed as a coating production technique, and it has been applied to prepare various functional coatings, such as wear-resistant coatings [21,22], corrosion-resistant coatings [23,24], high-temperature-resistant coatings [25], antibacterial coatings [26,27], photocatalytic coatings [28,29], superhydrophobic coatings [30,31], conductive and thermally conductive coatings [32]. **Fig. 2.3** shows some cold-sprayed coatings with different functions manufactured by Impact Innovations.



Cold-sprayed magnetic coating on cookware



Cold-sprayed hybrid heatsinks (Cu onto Al)

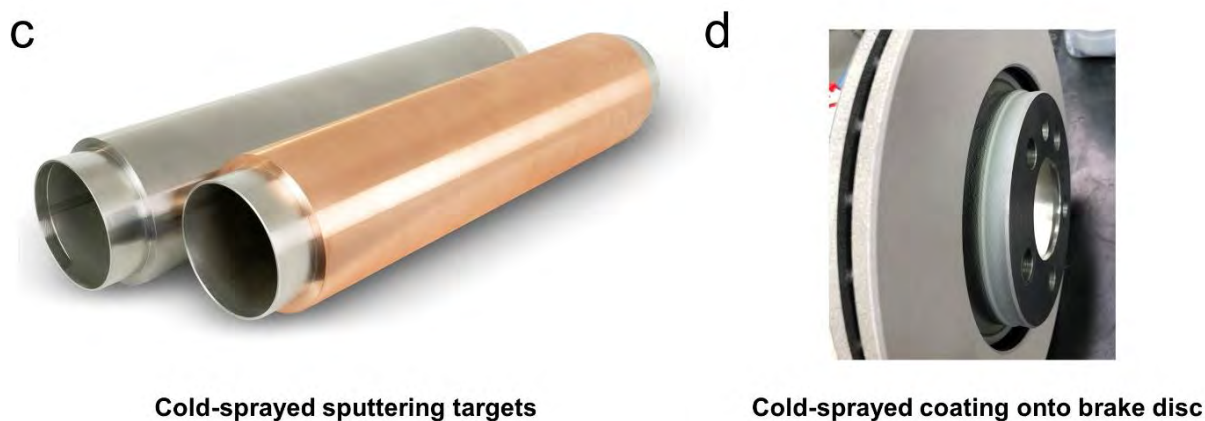


Fig. 2.3 Different functional coatings deposited by cold spray: (a) Cold-sprayed magnetic coating on the bottom of cookware, (b) Cold-sprayed hybrid heatsinks, (c) Cold-sprayed sputtering targets, and (d) Cold-sprayed wear-resistant coating onto a brake disk [33].

In addition to preparing functional coatings, cold spray also shows great potential in repairing and refurbishing worn or damaged components due to its low temperature deposition characterization and rapid manufacturing capability. Parts and components usually suffer from various types of damages (e.g., wear, corrosion, and crack failures) during their long-term service, which poses a threat to the safe operation of the mechanical equipment. The repair of damaged parts and components enables to restore their function and prolong their life cycles. In the past decades, cold spray has been applied as a promising, cost-effective, and environmentally friendly repair technique in aerospace, military, and marine fields (e.g., repair of aircraft skin and access panel repairs, damaged gearbox and engine block [34]). Generally, the repairing procedures for damaged parts by cold spray include four steps, which are pre-machining of the damaged area, material deposition, post-machining on the repaired zone, and integrity and functionality evaluation [11], as shown in Fig. 2.4a. Due to the complex surface topography of the damaged zone, pre-machining is indispensable to reconstruct the damaged surface before cold spraying. The pre-machined parts should have a clean and smooth surface, which favors particle deposition. The raw material at the stage of

material deposition should be properly selected. Generally, the feedstock powders should keep up with the composition and material properties of the damaged parts. However, dissimilar materials can also be used for the repair of some damaged parts. For example, the aluminum powders have been coated onto the corroded magnesium panel to protect it from corrosion [35]. After deposition, the repaired parts have to be post-machined to restore their original geometry and dimensions. In the end, structural integrity and performance evaluation of the repaired parts are required to meet the working conditions. Fig. 2.4b and c show typical damaged parts repaired by cold spray process.

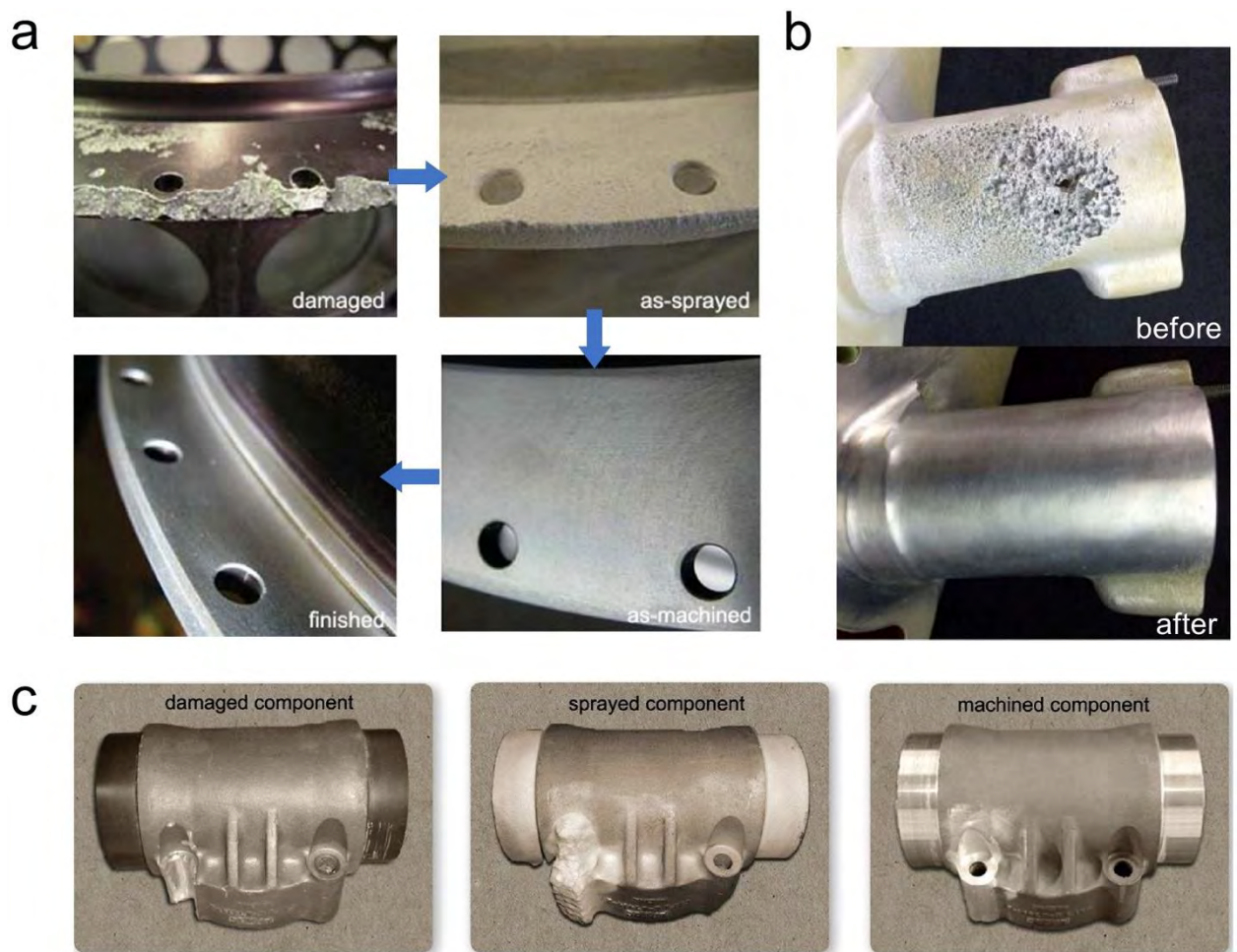


Fig. 2.4 Repairing damaged parts via cold spray. (a) Standard repairing procedure, (b) S-92 helicopter gearbox sump, (c) Flap transmission tee box housing of an aircraft [11].

Cold spraying can not only repair visible damaged surfaces, it can also be applied to repair invisible damaged zones, such as internal bore, by using custom nozzles [36]. Moreover, it is also achievable for the on-site repair of disassembled damaged parts or large equipment with a portable cold spray system, avoiding the removal process of damaged parts from a machine and thus shortening the repair period. Cold spray is expected to widely develop in the repair of worn or broken parts in the future due to its high efficiency and environment-friendly features.

In addition to demonstrating potential applications in functional coating preparation and damaged component repair, cold spray strides into the additive manufacturing family to fabricate freestanding parts and components in recent years. Compared with prevailing fusion-based additive manufacturing techniques (e.g., selective laser melting (SLM), laser metal deposition (LMD), laser beam melting (LBM)), cold spray additive manufacturing retains all the advantages of cold spray, and it can fabricate large-sized parts. In addition, cold spray is particularly suitable for the manufacturing of high-reflectivity metals such as copper and aluminum [37]. However, cold spray has difficulty in manufacturing parts with flexible geometry, and post-machining is generally required. Fig. 2.5 shows some typical parts or components fabricated by cold spray additive manufacturing. Early parts or components fabricated by cold spray additive manufacturing are mainly rotation-based parts or flat plate-based parts with relatively simple geometries, as shown in Fig. 2.5a to d. With the help of path planning and cooperation with a multi-axis collaborative robotic arm, parts with more complex geometries can be built up (see Fig. 2.5e, f and g), which promotes further industrial application of cold spray additive manufacturing. However, it should also be noted that the materials used for cold spray additive manufacturing at this moment are mainly metals with good ductility, represented by copper and aluminum. This can be attributed to the fewer manufacturing defects in the parts, which are expected to meet the usage requirements.

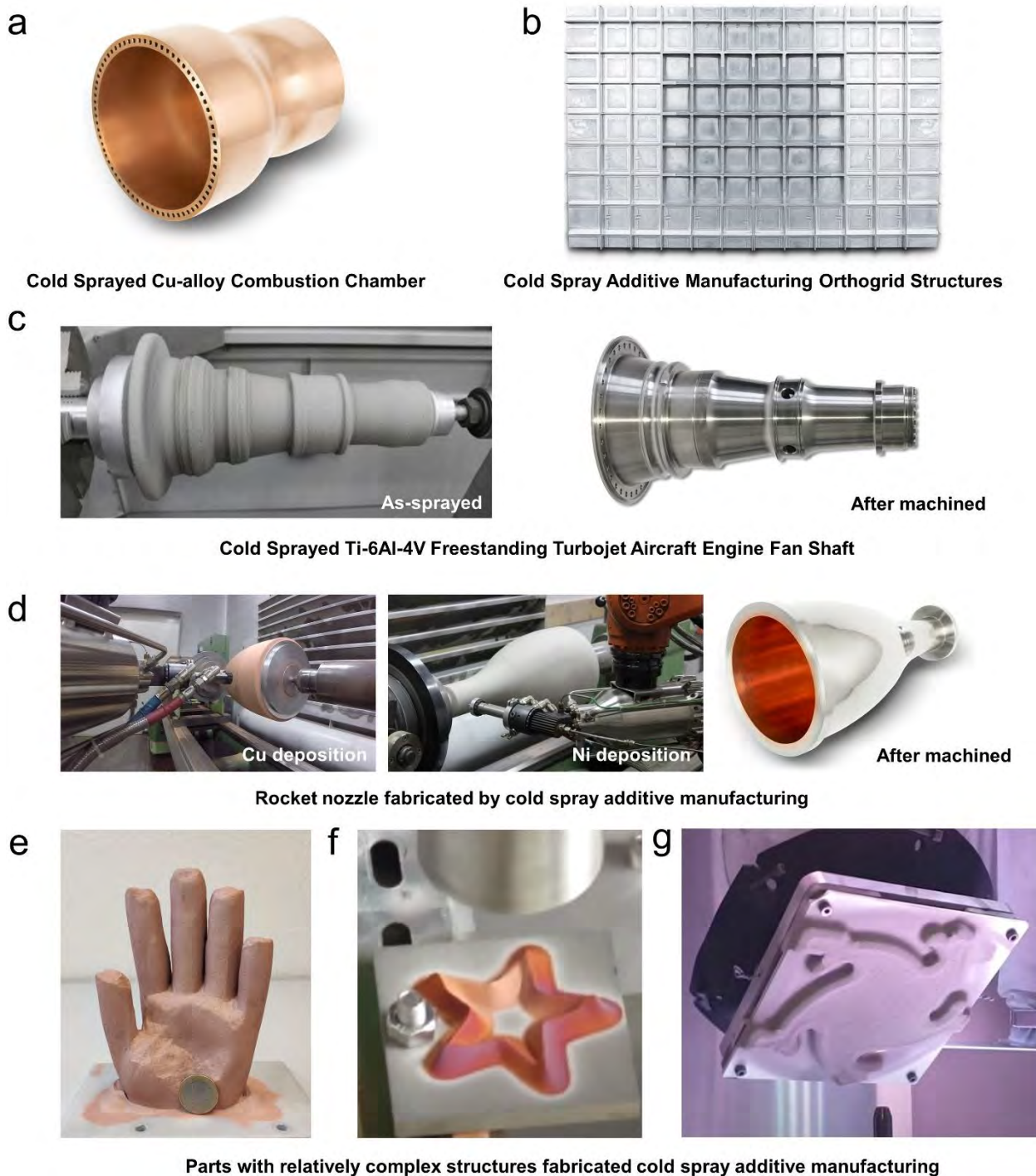
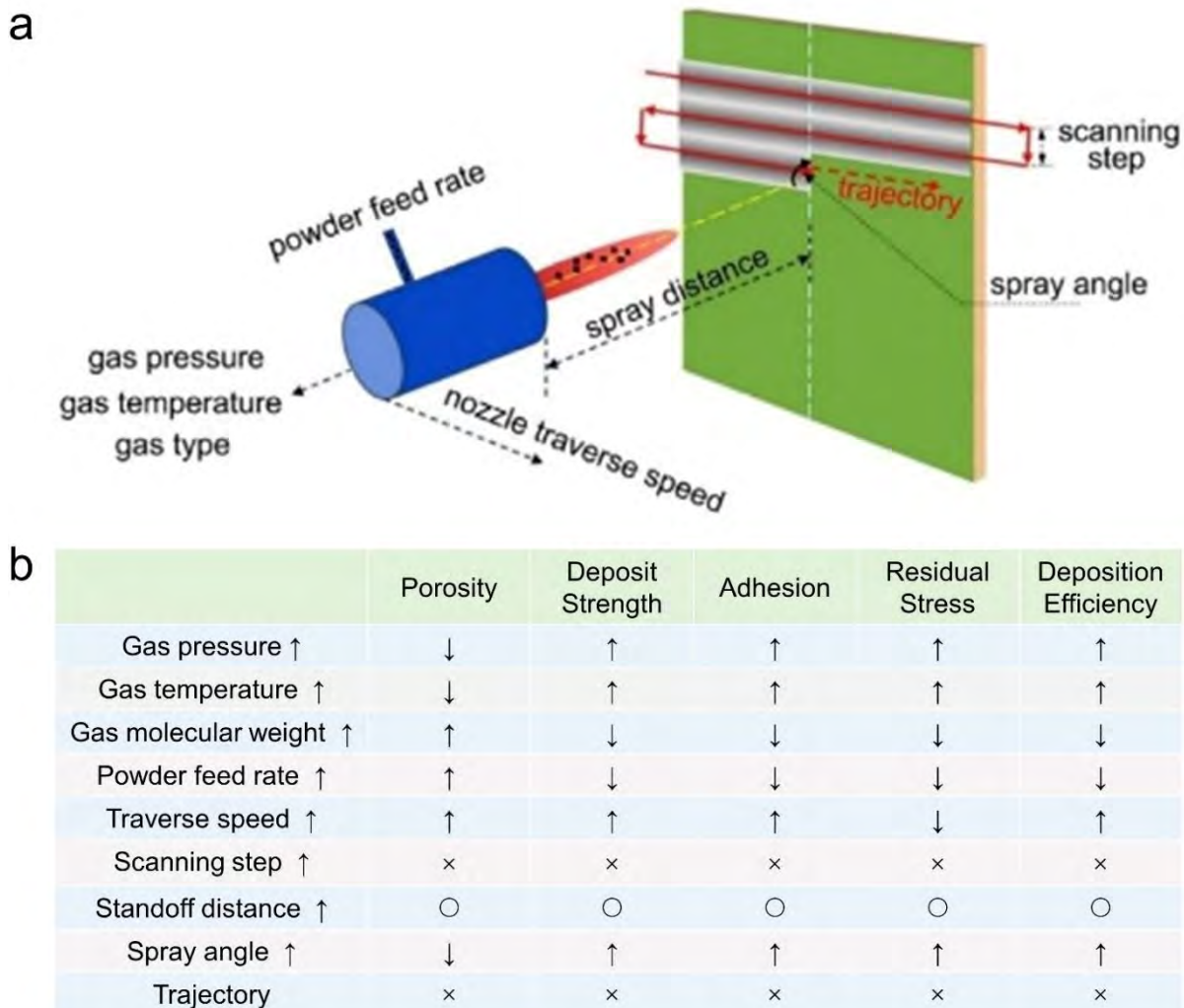


Fig. 2.5 Cold spray additive manufactured freestanding components. (a) Cu-alloy combustion chamber, (b) Orthogrid structures, (c) Ti-6Al-4V freestanding turbojet aircraft engine fan shaft, (d) Cu-Ni rocket nozzle. The parts from (a) to (d) are fabricated by Impact Innovation. (e) Cu hand deposited by Université de Technologie Belfort-Montbéliard, (f) Cu five-pointed star deposited by Shanxi DW automation, (g) A part fabricated by SPEE3D.

2.1.2 Cold spray processing parameters

The main processing parameters in cold spray include the propelling gas parameters (gas pressure, gas temperature, and gas type), powder feeder parameters (powder feed rate), and nozzle parameters (traverse speed, scanning step, standoff distance, spray angle, and trajectory), as shown in Fig. 2.6a. These parameters have a great effect on the deposition process and cold-sprayed deposit quality (see Fig. 2.6b). These processing parameters have to be properly selected and matched to fabricate high-performance cold-sprayed deposits.



Note: '↑' increase, '↓' decrease, '○' relevant but no common view, '×' no data available.

Fig. 2.6 (a) Schematic of the typical processing parameters used in cold spray, (b) Effect of processing parameters on the properties of cold-sprayed deposits [11].

► *Gas pressure, gas temperature and gas type*

In the process of cold spray, the particles are driven by supersonic gas flow and accelerated to high velocities. The propelling gas type, gas pressure, and gas temperature are the key gas parameters that have a great impact on particle acceleration behavior and deposit properties. The appropriate coordination of gas parameters contributes to the fabrication of high-performance cold-sprayed deposits. The propelling gas used in cold spray includes nitrogen, helium, or air. The acceleration effect of helium is much better than nitrogen and air. Therefore, helium is the most optimum candidate for propelling gas to produce high kinetic energy for plastic deformation, especially for difficult-to-deform materials (metal powders with high deformation resistance). However, the consumption of helium significantly increases manufacturing costs (around 5-10 times higher than the price of nitrogen), and it is also not eco-friendly due to the non-renewable feature of helium. The developed helium recovery and purification system can realize the reuse of helium and reduce the cost to a certain extent. In practice, nitrogen is much more commonly used than helium. At this point, higher gas pressure (generally < 5.0 MPa) or higher temperature (typically < 1100 °C for most commercial high-pressure cold spray systems) is indispensable to achieve efficient particle deposition and high deposition efficiency. The increased pressure mainly increases the particle velocity to realize more severe plastic deformation. While the increased gas temperature mainly increases particle impact temperature to promote particle softening [38,39]. The softened particles deform and compactly bond with the substrate or previously deposited layer with fewer defects (i.e., pores and cracks) in the deposit.

► *Nozzle parameters*

The nozzle parameters in cold spray include nozzle traverse speed, nozzle scanning step, standoff distance, spray angle, and nozzle trajectory. The nozzle traverse speed

determines the amount of powder impacting on the substrate or previously deposited layer in unit time, which influences the thickness of the deposit and cross-sectional profile of single track deposit [11]. Generally, lower nozzle traverse speed leads to a thicker single-track deposit and a sharper cross-sectional profile (see Fig. 2.7). Nozzle traverse speed also influences the microstructure and properties of deposits. The porosity increases with the increase of nozzle traverse speed. In addition, lower nozzle traverse speed results in higher temperatures at impacting regions, which favors particle bonding and deposit growth. However, this will also lead to the accumulation of thermal stress at the interface [40].

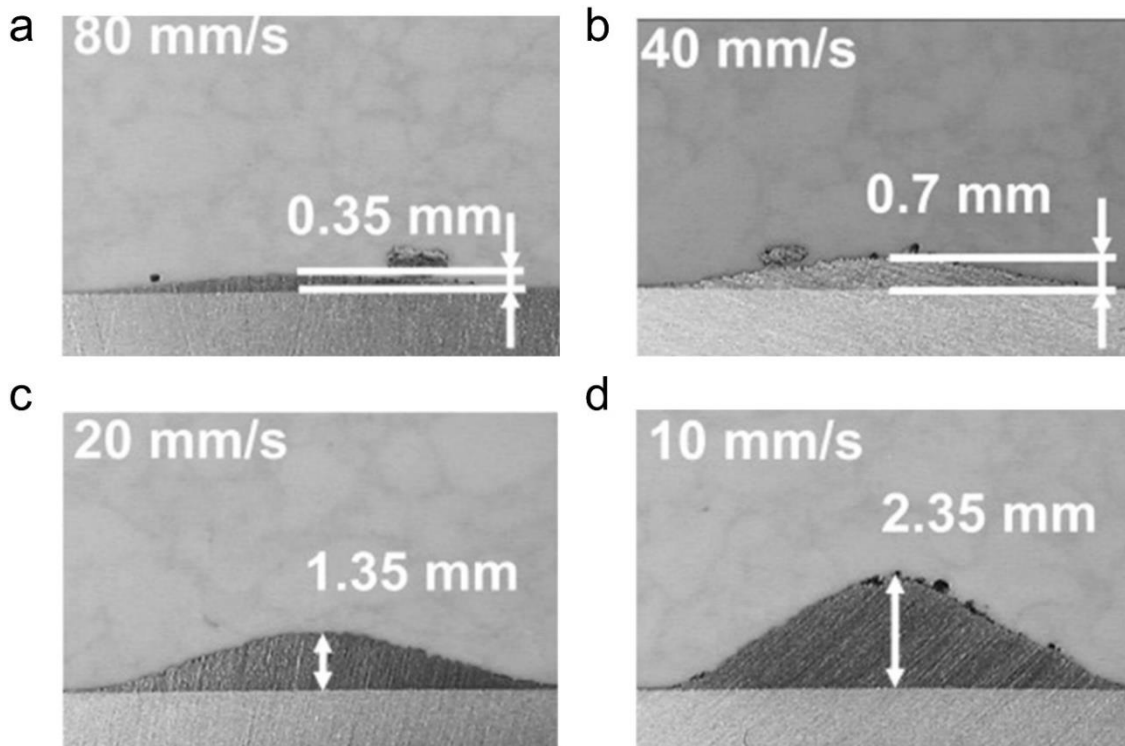


Fig. 2.7 Effect of nozzle traverse speed on the single-track deposit thickness and cross-sectional profile. (a) 80 mm/s, (b) 40 mm/s, (c) 20 mm/s, (d) 10 mm/s [41].

The nozzle scanning step is defined as the interval between the centerlines of two single-track deposits. The scanning step influences the uniformity of the deposit thickness and the surface morphology. A properly chosen scanning step favors receiving a homogeneous deposit and smooth surface. It is reported that the nozzle

scanning step is set as half of the single-track width from experience [11].

The standoff distance is defined as the distance between the exit of the nozzle and the substrate surface. It is reported that the deposition efficiency increases with the increase of standoff distance, followed by a decrease, as shown in Fig. 2.8a. However, Li et al. found that the deposition efficiency decreased with the increase of standoff distance experimentally (see Fig. 2.8b). The difference could be attributed to the equipment's capabilities. To prevent the deceleration and excessive oxidation of particles in the air, the standoff distance is generally set at around 30 mm.

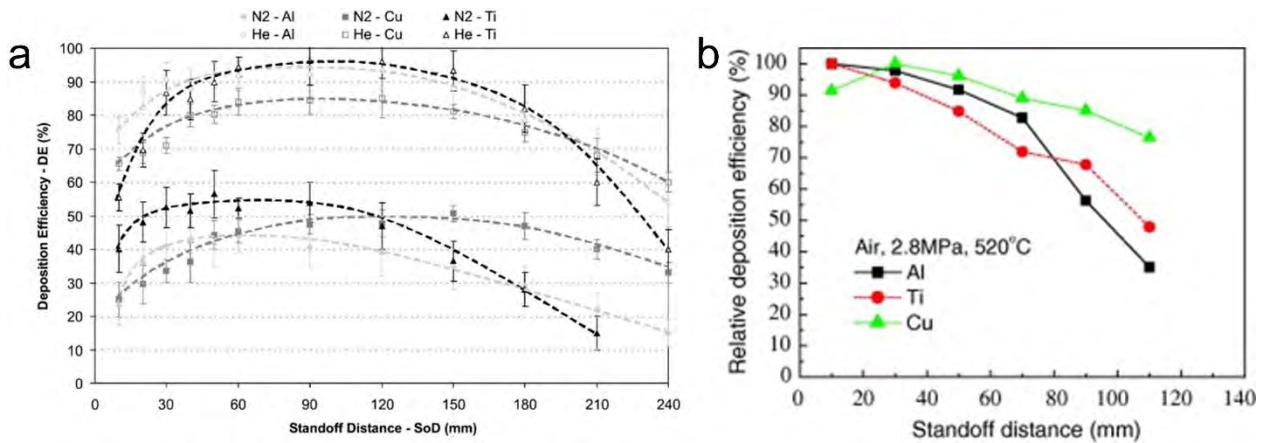


Fig. 2.8 Effect of standoff distance on the deposition efficiency (a) Ref [42] (b)Ref [43].

The spray angle is defined as the angle of the nozzle central axis to the substrate surface. It influences the effective particle impact velocity and deposit properties. When the particle impacts onto the substrate at an angle, the normal velocity favors particle deposition, while the tangential velocity makes the particles move laterally. Therefore, the effective particle impact velocity (normal velocity) decreases with the decrement of spray angle, resulting in a lower deposition efficiency, deposit strength, and adhesion strength [11,44–47]. In practice, the spray angle is generally set at 90°. However, the spray angle has to be dynamically adjusted when repairing damaged parts or manufacturing parts with relatively complex geometries.

The nozzle trajectory is defined as the path of the nozzle. In fact, there is no strict regulation on the nozzle trajectory. However, the definition of nozzle trajectory should follow the principles of convenience, high efficiency, and homogeneity. The trajectory with a zig-zag pattern is generally applied when spraying on a flat surface. However, for the parts with complex geometry, the nozzle trajectory should be properly defined to ensure that the standoff distance, spray angle, nozzle speed, and other manufacturing parameters are kept constant over the surface to receive deposits with homogeneous microstructure and properties [11].

► *Powder properties and feeding parameters*

The powder properties mainly include particle size, particle morphology, and particle material. At present, a variety of materials have been successfully deposited by cold spray, including pure metals and their alloys, metal matrix composites (MMC), cermet, ceramics, polymers, nanostructured materials, and advanced multi-component alloys (i.e., metallic glass and high-entropy alloys). The low temperature in the process of deposition has less thermal effect on the substrate and powder feedstock, thereby avoiding oxidation. As a result, it is particularly suitable for depositing temperature sensitive materials (i.e., nanomaterials [48], amorphous materials [49]), oxidizable materials (i.e., copper [50], titanium [51], aluminum [52]), and phase transition sensitive materials (i.e., WC-Co [53]).

The powder morphology is related to its manufacturing process. The powders prepared by gas atomization are usually spherical, while the powder prepared by hydrogenation dehydrogenation and mechanical alloying have non-spherical and irregular shapes. The particle velocity is related to the powder morphology, and therefore, different powder morphology will affect the microstructure and properties of the cold-sprayed deposits. Non-spherical particles are subject to greater drag force in the gas flow due to their larger surface area. Under the same conditions, non-spherical particles can reach higher impact velocities than those of spherical

particles, which contributes more to particle deposition [54]. However, on the other hand, using non-spherical particles may increase the risk of nozzle wear or nozzle clogging. In practice, the feedstock powder used in cold spray is manufactured by gas atomization.

The particle size has a significant effect on the acceleration behavior and particle impact velocity. The particle for cold spraying usually has a size distribution ranging from 10 to 50 μm . As shown in Fig. 2.9, under the same conditions, the particle impact velocity decreases with the increase of particle size, therefore it is easier for particles with relatively small sizes to obtain higher impact velocities and deposit on the substrate surface. However, the particles with too small sizes are greatly affected by the shock wave on the substrate surface caused by the high-speed gas flow, which will deviate before reaching the substrate and fail to deposit. In addition, the particle size also affects the critical velocity of particles. The increase in particle sizes leads to a sharp decrease in particle critical velocity, followed by a gentle descent. The optimization of particle size contributes to increasing deposition efficiency and promoting the sufficient plastic deformation of particles, leading to fewer manufacturing defects in the deposits.

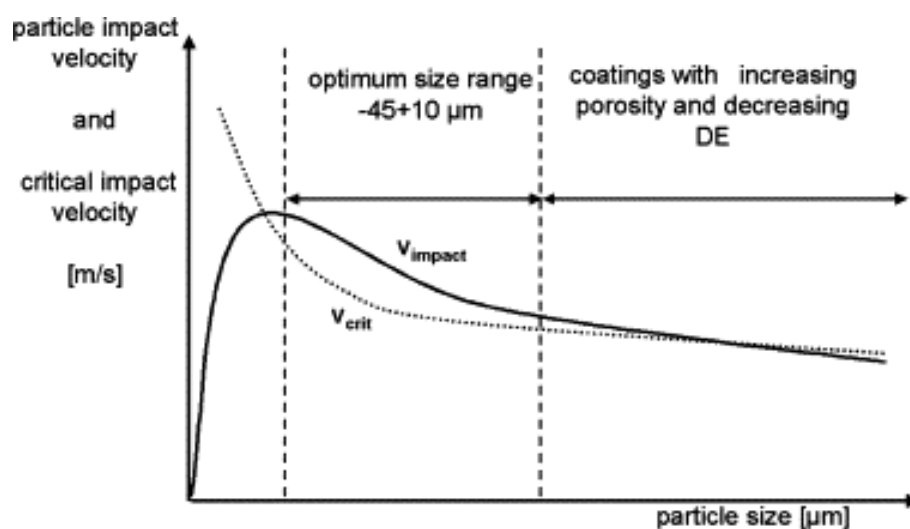


Fig. 2.9 Critical velocity and impact velocity over particle size [55].

The powder feed rate refers to the amount of powder introduced to the nozzle per unit of time, which is the only parameter controlled by the powder feeder. The powder feed rate affects the gas flow through the nozzle, thereby affecting the particle velocity. In general, particle velocity decreases with the increase of powder feed rate due to the strong gas-particle interaction, resulting in increased porosity and decreased deposition efficiency, hardness, and tensile properties [11]. Moreover, a high powder feed rate will generate high localized residual stress between deposits and substrate, which will lead to the delamination of the deposit from the substrate during cold spray [56]. In the process of cold spray, the powder feed rate is usually below 100 g/min [11].

2.1.3 Bonding mechanism of cold-sprayed particles

In cold spray process, the particle impact velocity is the key factor that determines whether the particle will bond with the substrate or previously deposited layer. The successful bonding happens when the particle impact velocity reaches or exceeds a value, which is called critical velocity (v_{critical}). The critical velocity is mainly dependent on the intrinsic properties of feedstock powders, such as material properties, particle morphology, particle size, and particle temperature upon impact with the impacting surface [57–59]. The particle will rebound from the substrate after impact if its impact velocity is below the corresponding critical velocity (i.e., $v < v_{\text{critical}}$). Increasing particle impact velocity or decreasing critical velocity contributes to particle deposition and deposit growth, leading to a higher deposition efficiency. However, excessive impact velocity (i.e., $v > v_{\text{erosion}}$) will cause erosion of the substrate or previously deposited layer. The interval between critical velocity and erosion velocity is defined as the window of deposition, which is considered to be effective for particle bonding, as shown in Fig. 2.10.

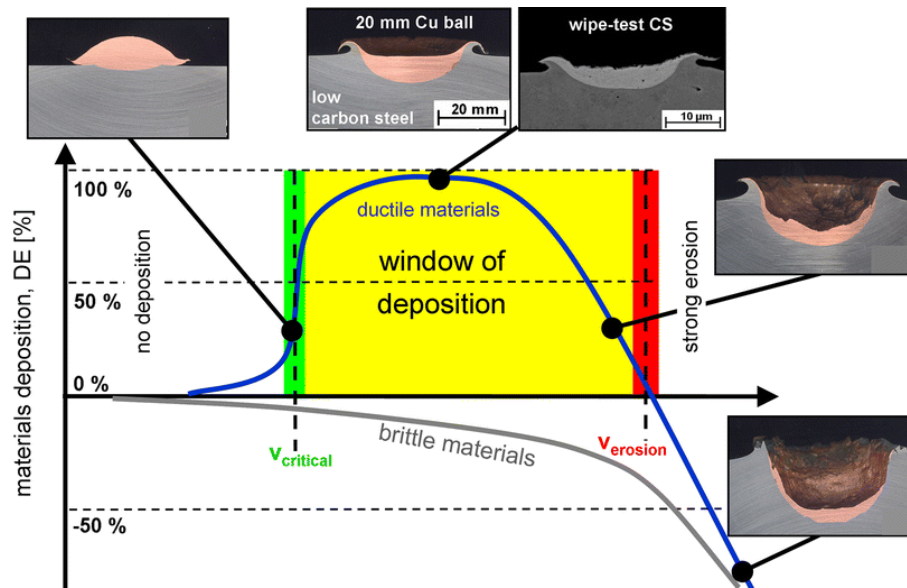


Fig. 2.10 Schematic correlation between particle velocity, deposition efficiency and impact effects for a constant impact temperature [60].

It is widely accepted that successful particle bonding is vitally important for the formation of cold-sprayed deposits. The particle bonding mechanisms in cold spray have been explored and investigated by numerical simulation or theoretical calculation combined with experimental observation over the past 30 years. At present, a lot of mechanisms, including adiabatic shear instability [57,61,62], oxide layer break up [63], localized melting [64–67], diffusion [68], interface amorphization [69] and mechanical interlocking [70], have been proposed to explain particle bonding in cold spray deposition process. These mechanisms are not mutually exclusive, and one or more of the above bonding mechanisms may exist in the deposition process at the same time, which is determined by the materials and processing conditions involved.

► *Adiabatic shear instability mechanism*

Adiabatic shear instability is the prevailing mechanism of particle bonding in the cold spray process [55,57,61,62,64,68,71,72]. Considering the extremely plastic deformation of both particle and substrate and the short impacting period ($\sim 10^{-8}$ s

[73]), the heat transformed from plastic work cannot dissipate in such a short period, and therefore, the cold spray is regarded as an adiabatic process. The increased strain leads to work hardening while the adiabatic temperature rising results in thermal softening. When the thermal softening effect is dominant, shear instability occurs due to the loss of shear strength. The contacting body shows excessive plastic deformation under low shear stress. Assadi et al. studied the deposition behavior of a Cu particle impacting onto Cu substrate using the finite element method and investigated the phenomenon of adiabatic shear instability [57]. It is found that there is a change in the trend of variation of plastic strain, temperature, and flow stress at impacting interface with time, as the particle velocity increased from 550 to 580 m/s, indicating the occurrence of shear instability. The critical velocity measured from the experiment is close to the particle velocity when shear instability occurs, suggesting that adiabatic shear instability is of great importance for particle bonding. Further study pointed out that the plastic deformation localizes at a thin region adjacent to the particle/substrate interface [61]. The localized plastic strain and the thermal softening effects lead to adiabatic shear instability, resulting in the formation of jets, as shown in Fig. 2.11.

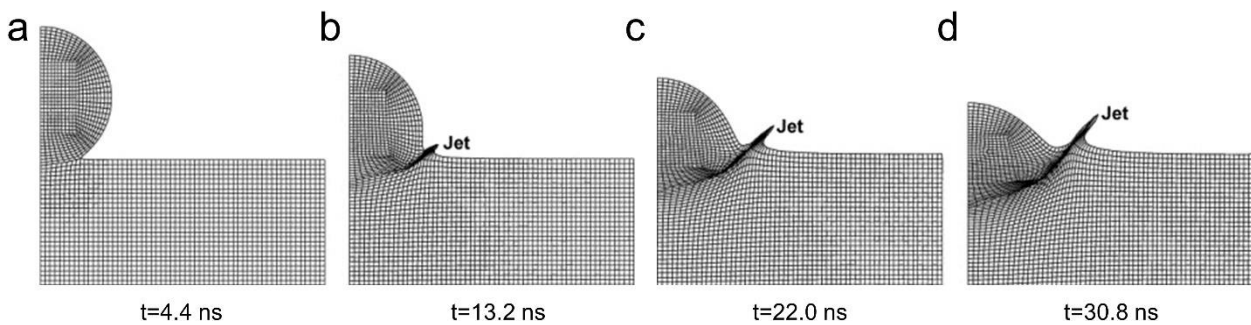


Fig. 2.11 The time evolution of particle and the substrate shapes during impact of a 25- μm Cu particle onto the Cu substrate at 550 m/s: (a) 4.4 ns; (b) 13.2 ns; (c) 22.0 ns and (d) 30.8 ns [61].

Therefore, the adiabatic shear instability is considered to have a significant influence on particle bonding, and the resulting possible bonding modes are

summarized as follows:

(i) Mechanical bonding. The adiabatic shear instability of material and the plastic flow under high pressure contribute to the intermixing and mechanical interlocking between particle and substrate, resulting in mechanical bonding. Grujicic et al. proposed that interfacial instability and resultant roll-ups and vortices may favor interfacial bonding by increasing the contacting area and promoting material mixing at the impacting interface [65].

(ii) Physical bonding. Due to the occurrence of adiabatic shear instability, the interfacial jet helps to remove the oxide films from the particle surface and substrate, leading to an intimate contact of clean metallic surfaces and thereby triggering particle adhesion through physical bonding (van der Waals force) [61].

(iii) Metallurgical bonding. Based on the simulation results, the localized temperature at the impacting interface under adiabatic shear instability could reach as high as the melting temperature of the material. The high temperature can promote atomic diffusion at the impacting interface, resulting in localized metallurgical bonding [65]. However, it is notable that the metallurgical bonding may not apply to materials with high melting temperatures.

► ***Stress wave induced material jet formation mechanism***

The mechanism of adiabatic shear instability induced particle bonding is mainly based on finite element simulation. There is a lack of evidence from experiments to support the view of adiabatic shear instability as the bonding mechanism. The observation of the high-speed impact process of particles during cold spray process is crucial for understanding the particle bonding mechanisms. Hassani et al. observed the supersonic impact process of individual particles by using a high-frame-rate camera and a synchronized quasi-cw laser imaging pulse for illumination and proposed that the formation of material jet for particle bonding was induced by

stress wave [74]. The in-situ observation was performed at higher spatial (micron) and temporal (nanosecond) resolutions. As shown in Fig. 2.12, the Al particle rebounded from the substrate after impact when the measured impact velocity was below critical velocity, while as the impact velocity increased to higher values, the particle adhered with the substrate, and the material jetting can be observed along the direction of shear deformation (as pointed by the white arrows). The numerical simulation results also indicated that the jetting was formed at the edge of the interface when the pressure generated at the impacting interface reached a critical value. Therefore, the formation of material jetting triggered by the release of high stress waves at the particle impacting interface is considered as the interparticle bonding mechanism. In addition, by reproducing the simulation work of a 10- μm Cu particle impacting a Cu substrate at 550 m/s, the author found that the jetting occurred whether the thermal softening behavior of the particle was considered or not, indicating that the adiabatic shear instability is not necessary for particle bonding in cold spray process [75]. It is believed that the jetting occurs due to the pressure released at the particle edge rather than the thermal effect [75]. To be specific, the formation of jetting can be divided into three stages (see Fig. 2.13): impact-induced shock, shock detachment, and jet formation. Higher particle impact velocity results in higher pressure and higher reflected tensions, and when the transient state of hydrodynamic tension is higher than the material dynamic strength, a spall phenomenon occurs and the ejection of material in the form of jetting and subsequent fragments are observed [75].

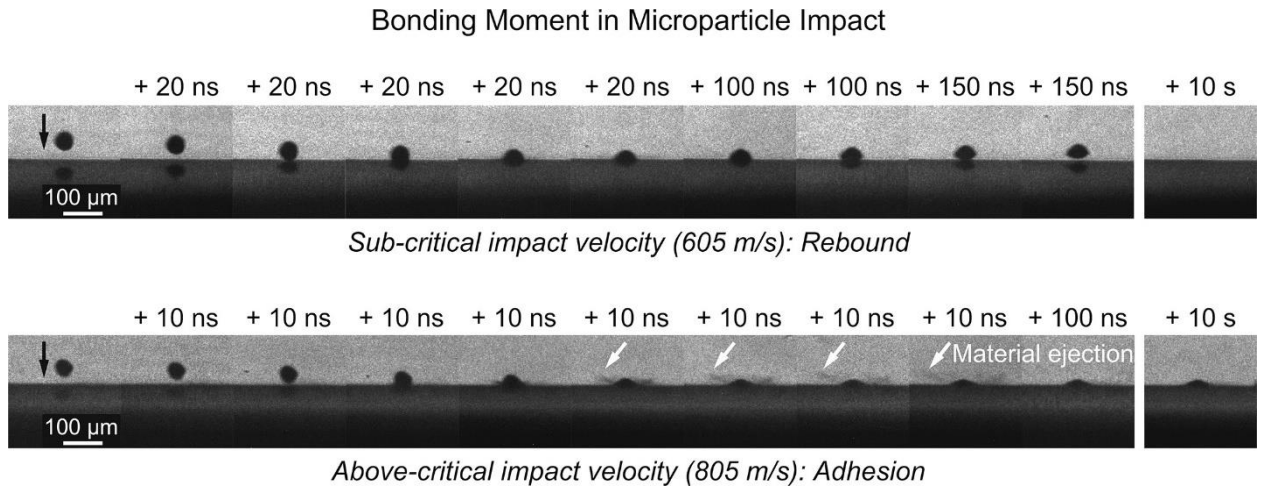


Fig. 2.12 In-situ observation of the bonding moment in microparticle impact (45- μm Al particle impacts onto Al substrate at 605 m/s and 805 m/s, respectively). Material jetting is pointed with white arrows [74].

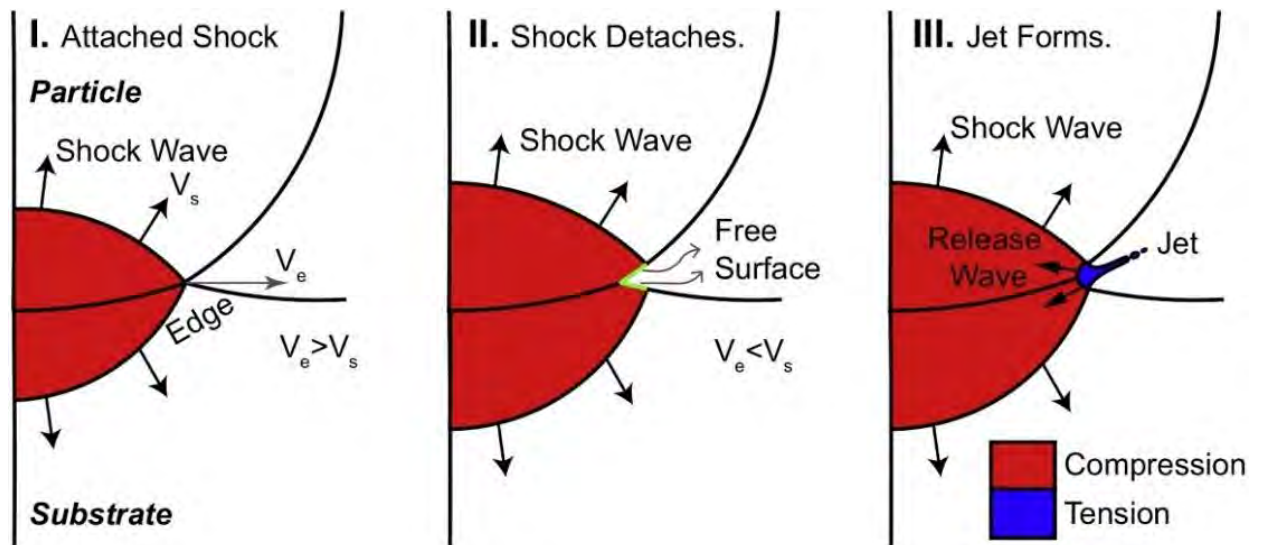


Fig. 2.13 Schematic representation of jetting in cold spray: Stage I. Impact induces a shock wave; Stage II. Shock detaches from the leading edge; Stage III. Jet forms on the basis of pressure releases [75].

► *Oxide layer break up mechanism*

The particle oxidation condition has a significant influence on the particle critical velocity in cold spray process, and the thicker oxide films can lead to higher critical

velocity [76]. For example, with the increase of oxygen content from 0.02 wt.% to 0.14 wt.%, the critical velocity of Cu particles increased from 310 m/s to 550 m/s. However, the critical velocity only increased to 610 m/s when the oxygen content was 0.38 wt.% [76]. This suggests that a low oxygen content level has a more remarkable impact on the particle critical velocity than a high oxygen content level. Further study shows that the increased oxygen content of Cu feedstock powder led to a significant decrease in deposition efficiency and adhesive strength of the coating, which also supported the aforementioned findings. This can be attributed to the oxide inclusions at the interfaces which inhibit the effective metallurgical bonding between deposited particles [63]. Given this, in-depth investigations were conducted on the microstructure at interparticle interfaces. By performing auger electron spectroscopy analysis of the fracture interface between Al substrate and Cu deposit, it was found that the center of the crater was covered by native oxide films, exhibiting incomplete bonding. While an oxide-free region can be found at the edge of the interface, which exhibited higher adhesion strength than the whole deposit [77]. This can be attributed to the inhomogeneous plastic deformation at the interparticle interface. The edge of the interface generally undergoes higher plastic strain than the center area, and therefore, the oxide film at the edge of the interface can be broken up and stripped from the particle, which contributes to the metallurgical bonding between fresh metal surfaces and the resultant higher adhesion strength than the whole deposit. Moreover, the oxide distribution at the center region of the interface of Cu particles deposited at different impact velocities also exhibited that higher particle impact velocity promoted the break-up of oxide films, as compared with the continuous oxide band at the interface (see Fig. 2.14d and h) [78].

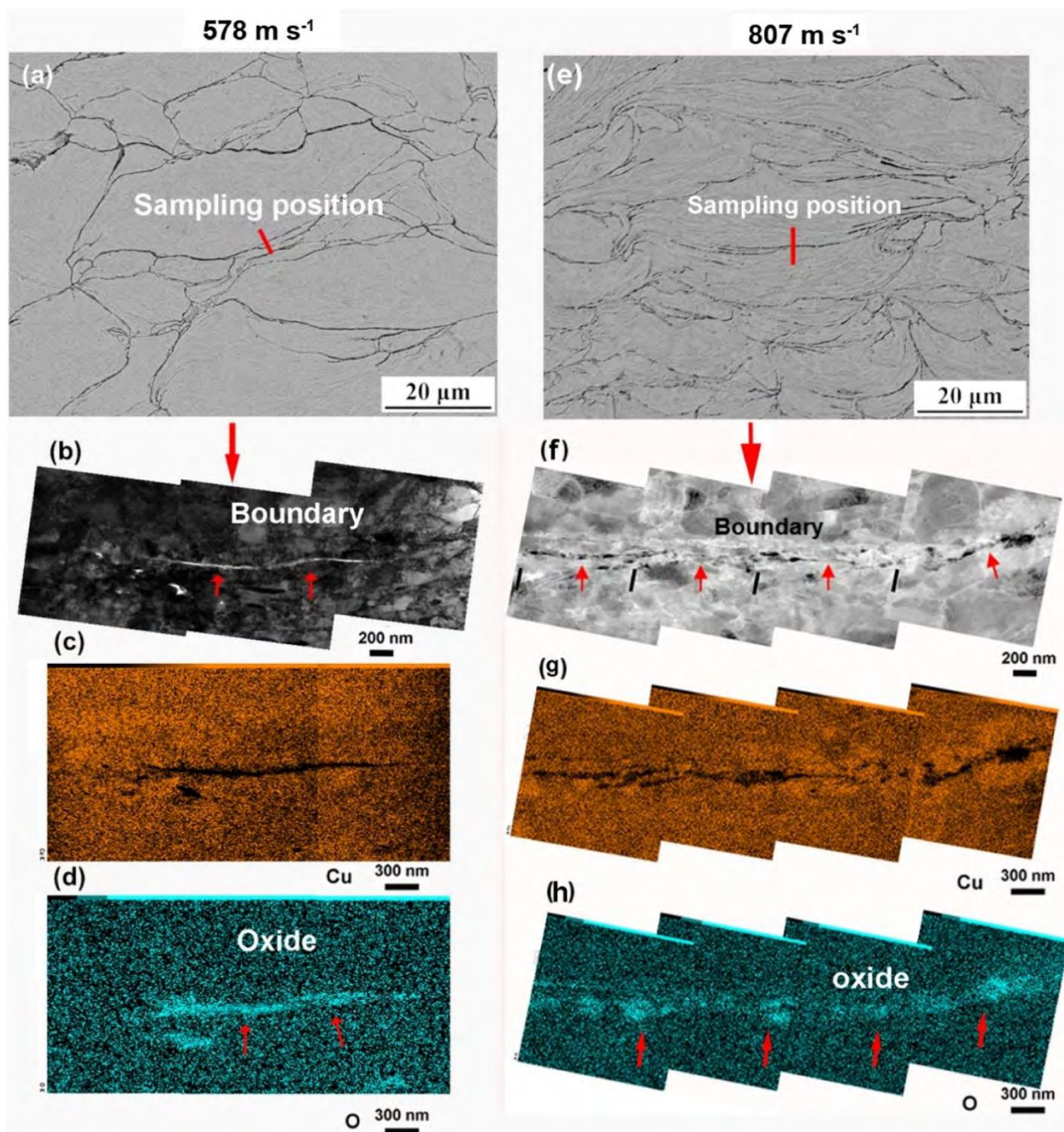


Fig. 2.14 Characterization of the regions at the center of the interparticle interface of Cu deposits fabricated by cold spray at low (578 m/s, left side) and high (807 m/s, right side) particle impact velocity, respectively. (a) and (e) SEM images, (b) and (f) TEM images, (c) and (g) STEM-EDS mapping of Cu, (d) and (h) STEM-EDS mapping of oxygen [78].

Given these facts, the oxide layer break-up mechanism associated with cold-sprayed particle bonding can be summarized as follows (see **Fig. 2.15**) [63,77]. In general,

there are native oxide films covered on the surface of particles and substrate (see [Fig. 2.15a](#)). When the microparticle impacts onto the substrate at supersonic speed, the impacting interface will undergo extreme plastic deformation. The oxide films break up due to the hard and brittle feature (see [Fig. 2.15b](#)). The exposed fresh metallic surfaces contact intimately under high pressure, which promotes effective metallurgical bonding (see [Fig. 2.15c](#)). While the residual oxides at the interparticle interface will hinder the effective bonding of particles, particularly at the center region of the interfaces (see [Fig. 2.15d](#)). By increasing the processing parameters, cold spray particles can obtain higher impact velocity, which promotes more severe plastic deformation and the breaking up of oxide films into smaller pieces. Therefore, metallurgical bonding is further promoted due to the increased contact areas. For the particles with thicker oxide films, higher kinetic energy is consumed for the breaking up of oxide films, and this leads to increased critical velocity. Therefore, using powders with low oxide content or even oxide-free powders as feedstock is significant to manufacture high-performance coatings or deposits via cold spray.

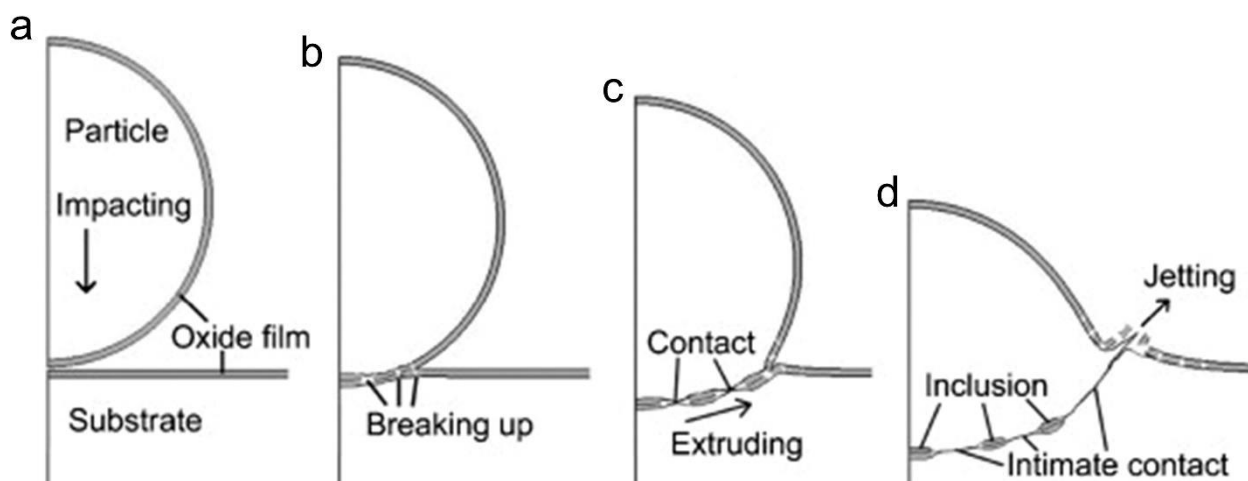


Fig. 2.15 Schematic diagram of the bonding process of cold-sprayed particles accompanying with the breaking-up and extruding of surface oxide films and the formation of jetting [63,79].

2.1.4 Strengthening strategies for cold-sprayed Deposits

Due to the solid-state deposition feature of cold spray particles, the incomplete interparticle bonding and the existence of inherent defects generally make the cold-sprayed bulk deposits exhibit unsatisfactory mechanical properties, particularly negligible tensile ductility when compared with their counterparts that are manufactured by prevailing processes based on melting-solidification. This is particularly noticeable during the deposition of particles with high deformation resistance even using high processing parameters (e.g., using nitrogen at high temperature and high pressure, or using expensive helium). The premature failure of deposits initiated from particle-particle interfaces fails to make them meet the requirement of practical structural engineering materials. The poor mechanical properties significantly slow down the pace of cold spray as a fast, efficient, and economical solid-state metal deposition process towards further development and industrialization.

To mitigate the negative downsides of cold spray, several strengthening technologies have been developed in the past decades. These processes have shown the capability to reduce manufacturing defects associated deposition process and enhance interparticle bonding at interfaces, which can result in the improvement of mechanical properties, particularly the tensile strength of cold-sprayed deposits. According to the stage that these strengthening technologies are applied in cold spray process, they can be classified into three categories, namely pre-process (i.e., powder heat treatment), in-process (i.e., powder preheating, in-situ micro-forging, laser-assisted cold spray), and post-process (i.e., post heat treatment, hot isostatic pressing, hot rolling, friction stir processing). The schematic showing the working mechanism of each process is provided in [Fig. 2.16](#).

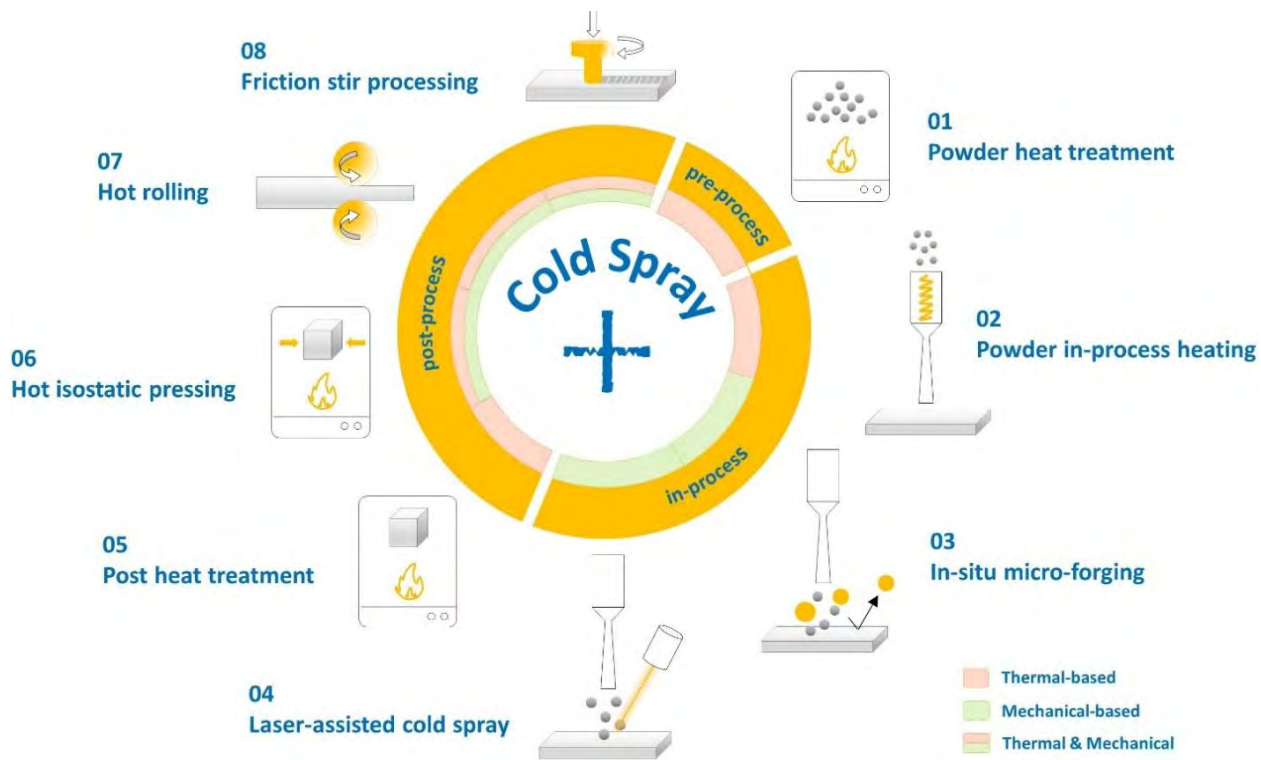


Fig. 2.16 Schematic of available strengthening technologies for cold-sprayed deposits. According to the stage that these strengthening technologies are utilized in cold spray process, the strengthening technologies are classified into three categories, namely pre-process, in-process, and post-process.

► *Powder heat treatment*

Gas-atomized powders are the major feedstock for cold spray. For metals such as Al alloys, powders produced via gas atomization exhibit cellular/dendritic microstructure with localized segregation of solute elements existing along cell boundaries and thus have high hardness and low ductility, which makes deposition more difficult. To remove the cellular/dendritic microstructures and facilitate the deposition, heat treatment to the powders before cold spraying has been considered a pre-processing method in recent years (as schematized in [Fig. 2.16](#)). In addition to the elimination of cellular/dendritic microstructure, the size of the grains increased after heat treatment [80–83]. These microstructural evolutions result in the reduction of powder hardness [80,83–85] and strength [86]. When these softened

powders are used for cold spray, more severe plastic deformation can occur in the powders. Thus, higher deposition efficiency [80,82,84,85,87] and denser deposits [83,84] can be achieved when using heat-treated powders. More importantly, larger plastic deformation leads to improved metallurgical bonding at interparticle interfaces, leading to the strengthening of the resultant deposits.

► ***In-process powder preheating***

The consolidation of cold-sprayed deposits relies on the plastic deformation of starting powder particles. Typically, ductile or soft metal powders are easy to be deposited, resulting in dense and strong deposits due to their sufficient plastic deformation upon impact. Considering this fact, the preheating chamber has been developed to heat and thermally soften powders before they enter a cold spray nozzle to facilitate their plastic deformation [88]. The powder heating chamber can be either a separated powder heater device (as schematized in Fig. 2.16 or a long pre-chamber connected to the nozzle inlet. For a specific metal, thermally softened particles can experience more severe plastic deformation during cold spray deposition than conventional particles. In addition, the area of the regions that experience adiabatic shear instability significantly increases by applying powder preheating, and the particle deposition quality is thus improved [88]. As such, using in-process powder preheating can produce cold-sprayed deposits with higher compactness and strength [64,89].

► ***In-situ micro-forging***

Shot peening is a surface modification process in which shot particles impact a part surface to induce plastic deformation and compressive stress. Inspired by this technique, the research group from Xi'an Jiaotong University developed an in-process strengthening technique for cold spray, which is named in-situ micro-forging (also known as in-situ shot-peening, in-situ tamping, or in-situ hammering)

assisted cold spray [24,90–97]. **Fig. 2.16** schematizes the working mechanism of in-situ micro-forging assisted cold spray. In the process, feedstock powders are mixed with peening particles with a size range of 100~300 μm , and then the mixture is accelerated and impacts towards a substrate to form deposits. During the deposition, heavy peening particles continuously tamp the previously deposited layer to induce secondary plastic deformation of the deposited particles. Consequently, the defects in the deposits (e.g., pores and incomplete interparticle bonding) are significantly mitigated, which eventually results in the densification and strengthening of cold-sprayed deposits.

► ***Laser-assisted cold spray***

Laser-assisted cold spray (LACS), also known as supersonic laser deposition, is a novel material deposition process that utilizes the transient heating of laser irradiation to heat up and soften the substrate/previous deposited layer and particles so that the particles can be deposited at lower critical velocities and experience more severe plastic deformation [98]. A LACS system typically consists of a cold spray system, a laser, and an infrared pyrometer, as schematized in **Fig. 2.16**. During the LACS process, the laser spot moves synchronously with the deposition spot, heating the incoming particles and deposition site to temperatures below their melting points. The densification and strengthening are achieved through enhanced particle plastic deformation and interparticle metallurgical bonding by laser irradiation. The LACS process exhibits great potential in increasing deposition efficiency and improving deposit properties, in particular during the deposition of high-strength materials. The low heat input ensures that the deposit can retain the original phase structure and composition as feedstock powder. In addition, the LACS process can reduce the requirement of processing parameters, which makes it more cost-effective.

► ***Post heat treatment***

Conventional post-spray heat treatment is the most effective, economical, and common strengthening technique for cold-sprayed deposits. The strengthening mechanism of heat treatment is simple. The high-temperature environment promotes atomic diffusion across interparticle boundaries, enhances the metallurgical bonding between adjacent particles, and induces recrystallization and grain growth in deposits. As a consequence, mechanical properties, particularly ductility, are considerably improved [37]. Tensile strength is also enhanced in certain deposits that are produced under low gas parameters or have poor interparticle bonding because of the dramatically improved metallurgical bonding [99,100]. For the deposits fabricated under high gas parameters, interparticle bonding is already excellent, and the refined grains within highly work-hardened areas significantly increase the strength of the deposits. In this case, annealing reduces their tensile strength due to the occurrence of recrystallization that eliminates the grain boundary strengthening effect [99].

► ***Hot isostatic pressing***

Hot isostatic pressing (HIP) is a thermo-mechanical technique to compact materials by reducing or eliminating their porosity. It was successfully used to densify and strengthen cold-sprayed deposits [101]. In this process, cold-sprayed deposits are subject to high pressure and high temperature environment in a pressurized vessel filled with inert gas, as schematized in Fig. 2.16. In the vessel, the softened deposits are greatly compacted by high pressure, which leads to significant improvement in density, interparticle bonding, and mechanical properties.

► ***Hot rolling***

Hot rolling as a thermo-mechanical process was used to post-process cold-sprayed deposits in recent years. In this process, cold-sprayed deposits are heated to a temperature above recrystallization temperature in a furnace first and then fed into

a rolling apparatus to induce severe plastic deformation [102–108]. Fig. 2.16 shows the schematic of the working mechanism of hot rolling. The thermo-mechanical process significantly compacts the deposit, improves the interparticle bonding, and alters the microstructure. Consequently, the hot-rolled deposits can have higher density and better mechanical properties.

► *Friction stir processing*

Friction stirring processing (FSP) is derived from friction stir welding and has been developed into a post-processing method for strengthening cold-sprayed deposits [109–115]. As schematized in Fig. 2.16, FSP uses a rotating cylindrical tool consisting of a shoulder with a pin at the tip to penetrate through cold-sprayed deposits. The material in the stir zone is totally softened and plasticized under the strong combined effect of compacting and friction caused by the shoulder and pin, together with the intense stirring action of the pin. FSP strengthens cold-sprayed deposits by introducing extensive plastic deformation and friction heating, which break and redistribute the particles and eliminate poor interparticle boundaries in cold-sprayed deposits. This intense thermo-mechanical effect also leads to the formation of a dense and homogeneous structure with fine and completely recrystallized equiaxed grains.

2.2 Metallic Glass

2.2.1 *Historical evolution*

Metallic glasses (MGs), also known as amorphous alloys, are a type of non-crystalline solid material with long-range disordered arrangement of atoms. Combining the advantages of both metal and glass, MG has received extensive attention and research interest since its discovery in 1960, when the Au₇₅Si₂₅ MG

was first reported by Duwez et al. [116]. The unique disordered structure of MG results in the absence of defects associated with the crystalline state (i.e., grain boundaries, dislocations, and stacking faults), rendering them superior mechanical properties, exceptional soft magnetic properties, excellent wear- and corrosion-resistance and remarkable thermoelectricity [117–119]. Such excellent properties make MGs excellent structural and functional materials with extremely promising applications in sporting goods, biomedicine, and electronics [120–122]. However, the fabrication of MGs is challenging. The early MGs were prepared by cooling molten alloys at an extremely rapid cooling rate (10^4 - 10^6 K·s⁻¹) to bypass the crystallization and the amorphous structure can retain in the solid state. Therefore, MGs are typically regarded as frozen liquids [123]. The required high cooling rates for achieving the fully amorphous structure of MGs restricted the maximum size and resulted in limited forms (i.e., powders, ribbons, foils, or wires) with dimensions in micron scale, particularly in the infancy of MGs, as shown in Fig. 2.17. The limited glass formation ability makes it difficult to prepare large-sized MGs, which impedes the further development of MGs [124].

In order to reduce the critical cooling rates and improve the glass forming ability of MGs, two typical strategies (i.e., purify the melts and design alloy composition) were proposed in the past decades [126]. Turnbull et al. employed the boron oxide fluxing technique to remove impurities by repeated melting and solidifying a Pd-Ni-P alloy in molten B₂O₃ fluxes [127]. Consequently, the critical cooling rate for glass forming was dramatically reduced, and the amorphous Pd₄₀Ni₄₀P₂₀ MG specimen was manufactured with a minimum linear dimension of 1.0 cm [127]. The second strategy is from the perspective of alloy composition design, which significantly promotes the rapid development of MGs. Prof. Johnson from Caltech and Prof. Inoue from Tohoku University found the glass forming ability of alloys can be improved by mixing multiple elements with different atomic sizes [128,129]. Specifically, Prof. Inoue proposed the best-known three empirical rules to form

alloys with good glass-forming ability: (i) the alloy must contain at least three or more components, and it will be easier to form a glassy structure with an increasing number of components, (ii) the atomic size differences among main constituent elements should be above 12%, (iii) the heat of mixing among major constituent elements should be negative [129,130]. The composition designing of MGs leads to complex crystal units with high potential energy, and the nucleation and growth of crystals would be suppressed during the cooling process. The proposed rules provide an important theoretical basis for the subsequent composition design of MGs, and based on this, a series of alloy systems with glass forming abilities in millimeter-scale have been developed in the following years, such as Pd-based, Pt-based, Mg-based, Ti-based, Ni-based, Fe-based, Zr-based, La-based, Cu-based, Co-based, Al-based and so on [131]. These MGs, which can be prepared typically in a millimeter scale in more than one dimension, are termed bulk metallic glasses (BMGs). Compared with the necessarily high critical cooling rates of traditional MGs, BMGs can be produced at lower critical cooling rates (typically less than 10^3 K/s). For example, the critical cooling rate of $Zr_{41.2}Ti_{13.8}Cu_{12.5}Ni_{10.0}Be_{22.5}$ BMG (also named Vit-1) is as low as 1 K/s, which became the first commercial BMG system [132]. The BMG system with the most excellent glass-forming ability until now is $Pd_{42.5}Ni_{7.5}Cu_{30}P_{20}$, which can be fabricated with a critical size of about 80 mm [133]. The critical cooling rate for the glass formation of this alloy is reported as 0.067 K/s [134]. It is estimated hundreds of BMG systems have been developed (see Fig. 2.17). Each BMG system exhibits different glass forming abilities, mechanical properties, as well as physical and chemical properties.

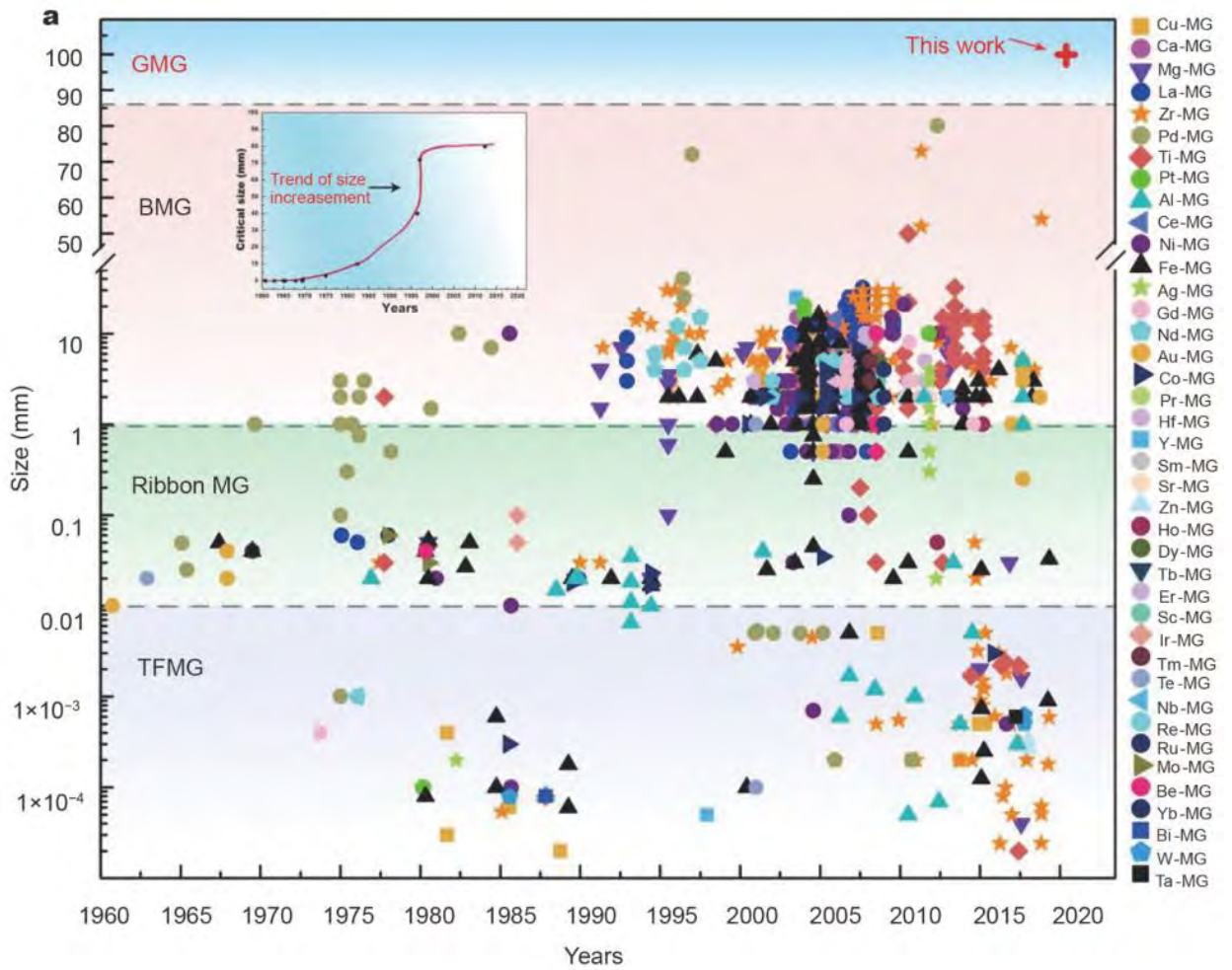


Fig. 2.17 The size development of metallic glass since 1960s, exhibiting an evolution from film, ribbon to bulk components [125].

2.2.2 Manufacturing Processes

Fig. 2.18 shows the development road of the MGs manufacturing from ribbon, powder, and film to BMGs. As mentioned earlier, the first reported MG $\text{Au}_{75}\text{Si}_{25}$ was manufactured by the extremely rapid cooling technique in 1960 [116]. The production of amorphous alloys by rapid cooling technique requires an extremely high cooling rate to bypass the crystallization and achieve a fully amorphous structure of MGs, which restricts the maximum size and results in limited forms with dimensions in micron scale. Other manufacturing techniques of MGs, such as

arc melting drop/suction casting, high-pressure die casting, and cooper mold casting, emerged over time which enriched the types of metallic glasses and further increased the size limit of MG [135]. However, some problems, such as decreased cooling rate, weakened amorphous forming ability, and the precipitation of crystalline phases, may occur during the fabrication of BMGs. Compared with casting methods, powder metallurgy is another commonly used technique to produce BMGs, which exhibits the advantage of low manufacturing cost, near-net forming, and high flexibility. Moreover, the powder metallurgy technique can break through the limitations of the alloy size and composition to a certain extent, which is becoming an ideal method for BMGs.

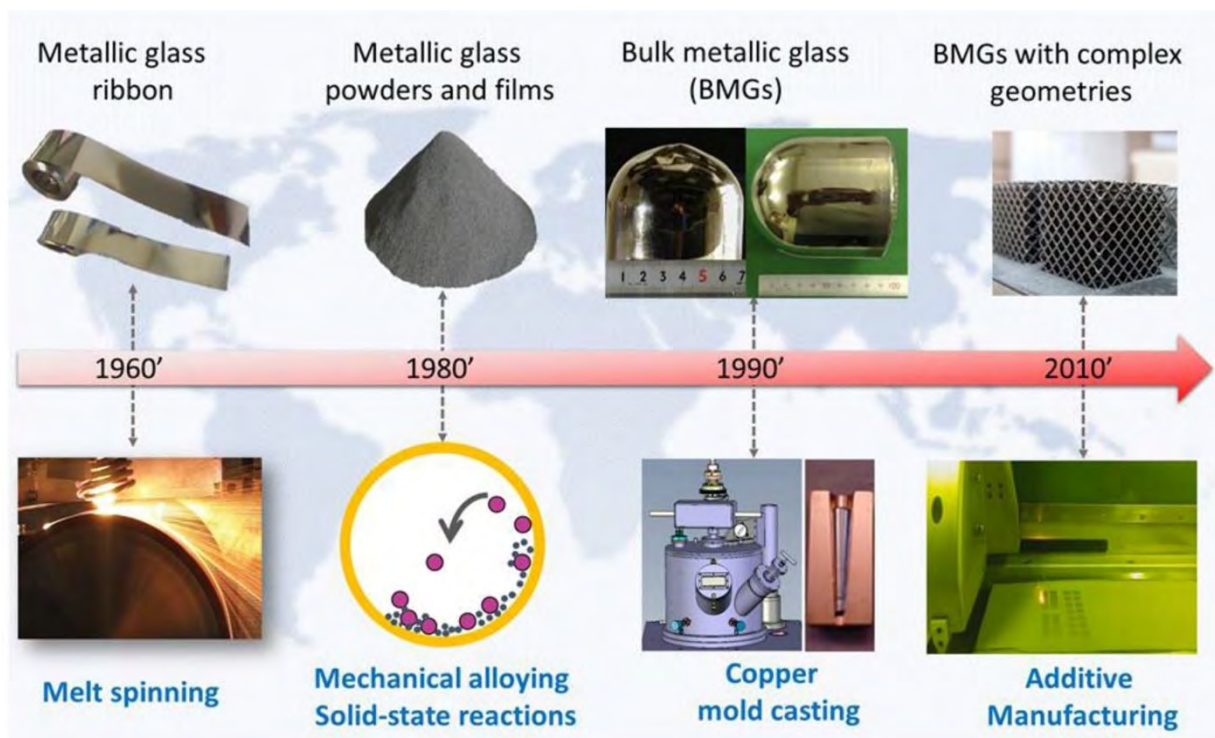


Fig. 2.18 The road of manufacturing metallic glasses towards bulk metallic glasses with complex geometries [124].

The rapid development of additive manufacturing technology provides an alternative for fabricating BMGs over the past decade. Several additive manufacturing techniques have been reported as feasible approaches to fabricate

BMGs including laser-based AM techniques (i.e., laser foil printing (LFP) [136], laser cladding [3], laser solid forming [137] and selective laser melting (SLM) [1]) and thermal spray (i.e., high-velocity oxygen/air fuel (HVOF/HVAF) [5,6], plasma spray [7], arc spray [9] and detonation spray [138]). However, the complicated thermal history during the process of these techniques based on the fusion-solidification principle generally leads to unwanted metallurgical defects, undesirable oxidation behavior, and inevitable crystallization in the deposit. The formation of metallic oxides and intermetallic leads to structural heterogeneity, which may further deteriorate the mechanical properties of the deposits.

2.2.3 Plastic Deformation Behavior

The plastic deformation behavior of MGs highly depends on the temperature and strain rate, which can be categorized into inhomogeneous deformation and homogeneous deformation [139,140]. MG experiences inhomogeneous deformation at low temperatures and high strain rates (see Fig. 2.19), which can be characterized by linear elastic behavior followed by severe localized plastic flow concentrated within thin shear bands and the consequent catastrophic fracture. In contrast, homogeneous deformation of MGs refers to uniform deformation at a macroscopic scale and generally takes place at a lower strain rate or a higher temperature. Furthermore, it features a transition from non-Newtonian flow to Newtonian flow with the increasing temperature at a given strain rate, and an increasingly higher temperature is required for the transition with an increased strain rate. In the supercooled liquid region, which is defined as the temperature interval between glass transition temperature (T_g) and crystallization temperature (T_x), MGs generally exhibit distinct viscous flow and superplastic deformation characteristics. The excellent formability of MGs in the supercooled liquid region allows net-shape forming.

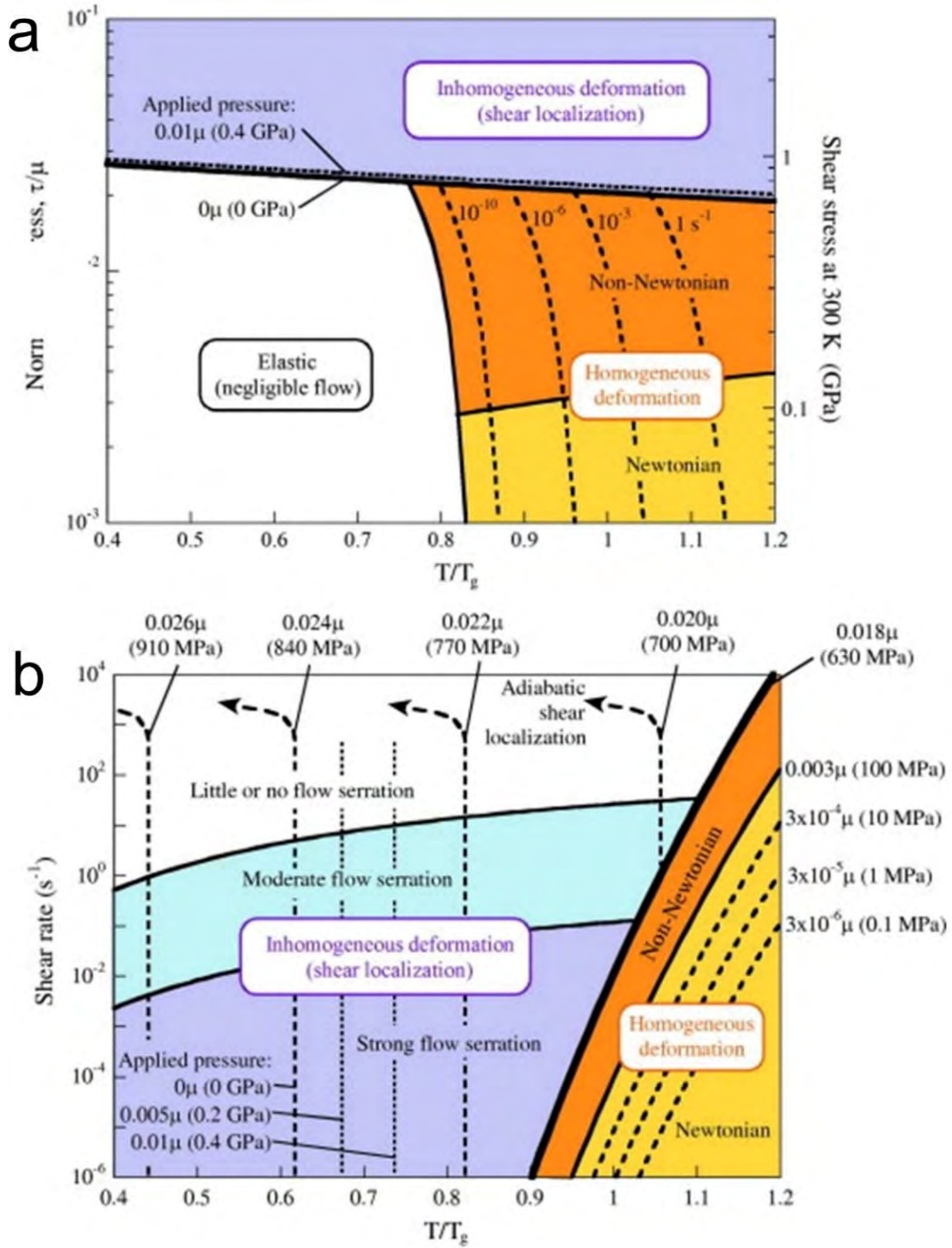


Fig. 2.19 Deformation map for metallic glasses in (a) stress–temperature and (b) strain rate–temperature axes [139].

2.3 Research Progress on Cold-sprayed Metallic Glasses

Cold spraying is a burgeoning metal deposition and solid-state additive manufacturing technology that provides an alternative to allow the fabrication of metallic glasses (MGs). **Fig. 2.20** and **Table 2.1** summarize previous studies that have demonstrated the feasibility of fabricating multiple MG systems by cold spray, such as Ni-based, Cu-based, Fe-based, and Al-based MGs. In the case of MGs, cold spray process helps to minimize thermal influences to retain a high extent of amorphous structure in the deposit as the original feedstock. Moreover, cold spray is in prospect to fabricate parts with larger sizes (i.e., from millimeters to centimeter scale) than prevailing laser-based additive manufacturing technologies.

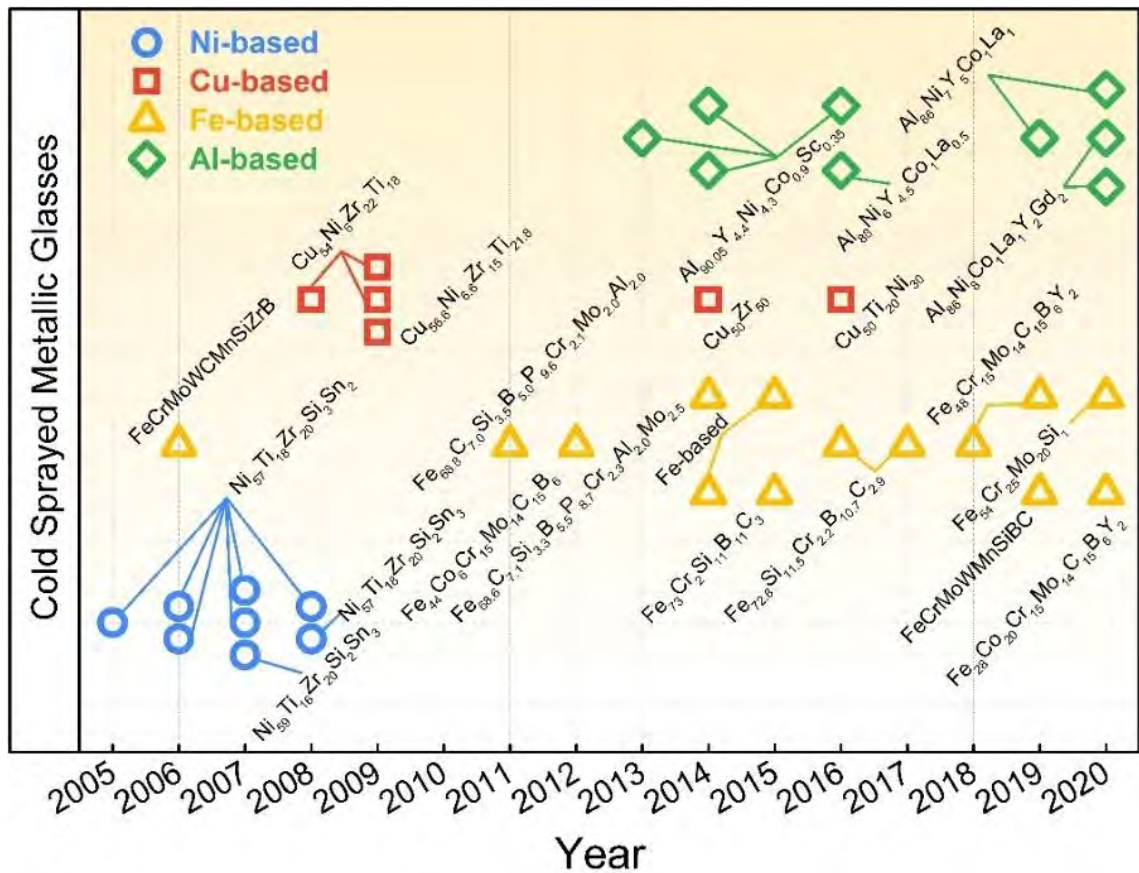


Fig. 2.20 Research articles on cold-sprayed metallic glass deposits (Data collected from Scopus).

Table. 2.1 Summarization of published works regarding cold-sprayed MG deposits

Feedstock	Substrate	Gas parameters			Preheating Temp. (°C)	Thickness (mm)	Porosity (%)	Hardness	Ref.
		Type	Pre. (MPa)	Temp. (°C)					
Ni ₅₇ Ti ₁₈ Zr ₂₀ Si ₃ Sn ₂	-	He	3.0	600		~ 0.2	-	-	[141]
Ni ₅₇ Ti ₁₈ Zr ₂₀ Si ₃ Sn ₂ (5-45 μm)	Mild steel	N ₂	2.9	600	RT	~ 0			
					550	~ 0			
		He	2.9	600	RT	~ 0.13	-	-	[142]
					550	~ 0.14			
Ni ₅₇ Ti ₁₈ Zr ₂₀ Si ₃ Sn ₂	Mild steel	He	2.9	600	RT		~11.5	~ 728 HV _{0.3}	
					450	~ 0.25	~5.7	~ 713 HV _{0.3}	[89,143]
					550		~4.0	~ 688 HV _{0.3}	
FeCrMoWCMnSiZrB	Al6061	-	1.0	300	-	~0.3	~ 0	639 HV _{0.3}	[144]
Ni ₅₇ Ti ₁₈ Zr ₂₀ Si ₃ Sn ₂ (d _{ave} =27 μm)	Mild steel	He	2.5	550	550	~0.4	~ 2.2	685	[145]
Ni ₅₇ Ti ₁₈ Zr ₂₀ Si ₃ Sn ₂	Mild steel	He	2.9	550	-	~0.4	-	-	[146]
Cu ₅₄ Ni ₆ Zr ₂₂ Ti ₁₈ (10-45 μm)	Mild steel	He	2.9	550	-	-	-	-	[147]
Cu ₅₄ Ni ₆ Zr ₂₂ Ti ₁₈ (10-45 μm)	-	He	1.5	550					
			2.0	550		0.4-0.45	-	-	[148]
			2.5	550					
			3.0	550					
Cu ₅₄ Ni ₆ Zr ₂₂ Ti ₁₈	Cu BMG	He	2.9	550	470	-	-	-	[73]
Cu _{56.6} Ni _{6.6} Ti ₁₅ Zr _{21.8} (2-40 μm)	Cu BMG	He	2.5	550	470	-	-	-	[149]
Fe _{68.8} C _{7.0} Si _{3.5} B _{5.0}	Mild steel	He	2.1			~0.04			
P _{9.6} Cr _{2.1} Mo _{2.0} Al _{2.0}			2.5	550	570	~0.07	-	~833 HV _{0.1}	[150]
(5-45 μm)			2.9			~0.08			
Fe ₄₄ Co ₆ Cr ₁₅ Mo ₁₄ C ₁₅ B ₆ (25-45 μm)	Austenitic steel	N ₂	4.0	900	-	~0.35	~2.3	> 1100 HV _{0.3}	[151]
				950		~0.89	~2.7		
Al _{90.05} Y _{4.4} Ni _{4.3} Co _{0.9} Sc _{0.35} (2.5-45 μm)	Al6061	N ₂	3.8	400	-	~0.25	~2	3.36 GPa	[152,153]
Fe _{68.8} C _{7.0} Si _{3.5} B _{5.0}	Cu	-	2.8	800	550	~0.65	-	-	[154]
P _{9.6} Cr _{2.1} Mo _{2.0} Al _{2.0} (~45 μm)									
Fe-based	Soda-lime glass	He	0.6	-	-	0.003	~1.5	-	[155]
						0.055	~2.25		

						~0.1	~3.0		
Cu50Zr50	Stainless steel	N ₂	4.0	600	-	~0.55	0.62	455 HV _{0.3}	[156]
				800		~0.16	0.20	596 HV _{0.3}	
Fe-based	Mild steel	N ₂	4.0	900	-	~0.8	~1.07	~729 HV _{0.3}	[157]
				1000		~0.5	~2.60	~736 HV _{0.3}	
				900		~0.7	~2.20	~767 HV _{0.3}	
				1000		~0.45	~2.83	~816 HV _{0.3}	
Fe ₇₃ Cr ₂ Si ₁₁ B ₁₁ C ₃ (20-40 μm)	Carbon steel	N ₂	4.0	700	-	< 0.2	> 8	-	[158,159]
				750		0.25	~ 5		
				800		0.68	< 1		
				850		0.69	< 1		
				900		0.60	--		
Fe _{72.8} Cr _{2.2} Si _{11.5} B _{10.7} C _{2.9} (20-40 μm)	Mild steel, Stainless Steel, Al7075-T6, Pure Cu, Inconel-625	N ₂	4.0	750	-	-	-	-	[160]
				800		-	-		
				800		-	-		
				800		-	-		
Cu ₅₀ Ti ₂₀ Ni ₃₀	Stainless steel	He	-	400	-	~ 0.01	-	2.97-3.20 GPa	[161]
Al ₈₈ Ni ₆ Y _{4.5} Co ₁ La _{0.5} (20-40 μm)	Al 7075 T6	N ₂	4.0	400	-	~0.4	~1.6	220 HV _{0.1}	[162]
Fe ₄₈ Cr ₁₅ Mo ₁₄ C ₁₅ B ₂₆ Y ₂ (5-45 μm)	AISI 4140 steel	N ₂	4.0	850	-	-	-	15.7 GPa	[163]
				900					
				950					
				1000					
				280					
Al ₈₆ Ni ₇ Y ₅ Co ₁ La ₁ (5-65 μm)	Al6061	N ₂	3.0	320	-	1.26	3.33	-	[164]
				360		1.53	3.05		
				280		0.71	4.36		
	Al6061	N ₂	4.0	320	-	1.36	2.83	-	
				360		1.67	3.96		
				280		0.90	3.42		
Al7075	N ₂	3.0	320	-	0.56	3.04	-		
			360		1.73	2.69			
			280		0.18	3.31			
Al7075	N ₂	4.0	320	-	0.71	4.37	-		
			360		1.80	3.31			
			400		1.63	2.93			
			970		~ 0.6	-		6 ~ 10 GPa	[165]

$\text{Fe}_{48}\text{Cr}_{15}\text{Mo}_{14}\text{C}_{15}\text{B}_6\text{Y}_2$ (10-30 μm)	35CrMo	N_2	4.5	900	-	~ 0.9	2.0	1002 HV _{0.1}	[166]
$\text{Fe}_{54}\text{Cr}_{25}\text{Mo}_{20}\text{Si}_1$ (2-25 μm)	40Cr high strength steel	N_2	5.5	900	-	~ 0.248	2.97	720 ~ 1030 HV _{0.1}	[167]
$\text{Al}_{86}\text{Ni}_8\text{Co}_1\text{La}_1\text{Y}_2\text{Gd}_2$ (3-23 μm)	-	N_2	4.0	400 500 600	-	~ 0.6	1.3 0.5	-	[168]
$\text{Al}_{86}\text{Ni}_8\text{Co}_1\text{La}_1\text{Y}_2\text{Gd}_2$ (4-15 μm)	Al 7075 T6	N_2	4.0	800	-	~ 0.9	3.2	300 HV _{0.2}	[169]
FeCoCrMoBCY (2-25 μm)	40Cr	N_2	3.5 4.5 5.5	700 800 900	-	~ 0.16 ~ 0.18 ~ 0.19	10.02 8.67 3.51	820~880 HV _{1.0} 910~920 HV _{1.0} 920~930 HV _{1.0}	[170]

2.3.1 Feedstock Powder

The materials-related parameters (i.e., particle size, flowability, surface state, and mechanical properties) have a great impact on the successful particle deposition and the quality of cold-sprayed MG deposits [54]. The feedstock powder for cold spraying is generally produced by inert gas atomization, and the powders feature high sphericity with a particle size range between 5 and 50 μm in diameter. Apart from gas atomization, water atomization [157,167] and mechanical alloying [161] were also employed for MG feedstock powder fabrication. No matter which production method is used, the produced feedstock powder is expected to have a high extent of amorphous content and good glass forming ability (GFA). For MG powder characterization, X-ray diffraction (XRD) and transmission electron microscopy (TEM) in combination with selected area electron diffraction (SAED) patterns or fast Fourier transform (FFT) patterns are usually conducted to confirm the amorphous structure of powder. In addition, the thermal properties of MG also play an important role in particle deformation and deposition. Therefore, differential scanning calorimeter (DSC) is usually applied for the measurement of glass

transition temperature (T_g) and crystallization temperature (T_x), which could provide guidance for optimal manufacturing parameters selection. Fig. 2.21 provides an example of Cu-based MG powder characterization [73]. The powder features high sphericity with few satellite powders attached to the surface of the particles particularly with larger sizes (see Fig. 2.21a), which can be attributed to their different condensation rates. The high-resolution electron microscopy shows a highly disordered structure without any sign of nanocrystals or ordered clusters. Moreover, the diffusion halo in the FFT pattern shows a diffusion halo (see Fig. 2.21b), suggesting the amorphous structure of the powder [73]. The amorphous structure can also be demonstrated by the XRD spectrum, which exhibited a broad diffraction peak maximum at around $2\theta = 40^\circ$ (see Fig. 2.21c). In addition, the amorphous content of the MG powder can be estimated by the XRD and DSC results.

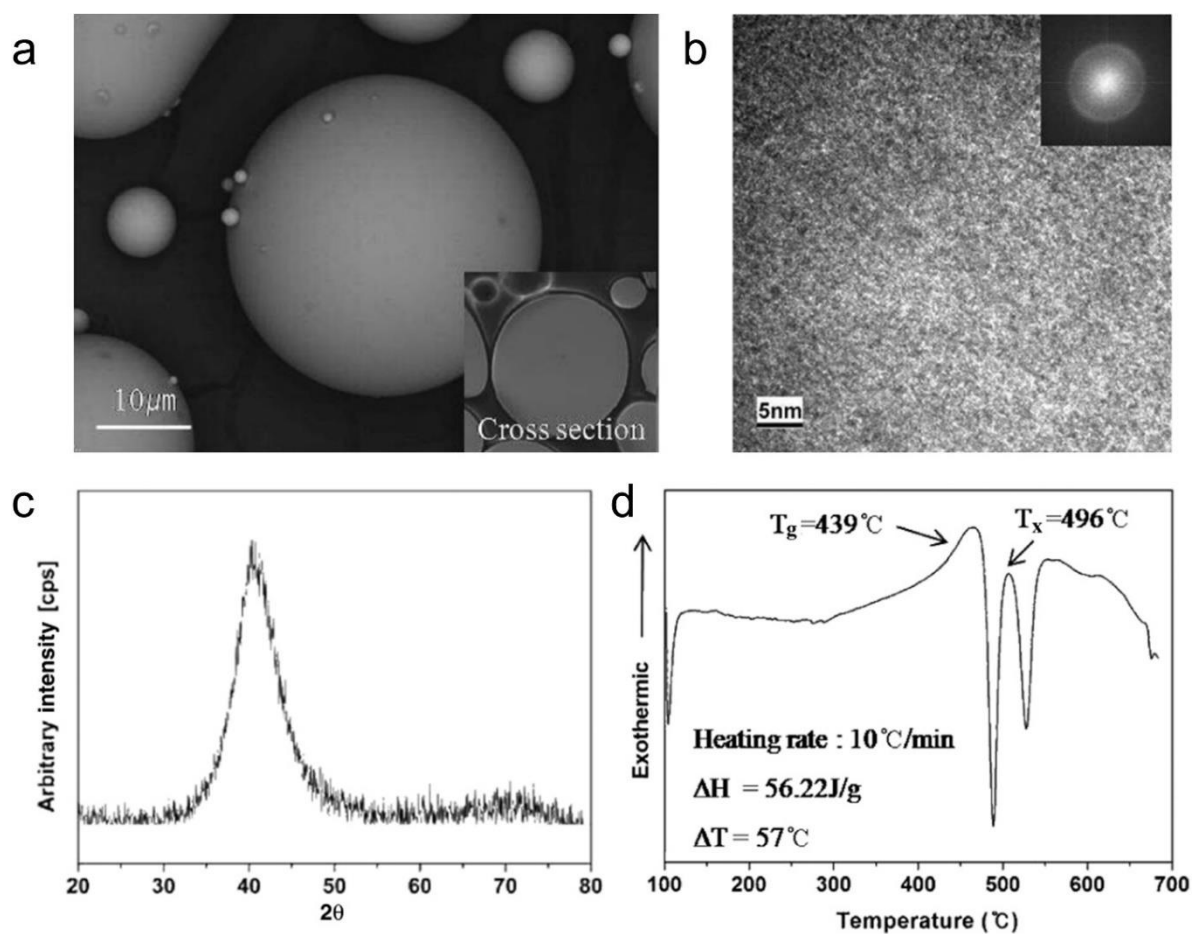


Fig. 2.21 Characteristics of the $\text{Cu}_{54}\text{Ni}_6\text{Ti}_{22}\text{Zr}_{18}$ metallic glass feedstock powder [73]. (a)

Particle surface morphology, (b) High-resolution electron microscopy images with corresponding FFT insets, (c) XRD pattern, (d) DSC curve. Note the diffusion halo in FFT and broad diffraction peak in the XRD pattern indicated the feedstock powder had an amorphous structure.

2.3.2 Processing Parameters

Compared with conventional metals or alloys, the gas parameters are more important for the deposition of MG particles as the plastic deformation behavior of MGs highly depends on the temperature and strain rate, which can be categorized into inhomogeneous deformation and homogeneous deformation [140]. The homogeneous deformation of MG particles is expected and generally takes place at lower strain rates or higher temperatures. Fig. 2.22 shows the effect of gas temperature, gas pressure, and stand-off distance on the deposition efficiency, thickness, porosity, and microhardness of the cold-sprayed $\text{Al}_{88}\text{Ni}_6\text{Y}_{4.5}\text{Co}_1\text{La}_{0.5}$ MG deposit. Higher gas temperature led to higher deposition efficiency (see Fig. 2.22a), which can be attributed to the better acceleration effect and thermal softening effect induced by high temperatures. For MG powders, the thermal softening and homogeneous deformation of feedstock happens when they are heated to the supercooled liquid region, which is defined as the temperature region between glass transition temperature (T_g) and crystallization temperature (T_x) [141]. In the supercooled liquid region, MGs exhibit distinct viscous flow and superplastic deformation characteristics, and the softened particles deform and compactly bond with the substrate or previously deposited layer, resulting in fewer defects (i.e., pores and cracks) in the deposit. The increased gas pressure led to higher deposit thickness and density, as shown in Fig. 2.22b and c. Consequently, the deposit fabricated at higher gas pressure exhibited enhanced microhardness (see Fig. 2.22d). However, the increased gas pressure resulted in a decrease in amorphous content in cold-sprayed MG deposits because of the high strain and heat input at the impacting

interface [148]. As for the stand-off distance, the optimal distance under each condition was different, suggesting that the distance should be selected according to the match of gas temperature and pressure. When under the highest temperature and pressure (C8), the optimal distance was 30 mm and further increase or decrease of stand-off distance led to the increased porosity and the decreased hardness.

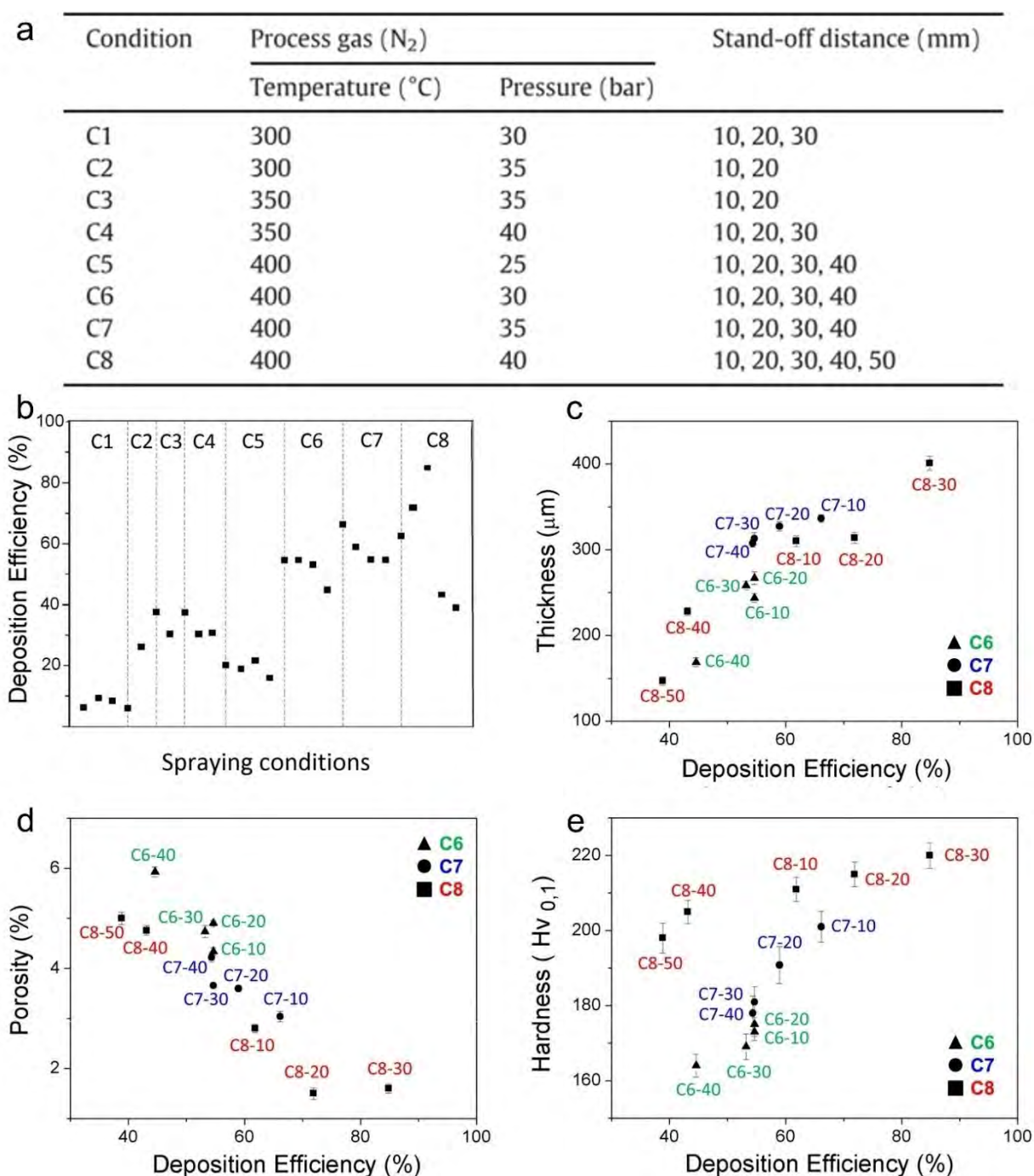


Fig. 2.22 Effect of gas temperature, gas pressure and stand-off distance on the (a) deposition

efficiency, (b) thickness, (c) porosity and (d) microhardness of the cold-sprayed $\text{Al}_{88}\text{Ni}_6\text{Y}_{4.5}\text{Co}_1\text{La}_{0.5}$ metallic glass deposit [162].

Apart from increasing gas temperatures, powder preheating was also employed to increase the initial particle temperature to promote superplastic deformation in earlier studies [89]. The powder preheating process can densify the deposit, enhance the bond strength, and improve the hardness of the cold-sprayed deposit, as shown in Fig. 2.23 and Fig. 2.24. However, the rising of powder preheating temperatures could lead to a higher risk of increased oxygen content and the decreased amorphous fraction of MG deposit at the same time (see Fig. 2.24e). The decreased amorphous content was also found in the fabrication of an Al-based MG deposit when the gas temperature increased from 400 to 600 °C [168]. Therefore, the gas preheating temperatures and/or gas temperatures during the deposition of MG powders should be carefully controlled to achieve homogenous plastic deformation and avoid oxidation and crystallization at the same time.

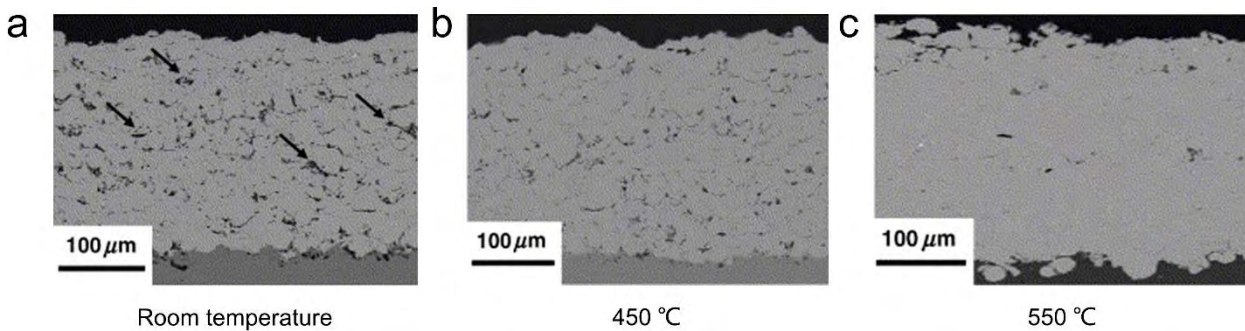


Fig. 2.23 Cross-sectional morphology of the as-sprayed Ni-based metallic glass coatings under different powder preheating temperature, (a) room temperature, (b) 450 °C, (c) 550 °C [89].

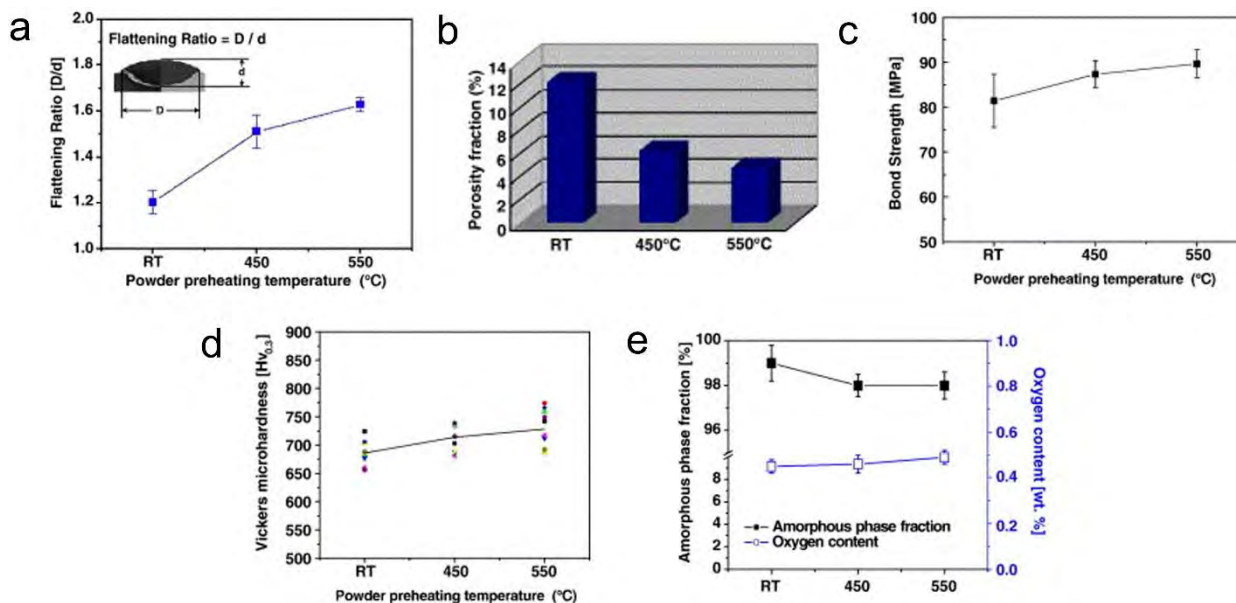


Fig. 2.24 Effects of powder preheating temperature on the (a) flattening ratio, (b) porosity, (c) bond strength, (d) microhardness and (e) amorphous phase fraction and oxygen content of the as-sprayed Ni-based metallic glass deposit [89].

2.3.3 Particle Bonding Mechanism

Researchers have studied the formation mechanism of cold-sprayed MG deposits experimentally by investigating the deformation behavior of individual particles after high-velocity impact. Yoon et al. [142] classified a deposited Ni-based MG particle into three characteristic regions: “little (or no) deformation” at the north pole of a particle, “shear bands and fracture” at the periphery of a particle, and “melting and viscous flow” features at the bottom (see Fig. 2.25a), which suggested the generation of strain and temperature gradients in deposited particles. The successful bonding of particles was considered to be related to the viscous flow and melting at the impacting interface, driven by adiabatic heating [142]. Further, another study pointed out that melting only occurred at the bottom periphery (the fringe of the interface) rather than the entire region, as evidenced by the pronounced vein patterns at the bottom of a detached Cu-based metallic glass particle (see Fig. 2.25b) [156]. Henao et al. [159] investigated the homogeneous deformation of

individual Zr-based metallic glass particles with the finite element method, which used the viscoplastic equations based on free-volume constitutive theory [159]. The study revealed that the viscoplastic deformation of particles was activated firstly due to the feature of non-Newtonian flow (shear thinning) under high impact velocity and high impact temperature, followed by the Newtonian flow induced by the heat energy converted from viscoplastic deformation work. The homogeneous deformation, including both non-Newtonian and Newtonian flow, promoted the lateral viscous flow of metallic glass. The high temperature at the impacting interface allowed particles to bond with the substrate by metallurgical bonding. These two factors resulted in the formation of the cold-sprayed MG deposits [159]. Besides, for the MG particles with low impact temperature, the viscous flow can also be induced by the high temperature within adiabatic shear bands, which promotes particle deformation and bonding [143,171].

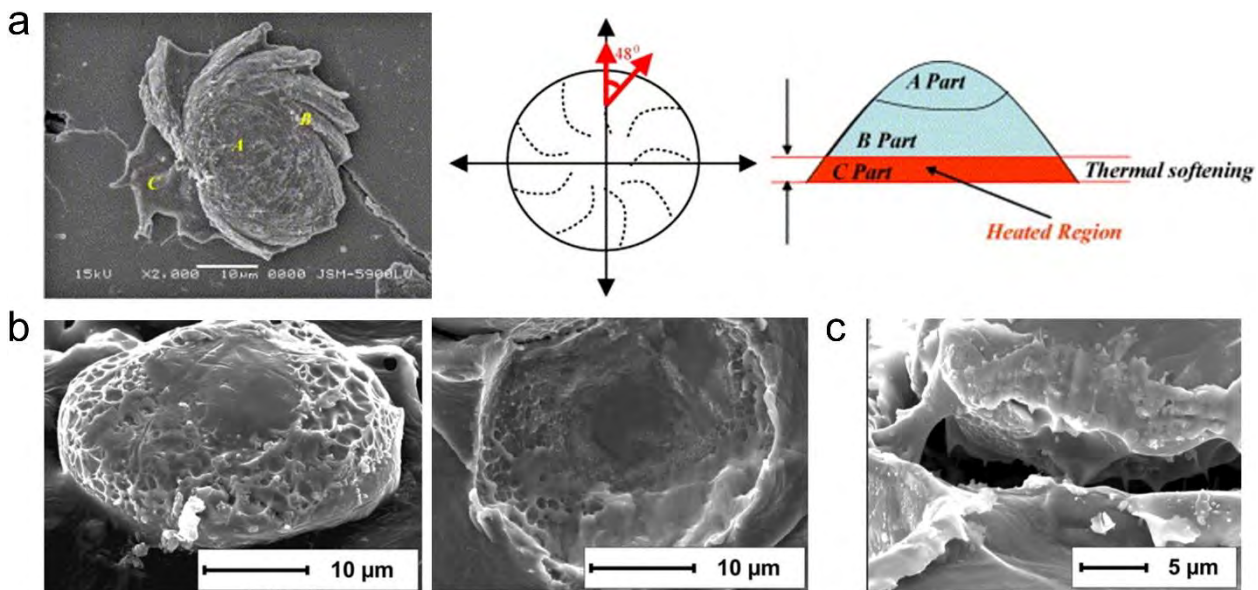


Fig. 2.25 Individual particle deposition behavior of MG particles. (a) Deposition behavior of NiTiZrSiSn MG particles, exhibiting three characteristic regions [142], (b) A single Cu₅₀Zr₅₀ MG particle detached after cavitation testing and a corresponding crater on the substrate surface, both showing pronounced vaine pattern [156], (c) An incompletely detached particle by showing the vaine pattern and the associated gap between the particle and the substrate [156].

In the deposition process of crystalline materials, successful particle bonding is generally regarded to be associated with the occurrence of adiabatic shear instability at the impacting interface, resulting in material softening and metallurgical combination [57]. The adiabatic shear instability happens when the particle impact velocity reaches or exceeds a value, which is called "critical velocity" (v_{crit}). From the empirical formula for calculating critical velocity, it is known that the critical velocity is dependent on the intrinsic properties of feedstock powders (i.e., density, melting point, and ultimate strength) and initial particle temperature [57–59]. According to the thermal and mechanical properties of the feedstock materials, the graph of the impact velocity and critical velocity versus processing parameters or particle size, also known as "deposition window", was established for selecting optimized manufacturing parameters or particle size range. While in the case of MG particles, their successful bonding was considered to be related to the viscous fluid and melting at the impacting interface, which are induced by the adiabatic heat [142]. List et al. used the method of calculating deposition window for crystalline materials and established the deposition window of Fe-based MG [151]. However, it was found that either using melting temperature (T_m) or using T_g as a reference for softening temperature (T_s) failed to get the actual deposition window. This is because the softening behavior of MGs above T_g varies from the Johnson-Cook plasticity model. The critical velocity was estimated from the experiment by using the 50% deposition efficiency (DE) rule, and a softening temperature was adjusted to 1.3 times the T_g (i.e., $T_s = 1.3 T_g$) [55,151]. It is widely accepted that the viscosity of MGs versus temperature in the supercooled liquid region changes sharply. In addition, the level of temperature dependence of viscosity varies among different types of MGs. Therefore, the use of $1.3 T_g$ as a reference for T_s is not universal for all MGs. Furthermore, a recent work found there was no good correlation between DE and particle impact velocity in the deposition of Fe-based MGs [158]. Thus, the critical velocity from experiment using the 50% DE rule may lead to distortion.

Concustell et al. proposed a model regarding the MG particle as a liquid droplet impacting onto a surface and made a connection of DE obtained from experiment measurement and Reynolds number (Re) of MG particle [158]. The Re number is defined by the ratio of inertial and viscous forces of MG particles upon impact:

$$Re = \rho v_i d / \eta \quad (\text{Eq. 2.1})$$

where ρ is the density of the liquid, v_i is impact velocity, d is particle diameter and η is viscosity of the liquid. The viscosity of MGs can be described with the Vogel-Fulcher-Tammann relation [172]:

$$\eta = \eta_0 \cdot \exp[D \cdot T_0 / (T - T_0)] \quad (\text{Eq. 2.2})$$

where T_0 is the Vogel-Fulcher-Tammann temperature and D is the fragility parameter. The viscosity of MG at T_m is about ten orders of magnitude greater than that of MG at T_g , indicating the significant temperature dependence. Therefore, it is suggested that the deposition of MG particles is dependent on the particle impact temperature and impact velocity. High impact temperature leads to low viscosity, and high impact velocity indicates high inertial force which promotes the activation of viscous flow. Obviously, a higher Re value favors particles to experience homogeneous deformation, leading to a high DE. Similar to the critical velocity defined for crystalline materials to predict particle bonding, the critical Reynolds number (Re_{crit}) was defined as the point where inertial forces enable to active viscous flow of metallic glass [159]. Then the relationship between V_{crit} and Re_{crit} was as follows [158]:

$$v_{crit} = \frac{Re_{crit} \cdot \eta(T)}{\rho \cdot d} \quad (\text{Eq. 2.3})$$

By calculating the particle impact velocity and corresponding DE under different manufacturing parameters, the relation between DE and Re can be built. And then the Re_{crit} can be determined from the curve where a sharp increase of DE occurred,

(see Fig. 2.26a). Fig. 2.26b shows the cross-sectional morphology of the cold-sprayed Fe-based MG deposit at a high and a low Re number respectively. The deposit fabricated at a low Re value exhibited a porous structure and low DE, and the particle mainly experienced inhomogeneous deformation and was less deformed. While at a higher Re number, the deposit was dense with fewer manufacturing defects, and the viscoplastic flow of the particle can be observed, indicating the homogeneous deformation of MG particles under the current processing parameters.

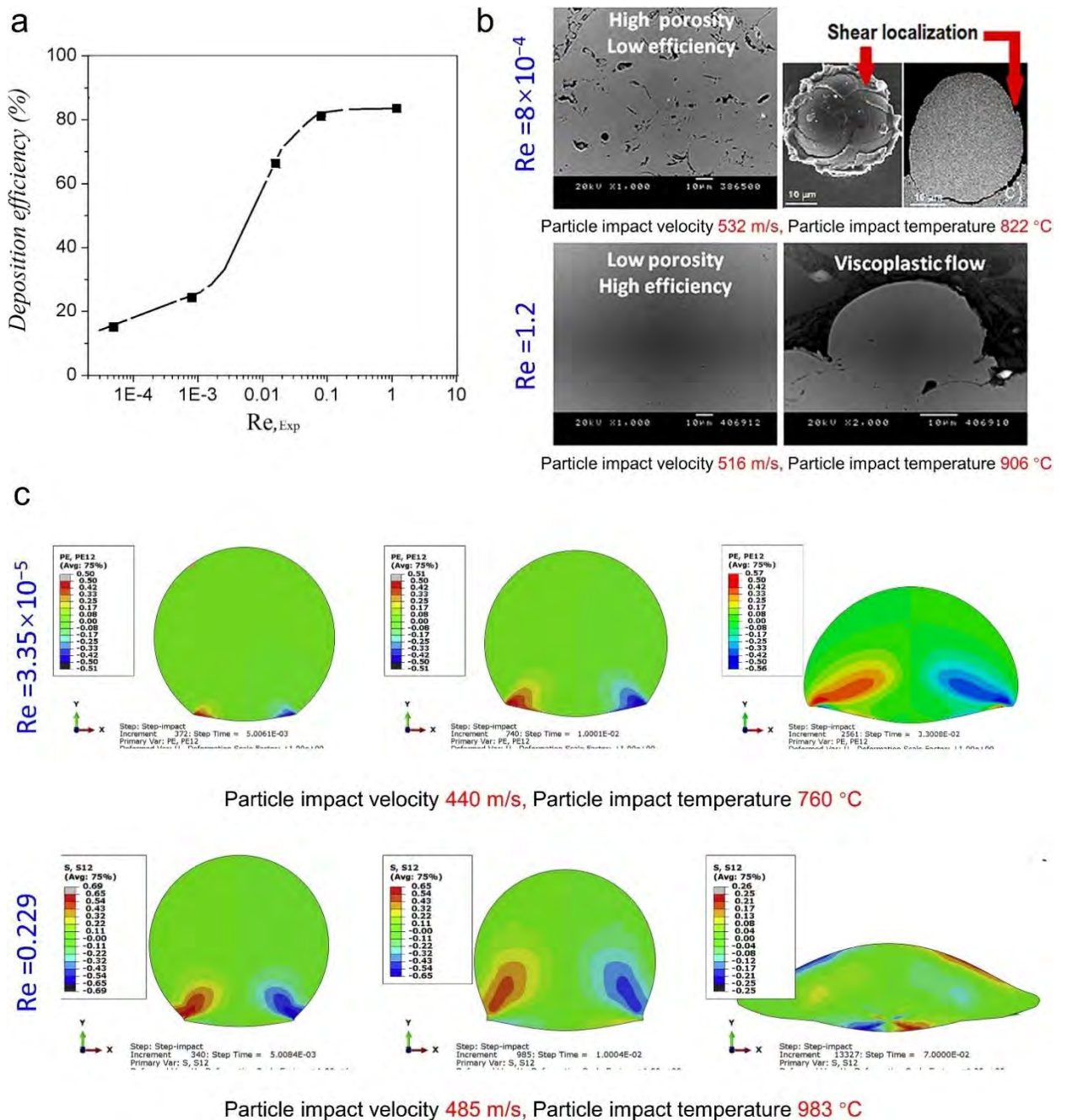


Fig. 2.26 (a) Deposition efficiency and (b) Cross-sectional morphology of the cold-sprayed $\text{Fe}_{72.8}\text{Si}_{11.5}\text{Cr}_{2.2}\text{B}_{10.7}\text{C}_{2.9}$ metallic glass deposits or particles at different Re numbers, (c) Deposition behavior of individual $\text{Zr}_{41.2}\text{Ti}_{13.8}\text{Cu}_{12.5}\text{Ni}_{10}\text{Be}_{22.5}$ metallic glass particles at two typical Re numbers [159].

Henao et al. investigated the deposition behavior of Zr-based metallic glass particles at different Re using finite element simulation [159]. The simulation used the viscoplastic equation based on the free volume constitutive theory. It confirmed that Re acted as an important parameter for particle effective bonding. When Re was above a threshold value, also known as Re_{crit} , the viscoplastic flow in the particle was significantly enhanced due to enhanced softening (see Fig. 2.26c). The particle can flow easily upon impact and bond with the substrate/previous layer. While at lower Re, the metallic glass deformed with the feature of severe localized plastic flow (i.e., shear band formation and fracture). However, the model is only able to describe the deformation behavior of MGs within the supercooled liquid region.

Although the formation mechanism of cold-sprayed MG deposits has been widely discussed through both experiment and numerical simulation approaches, there are still some key issues that need to be resolved. For one thing, the direct evidence of metallic glass interparticle bonding across their interfaces has yet to be observed experimentally, which limits our further understanding of their bonding mechanisms. For another, most of the existing studies revealed that melting and viscous flow only occurred at the interparticle interface to induce bonding, and it is unclear whether there exist any other mechanisms dominating the deposition of cold spray metallic glasses as well.

2.3.4 Crystallization Behavior

MGs are thermodynamically in metastable states and tend to transform into their crystalline counterparts spontaneously under certain conditions (i.e., mechanical

deformation [173,174], isothermal annealing [175,176], and electron irradiation [177,178]). The crystallization of MG particles can hinder their deformation and result in reduced deposition efficiency in cold spray process [157,158,160]. In addition, the crystallization will lead to a decreased fraction of amorphous phases in the deposit, which may deteriorate its material properties. The crystallization event of MG particles during cold spray can take place in two stages: before leaving the exit of the nozzle (i.e., preheating process or in-flight process in the nozzle) and in the process of high-velocity impact respectively. The former case can be attributed to the exposition at elevated temperature (typically above T_x) for a period, rendering the formation of oxide layers or pre-crystallized layers on initial powders [73,89,158]. While crystallization of MG particles during deposition is a more usual phenomenon [73,148,149]. MG particles experience intensive plastic deformation upon impact, inducing abnormally increased strain and considerable temperature rise at the impacting interface, particularly localized at the edge of the interface. By observing the nanostructure at the interface of a deposited Cu-based metallic glass particle, nano-sized crystals were found at the edge of the interface, while the amorphous structure was retained at the center of the interface. Furthermore, a larger area with crystalline phases was found at the edge of the interface under increased gas pressure, while the nanostructure at the center of the interface remained highly disordered, as shown in **Fig. 2.27** [148]. Therefore, the crystallization is considered to be associated with the extremely high strain and temperature, which are dependent on the kinetic energy of the particle upon impact. For one thing, the adiabatic temperature rise at the edge of the interface can reach T_x or even melting temperature (T_m), which provides driving force for crystallization. For another, the high pressure and strain compress the amorphous structure and reconstruct the atomic configuration, which results in the annihilation of the free volume and the reduction of voids. The strain energy has a great influence on the nucleation rate and higher strain energy enables to accelerate nucleation [179,180]. These factors

promote the formation of the ordered structure at the edge of the interface [148]. However, considering the extremely high cooling rates ($\sim 10^{10} \text{ K}\cdot\text{s}^{-1}$ [55]) and short impacting period ($\sim 10^{-8} \text{ s}$ [73]), the growth of the nucleus is limited and thus crystallization is highly localized [148]. Although the crystallization during deposition has been explored and the causes of crystallization were also well-explained, the detailed formation process of the localized ordered structure has not yet been reported. Moreover, the dynamic evolution of thermal-mechanical-induced crystallization needs to be further investigated.

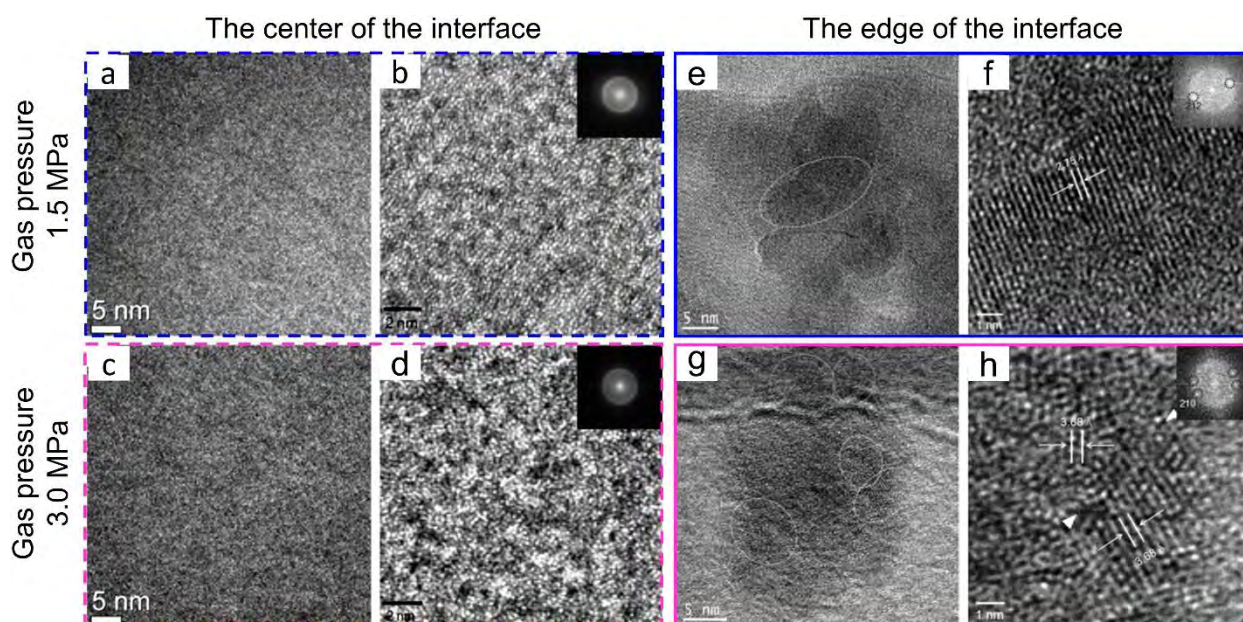


Fig. 2.27 Microstructure evolution at the impacting interface of the cold-sprayed Cu-based MG deposits. (a, b) The center of the interface at low gas pressure, (c, d) The center of the interface at high gas pressure, (e, f) The edge of the interface at low gas pressure, (g, h) The edge of the interface at high gas pressure. Note the nanocrystallization can be found at the edge of the impacting interface, and the increased gas pressure led to the increased nanocrystals [148].

2.4 High-entropy Alloys

2.4.1 Definition

High-entropy alloys (HEAs), also known as multi-principal element alloys (MPEAs), are a type of disordered alloys (chemical disorder) discovered based on the exploration of bulk metallic glasses (BMGs). One of the three empirical rules proposed by Prof. Inoue to form BMGs with good glass forming ability is three or more principal elements are required [129,130]. Prof. Greer from Cambridge University proposed the confusion principle in 1993, which stated that the more principle elements involved, the lower the chance that the alloy can select viable crystal structures and the greater the chance of glass formation [181]. Based on this, Prof. Cantor manufactured alloys containing 20 or 16 elements in equimolar ratios by casting method, but the result showed that brittle crystalline phases were formed rather than the expected amorphous phase. Moreover, the alloy was mainly composed of FCC phase especially in Cr, Mn, Fe, Co, and Ni regions [182]. According to this surprising phenomenon, $\text{Cr}_{20}\text{Mn}_{20}\text{Fe}_{20}\text{Co}_{20}\text{Ni}_{20}$ alloy in equiatomic ratio was designed and manufactured, and the as-casted alloy exhibited a single-phase solid-solution structure [182]. This alloy was later known as Cantor alloy, which marked the birth of HEA.

Unlike traditional alloys that are generally dominated by one or two elements and supplemented with a minority of metallic or non-metallic elements to achieve desired material properties, HEAs are formed by mixing five or more principal elements in various proportions, with each principal element carrying a concentration of 5%–35% [183,184]. Such a unique multi-principal element design strategy significantly increases the mixing entropy of alloys, as shown in Fig. 2.28. The HEAs exhibit excellent mechanical properties (e.g., high hardness, high strength, and high fracture toughness), superior wear resistance and corrosion

resistance, good irradiation resistance, thermodynamic stability, and show great application prospects [183,185,186].

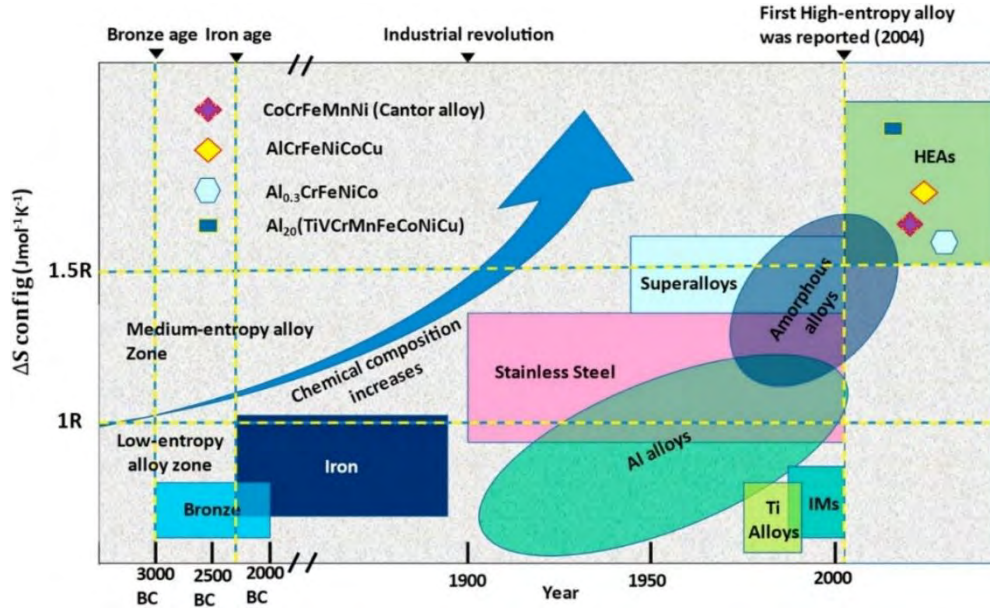


Fig. 2.28 Periodic development in metals. [187,188]

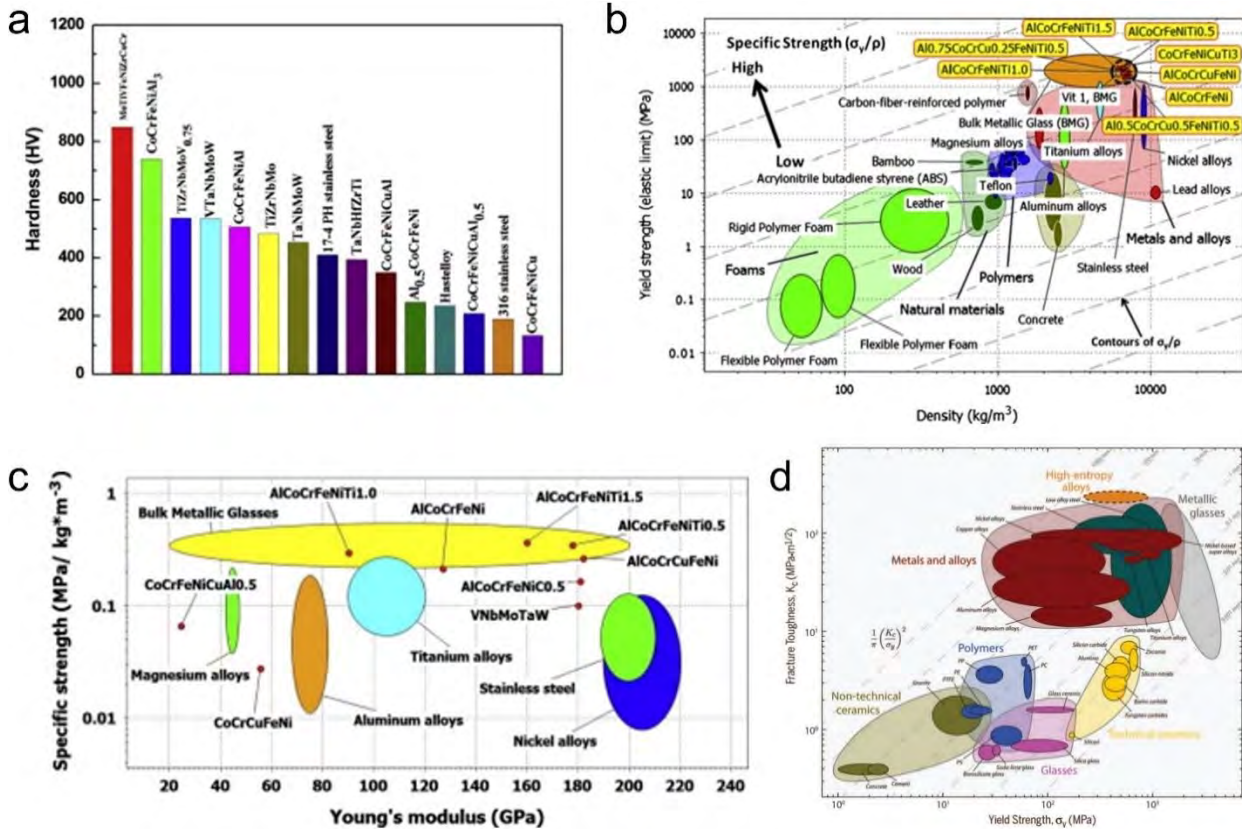


Fig. 2.29 Excellent properties of High-entropy alloys (HEAs). (a) Hardness of HEAs compared with 17–4 PH stainless steel, Hastelloy, and 316 stainless steel [184], (b) Yield strength as a function of density for HEAs compared with other materials, particularly structural alloys [189], (c) Specific-yield strength versus Young's modulus of HEAs compared with other materials, particularly structural alloys [189], (d) Fracture toughness as a function of yield strength for HEAs in relation to a wide range of material systems [190].

2.4.2 Core effects of HEAs

Due to the unique alloy design strategy, HEAs exhibit four core effects including high-entropy effect in thermodynamics, severe lattice distortion effect in structures, sluggish diffusion effect in kinetics, and cocktail effect in properties. These effects endow HEAs with excellent material properties compared to conventional alloys.

► High entropy effect

High entropy is the typical characteristic of HEAs. Entropy is a parameter representing the state of disorder of a system in thermodynamics, and the greater the disorder, the higher the entropy. According to Gibbs phase rule for metallurgical system,

$$P=C+1-F \quad (\text{Eq. 2.4})$$

where C is the number of components in the system, F is the degree of freedom, and P is the number of phases. Based on the rule, it can be found that a higher number of components will lead to a higher number of phases. However, early experimental results show that HEAs tend to form single phase solid-solution structures (e.g., FCC or BCC) rather than multiple phases as predicted by the Gibbs phase rule [182].

According to Gibbs free energy theory, the Gibbs free energy in HEA can be expressed as follows,

$$\Delta G_{\text{mix}} = \Delta H_{\text{mix}} - T\Delta S_{\text{mix}} \quad (\text{Eq. 2.5})$$

where ΔG_{mix} is the Gibbs free energy of mixing, H_{mix} is defined as enthalpy of mixing, T is temperature, and S_{mix} is the entropy of mixing respectively. It can be found that higher ΔS_{mix} leads to lower free energy of the system, which indicates the alloy system is more stable particularly at high temperatures. According to Boltzmann's thermodynamic theory, the configurational entropy of an alloy can be expressed as,

$$\Delta S_{\text{mix}} = -R\sum_i C_i \ln C_i \quad (\text{Eq. 2.6})$$

where R is the gas constant (8.3144J/ (mol·K)), C_i is the Molar fraction of the i -th element. For equimolar ratio HEA, the configurational entropy can be expressed as $\Delta S_{\text{mix}} = R \ln N$, and the configurational entropy increases with the increased number of element types in HEAs. The high entropy effect in HEA promotes the formation of solid solution phases (e.g., FCC and BCC) rather than compound and intermetallic.

► *Severe lattice-distortion effect*

For conventional alloys, the lattice site is occupied by the dominant constituent. For HEAs, it is generally assumed that each element is expected to randomly occupy the crystal lattice with equal probability [184]. In other words, there is no clear distinction between solutes and solvents. The different sizes of elements in HEA will lead to lattice distortion. Fig. 2.30a shows a comparison between a perfect lattice with the same atoms and a distorted lattice with a solid solution of different-sized atoms [191]. The severe lattice distortion also influences the XRD diffraction peak intensities, as shown in Fig. 2.30b. Yen et al. [191] gradually added elements into Cu to form multiple principle alloys and investigated the phase structure (see Fig. 2.30c). With the addition of elements from pure Cu to AlSiCrFeCoNiCu HEA,

the phase structure changed from FCC structure to FCC + BCC structure. Moreover, the anomalous decrease in XRD intensities of the alloys was observed with the addition of more elements. The intrinsic lattice distortion induced by the addition of multi-principal elements with various atomic sizes is considered the reason for the anomalous decrease in the XRD intensities [184]. The severe lattice distortion effect can effectively impede dislocation movement and produce significant strengthening effects. It has become an effective strengthening strategy to strengthen HEAs by adjusting the principal elements in HEAs to achieve different levels of lattice distortion.

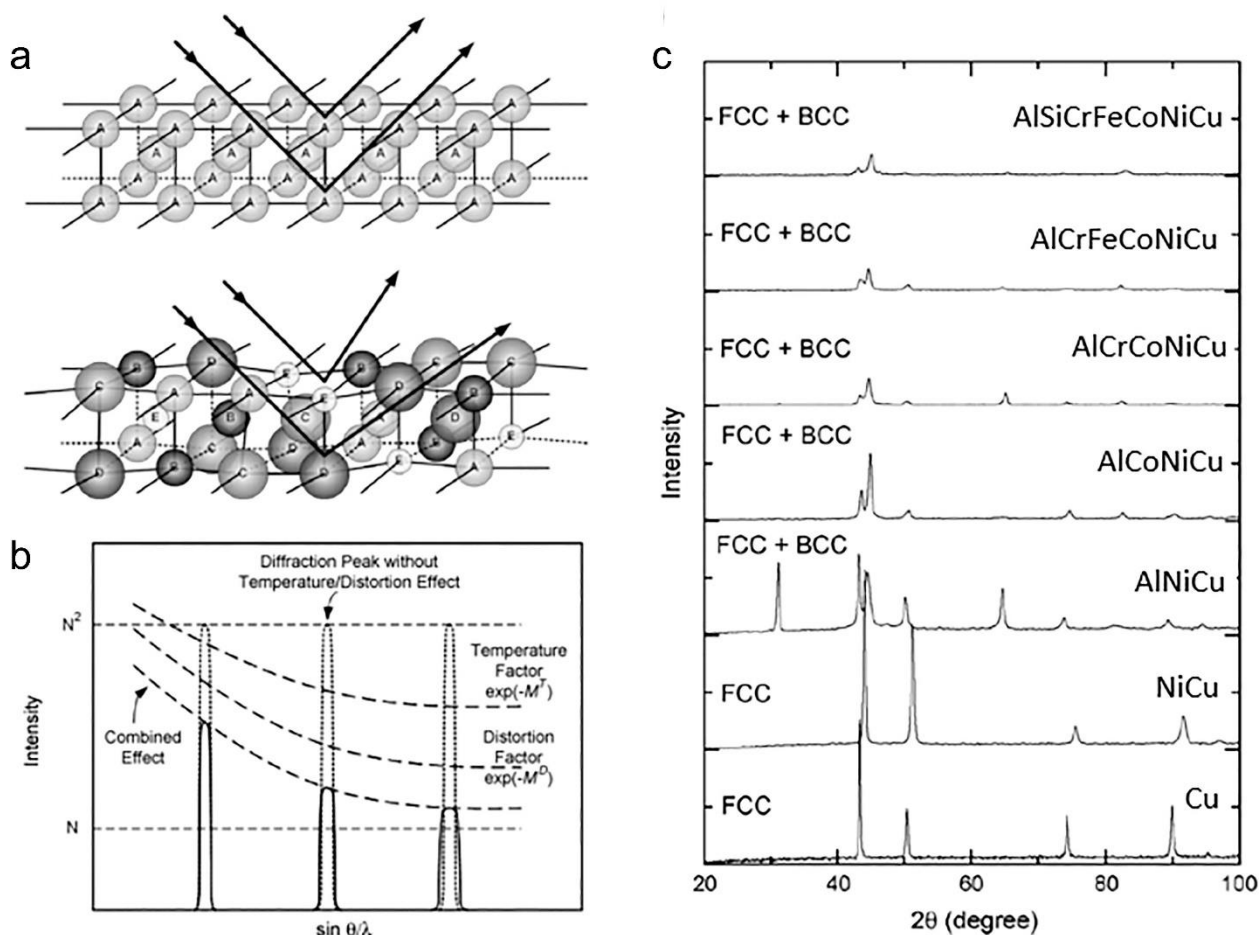


Fig. 2.30 (a) Schematic illustration of intrinsic lattice distortion effect on Bragg diffraction. A comparison between a perfect lattice with the same atoms and a distorted lattice with a solid solution of different-sized atoms which are expected to randomly distribute in the crystal lattice [191], (b) Effect of temperature and distortion on XRD intensity [191], (c) XRD patterns of Cu-

Ni–Al–Co–Cr–Fe–Si alloy series with the increasing number of incorporated principal elements [191].

► *Sluggish diffusion effect*

The sluggish diffusion effect indicates that the diffusion in HEAs is slower than that in pure metals and traditional alloys. As shown in Fig. 2.31, the diffusion coefficients for Cr, Mn, Fe, Co, and Ni in CoCrFeMnNi HEA are the lowest compared to other matrices. This can be attributed to the interaction between different atoms in HEA together with the lattice distortion, which severely affects the effective diffusion rate of the atoms [192]. The slow diffusion rate makes it difficult for HEAs to experience grain coarsening and recrystallization at elevated temperatures, and HEAs can exhibit good thermal stability. Moreover, the sluggish diffusion effect also helps HEAs to form supersaturated solid solutions, which is conducive to the precipitation of nano-sized phases [184,193]. This will lead to the significant enhancement of the hardness and strength of HEAs due to precipitation strengthening.

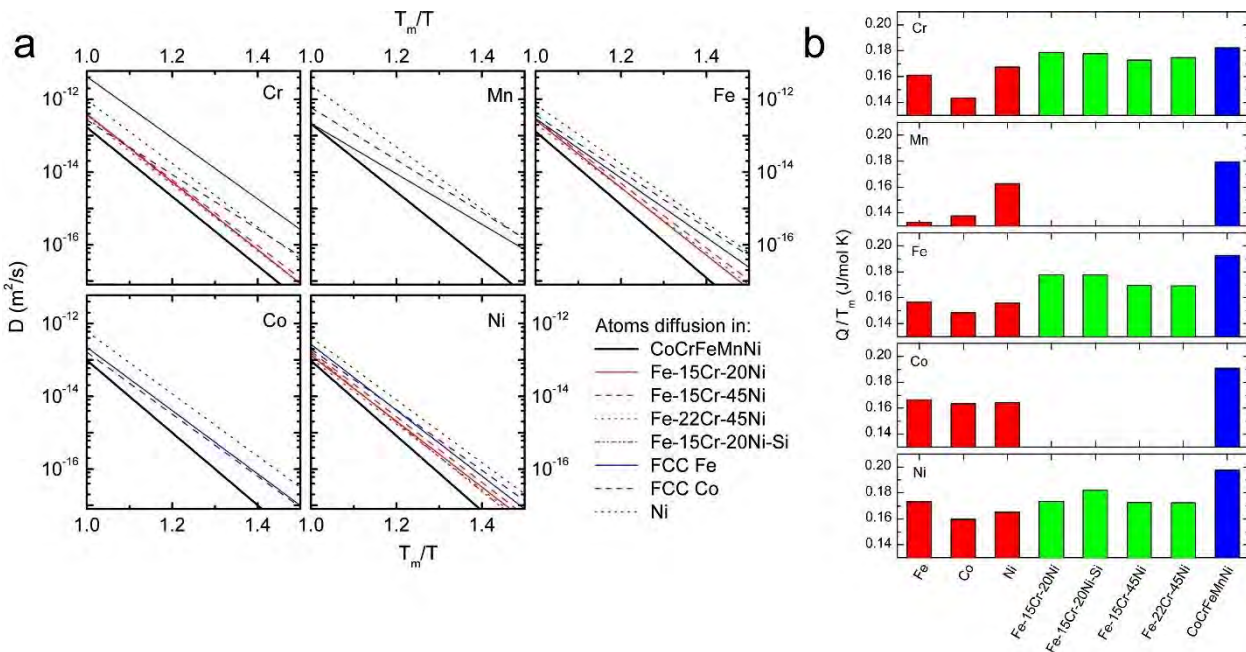


Fig. 2.31 (a) Temperature dependence of the diffusion coefficients for Cr, Mn, Fe, Co, and Ni in

different matrices [192], (b) Normalized activation energies of diffusion for Cr, Mn, Fe, Co, and Ni in different matrices [192]. Note the normalized activation energies indicate Q/T_m (or Q/T_s , where T_s is the solidus temperature for alloys), and the higher Q/T_m indicates the lower diffusion coefficient.

► **“Cocktail” effect**

The different elements in HEAs have various characteristics, and the overall properties of HEAs are related to each element and the interaction effect between elements. This is the so-called “cocktail” effect in HEA, which was proposed by Indian scientists [194]. For example, the addition of oxidation-resistant elements (e.g., Al, Cr, and Si) will increase the oxidation-resistant ability of the alloy. While the addition of light elements, such as Al, will reduce the density of the HEA. In addition to the characteristics of individual elements, the interaction among composing elements may lead to some unexpected performance in HEAs. Such performance cannot be obtained from any one individual element.

Fig. 2.32a shows the hardness and lattice variation of $\text{CuCoNiCrAl}_x\text{Fe}$ HEA with different Al ratios. With the increase of Al content, the phase structure changed from FCC to FCC + BCC and then to BCC. Moreover, the increased Al content also led to the increase of lattice constant for both FCC and BCC, resulting in an increase in hardness. This can be attributed to the negative enthalpy of mixing between the Al atom and other atoms, leading to stronger attractive interaction [195]. **Fig. 2.32b** exhibited the hardness variation of $\text{CoNiCrAl}_x\text{Fe}$ HEA with different Al ratios. There is no significant change in hardness when the molar ratio of Al is below 0.45. However, the increased molar ratio of Al from 0.45 to 0.88 led to the sharply increased hardness to 538 HV followed by a slight decrease of hardness with the Al content increasing from 0.88 to 2.00. In addition, compared with $\text{CuCoNiCrAl}_x\text{Fe}$ HEA, the two-phase region of $\text{CoNiCrAl}_x\text{Fe}$ became narrow, suggesting that the Cu element can stabilize the FCC phase [196]. Therefore, the cocktail effect can be used

to modify the microstructure and mechanical properties of HEAs by adjusting the content of elements or microalloying.

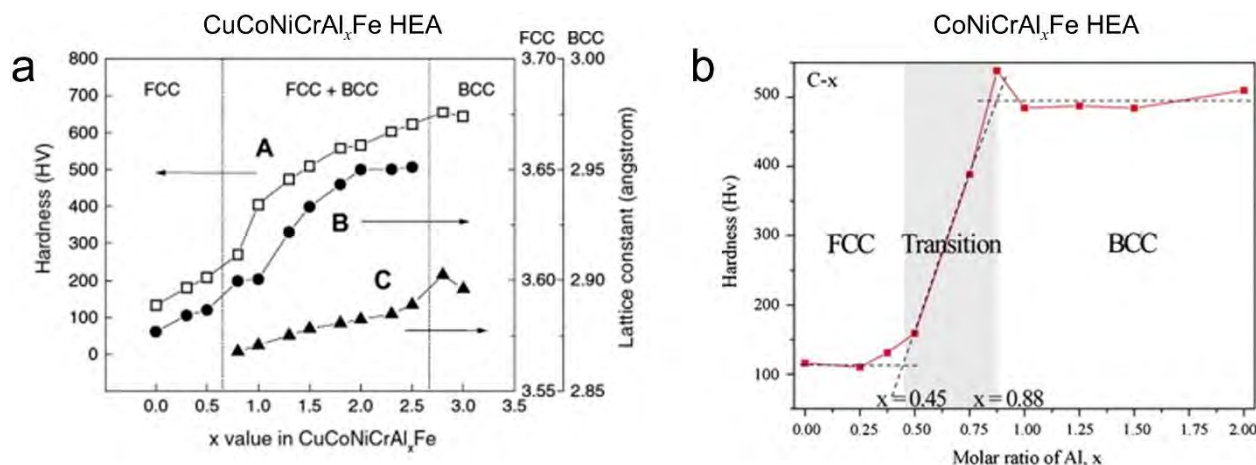


Fig. 2.32 (a) Hardness and lattice constants of CuCoNiCrAl_xFe HEA with different Al ratios [195], (b) Hardness of CoNiCrAl_xFe HEA with different Al ratios [196]. Note the A, B, and C in (a) indicate hardness and lattice constants of FCC phase and BCC phase.

2.4.3 Manufacturing processes

The preparation method of HEAs is similar to that of conventional alloys. Fig. 2.33 shows the typical manufacturing processes for HEAs from powder (0D) to parts (3D) over the past two decades. The prevailing manufacturing routes of bulk HEAs are mainly through conventional vacuum arc melting or induction melting, followed by casting methods. The principal alloying elements are generally required to be remelted several times to receive a homogeneous microstructure, making the fabrication process a laborious task.

In addition to the traditional casting methods, the emerging additive manufacturing technology is also widely utilized for the production of HEAs in recent years. Additive manufacturing technology has the characteristics of short production cycles, high material utilization, near-net shaping of complex structures, and material–structure–function integration, which provides a new pathway for the

manufacturing of high-performance HEAs. At present, laser-based and electron beam-based technologies, such as selective laser melting, direct laser deposition, and selective electron beam melting, have been utilized to fabricate HEAs [197].

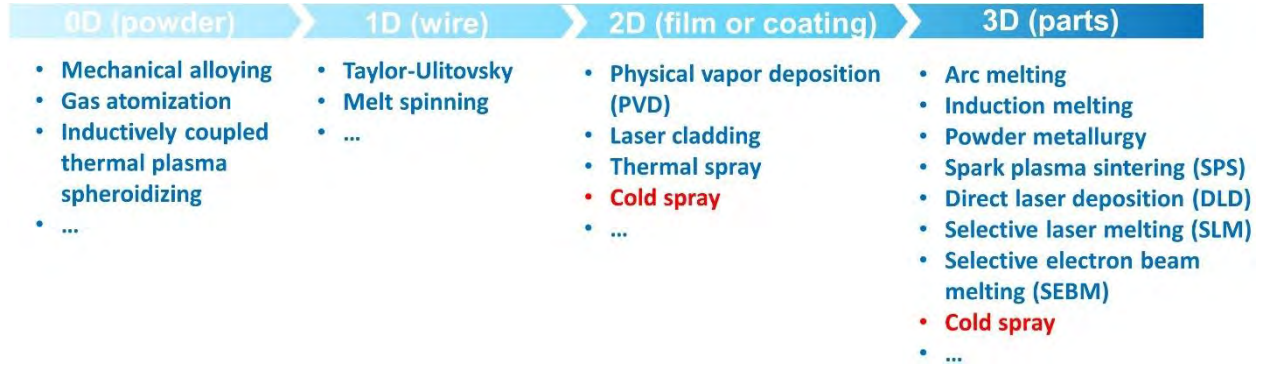


Fig. 2.33 Summarization of current manufacturing processes for multi-scale high-entropy alloys.

2.5 Research Progress on Cold-sprayed High-entropy Alloys

At present, the research on the preparation of high-entropy alloy (HEA) coatings or deposits through cold spraying is still limited. In 2019, the research group at Trinity College Dublin reported the basic processing parameters, microstructure evolution, and mechanical properties of the cold-sprayed FeCoNiCrMn HEA coating, which confirmed the feasibility of preparing HEA deposits by cold spraying for the first time [16]. **Table. 2.2** summarized the published works about cold-sprayed HEA deposits. It can be found that the existing research mainly focuses on FeCoNiCr-based HEA systems.

Table. 2.2 Summarization of published works about cold-sprayed HEA deposits

Feedstock	Substrate	Gas parameters			Heat treatment	Thickness (mm)	Porosity (%)	Hardness	Ref.
		Type	Pressure (MPa)	Temp. (°C)					
FeCoNiCrMn ($d_{ave}=32 \mu\text{m}$)	C40 carbon steel	N ₂	7.0	1100	-	~0.5	-	1.6-3.6 GPa	[198]

AlCoCrFeMo (3~30 μm)	Low carbon steel	compressed air	6.3	450	-	0.17 ± 0.025	< 1	362 ± 48 HV _{0.3}	[199]
AlCoCrFeMoW (8-48 μm)	Low carbon steel	compressed air	6.3	450	-	0.615	1.2 ± 0.2	415 ± 49 HV _{0.3}	[200]
AlCoCrFeMoV (10-55 μm)	Low carbon steel	compressed air	6.3	450	-	0.636	< 1	561 ± 63 HV _{0.3}	[200]
Al _{0.5} CoCrFeNi ₂ Ti _{0.5}	Hard carbon steel Soft AA6061	N ₂	5.0	1000	-	-	-	426.58 HV _{0.3} 420.70 HV _{0.3}	[201]
FeCoCrNiMn (15~53 μm)	6082 Al alloy	He	3.0	300	-	> 1.5	-	258.4 ± 22.6 HV _{0.3}	[202]
CrMnFeCoNi (d _{ave} =26 μm)	Nickel SS304 In625	He	3.2	400	-	-	-	-	[155]
CoCrFeNiMn (20~32 μm)	-	N ₂	3.0	600	As-sprayed 650 °C/ 1 h 1150 °C/ 1 h	-	0.6 ± 0.2 0.7 ± 0.2 0.8 ± 0.2	5.64 ± 0.38 GPa 4.95 ± 0.28 GPa 3.61 ± 0.21 GPa	[203]
FeCoCrNiMn (d _{ave} =32 μm)	carbon steel	N ₂	7.0	1100	-	> 0.5	< 1	2.0-3.8 GPa	[204]
AlNiCoFeCrTi (1~125 μm d ₅₀ =21 μm)	low-carbon steel	Air	0.7	500	-	0.405	0.5 ± 0.18	10.0 ± 0.3 GPa	[205]
CrMnCoFeNi (d ₅₀ =25.5 μm d ₉₀ =44.6 μm)	-	N ₂	4.9	950	-	< 0.25	-	361 ± 50 HV _{0.1}	[206]
CoCrFeNi (5~45 μm d _{ave} =25 μm)	AZ91	N ₂	3.0	200	-	~ 0.2	0.59	~ 315 HV _{0.05}	[207]
CoCrFeMnNi (d ₅₀ =27 μm d ₉₀ =55 μm)	Al	N ₂	-	900	-	3	-	351 ± 32 HV _{0.3}	[208]
CoCrFeNiMn (10~30 μm)	35CrMo	N ₂	7.0	1100	As-sprayed 500°C /2h 700°C /2h 900°C /2h	0.3	1.1	317.1 HV _{0.1} 487.6 HV _{0.1} ~300 HV _{0.1} ~170 HV _{0.1}	[209]
FeCoNiCrMn (15~53 μm)	6082 Al alloy	He	3.0	300	-	1.5	0.47± 0.17	332.91± 34.74 HV _{0.1}	[16]

AlCoCrFeNi ($d_{50}=7\ \mu\text{m}$)	Ni-based superalloy	compressed air	1.0	400	1100 °C / 25 h	-	-	-	[210]
CrFeNiMn (20~45 μm)	Fe52 steel	N ₂	5.0-6.0	-	-	0.23-0.49	3-10	> 300 HV _{0.3}	[211]
CoCrFeMnNi (10~60 μm)	Steel	He	3.0	300	As sprayed 550 °C/ 2 h 850 °C/ 2 h	1 - -	0.32 - -	423.8 HV _{0.5} 399.6 HV _{0.5} 219.9 HV _{0.5}	[212]
FeCoCrNiMn (15~53 μm)	6082 Al alloy	He	3.0	300	As sprayed 600 °C/ 1 h	> 3	~ 0.5 -	- -	[213]
AlNiCoFeCrTi (1~125 μm)	Low carbon steel	air	0.9	450	-	~ 0.45	< 1	1030 ± 30 HV _{0.1}	[214]
FeCoCrNiMn ($d_{10}=19.56\ \mu\text{m}$ $d_{90}=52\ \mu\text{m}$)	Carbon steel	N ₂	7.0	1100	-	~ 0.593	< 1	382 ± 6.0 HV _{0.1}	[215]
CoCrFe _{0.75} NiMo _{0.3} Nb _{0.125} ($d_{ave}=38 \pm 7\ \mu\text{m}$)	Al 6061	N ₂	5.0	-	-	~ 4	< 0.5	5.88 ± 0.17 6.40 ± 0.20 GPa	[216]
FeCoNiCrMn ($d_{ave}=42.9\ \mu\text{m}$)	2024 Al alloy	N ₂ He	2.5	700 700	-	1.50 1.89	7.86 0.45	-	[217]
CoCrFeNiMn	SS304	He	3.3	400	-	1.67	2.4 ± 0.3	5.14 GPa	[218]
CoCrNi (15-53 μm)	6082 Al alloy	N ₂	5.0	1000	As-sprayed 1200 °C/ 0.5 h 1250 °C/ 0.5 h 1300 °C/ 0.5 h 1350 °C/ 0.5 h	> 2	-	375.8 HV _{0.2} 239.3 HV _{0.2} 211.1 HV _{0.2} 172.7 HV _{0.2} 169.4 HV _{0.2}	[219]
AlCrCoFe _x NiCu $x = (0, 0.5, 1, 1.5, 2)$	45 [#] steel	Air	0.7-0.8	490- 510	-	-	-	-	[220]

2.5.1 Feedstock Powder

The properties of feedstock powder for cold spray deposition (e.g., particle size, flowability, surface status, and mechanical properties) not only have an impact on the cold spray process but also affect the surface quality, microstructure, and mechanical properties of cold-sprayed deposits. At present, the HEA feedstock powders used in the cold spray process are mainly prepared through gas atomization [16,211,213,215], mechanical alloying [205,210,214], and mechanical blending

[221]. Gas atomization is a widely used powder production technique where the liquid metal is disintegrated into small droplets by high-pressure gas flow (e.g., air, nitrogen, or helium) and then solidified into powder. The cooling rate in the gas atomization process can reach as high as 10^5 K/s, which helps to receive powder with fine structure and homogeneous composition. The gas-atomized powder is usually spherical or near-spherical with high purity and fine particle size, as evidenced by the FeCoNiCrMn HEA in Fig. 2.34a. In most cases, the feedstock used for cold spraying is gas-atomized powder.

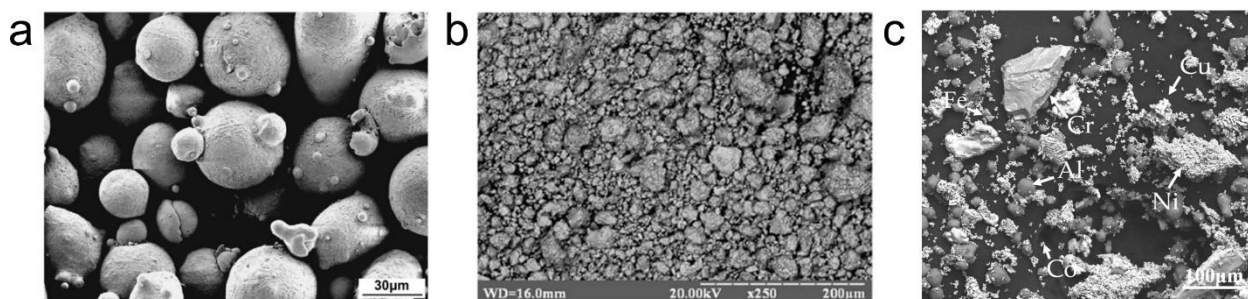


Fig. 2.34 Different methods for the preparation of the feedstock powder used for cold spray deposition: (a) Gas-atomized FeCoNiCrMn HEA powder [16], (b) Mechanical alloyed AlNiCoFeCrTi HEA powder [214], (c) Mechanical mixed AlCrCoFe_xNiCu [220].

Mechanical alloying, also known as mechanical ball milling, is a solid-state powder manufacturing technique. Different types of pure metal powder are put in a high-energy ball mill and experience repeated cold welding, fracturing, and re-welding to achieve a homogeneous material [222]. Fig. 2.34b shows the AlNiCoFeCrTi HEA powder prepared by mechanical alloying. The powder has irregular shapes with a wide range of particle size distribution.

Mechanical blending is another method to prepare HEA powder for cold spray, which involves a simple mixing procedure of pure metal powder of each principal element in the target alloy or a combination of pure metal and alloys. For example, Sova et al. mixed four kinds of powders including 316L, Tribaloy T700, copper, and aluminum, and used the mixture as feedstock powder for cold spray to manufacture

Al-Cu-Cr-Fe-Ni-Mo-Si HEA deposit [221]. The major problem of using such mixed powder is that the received cold-sprayed deposit is composed of a random combination of different powders rather than the HEA particles. Therefore, in-situ or post-processing technique, such as laser melting [221] and induction remelting [220], has to be combined with the cold spray process to manufacture HEA deposits with more homogeneous microstructure.

2.5.2 *Processing Parameters*

The typical processing parameters in cold spray mainly include gas parameters (i.e., gas type, gas pressure, and gas temperature), powder feeding parameters (e.g., powder feeding rate), and nozzle parameters (e.g., nozzle transverse speed, stand-off distance, spraying angle and spraying trajectory) [11]. Gas parameters play a significant role in particle acceleration and particle plastic deformation, which will influence the microstructure and properties of cold-sprayed deposits to a large extent. It can be seen from **Table. 2.2** that cold-sprayed HEA deposit with a thickness of more than 1 mm can be manufactured using helium as propulsion gas at high pressure (3.0 MPa) and low temperature (300 °C). The porosity of the deposit is measured below 0.5 %, which can be attributed to the sufficient plastic deformation of particles triggered by the excellent acceleration effect of helium [16]. Compared to helium, nitrogen is more widely used in cold spray due to its economical and renewable. However, the acceleration effect of nitrogen is inferior to helium. For example, the cold-sprayed CrFeNiMn HEA deposit, which was fabricated using nitrogen as the propelling gas under the temperature of 1000 °C and the pressure of 6.0 MPa, exhibited a porosity of $3.3 \pm 0.8\%$ [211]. It can be inferred that the critical impact velocity of HEA particles is higher than that of common metal particles, which increases the difficulty of particle deposition and leads to low deposition efficiency. The particles may experience partial oxidation under such high gas

temperatures, which will hinder the particle bonding and result in the deterioration of deposit properties. In addition, compressed air at low temperatures and low pressure can also be applied for particle deposition, particularly for mechanical-alloyed powder and mechanical-mixed powder. However, the as-sprayed deposits have to be laser-remelted or induction-heated during or after cold spray deposition.

Fig. 2.35 shows the microstructure of the cold-sprayed FeCoNiCrMn deposits under various combinations of processing parameters. The accelerating ability of the nitrogen and helium can be clearly distinguishable from the deposits that were fabricated under the same gas pressure and temperature. Only a discontinuous deposit with limited thickness was formed when using nitrogen as the propelling gas, in comparison to the thick deposit (> 1 mm) fabricated using helium (see **Fig. 2.35a** and **b**). Higher gas temperature led to the increased deposit density, as shown in **Fig. 2.35c**. This is because the increased gas temperatures increased the particle impact temperatures, which promoted particle softening [38,39]. The softened particles can experience more severe plastic deformation and compactly bond with the substrate or the previously deposited layer, resulting in an increase in the deposit density (see **Fig. 2.35d**). The spraying distance (i.e., standoff distance) can also influence the particle deposition behavior by influencing the particle impact velocities. The increased standoff distance generally led to a decrease in deposition efficiency and increased porosity, as shown in **Fig. 2.35c** and **d**. Compared with traditional metals and alloys, high gas processing parameters are required for the fabrication of HEAs especially when using gas-atomized HEA particles as cold spray feedstock.

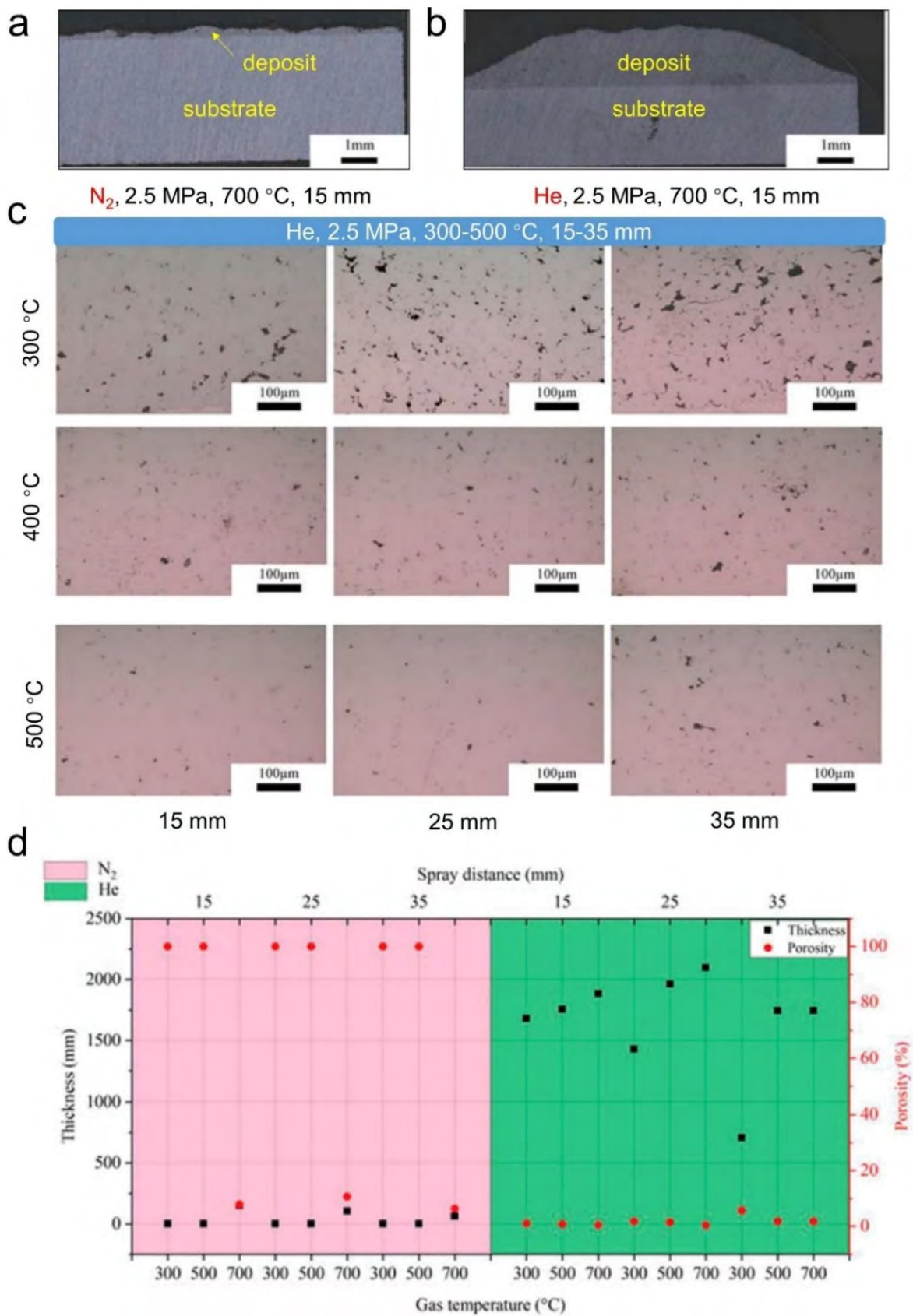
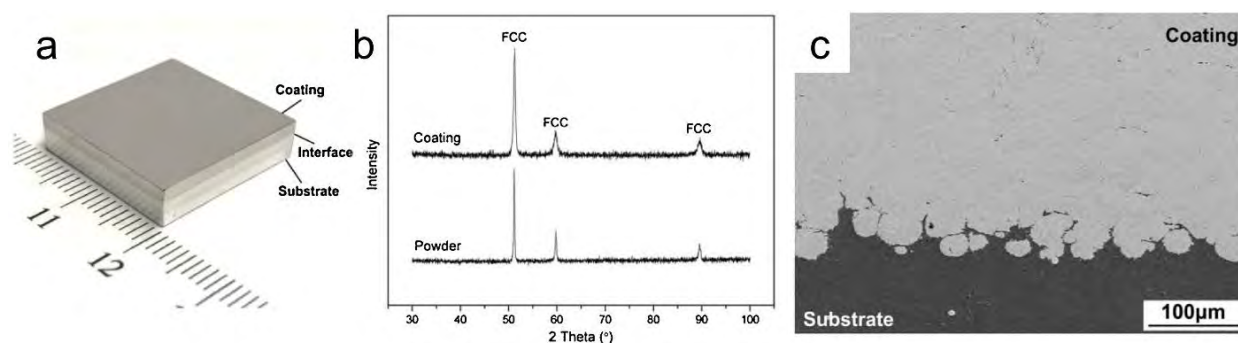


Fig. 2.35 Microstructure of the cold-sprayed FeCoNiCrMn HEA deposits under various

processing parameters. A comparison of the deposits fabricated using (a) nitrogen and (b) helium, (c) Effect of gas temperature and spraying distance on the microstructure of the deposits, (d) Deposit thickness and porosity data under different gas temperatures and spraying distances.

2.5.3 Microstructure Evolution and Deposit Properties

Fig. 2.36 shows the representative microstructure of the cold-sprayed FeCoNiCrMn HEA coating, which was fabricated with gas-atomized FeCoNiCrMn HEA powder. The deposit presents a dense structure without visible pores and cracks. The coating retains a single FCC structure as the original feedstock powder, as shown in **Fig. 2.36b**, which shows the superiority of cold spray compared with laser-based and electron beam-based additive manufacturing techniques. The diffraction peak of the coating broadened due to grain refinement and higher micro-stress induced by the severe plastic deformation of particles during the deposition process. Compared with the near equiaxed grains in the feedstock powder (see **Fig. 2.36d**), the significant grain refinement near interfacial regions can be seen from the EBSD characterization results (see **Fig. 2.36e**). The ultra-fine grains were formed at the interparticle interfaces due to the dynamic recrystallization, while the grains in the particle interior had the original size. This is the typical bi-modal grain structure in the deformed particles in cold spray, and such heterogeneous microstructure can be attributed to the existence of temperature and strain gradients during the high-velocity impact process [218].



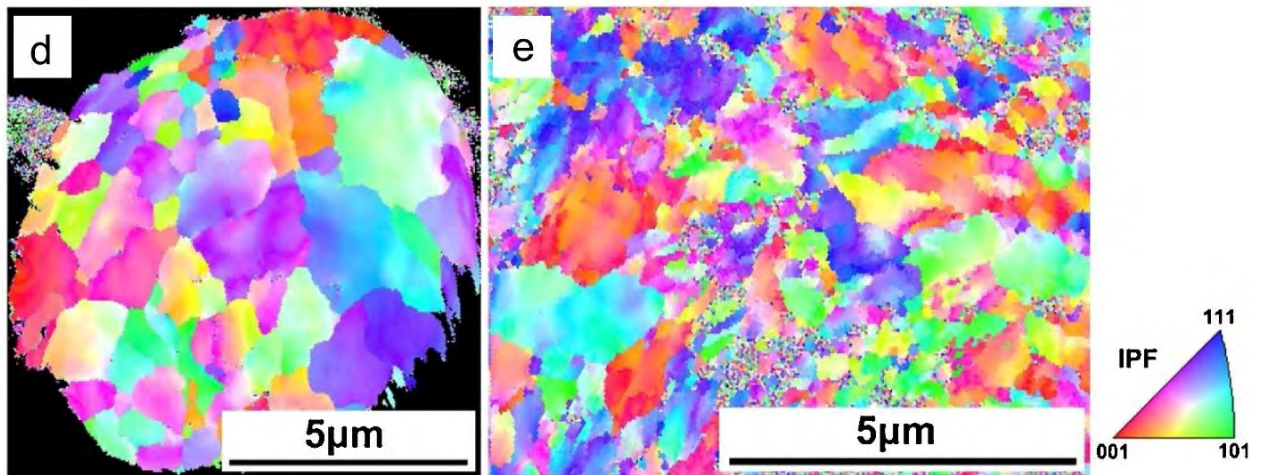


Fig. 2.36 Representative microstructure of the cold-sprayed FeCoNiCrMn HEA coating [16].

► *Microhardness*

The current research on the properties of cold-sprayed HEA deposits is relatively limited and mainly focuses on microhardness, wear and corrosion resistance, and oxidation behavior. In cold spray, the particles impact onto a substrate at supersonic velocities and experience severe plastic deformation, which increases the dislocation density in deposits. Furthermore, the tamping effect from the impact of subsequent particles promotes further plastic deformation of deposited particles. The resultant work-hardening effect results in the significantly increased microhardness of the cold-sprayed HEA deposits. As summarized in Table. 2.2, the hardness of the cold-sprayed CrFeNiMn HEA deposit is about 25% higher than that of the feedstock powder even using nitrogen as the propelling gas [211]. The nano-hardness of the cold-sprayed FeCoNiCrMn HEA deposit reached 10.9 GPa, which is three times higher than that of the as-cast counterpart [212]. The increase in nano-hardness can be attributed to the synergistic effect of working hardening and grain refinement strengthening [218].

► *Wear-resistance properties*

According to Archard's law, the volume of the worn material is inversely proportional to the material's hardness [223]. The enhanced hardness of the cold-sprayed HEA deposits generally exhibited good wear resistance compared to their counterparts that were manufactured by conventional methods [16], which made cold-sprayed HEA deposits excellent wear-resistant material candidates. **Table. 2.3** summarizes the tribological properties of the as-sprayed HEAs. The research on the wear properties of the as-sprayed HEAs is rather limited, and most of the tests were conducted at low loads and room temperature. The tribological performance under extreme conditions (e.g., high loads, high temperatures) is still lacking, which certainly needs more investigation.

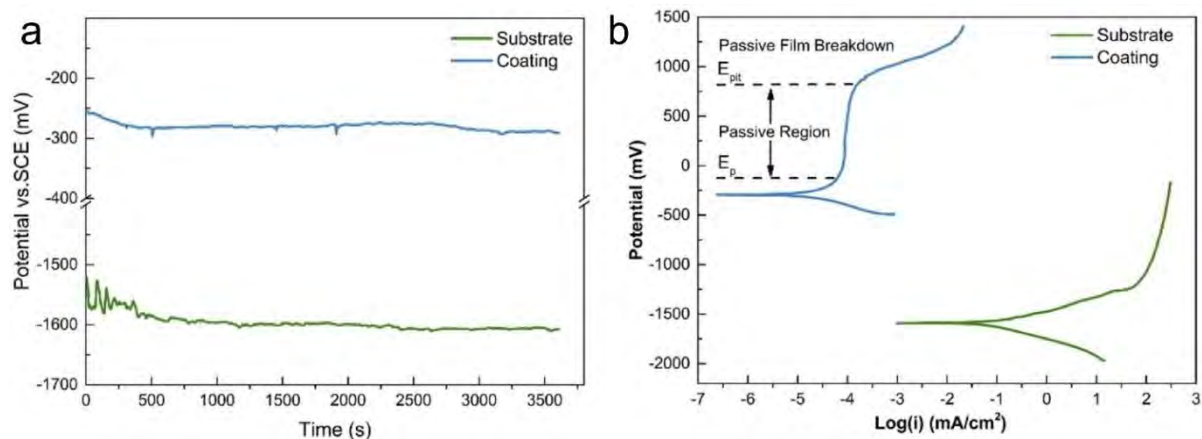
Table. 2.3 Summarization of the tribological properties of the as-sprayed high-entropy alloys

Feedstock	Gas parameters			Counterpart	Wear test parameters			COF	Wear rate $\times 10^{-5}$ mm ³ /Nm	Ref.
	Type	Pressure (MPa)	Temp. (°C)		Load (N)	Distance (m)	Speed			
AlCoCrFeMo	compressed air	6.3	450	Al ₂ O ₃	5	100	1 HZ	~0.5	140	[199]
					10				~0.4	
AlCoCrFeMo								72		
AlCoCrFeMoV	compressed air	6.3	450	Silica sand	130	718	-	-	59	[200]
AlCoCrFeMoW									66	
FeCoCrNiMn	He	3.0	300	WC-Co	5	200	-	~1.04	47.3	[202]
CoCrFeNi	N ₂	3.0	200	Al ₂ O ₃	30	10.8	3 mm/s	0.5	21.6	[207]
FeCoCrNiMn	N ₂	7.0	1100	WC-Co	-	999.5	0.13 m/s	0.73	28	[215]
FeCoNiCrMn	He	3.0	300	WC-Co	5	200	0.1 m/s	-	47.6	[16]

► *Corrosion-resistance properties*

HEAs generally exhibit excellent corrosion-resistance properties, particularly for HEAs containing a high content of passivation elements, such as Cr, Ni, Al, Mo, and Ti [224]. The corrosion property of the cold-sprayed FeCoNiCrMn HEA deposit

in a 3.5 wt.% NaCl water solution was evaluated, and the results showed that the corrosion potential (E_{corr}) and corrosion current (I_{corr}) were -65mV and 1.20 μA , which were both higher than that of the FeCoNiCrMn HEA deposit fabricated through high-velocity oxygen-fuel [215]. The high I_{corr} of the deposit was considered to be associated with the unavoidable interparticle boundaries [215]. Fig. 2.37 shows the corrosion behavior of the AZ91 Mg alloy with and without cold-sprayed CoCrFeNi HEA coating. The cold-sprayed CoCrFeNi HEA coating exhibited higher open circuit potential (OCP) than the substrate, suggesting better corrosion resistance (see Fig. 2.37a). High corrosion potential (E_{corr}) and low corrosion current (I_{corr}) indicate stable and uniform corrosion resistance properties. The E_{corr} of the cold-sprayed CoCrFeNi HEA coating was significantly improved, and the I_{corr} was decreased by 4-5 orders of magnitude compared to the substrate [215]. Fig. 2.37c shows the surface morphology of the bare substrate and CoCrFeNi coating after long-term immersion tests. Compared with the severely corroded substrate surface shortly after the test, the CoCrFeNi HEA coating exhibited remarkably improved surface morphology. There was no peeling of coating from the substrate, and the penetrating corrosion holes were also not found [215]. Moreover, the Mg alloy coated with the cold-sprayed CoCrFeNi HEA deposit exhibited a weight loss percentage below 1%, indicating excellent corrosion resistance properties. The current research on the corrosion-resistance properties of the cold-sprayed HEA deposits is also lacking, and the alloy system is monotonous.



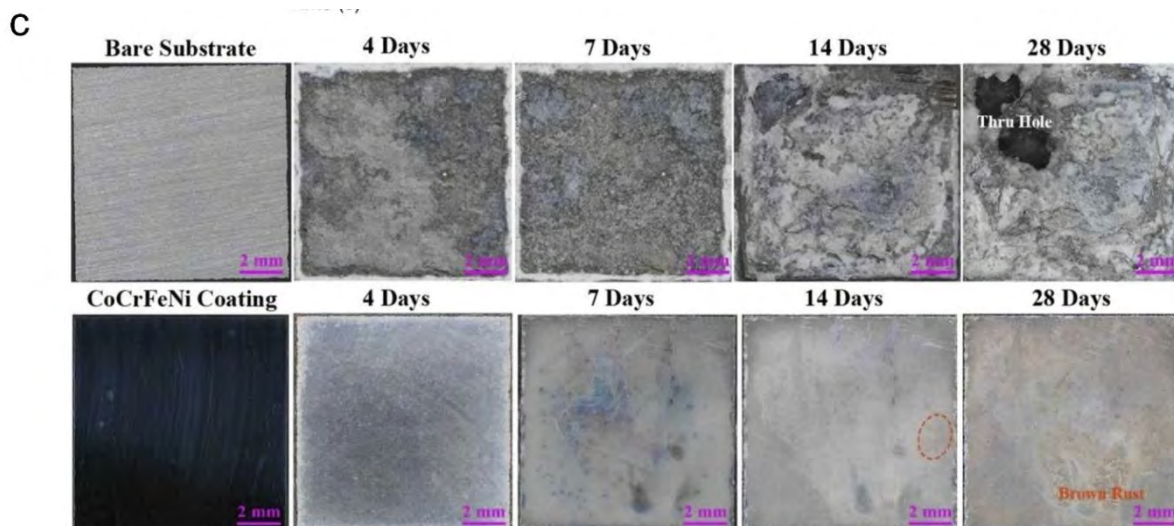


Fig. 2.37 Electrochemical test results of the substrate with and without cold-sprayed CoCrFeNi HEA coating in 3.5 wt% NaCl solution at room temperature. (a) Open circuit potential, (b) Potentiodynamic polarization. (c) Surface morphology of the substrate with and without cold-sprayed CoCrFeNi HEA coating after immersion tests for 28 days [207].

► *High-temperature oxidation behavior*

The high-temperature oxidation behaviors of cold-sprayed HEA deposits were also studied. For example, cold-sprayed FeCoNiCrMn HEA deposit was exposed to high temperatures ranging from 700 °C to 900 °C for 100 h [225]. With the increase in temperature, the oxidation gradually diffused from the outer layer to the inner layer of the deposit. The oxide scales were composed of a Mn_2O_3 or Mn_3O_4 for the outer layer, a Mn-Cr spinel intermediate layer, and a Cr_2O_3 inner layer [225]. The microstructural defects (e.g., pores and interparticle interface) in cold-sprayed deposits promoted the diffusion of metal cations and oxygen anions, resulting in the formation of oxide scales on the outer layer of the deposit. The increased grain boundaries triggered by significant grain refinement, particularly at interfacial regions, also provide pathways for element diffusion and promote the formation of Mn oxide and Cr oxide [225], as shown in Fig. 2.38. Oxide scales (Al_2O_3) were also found on the surface of the cold-sprayed AlCoCrFeNi HEA deposit and deposit

interior with a constant temperature oxidation treatment at 1100 °C for 25 hours [210]. The potential oxidation mechanism was given through single splat deposition. The oxidation started from grain boundaries and further diffused along interparticle interfaces, leading to the formation of Al_2O_3 on both the coating surface and deposit interior. This prevented the further oxidation of the substrate and therefore effectively protected the substrate. By optimization of cold spray processing parameters and/or combination with other strengthening techniques (e.g., the doping of specific elements), the cold-sprayed HEAs are expected to be the next generation of high-temperature resistant and oxidation-resistant coatings.

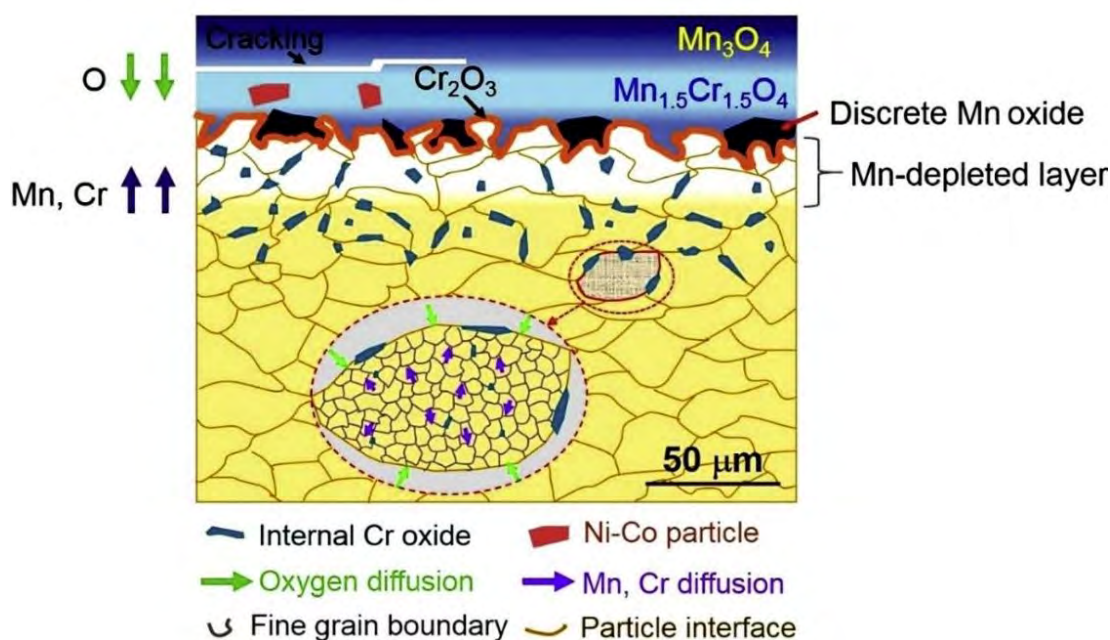


Fig. 2.38 Oxidation mechanism of the cold-sprayed FeCoCrNiMn at 900 °C [225].

2.5.4 Particle Bonding Mechanism

The adiabatic shear instability (ASI) mechanism is the most widely accepted particle bonding mechanism in cold spray. The particle deposition is achieved through localized metallurgical bonding and mechanical interlocking triggered by severe plastic deformation at interfacial regions. There is a critical velocity for

particle deposition and effective bonding can be achieved only when a particle impact velocity exceeds the corresponding critical velocity [57,226,227]. As shown in Fig. 2.39, the bonding of CrMnCoFeNi HEA particles only occurred at the fringe of the interparticle interfaces, while visible gaps existed at most of the interfacial regions, as pointed by the green and red dotted lines respectively [155]. This can be attributed to the high yield strength of CrMnCoFeNi even at elevated temperatures. In addition, the strain-hardening rate of HEA is high [155]. The thermal softening effect induced by adiabatic temperature rise is difficult to exceed the work-hardening effect resulted from increased strain, which could prevent the occurrence of shear instability and the localized metallurgical bonding of particles. Therefore, there is reasonable speculation that HEA particles have higher critical velocity than conventional metallic particles, which is a major challenge to fabricating high-performance HEA coatings or deposits by cold spray.

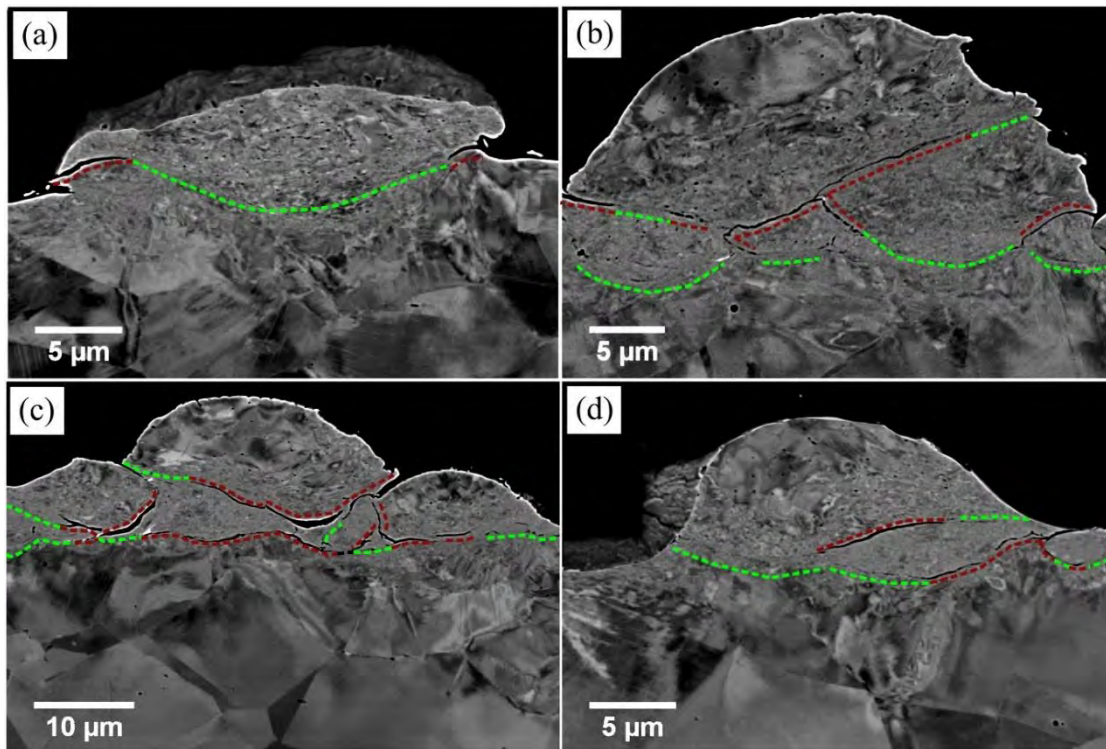


Fig. 2.39 Cross-sectional morphologies of multi-particle impacts of CrMnCoFeNi HEA powder onto SS304 substrate (He, 3.2 MPa, 400 °C). Green and red dotted lines show bonded and not bonded areas, respectively [155].

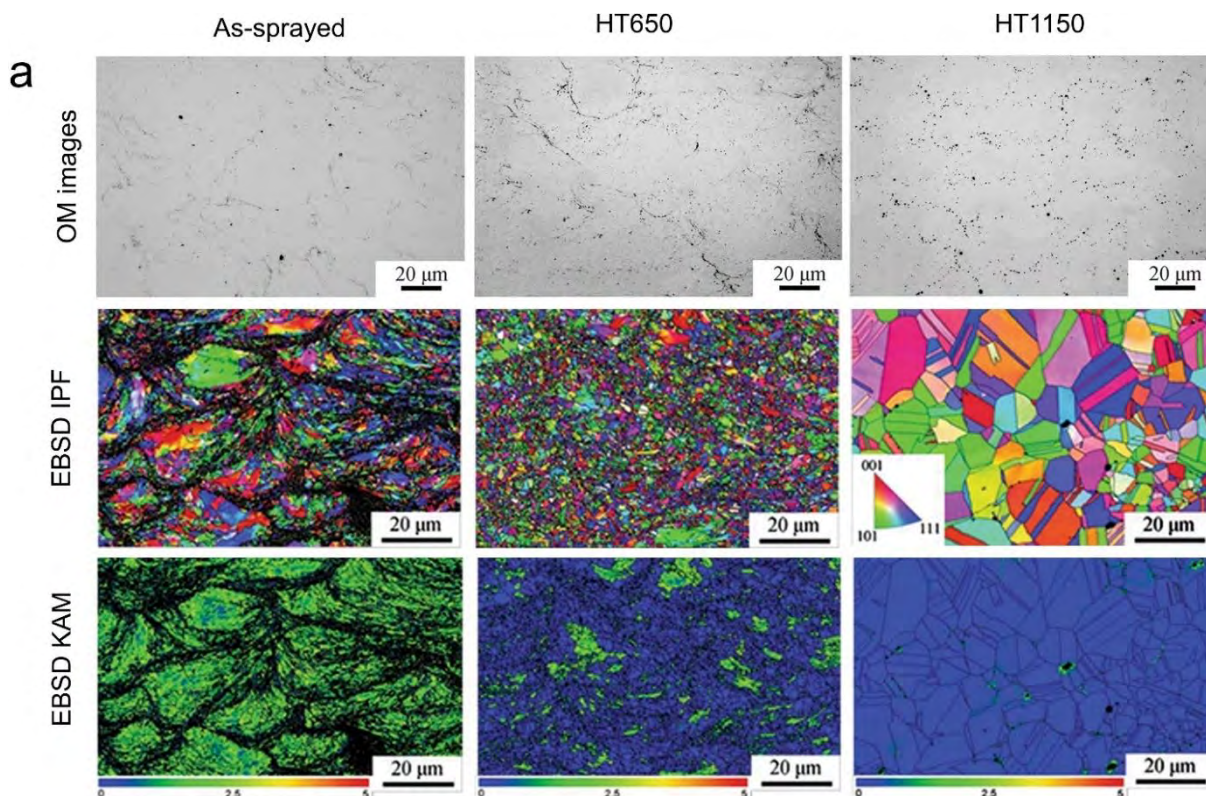
2.5.5 *Strengthening Cold-Sprayed High-entropy Alloy Deposits*

Due to the high deformation resistance of HEAs, insufficient plastic deformation generally occurs even under high processing gas parameters, which results in the formation of micropores and obvious interparticle boundaries. Various strengthening strategies, such as post-heat treatment, laser melting, laser-assisted cold spray, or element doping, have been combined with cold spray to modify the microstructure and enhance the mechanical properties of the cold-sprayed HEA deposits. Therefore, in this section, the research progress of the cold-sprayed HEA deposits strengthened by various strengthening strategies will be given.

► *Post Heat Treatment*

To heal the interparticle interfaces and improve the mechanical properties of as-fabricated HEA deposits, post heat-treatment can be applied to promote atomic diffusion at interparticle boundaries and enhance the metallurgical bonding between adjacent particles. **Fig. 2.40a** shows the microstructure of the cold-sprayed FeCoCrNiMn HEA deposits before and after annealing [203]. The as-sprayed HEA deposit exhibited a rather dense microstructure with partially visible interparticle boundaries. After annealing, the particle boundaries became indistinguishable due to improved atomic diffusion, particularly at a higher annealing temperature (i.e., 1150 °C). The grains in the as-sprayed HEA deposit present a heterogeneous structure. Coarse grains are present at the central region of each particle, and ultra-fine grains are produced at the interfacial regions, which could be attributed to the localized severe plastic deformation and the resultant dynamic recrystallization [16,213]. The high KAM value in the as-sprayed deposit indicated the widely distributed dislocation network within the HEA particles, which can be attributed to the severe plastic deformation of particles. The significant work-hardening effect led to the high hardness of the as-sprayed deposits [203,209,212]. After

recrystallization annealing, the grains experienced significant growth and the highly deformed grains were replaced by the equiaxed or near-equiaxed grains with negligible dislocation inside. The recrystallization annealing process led to a decrease in hardness due to the elimination of the work-hardening effect [203,209,212]. The decreased hardness resulted in deteriorated wear resistance, as evidenced by the increased wear rate with the increase in annealing temperatures (see Fig. 2.40c) [209]. However, the annealing treatment can lead to the recovery of ductility. It is reported that the as-sprayed CoCrNi medium entropy alloy (MEA) exhibited a brittle feature with an ultimate tensile strength (UTS) of ~ 220 MPa and an elongation (EL) of $\sim 2\%$ [219]. After sintering at 1350 °C for 0.5 h, both the UTS and EL were significantly improved (~ 660 MPa and $\sim 43\%$) due to the closure of pores and enhanced metallurgical bonding between adjacent particles. Overall, post-spray heat treatment can be taken as the most simple and economical strategy to modify the microstructure and balance the strength and ductility of the cold-sprayed HEA or MEA deposits.



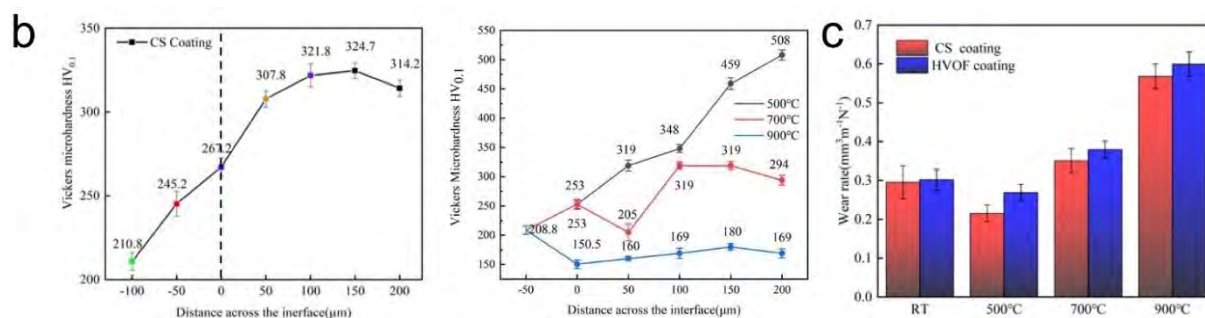


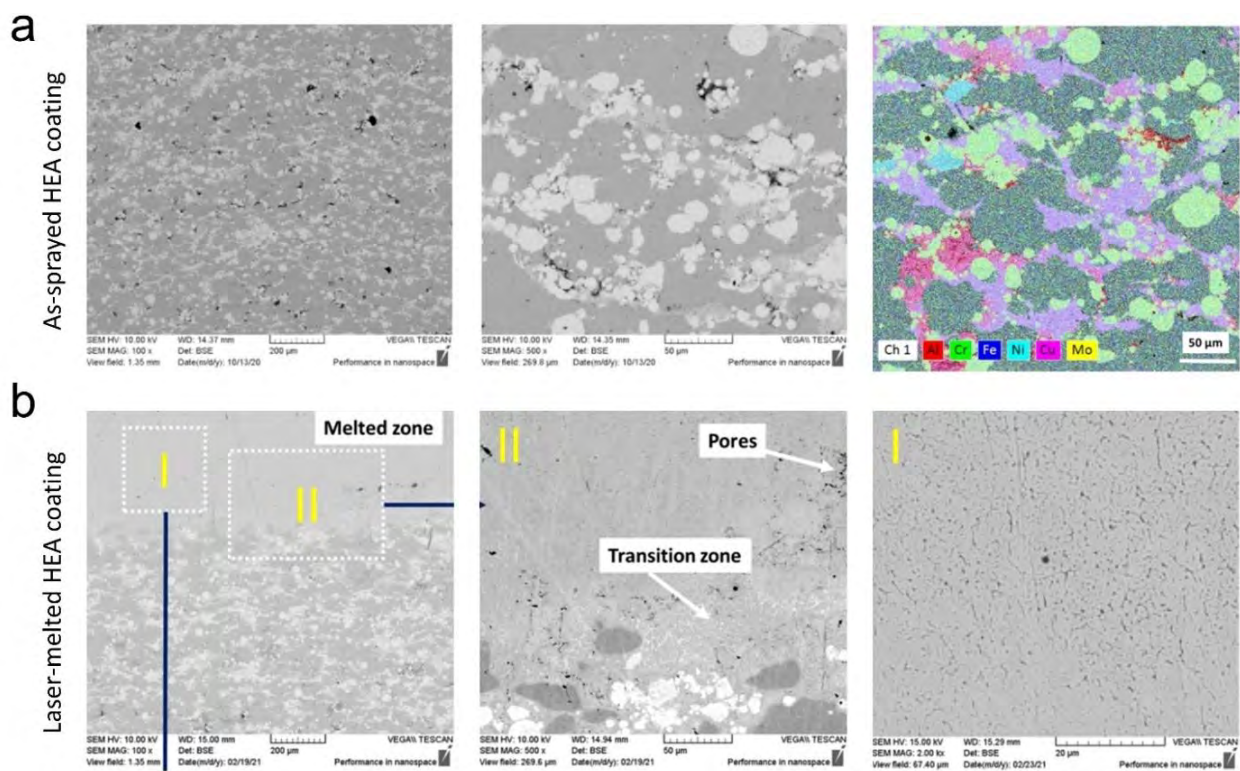
Fig. 2.40 Microstructure and mechanical properties of the cold-sprayed FeCoNiCrMn HEA deposits before and after heat treatment. (a) OM images, EBSD IPF maps, and KAM maps [203], (b) Microhardness, and (c) Wear rate [209].

► *Post Remelting*

Due to the high deformation resistance of HEA particles, it is challenging to make HEA particles experience sufficient plastic deformation by simply optimizing the gas processing parameters. Hence, an alternative solution to this problem is using several low-entropy metal powders (i.e., pure metals or alloys), which have the same elements and similar element contents as the expected HEA deposits, followed by mechanical alloying or mechanical mixing of these powders. These pure metal or alloy powders are expected to undergo more severe plastic deformation and bond with adjacent particles intimately. However, compared with the deposits fabricated using HEA powder as feedstock, the deposits fabricated using mechanical alloyed or mechanical mixing powders generally exhibited an inhomogeneous microstructure. Therefore, a two-stage strategy (i.e., cold spraying and post-laser-melting) was proposed by Sova et al. to prepare HEA deposits [221]. After cold spray deposition, the as-sprayed deposit is then melted by laser to achieve a homogenous element mixing. As a result, HEAs are expected to form in the melting zone during solidification. The two-stage process can not only bypass the use of high-cost HEA powder but also allow the fabrication of HEA deposits under lower processing parameters with better mechanical performance. Apart from using a laser,

the post-remelting process can also be achieved with induction remelting [220].

Fig. 2.41 shows the microstructure of as-sprayed and laser-melted Al-Cr-Fe-Ni-Mo-Si-Ti HEA coatings. The as-sprayed deposit exhibited a nonuniform microstructure due to the simple mixing of different powders (see **Fig. 2.41a**). This can be demonstrated by the nonuniform element distribution too. After laser remelting, the deposit shows a rather homogeneous microstructure (see **Fig. 2.41b**) and stable microhardness values in the melted zone, as compared to the significant fluctuation of microhardness in the non-melted zone (see **Fig. 2.41c**). Moreover, the rapid temperature increase could modify the residual stress level in the non-melted layers [221]. Although the feasibility of cold spray combined with laser melting for manufacturing HEA deposits has been demonstrated, this approach cannot precisely control the element composition in the HEA deposit [221]. In addition, only the top layer(s) of the deposit was remelted by the laser rather than the full deposit to avoid the melting and damage of the substrate, as schematically illustrated in **Fig. 2.41d**.



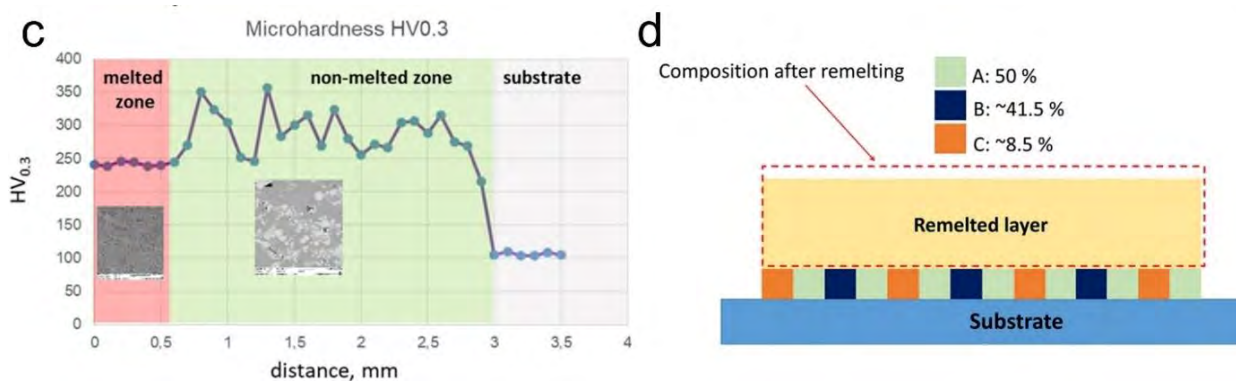


Fig. 2.41 Microstructure of the (a) as-sprayed and (b) laser-melted HEA coatings [221]. The feedstock powders used in cold spray process were composed of ~3.5 wt.% Cu, ~0.5 wt.% Al, ~21 wt.% 316L and ~75 wt.% T700. Due to the different deposition efficiency of each kind of powder, the content of each powder in the target coating was calculated to be 10.5 wt.% Cu, 1.5 wt.% Al, 47 wt.% 316L and 47 wt.% T700. The final composition of laser-melted HEA coating can be expressed as $\text{Al}_{0.1}\text{Cr}_{0.4}\text{FeNi}_{0.8}\text{Mo}_{0.2}\text{Si}_{0.05}\text{Ti}$.

► *Laser-assisted Cold Spray*

To promote the plastic deformation of HEA particles and enhance the interparticle bonding, the laser-assisted cold spray (LACS) was applied for the fabrication of HEA deposits. **Fig. 2.42** shows the microstructure of the CrMnCoFeNi HEA deposit manufactured using nitrogen as the propelling gas. Compared with the clearly observed particle-particle boundaries in the as-sprayed CrMnCoFeNi HEA deposit, the LACS deposit exhibited less visible gaps between adjacent particles (see **Fig. 2.42a** and b). The thermal softening effect induced by laser promotes the more extensive plastic deformation of HEA particles, and the high temperature can also enhance the atomic diffusion between interparticle interfaces and thus increase the interparticle metallurgical bonding [228]. This leads to the improvement of microhardness from 361 HV_{0.1} to 391 HV_{0.1} [206]. Both the CS and LACS deposits retain the original FCC structure as feedstock powder, as evidenced by the XRD pattern in **Fig. 2.42c**. The LACS is expected to be one of the effective strengthening strategies for the deposition of high-performance HEAs. However, the laser

parameters must be carefully selected to avoid potential oxidation and high thermal stress. Moreover, a comparison of the global mechanical properties between conventionally cold-sprayed and LACSed HEA deposits (e.g., tensile properties) is still lacking, which certainly needs more investigation.

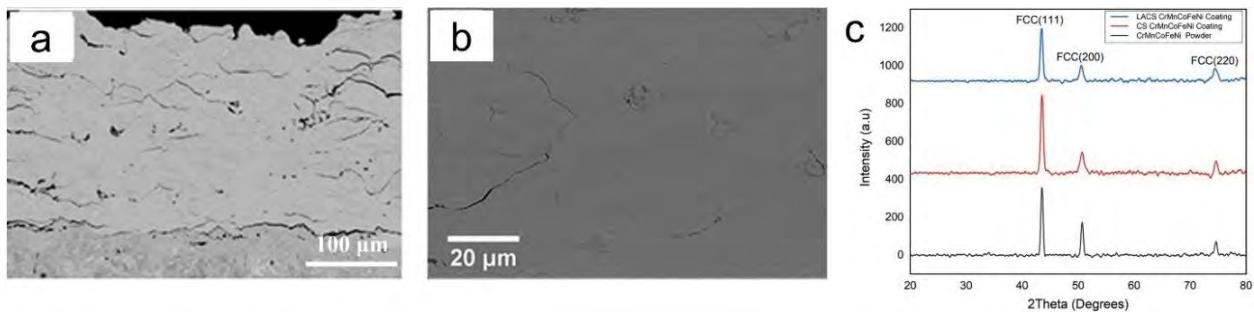


Fig. 2.42 Microstructure and phase structure of the cold-sprayed and laser-assisted-cold sprayed CrMnCoFeNi HEA deposits. (a) Cross-sectional microstructure of the as-sprayed CrMnCoFeNi HEA deposit, (b) Cross-sectional microstructure of the laser-assisted cold-sprayed CrMnCoFeNi HEA deposit, (c) Phase structure of the powder, CS, and LACS CrMnCoFeNi deposits [206].

Note the deposit was manufactured using nitrogen as the propelling gas under the pressure of 4.9 MPa and the temperature of 950 °C.

Apart from the in-process laser-assisted cold spray, the laser was also applied to irradiate cold-sprayed HEA deposits to induce dynamic recrystallization. Laser irradiation played an important role in the recrystallization and refinement of cold-sprayed HEA deposits, leading to the refinement of grains with irregular and varied preferred orientations and isotropic features [229]. The recrystallized HEA exhibited simultaneously improved UTS and EL. Moreover, the laser-irradiated Ni-Fe-Cr-Nb-Ti-Al HEA also exhibited the highest microhardness and lowest friction coefficient, suggesting enhanced wear resistance [229].

► *Particle-reinforcing in HEA Deposits*

Metal matrix composites (MMCs) are composite materials consisting of metals as matrix and dispersed reinforcement (i.e., metal, ceramic, or intermetallic) for

improving the properties of the matrix. The most used reinforcements in cold-sprayed MMCs are ceramic particles (e.g., oxide, carbide, nitride, sulfide, and diamond). The starting powders for the fabrication can be prepared through various routes such as mechanical mixing [230], mechanical ball milling [231], dry spraying [232], or satelliting [233]. The prepared powders are subsequently injected into a cold spray nozzle and projected onto a substrate to form deposits. During the co-deposition, hard reinforcing particles densify the formed layer in a manner similar to in-situ micro-forging [234]. They then remain in the deposit, either intact or fractured, and provide an additional strengthening effect to the deposit by dispersion strengthening mechanism [235].

Fig. 2.43 shows the microstructure and mechanical properties of the Al_2O_3 -reinforced FeCoNiCrMn HEA deposits fabricated by cold spray. The Al_2O_3 particles with smaller sizes were randomly distributed in the FeCoNiCrMn matrix due to the fragmentation induced by high-velocity impact. Compared with the as-sprayed FeCoNiCrMn HEA deposit, the Al_2O_3 reinforced FeCoNiCrMn deposits show increased microhardness and decreased wear rate, indicating the improved wear-resistance property. Moreover, the higher content of Al_2O_3 particles resulted in higher microhardness due to the increased amount of hard phase and enhanced dispersion strengthening mechanism. This led to a nearly 50% reduction in the wear rate as compared with the pure FeCoNiCrMn HEA deposit (see **Fig. 2.43e**) [202].

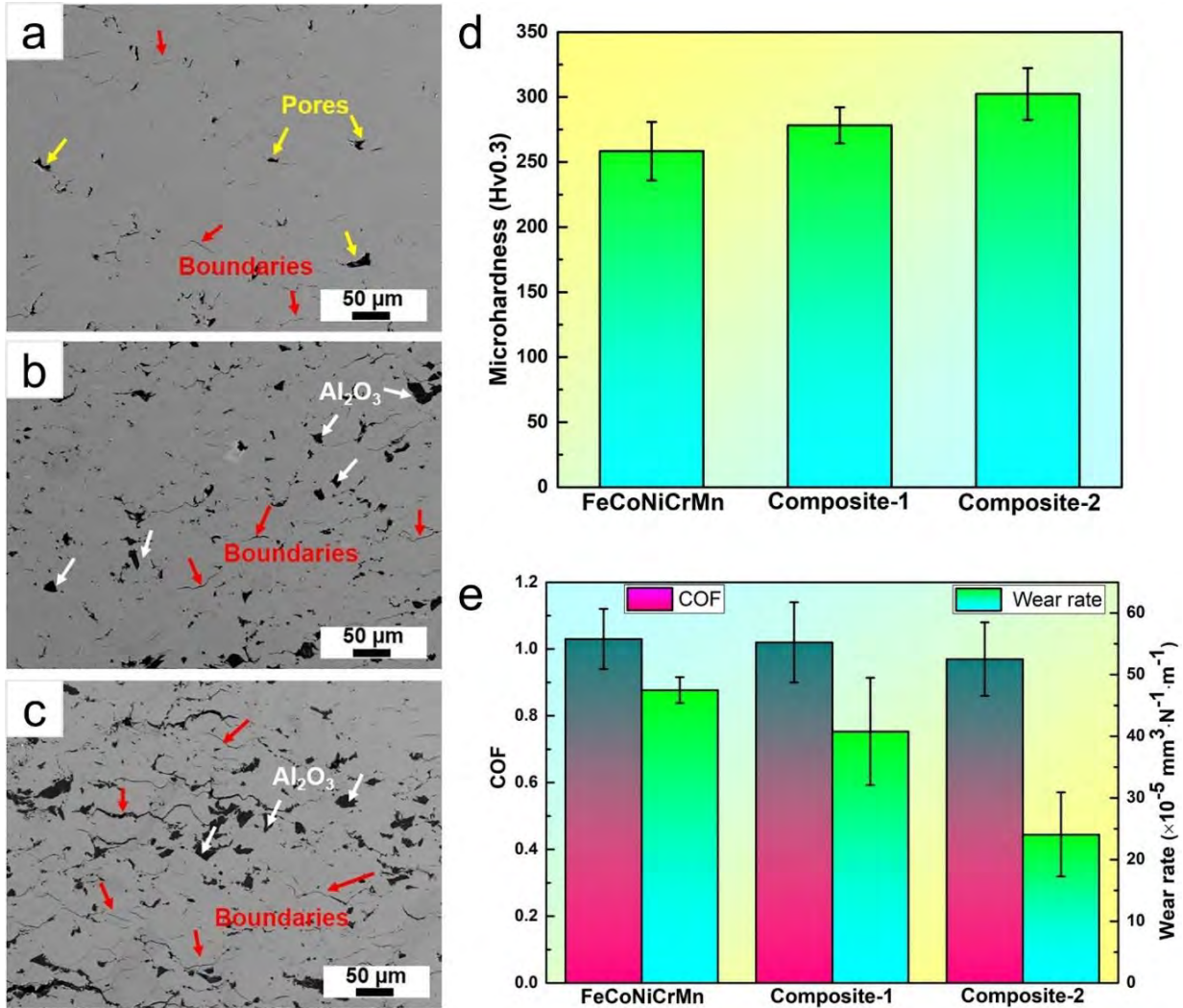


Fig. 2.43 Microstructure and mechanical properties of the cold-sprayed Al₂O₃-reinforced FeCoNiCrMn HEA deposits. Cross-sectional microstructure of the as-sprayed (a) FeCoNiCrMn, (b) Al₂O₃-FeCoNiCrMn (1:8), (c) Al₂O₃-FeCoNiCrMn (1:4), (d) Microhardness and (e) Tribological properties [202].

► *Microalloying*

Similar to the design concept of traditional alloys, which are generally dominated by one or two elements and supplemented with a minority of metallic or non-metallic elements to achieve desired material properties, one or more types of elements can also be added into the original HEA system to modify its microstructure and obtain expected material properties. For example, the increase

in Al content in HEA leads to the phase change from FCC to BCC and results in an increase in hardness and wear resistance [236]. The increase in Ti content in HEA can significantly increase the lattice distortion due to the large size of the atomic radius, leading to an increase in strength and microhardness [236]. Fig. 2.44 shows the microstructure, phase composition, and mechanical properties of the cold-sprayed AlCrCoFe_xNiCu (x=0, 0.5, 1.0, 1.5, 2.0) HEA deposits followed by induction remelting. The AlCrCoNiCu HEA deposit is composed of dendritic (DR) and interdendritic (ID). The increase in Fe content in the deposit can promote the growth of dendrites, as evidenced by the coarsened dendritic structure, as shown in Fig. 2.44a [220]. Compared with the simple phases of pure metals in the XRD pattern, the deposit after induction melting exhibited FCC and BCC phases. The increase in Fe content resulted in the shift of main peaks due to the change of lattice parameters. With regard to the mechanical properties, as shown in Fig. 2.44c and d, the increase in Fe content led to the increase in microhardness and reached a maximum value when x=1, followed by a decreasing trend. Therefore, the AlCrCoFeNiCu exhibited the lowest friction coefficient and wear rate, indicating the best wear resistance. In addition, the V and W elements were doped into AlCoCrFeMo HEA powder through mechanical alloying and fabricated by low pressure cold spray process [200]. The cold-sprayed AlCoCrFeMoV HEA coating exhibited the highest average hardness of around $561 \pm 63\text{HV}_{0.3}$, which was 35% and 52% higher than that of AlCoCrFeMoW and AlCoCrFeMo HEA coatings, respectively. This led to the enhanced wear rate of the cold-sprayed AlCoCrFeMoV HEA coating ($59 \times 10^{-5} \text{ mm}^3/\text{Nm}$), as compared with AlCoCrFeMoW ($66 \times 10^{-5} \text{ mm}^3/\text{Nm}$) and AlCoCrFeMo HEA coatings ($72 \times 10^{-5} \text{ mm}^3/\text{Nm}$) [200].

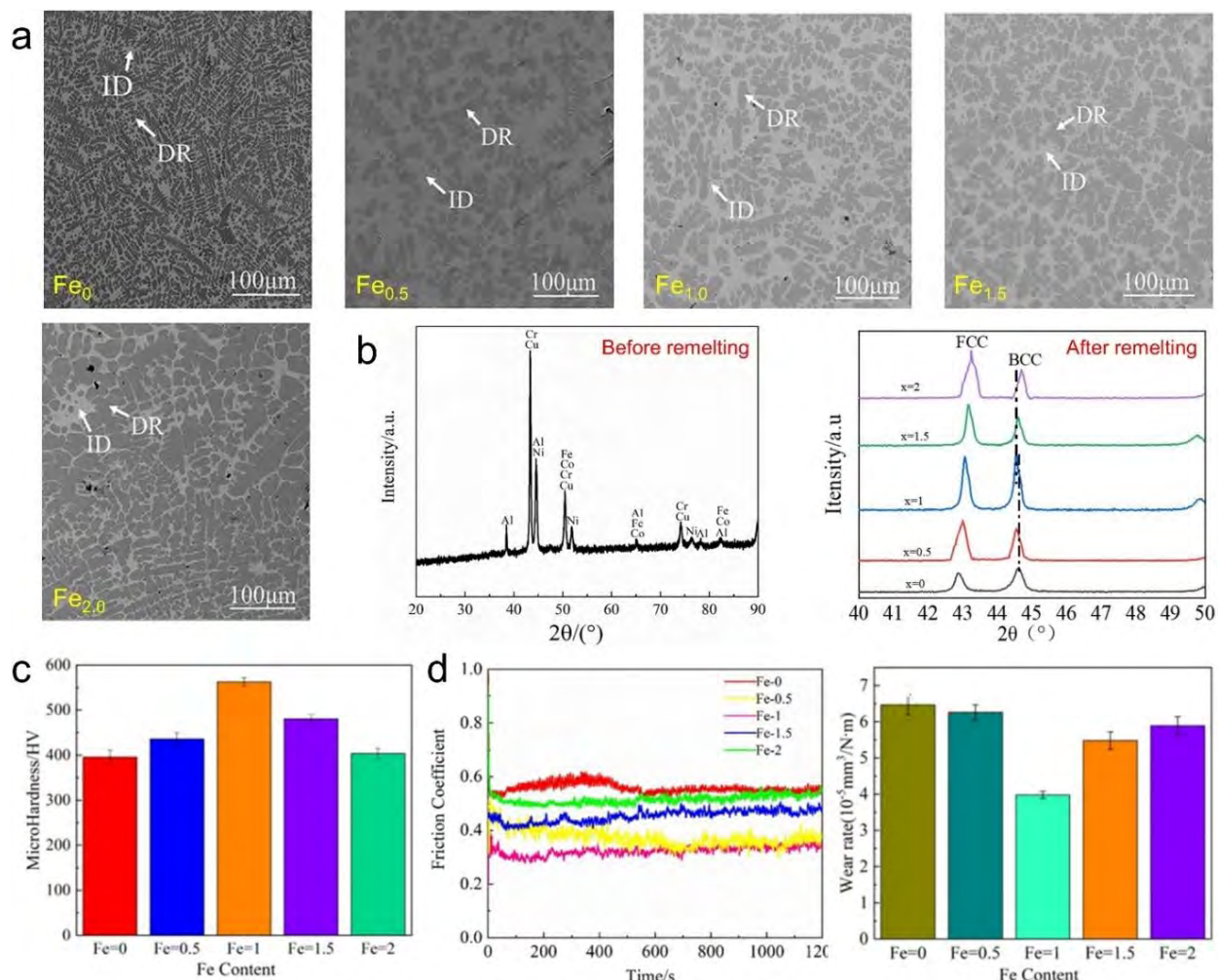


Fig. 2.44 Microstructure, phase composition, and mechanical properties of the cold-sprayed AlCrCoFe_xNiCu (x=0, 0.5, 1.0, 1.5, 2.0) HEA deposits followed by induction remelting. (a) Microstructure evolution, (b) XRD pattern of the deposits before and after induction treatment, (c) Microhardness, and (d) Tribological properties [220]. Note ID refers to interdendritic and DR refers to dendritic.

2.6 Research Objectives

According to the research progress of cold-sprayed metallic glasses (MGs) and high-entropy alloys (HEAs), it can be found that some critical issues need to be solved or explored. For MGs, although the study on cold-sprayed BMGs has been carried out in the past two decades, the interparticle bonding mechanism and

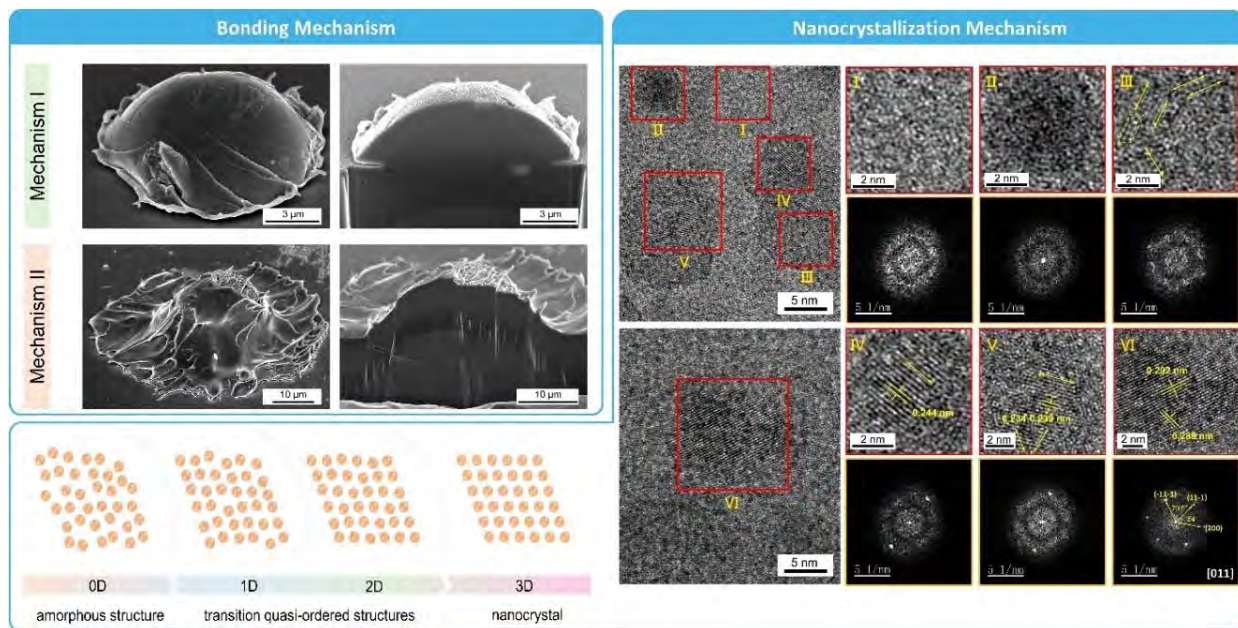
dynamic evolution of crystallization are both unclear and need further clarification. For HEAs, the study on microstructure evolution and mechanical properties of cold-sprayed HEAs is quite limited, and systematic research on cold spraying HEA coatings or deposits is imperative to widen their potential application. Considering the high deformation resistance of HEAs, which may lead to the formation of pores and poor interparticle bonding even under high processing parameters, the exploration of the combination of strengthening strategies and cold spray to modify the microstructure and improve the mechanical properties of the deposits is required. In view of this, the following objectives are defined for this work:

- (1) Manufacturing $Zr_{55}Cu_{30}Ni_5Al_{10}$ MG deposit by cold spray process, investigating the plastic deformation behavior and bonding mechanisms of metallic glass particles through single splat test, studying the nanostructure at the interparticle interface, and proposing the mechanistic nanocrystallization origins in the MG deposit.
- (2) Preparing CoCrFeNi HEA deposits by cold spraying, investigating the effect of post-spray annealing temperatures on the microstructure and mechanical properties (i.e., tensile properties and compression properties), and unveiling the origin of the high strength in the deposits.
- (3) Manufacturing CoCrFeNi HEA deposits by using different combinations of particle size ranges and gas processing parameters to realize in-process densification, investigating the microstructure evolution and mechanical properties of the deposits strengthened through in-process densification, and revealing the underlying strengthening mechanism.
- (4) Fabricating CoCrFeNiMo_x HEA deposits by cold spraying, exploring the effect of Mo element content on the microstructure evolution, deposition behavior, phase structure, mechanical properties, and tribological properties of Mo-doped CoCrFeNi HEA deposits, and analyzing the wear mechanisms.

Chapter 3

Interparticle Bonding and Interfacial Nanocrystallization Mechanisms in Cold-sprayed Bulk Metallic Glass

In this chapter, the amorphous Zr-based bulk metallic glass deposit was produced by cold spray additive manufacturing. The bonding mechanism of metallic glass particles was systematically investigated by studying the deformation behavior of individual particles after deposition. We revealed two collective particle bonding mechanisms that contributed to the formation of metallic glass deposits, i.e., high-velocity impact-induced localized metallurgical bonding at the fringe of the interface and high particle temperature-induced viscosity reduction and resultant annular metallurgical bonding band. Moreover, the dynamic evolution mechanism of the amorphous phase into nanocrystal structures at severely deformed interfacial regions during cold spray was carefully investigated. For the first time, we observed different amorphous/nanocrystal structures in cold-sprayed metallic glass deposits, representing different evolution stages in the nanocrystallization process. Based on the observation, it is inferred that the nanocrystallization process can be divided into the following three stages: composition segregation, the formation of ordered 1D and 2D transition structures, and 3D nanocrystals. The current study provides new insights into bonding mechanisms and the mechanistic nanocrystallization origins in cold-sprayed bulk metallic glass deposits.



3.1 Material and Methodology

3.1.1 Feedstock Powder

The $Zr_{55}Cu_{30}Ni_{15}Al_{10}$ (at%, hereafter referred to as Zr55) amorphous powder produced by high-pressure inert gas atomization was used as feedstock for cold spray due to its good glass forming ability. Fig. 3.1a and b show the surface morphology of the as-atomized Zr55 amorphous powder characterized by a scanning electron microscope (SEM, Carl Zeiss ULTRA Plus, Germany). The majority of the feedstock particles are highly spherical with smooth surfaces. Some micro-satellite particles were attached to larger powder due to their different condensation rates. The phase structure of the Zr55 feedstock powder was analyzed by X-ray diffraction (XRD, Bruker D8, Germany) equipped with Cu-K α radiation from a range of 2θ values between 20° and 80° (40 kV, 40 mA) at a scanning rate of $1.2^\circ \text{ min}^{-1}$. The XRD spectrum of feedstock powder in Fig. 3.1c only shows broad diffraction humps, indicating a fully amorphous structure. The size distribution of the powder was measured by a laser diffraction particle analyzer

(Mastersizer 2000, Malvern Instruments, UK). As shown in **Fig. 3.1d**, the powder has a size range between 5 and 90 μm and a median D10, D50, and D90 of 15.68, 32.91, and 58.65 μm , respectively.

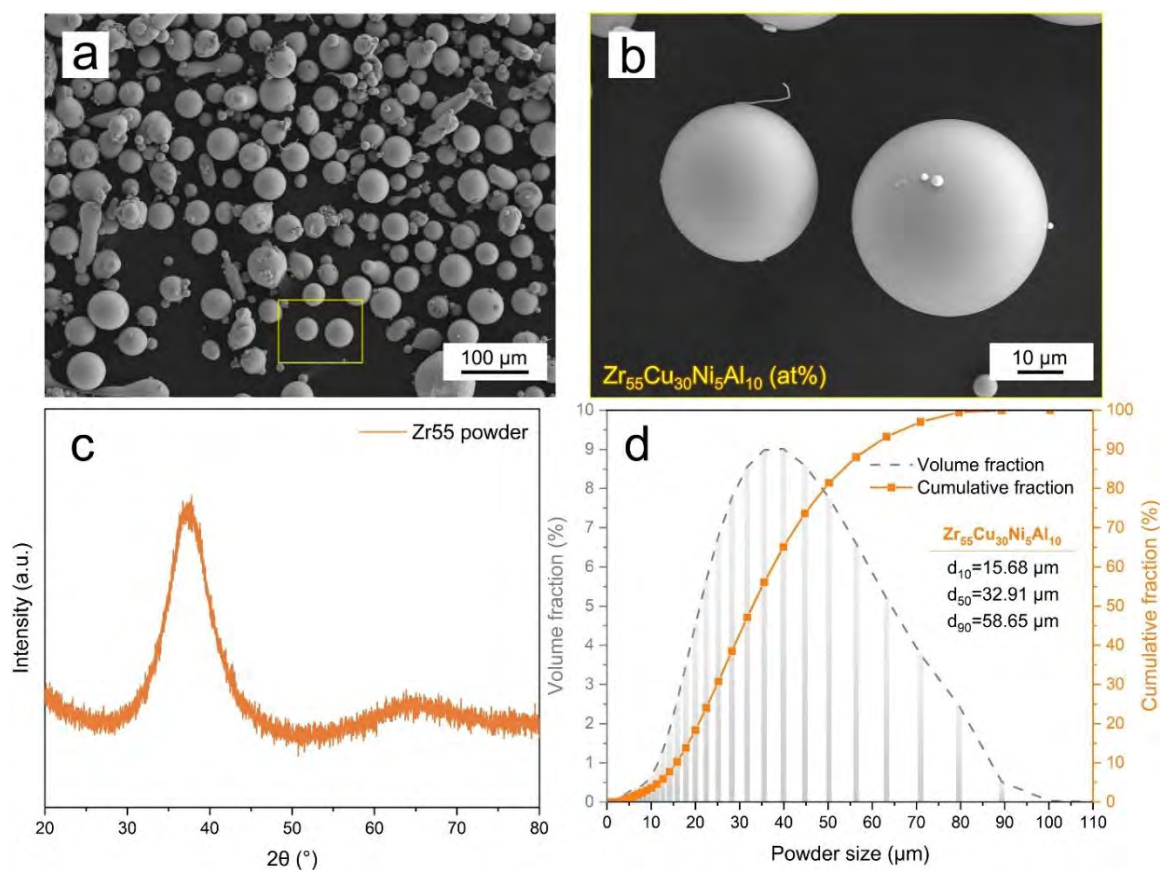


Fig. 3.1 Characterization of the as-atomized Zr55 amorphous powder used for deposit manufacturing. Surface morphology at (a) low magnification and (b) high magnification, (c) XRD spectrum, and (d) Particle size distribution.

3.1.2 Cold Spray Deposition Process

The deposition of Zr55 was achieved by using an in-house cold spray system (Trinity College Dublin, Ireland), which is composed of high-pressure gas cylinders, a gas heater, a powder feeder, a CNC working platform, a de-Laval nozzle, and a computer control module, as shown in **Fig. 3.2**. The de-Laval nozzle has a round cross-sectional shape with a convergent length of 30 mm, a divergent length of 180 mm, an inlet diameter of 10 mm, a throat diameter of 2 mm, and an outlet diameter

of 6 mm. The nozzle was water-cooled by a jacket in case of nozzle clogging at elevated temperatures. By referring to the processing parameters reported in previous studies [151,156,159,166] and considering the maximum capacity of the self-made cold spray system, compressed nitrogen was selected as propelling gas, and the gas pressure and the temperature were maintained constant at 3.0 MPa and 800 °C, respectively. The standoff distance from the exit of the de-Laval nozzle to the target surface was kept at 30 mm. Two experiments, namely full deposit and single splat deposit, were performed to explore the microstructural evolution and the formation mechanism of the cold-sprayed Zr55 deposits. For the full deposit, a thick Zr55 deposit was deposited onto the Al substrate under a nozzle traversal speed of 50 mm/s and a powder feeding rate of 50 g/min. The nozzle moving trajectory followed a reciprocating zigzag strategy, and the space between two neighboring tracks was 3.0 mm. For the single splat deposit, Zr55 particles were deposited onto mirror-polished cold-sprayed Zr55 deposit under a nozzle traversal speed of 150 mm/s and a lower powder feeding rate (10 g/min). The reason for using the as-sprayed Zr55 deposit as the substrate material is to simulate the particle-on-particle deposition process during the practical cold spray.

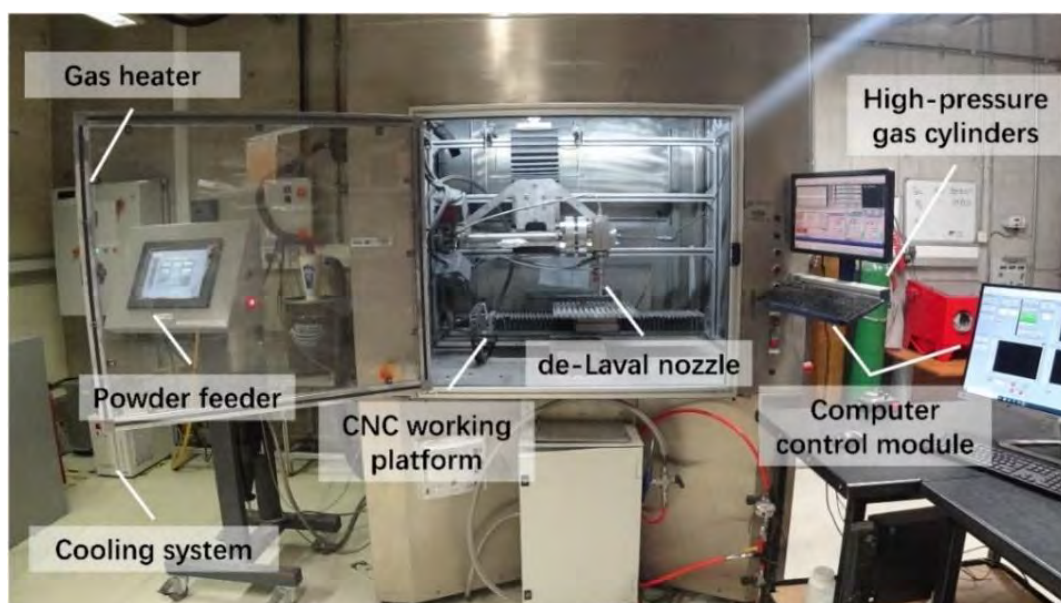


Fig. 3.2 In-house cold spray system in Trinity College Dublin

3.1.3 *Microstructure Characterization*

As preparatory work for microstructure analysis, the cross-sectional sample was prepared using standard metallographic procedures. To reveal the interparticle boundaries, the polished sample was etched with a corrosive agent (a mixture of 15 ml H₂O, 15 ml HNO₃, and 3 ml HF). The microstructure of the cold-sprayed Zr55 deposit before and after etching was characterized by SEM. The element compositions of the Zr55 deposit were examined by energy-dispersive X-ray spectroscopy (EDS, Oxford Instruments INCA, UK). The density of the deposit was estimated by optical microscopy (Leica DM LM, Germany) with an image analysis method based on the ASTM E2109-01 standard. The result was averaged from five different regions of the deposit to ensure the reliability of the data. The phase structure of the Zr55 deposit was analyzed by XRD. The micro- and nano-structure at the highly deformed region near the interparticle interface were characterized by transmission electron microscopy (TEM, FEI Tecnai G2 F20) in combination with selected area electron diffraction (SAED). The lamella for TEM characterization was extracted by focused ion beam (FIB, FEI Scios). The Fast Fourier transformation (FFT) patterns of the selected regions on TEM images were converted by commercial software (Digital Microscopy, Gatan). Furthermore, the surface and the cross-sectional morphologies of individual Zr55 splats were characterized by SEM, and the cross-sections were prepared through FIB milling.

3.2 **Microstructure of the Cold-sprayed Zr55 deposit**

Fig. 3.3a shows the cross-sectional microstructure of the cold-sprayed Zr55 deposit. The deposit is highly dense with few microstructural defects such as pores and cracks. Quantitatively, the density of the deposit was measured to be $99.70 \pm 0.13\%$. The formation of micro-sized pores between some particles can be attributed to the insufficient plastic deformation of particles. In cold spray, a deposit with high

density normally suggests that most of the particles experience extensive plastic deformation during deposition and interparticle bonding is promising [37,237]. This is also evidenced by the etched cross-sectional microstructure of the cold-sprayed Zr55 deposit shown in Fig. 3.3c, where most of the Zr55 particles were found severely flattened into lamellar shape. However, some of the particles remained spherical or near-spherical due to their insufficient plastic deformation, as pointed out by the yellow arrows in Fig. 3.3c. The EDS mapping results provided in Fig. 3.3b indicate that there is no chemical segregation or oxide inclusion in the deposit. This fact suggests the promise of cold spray for manufacturing BMGs with high purity.

Fig. 3.3d displays the XRD spectrum conducted on the cross-sectional Zr55 deposit. The XRD spectrum shows a broad diffraction peak maximum at around $2\theta = 37^\circ$ without any sharp diffraction peaks as Zr55 feedstock powder, indicating that the deposit retained an amorphous structure within the detection limit of XRD. This result stands in contrast with the XRD spectra of BMGs made by other fusion-based additive manufacturing techniques that often exhibit sharp crystallization peaks [137,238]. Therefore, compared with other additive manufacturing techniques, the inherent characteristics of cold spray, such as low temperature, short impacting period, and high cooling rate, mitigate the challenge of crystallization during the deposition process. However, it is noteworthy that the deposit may experience nanocrystallization, particularly at the highly deformed impacting interface, as previously reported [148].

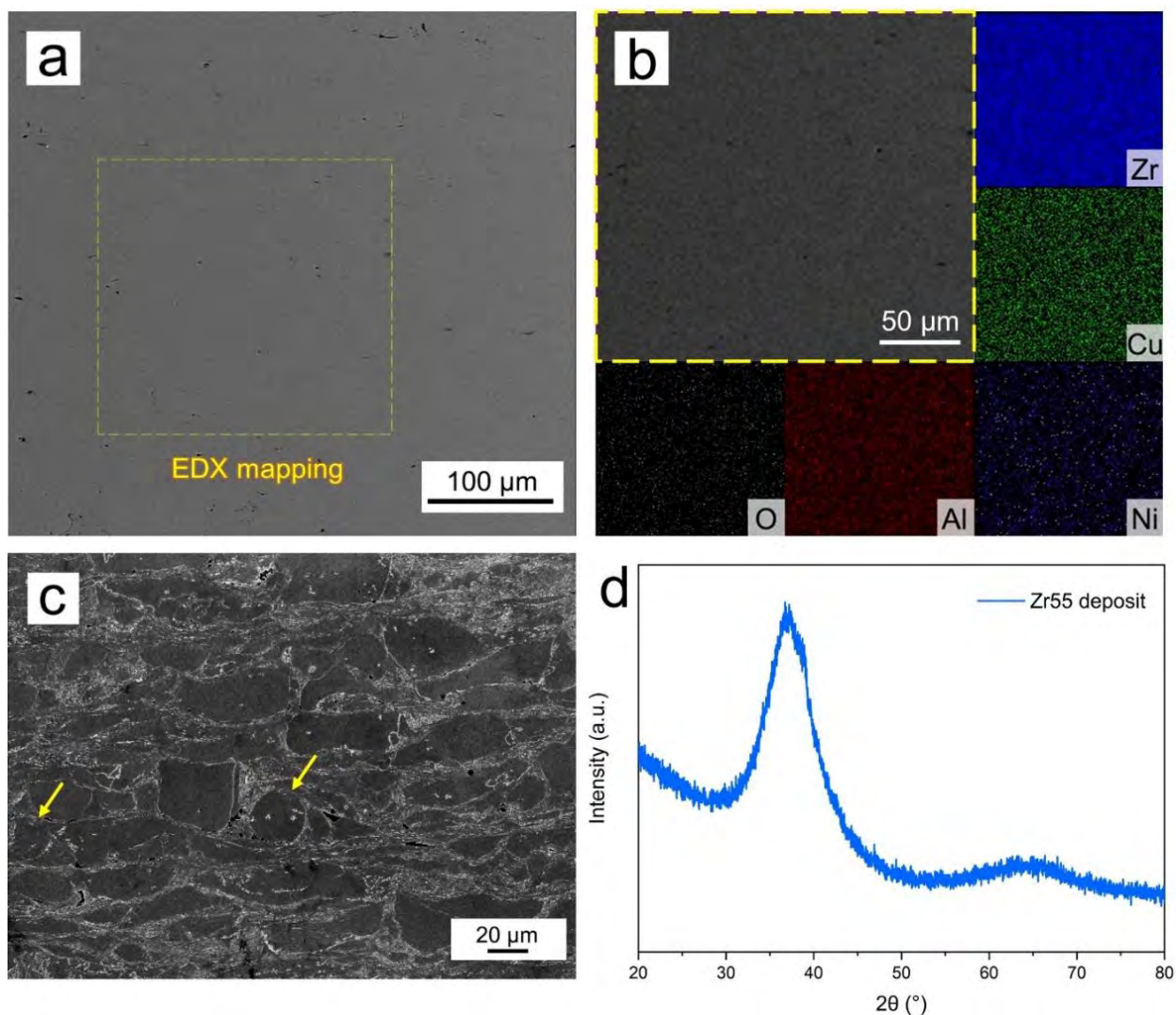


Fig. 3.3 Characterization of the cold-sprayed Zr55 deposit: (a) Cross-sectional microstructure, (b) EDS map of elements distribution, (c) Etched cross-sectional microstructure, and (d) XRD spectrum.

3.3 Bonding Mechanism of Individual Metallic Glass Particles

3.3.1 Mechanism I-High-velocity Impact Induced Localized Metallurgical Bonding at the Fringe of Interface

Fig. 3.4 shows the representative surface morphologies of individual Zr55 particles

after impact and craters created by rebound particles. **Fig. 3.4a** shows a deposited particle with high sphericity. It can be seen that shear bands and shear cracks were generated in the particle, which are the typical characteristics of localized flow (inhomogeneous deformation) of metallic glasses. When the particle impacted onto the substrate, the stress at the contact interface increased quickly. Once the stress reached a critical value, yielding occurred, and permanent shape change was observed macroscopically through the initiation of shear bands. The shear bands initiated from the bottom of the particle and propagated rapidly towards the north pole with the stress waves travelling the particle. The dominant shear bands finally developed into cracks. At a microscopic level, the formation of shear bands is considered to be associated with the shear transformation zone, in which a group of atoms under imposed shear obtained the stress or strain energy established during elastic loading and overcome the energy barrier by cooperative rearrangement [239]. In addition, thin squeezed material was found at the bottom periphery of the deposited particle, which is the evidence of viscous fluid or melting fluid induced by high temperature and shear strain. **Fig. 3.4b** shows a deposited particle with more significant localized flow features (i.e., increased number of shear bands and larger areas of shear surface), which could be attributed to the higher kinetic energy of the particle. The shear surface presents vein patterns and white ridge lines at the sub-micron scale, indicating the localized softening by adiabatic heating during the rapid shear. Besides, there are some splashing melting (or viscous fluid) jets around the particle, as pointed out by the yellow arrow, which suggests the extremely high temperature localized at the bottom of the particle. As shown in **Fig. 3.4c**, the particle experienced more severe localized plastic deformation and deformed to a propeller-like shape with a further increased area of the shear surface. In addition, the shear surface presents a flat and smooth appearance, which is quite different from that in **Fig. 3.4b**. This could be attributed to the extreme adiabatic temperature during shear banding at higher strain rates, and the temperature within the shear

bands may reach the melting point T_m (1028 K [240]). It is reported that the temperature rise associated with shear banding in metallic glass can reach up to a few thousand kelvins over a few nanoseconds [241]. Such high temperatures led to a sharply decreased viscosity, and thus, the smooth shear surface appeared.

Fig. 3.4d shows a deposited particle with its right part fractured and ejected after impact due to severe shear localization, which provides an opportunity to directly observe what happened at the bottom of the particle. A large volume of viscous fluid or melting fluid can be observed at the bottom region of the particle due to the adiabatic heating induced by highly localized plastic deformation upon impact. Accordingly, there is a reasonable prospect that the localized viscous fluid or melting fluid induced by high temperature occurred at the south pole of the deposited particle, resulting in the particle adhesion to the substrate. The viscous fluid or melting fluid is the strong evidence of homogeneous deformation of the metallic glass particle. The various impact morphologies of the particles shown in **Fig. 3.4a-d** can be attributed to their different impact velocities and impact temperatures induced by particle size effect during acceleration. For each single particle, the different deformation features presented from the bottom to the top of the particle are due to the generation of strain gradient, strain rate gradient, and temperature gradient upon impact.

Fig. 3.4e-f show craters on the substrate surface created by rebound Zr55 particles. As shown in **Fig. 3.4e**, the central region of the crater is rather clean with nearly no evidence of metallurgical bonding between the particle and substrate. However, a ring of dimple-like structure (vein pattern as marked by yellow arrows) can be observed in the surrounding area of the crater together with some “melting fluid jets” (or viscous fluid jets). These dimple-like features and viscous jets are the result of the high temperature at the impacting interface. The increased temperature led to a sharp decrease in viscosity, which promoted viscous flow at the bottom periphery

of the particle. The most interesting finding from **Fig. 3.4e-f** is that these dimple-like materials remained bonded with the substrate after particle rebounding. The detachment occurred in the particle rather than from the particle-substrate interface. This fact indicates that the Zr55 particle can bond with the substrate upon impact in the first place. However, the viscous force of the liquefied interface failed to surpass the particle rebounding force, thus the particle rebounded from the substrate after impact. Therefore, it can be inferred that successful bonding requires adequate viscous force generated by dimple-like materials between the substrate and the Zr55 particle.

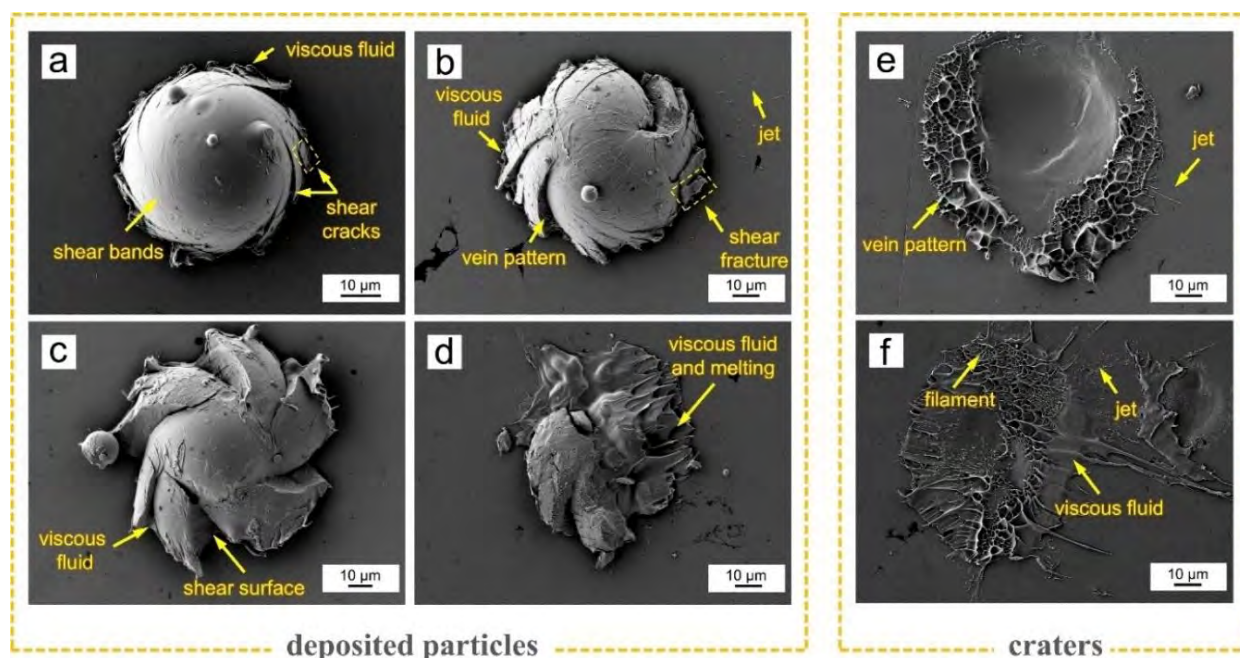


Fig. 3.4 Top view of the representative surface morphologies of (a)-(d) individual Zr55 deposited particles and (e)-(f) craters created by rebound Zr55 particles. Note the substrate used in single particle deposition is the polished cold-sprayed Zr55 deposit.

To observe what had happened at the interface exactly and how the metallic glass particles bonded with the previously deposited layer, a deposited Zr55 particle was dug from the top with FIB to display the entire particle-substrate interface. **Fig. 3.5** exhibits the surface morphology of a particle after impact and the corresponding

cross-sectional morphology including the particle-substrate interface. As shown in **Fig. 3.5a**, the deposited particle is characterized by severe shear localization, which is the feature of inhomogeneous deformation, representing the common deposition morphology of Zr55 particles. **Fig. 3.5b-c** show the cross-sectional morphology of the deposited particle. There is a nanoscale gap between the deposited particle and substrate except at the fringe of the interface at which the particle bonded with the substrate. The formation of the nanoscale gap can be attributed to the spring back elastic forces. The bonding only occurred at the fringe of the particle-substrate interface, which is consistent with what we see in the crater (see **Fig. 3.4e**). This is the first time that the exact bonding location of metallic glass particles was observed experimentally.

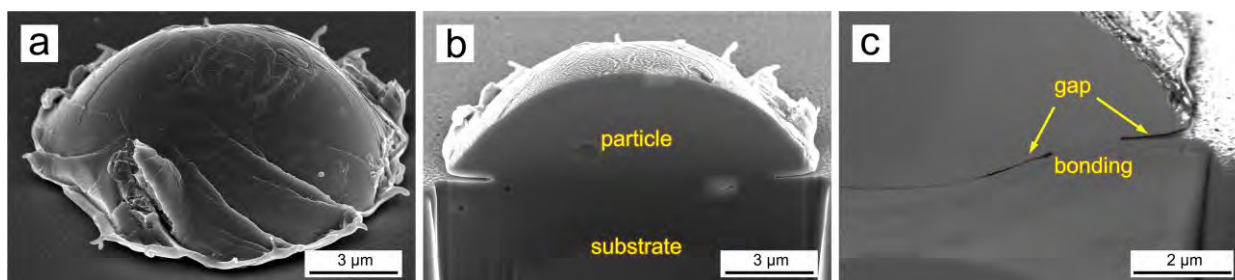


Fig. 3.5 FIB process of individual Zr55 deposited particle: (a) Surface morphology, (b) Cross-sectional morphology revealing particle-substrate interface, (c) Close view of metallurgical bonding at the interface.

3.3.2 Mechanism II- High particle temperature induced viscosity reduction and resultant annular metallurgical bonding band

The outer layers of all the deposited particles in **Fig. 3.4** exhibit the same surface status as feedstock without any trace of viscous fluid or melting fluid, which implies that the surface temperature of these particles was relatively low before impacting. However, the deposited particle, as shown in **Fig. 3.6a**, presents an exceptional status where the outer layer of the particle was viscous flowing. This is probably

because the temperature of the outer layer of the particle is much higher (e.g., typically in or above the supercooled liquid region) when impacting onto the substrate. The viscosity of metallic glasses is temperature sensitive and decreases with the increase in temperature. Similar to preheating particles, higher temperature favors particle global deformation and bonding. The bonding mechanism of such particles is associated with the liquid-like outer layer of the particle.

Fig. 3.6b shows the surface morphology of a deposited particle with a liquid-like surface. Compared with the particles in **Fig. 3.5**, there are no visible shear bands, cracks, or fractures, indicating the particle mainly experienced homogeneous deformation. **Fig. 3.6c-d** show the cross-sectional morphology of the deposited particle. A discontinuous gap between the particle and substrate was found at the highly deformed region. However, the close view at the side of the interface shows an annular metallurgical bonding band with a thickness of $\sim 1 \mu\text{m}$, which is quite different from the bonding location in **Fig. 3.5c**. When the particle impacted onto the substrate at a temperature in or above the supercooled liquid region, the viscous fluid was forced to flow to the periphery. The shear thinning induced by the high shear rate at the bottom of the particle can further promote the lateral viscous flow of the particle. The viscous fluid at the side of the interface adhered with the substrate through metallurgical bonding promoted by high temperature. In cold spray, particle impact velocities and impact temperatures are affected by many factors, such as particle size and in-flight trajectory. In general, large-sized particles are likely to experience high temperatures due to their longer residence. Moreover, particles travelling through the centre of the nozzle experience higher gas temperature, compared with those particles travelling near the inner wall of the nozzle. In brief, some particles probably impacted onto the substrate at temperatures in or above the supercooled liquid region. The viscous fluid was forced to flow to the periphery upon impact and adhered with the substrate through an annular metallurgical bonding band, which is different from the impact-induced localized

metallurgical bonding.

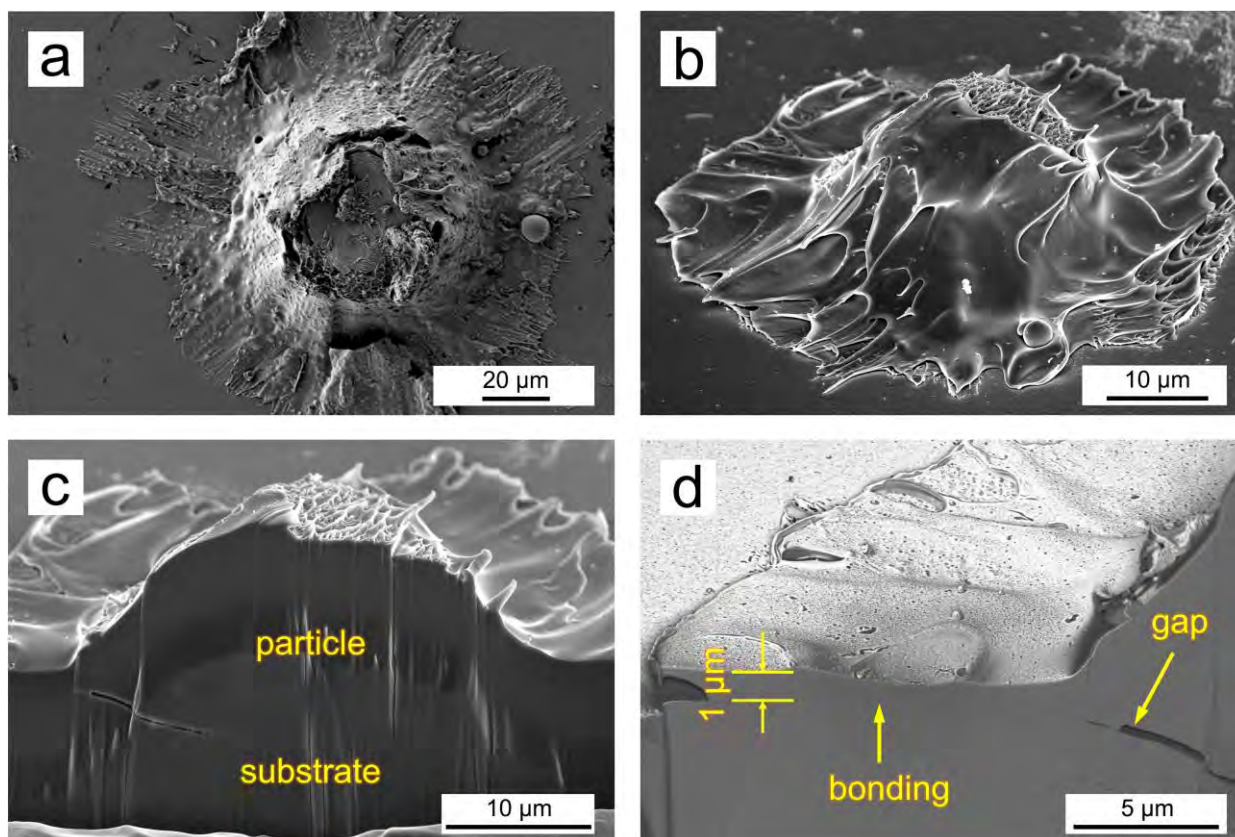


Fig. 3.6 (a) Top view of the surface morphology of an individual Zr55 deposited particle with the liquid-like surface, (b)-(d) FIB process of an individual particle with the liquid-like surface: (b) Surface morphology, (c) Cross-sectional morphology revealing the particle-substrate interface, (d) Close view of metallurgical bonding at the interface.

3.3.3 *A summary of the Bonding Mechanism of Cold-sprayed Metallic Glass Particles*

Based on the results and discussion presented above, it is sensible to conclude that the bonding of the cold-sprayed Zr55 particles can be achieved through two different mechanisms. For most of the deposited particles, the bonding was realized by the high-velocity impact-induced localized metallurgical bonding at the fringe of the interface. The rising temperature at the impacting interface led to a sharp decrease in viscosity and promoted lateral homogeneous deformation at the bottom

of the metallic glass particle. However, particles will rebound from the substrate if the impact velocities of particles are high enough. Apart from this, an unusual particle bonding mechanism that has never been reported was also found to contribute to the deposition of metallic glass particles. Some particles impacted onto the substrate at temperatures in or above the supercooled liquid region, leading to a decrease in viscosity. Upon impact, the viscous fluid was forced to flow to the periphery and adhered with the substrate through an annular metallurgical bonding band. The high impact temperature of a particle is related to the particle size and the in-flight trajectory. Specifically, a particle with a larger size or travelling through the center of the nozzle is more likely to experience high temperature due to longer residence or higher gas temperature. Both two particle bonding modes contribute to the formation of the cold-sprayed Zr55 deposit.

3.4 Nanocrystallization of Cold-sprayed Metallic Glass Particles

Fig. 3.7a shows the interface between two metallic glass particles in the cold-sprayed Zr55 deposit observed by SEM. The lamella containing the interparticle interface, as shown in **Fig. 3.7b**, was then lifted out by FIB. The nanostructure of two regions S1 (away from the interparticle interface) and S2 (near the interparticle interface) in **Fig. 3.7c** was investigated by TEM. **Fig. 3.7d** shows the TEM image and corresponding SAED pattern of a region in S1. The diffusion halo in the SAED pattern indicates that a glass structure in the amorphous phase was well-retained at the region away from the interparticle interface. However, it is interesting to find that a heterogeneous nanostructure with nano-scale dark polygon areas randomly dispersed in the amorphous matrix was observed at the extremely localized near-interface region (S2), as shown in **Fig. 3.7e**. The corresponding SAED pattern displays diffuse halo rings with few irregular bright specks, suggesting the

coexistence of amorphous and nanocrystal structures. These nanocrystals with dark polygonal structures were believed to be formed during the particle deposition.

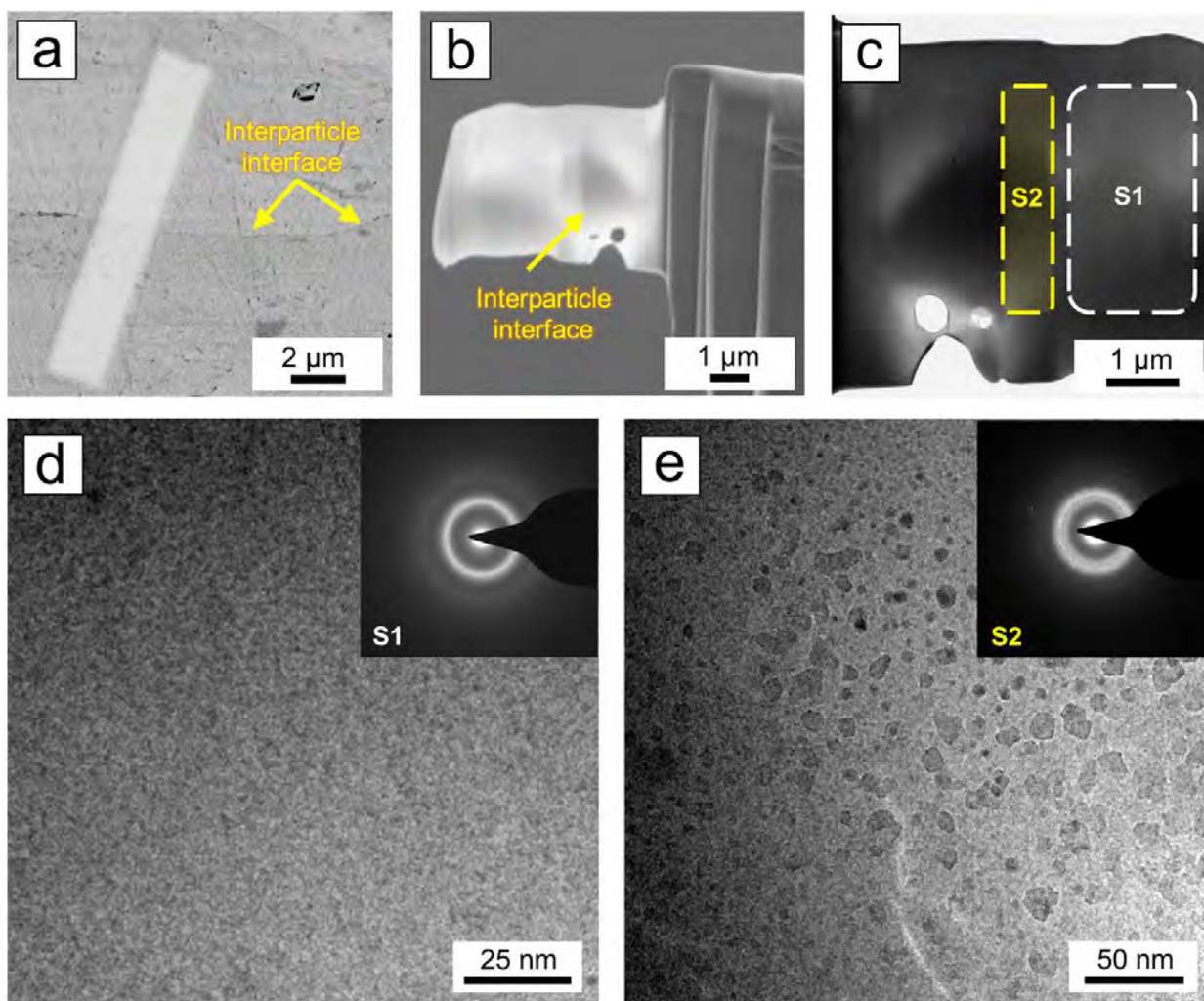


Fig. 3.7 Characterization of the nanostructure at the interparticle interface: (a) SEM image exhibiting interparticle boundary between two particles, (b) SEM and (c) TEM images of the lamella lifted out by FIB, (d)-(e) TEM micrograph with SAED pattern inset: (d) Away from the interparticle interface and (e) Near the interparticle interface, respectively.

3.4.1 *Nanocrystallization Conditions: Thermal and Mechanical Factors*

In cold spray process, adiabatic heating at the impacting interface is unavoidable during the high-strain-rate deformation of particles, which leads to considerable

temperature rise and material softening. The high temperature can reduce the energy barrier of atomic diffusion, and the formation of nanocrystals through the atomic diffusion mechanism of nucleation and growth in the amorphous matrix is possible. In this work, the high temperature can be inferred from the viscous fluid at the bottom of the particles and the metallurgical bonding at the interface (see [Fig. 3.4](#) and [Fig. 3.5](#)). However, the cooling rate in cold spray process can reach as high as $10^9\sim 10^{10} \text{ K}\cdot\text{s}^{-1}$ at the highly deformed interfacial regions [\[55\]](#), which is significantly higher than that of gas atomized droplets ($10^4\sim 10^6 \text{ K}\cdot\text{s}^{-1}$ [\[242,243\]](#)). The gas-atomized metallic glass powder can retain an amorphous structure, so the cooling rate of cold spray is high enough to bypass nanocrystallization. In other words, the effect of adiabatic heating on the formation of nanocrystals at the interparticle interface is considered to be very limited.

In general, the atomic mobility in metallic glasses is frozen when it is cooled below the glass transition [\[244\]](#). However, the plastic deformation can assist atomic transportation and evolution toward equilibrium, and thereby lead to the ordering of localized structures. In fact, the nanocrystallization of metallic glasses has been observed in various plastic deformation processes at room or cryogenic temperatures, such as rolling [\[173\]](#), nanoindentation [\[245\]](#), high-pressure torsion [\[246\]](#), and ball milling [\[247\]](#), particularly in the region of the deformed specimen under compressive stress. This indicates that the nanocrystals formed in these low-temperature plastic deformation processes are due to the strain rather than the deformation-induced temperature rise.

Nucleation is a key step in the crystallization process. Crystals can be produced only when the size of nucleation exceeds a critical size. According to classical nucleation theory, the nucleation rate (\dot{N}) can be described as [\[248\]](#):

$$\dot{N} = N \exp\left(-\frac{\Delta G^*}{kT}\right) \exp\left(-\frac{\Delta E}{kT}\right) \quad (\text{Eq. 3.1})$$

where N is a constant at a fixed temperature, ΔG^* is the energy barrier for nucleation required to form a critical sized nucleus, ΔE is the energy barrier for diffusion required to transport an atom from an amorphous matrix to an embryonic nucleus, k is the Boltzmann's constant. Therefore, the nucleation rate (\dot{N}) will increase if the energy barrier for nucleation (ΔG^*) and atomic diffusion (ΔE) is reduced.

The pressure (P) modified energy barrier to form a spherical crystal nucleus with a critical size (ΔG^*) can be expressed as [248]:

$$\Delta G^*(T, P) = \frac{16\pi\gamma^3}{3} \left(\frac{V_m^c}{\Delta G_m + E + P\Delta V_m} \right)^2 \quad (\text{Eq. 3.2})$$

where V_m^c is the molar volume of the crystalline phase, ΔG_m is the molar free energy difference between the amorphous and crystalline phases, E is the elastic energy induced by the volume change during the phase transformation in the solid state, γ is the interfacial free energy between the amorphous and crystalline phases, and ΔV is the volume change to form this crystalline nucleus from amorphous state.

During the phase transformation from amorphous to crystalline, the values of ΔG_m and ΔV_m ($\Delta V_m = V_m^c - V_m^a$) are negative, and E is rather small [249]. Therefore, the free energy required to produce a critical nucleus size (ΔG^*) decreases with the increase in pressure. In cold spray, the high pressure at the impacting interface leads to the decreased ΔG^* . Moreover, the crystalline phase possesses a smaller volume than that of the amorphous phase, and the crystalline nuclei inlaid in the amorphous matrix are under internal tension. Hence, the applied compressive stress can relieve the tensile stress in the crystalline nuclei and thereby stabilize the crystalline nuclei [250].

Based on the free volume theory, the strain during the plastic deformation of metallic glass could generate free volume and promote atomic transportation [251–253]. Furthermore, the increase rate of free volume and saturated free-volume

content increase with strain rate. A higher strain rate leads to a higher increase rate of free volume and the resultant more free volumes generation than a lower strain rate. Although the creation of free volume comes along with the annihilation of free volume, the creation rate of free volume at a high strain rate exceeds the annihilation rate. Therefore, high strain and high-strain rate deformation could generate more free volumes. The increase in free volume leads to atomic dilatation and thereby the reduction in the barrier for the mobility of atoms in metallic glasses [254]. In cold spray, the high strain and high strain rate at the impacting interface contribute to the rapid generation of free volume and the rapid transportation of atoms. From the perspective of kinetics, the enhanced atomic transportation can be understood as the decrease of the energy barrier for atomic diffusion (ΔE). According to Eq. 3.1, the decreased ΔG^* and ΔE work together to increase the nucleation rate, which promotes the precipitation of nanocrystals from the amorphous matrix. Therefore, the effect of mechanical factors on the nanocrystallization in cold-sprayed metallic glasses may be decisive.

3.4.2 Nanocrystallization Process: From Amorphous Structure to Nanocrystals

In order to investigate how amorphous structure dynamically evolved into nanocrystals during cold spray, high-resolution transmission electron microscopy (HRTEM) and corresponding FFT patterns of localized dark regions were achieved, as shown in Fig. 3.8. As a benchmark, the FFT pattern of the amorphous matrix (region I) is provided in the figure as well. Before the discussion, it is worth pointing out that in this work, we for the first time observed different amorphous/nanocrystal structures in cold-sprayed metallic glass particles, which are believed to represent different evolution stages in the nanocrystallization process, and this helps us to fully reveal the nanocrystallization mechanism of metallic glass particles during cold spray. In Fig. 3.8a, the contrast of region II is darker than that of the amorphous

matrix, which may indicate that the atomic arrangement here is special. However, the HRTEM image reveals a disordered atomic structure, and its corresponding FFT pattern displays a diffuse halo, which is nearly the same as that of the amorphous matrix (region I). This fact suggests that region II is still in an amorphous state. The difference in contrast is likely due to the composition segregation in region II [149]. Such segregation is believed to be induced by high mechanical stress and adiabatic temperature rise generated during the high-velocity impact of particles, resulting in the formation of a large number of free volumes and promoting atomic diffusion to accelerate the composition segregation [173,253]. The occurrence of composition segregation is closely related to the interatomic interactions in the alloy. A large difference in the heat of mixing or a positive heat of mixing between two components can result in phase separation or segregation [255]. In the Zr-Cu-Ni-Al alloy system, the Cu and Ni atomic pairs show a positive heat of mixing ($\Delta H_{\text{Cu-Ni}} = 4$ kJ/mol). The heats of mixing of Zr-Ni ($\Delta H_{\text{Zr-Ni}} = -49$ kJ/mol) and Zr-Al ($\Delta H_{\text{Zr-Al}} = -44$ kJ/mol) are more negative than that of other atomic pairs ($\Delta H_{\text{Zr-Cu}} = -23$ kJ/mol, $\Delta H_{\text{Ni-Al}} = -22$ kJ/mol and $\Delta H_{\text{Cu-Al}} = -1$ kJ/mol, respectively) [256]. The strong attractive interaction of Cu-Ni, Zr-Ni, and Zr-Al helps the occurrence of segregation in the amorphous matrix.

The atoms in region III show a disordered arrangement which is similar to the region I. However, localized ordered atomic lines (or columns) were found in certain directions, as pointed out by the yellow arrows. The clusters in the yellow box are regarded as the feature of imperfect ordered packing [257]. The corresponding FFT diffraction pattern displays a diffuse halo without any bright spots, indicating the entire atomic configuration in this region remains disordered. However, some blurred spots can be distinguished. Furthermore, the connection of any two blurred spots, which are symmetry of the central spot, is perpendicular to the corresponding atomic arrangement direction as pointed out in region III. This indicates some atoms started to adjust their position towards an ordered packing. It is more interesting that

the ordering process concurrently occurred along multiple directions.

In region IV, the formation of lattice fringes can be clearly observed. The atoms formed highly ordered atomic lines along an exclusive periodic direction by further adjusting their positions. The corresponding FFT diffraction pattern of this atomic configuration shows a diffuse halo together with clearly visible bright specks, indicating the coexistence of amorphous and ordering structures in the current region. In other words, nanocrystallization in this area was incomplete. Moreover, only two bright spots were observed in the FFT pattern, which indicates it has a 1D periodic arrangement [258]. Based on the FFT pattern, the 1D periodic arrangement has a plane space of about 0.244 nm, which is the typical (103) plane space of Zr_2Cu . It is worth noting that the maximum ramp peak of the deposit is located in the (103) plane of Zr_2Cu as well. Consequently, it can be inferred that the 1D periodic nanocrystal structure is Zr_2Cu . Furthermore, the (103) plane is a relatively low-index plane for the Zr_2Cu lattice, and the packing of atoms on this plane is denser than that of a plane with a higher index. In other words, it is easy for atoms to migrate to a stable site. Therefore, a cluster of single direction atomic columns (1D periodicity) was first formed along the low index or close packed direction. Such quasi-ordered structure with 1D periodicity has also been reported in the nanocrystallization of other metallic glasses or even proteins, which was regarded as a primary step to reach a localized equilibrium state [258,259]. Compared with the atoms in region IV, the atoms in region V also exhibit the feature of 1D periodicity. However, localized ordered atomic lines were also formed in other directions. The corresponding FFT diffraction pattern also supports what we observed. Aside from two bright specks indicating the 1D periodicity, other spots with lower brightness were also found. The connection of any two blurred spots, which are symmetry of the central spot, is perpendicular to the corresponding localized ordered direction as pointed out in region V. It can be inferred that the atoms continued to adjust their positions towards a higher-ordered atomic

configuration (i.e., 2D or 3D periodicity).

In region VI, as shown in Fig. 3.8b, almost all the atoms exist in a highly ordered arrangement with 3D periodicity, demonstrating a higher level of nanocrystallization. The nanocrystal structure could be AlZr_3 , AlCu_2Zr , or AlNi_2Zr on the $[011]$ zone axis by calibration. The formation of the above intermetallic is likely to be associated with the large difference in the heat of mixing of corresponding elements in the Zr55 alloy system. Although the arrangement of atoms in region VI was more orderly, crystal defects (e.g., dislocation or vacancy) still existed in the nanocrystal structure.

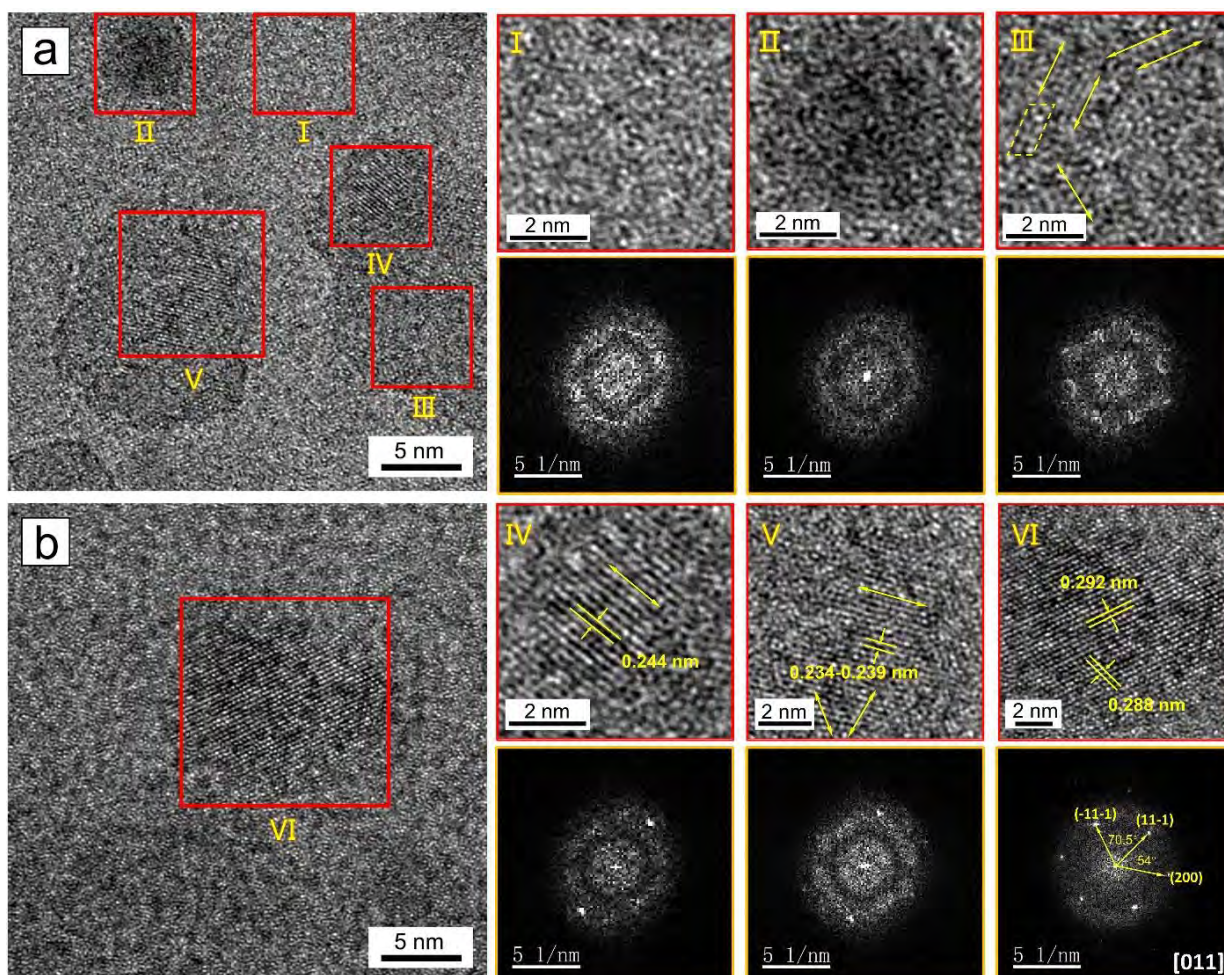


Fig. 3.8 HRTEM images and corresponding FFT diffraction patterns of localized ordered clusters near the interparticle interface: (a) Localized ordered atomic configuration, (b) Nanocrystal structure.

3.4.3 *Nanocrystallization Mechanism of Cold-sprayed Metallic Glass Particles*

Based on the results and discussion above, the nanocrystallization mechanism in the cold-sprayed Zr-based BMG deposit can be summarized as below. When the metallic glass particles impacted onto the substrate at high velocity, the localized interfacial regions underwent severe plastic deformation at extremely high strain rates. The composition segregation induced by mechanical and thermal activation was dramatically promoted due to the increased number of free volumes and enhanced atomic diffusion, as shown in region II which presents dark and light differences. The segregation acted as a precursor for further nanocrystallization process. The atoms started to adjust their positions to form localized ordered atomic lines towards multiple directions firstly, as shown in region III, followed by the appearance of 1D periodic lattice fringes. The 1D type ordering atomic clusters comprised an array of planes in the same direction, typically along the low index or close packed direction, as shown in region IV. As nanocrystallization proceeded, the 1D periodicity evolved to higher ordered structures through continuous atomic adjustment until the formation of nanocrystals, as shown in **Fig. 3.9**. However, due to the short impacting period ($\sim 10^{-8}$ s [260]) and high cooling rates ($10^9 \sim 10^{10}$ K s⁻¹ [55]) in cold spray process, the nanocrystallization level was very limited, and consequently, only nano-scale crystals could be formed at localized regions. In fact, similar evolution was also observed during the nanocrystallization of Zr-based metallic glasses induced by high-density pulse-current treatment [258] and annealing [261,262]. Besides, the nanocrystallization process in amorphous Ni investigated by using the molecular dynamics simulation method also showed the formation of ordered transition structures (1D and 2D structures) followed by 3D nanocrystals [258,262]. From the viewpoint of thermodynamics, the energy barrier to form 3D nanocrystals directly is much higher than that to form low dimensional ordered transition structures. While from the kinetic aspect, more atomic

rearrangement is required to form 3D nanocrystals, as compared to forming transition quasi-ordered structures [262]. The evolution process of atomic structure from an amorphous configuration to 3D nanocrystals is probably universal. Thanks to the nature of cold spray (e.g., extremely rapid heating and cooling rates, short impacting period, and high strain rate), the ordered atomic structures at different stages can be frozen and recorded, which offers us an opportunity to explore the nanocrystallization process of metallic glasses during cold spray process.

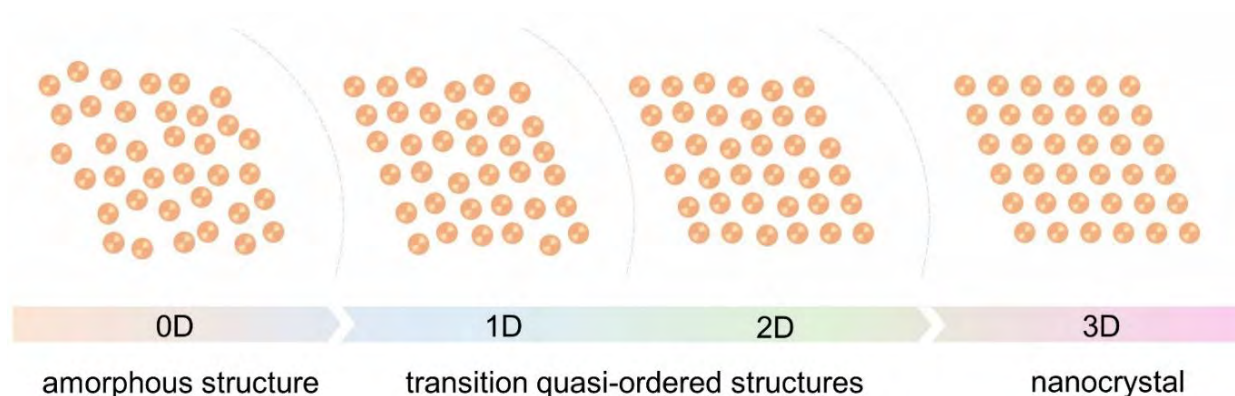


Fig. 3.9 Evolution of nanocrystals from an amorphous state.

3.5 Summary

In this chapter, the bonding and nanocrystallization mechanisms of cold-sprayed metallic glass particles were systematically investigated by using Zr55 metallic glass powder as feedstock. Based on the results and discussion, several important conclusions that can significantly enrich our knowledge and understanding of cold-sprayed BMG deposits were drawn and listed as follows:

- For the first time, the exact bonding location of metallic glass particles was observed experimentally. The interparticle bonding only occurred at the fringe area of the interface, which can be attributed to the high-velocity impact-induced localized metallurgical bonding.

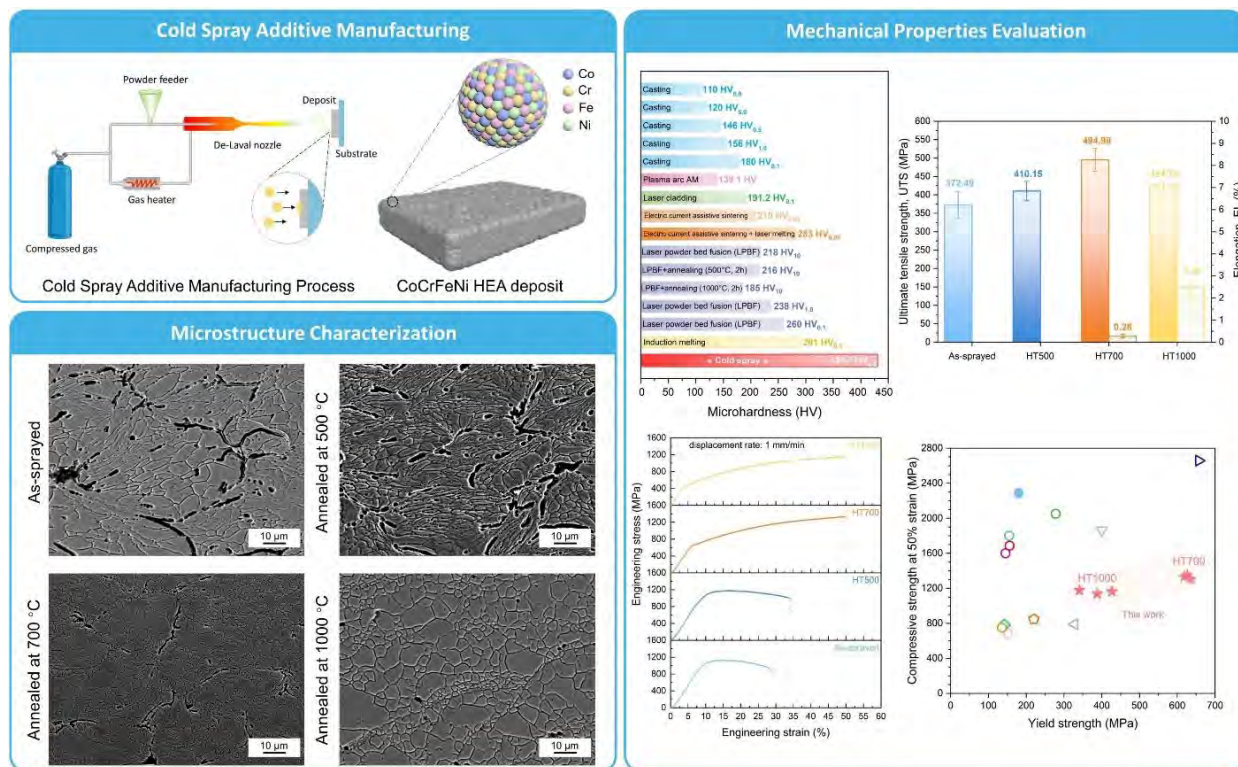
- A new mechanism that also contributed to the bonding of cold-sprayed metallic glass particles was first found. Some metallic glass particles impacted onto the substrate at temperatures in or above the supercooled liquid region, leading to a decrease in viscosity. The viscous fluid was forced to flow to the periphery upon impact and adhered with the substrate through an annular metallurgical bonding band.
- Ordered atomic structures at different levels were randomly dispersed in the amorphous matrix near the interparticle interface. The nanocrystallization at interfacial regions was mainly induced by mechanical factors (e.g., high strain and high strain rates) rather than adiabatic heating.
- The different amorphous/nanocrystal structures in cold-sprayed metallic glass particles can represent different evolution stages in the process of nanocrystallization. The formation of nanocrystals from an amorphous state can be divided into the following stages: composition segregation, the formation of ordered 1D and 2D transition structures followed by the 3D nanocrystals

Chapter 4

Microstructure Evolution and Mechanical Behavior of Additively Manufactured CoCrFeNi High-entropy Alloy Fabricated via Cold Spray and Post-annealing

In this chapter, equiatomic CoCrFeNi high-entropy alloy (HEA) was fabricated by solid-state cold spray additive manufacturing technology and then post-spray annealed at the temperature range of 500-1000 °C for 2 hours. By adjusting the annealing temperature, four types of deposits (i.e., as-sprayed, recovered (500 °C), partially recrystallized (700 °C), and fully recrystallized (1000 °C) deposits) were obtained, and their microstructure, compressive and tensile properties were systematically explored. The as-sprayed deposit exhibited high compressive yield strength due to the dislocation strengthening and grain boundary strengthening effects but fractured within the elastic deformation regime in the tensile test. Such significant tension-compression asymmetry can be attributed to the difference in the sensitivity of the deposit to interior defects (i.e., pores and particle boundaries) under tensile and compressive loads. Only recover annealing hardly influenced the microstructure and mechanical properties of the deposits. While recrystallization annealing could trigger enhanced interface diffusion and the resultant metallurgical bonding, as evidenced by the improved deposit density and less visible interparticle interfaces. The partially recrystallized and fully recrystallized deposits exhibited an

excellent combination of compressive strength and ductility. While the fully recrystallized deposit exhibited almost equal tensile and compressive yield strength and the best recovery of tensile ductility, indicating the weakened tension-compression asymmetry.



4.1 Material and methodology

4.1.1 Feedstock Powder and Cold Spray Process

Gas-atomized CoCrFeNi HEA powder (Institute of New Materials, Guangdong Academy of Sciences, China) was selected as the feedstock. The surface morphology (Fig. 4.1a) and etched cross-sectional microstructure (Fig. 4.1b) of the CoCrFeNi HEA powder were characterized by scanning electron microscope (SEM, Carl Zeiss Ultra Plus, Germany). Most of the powder featured high sphericity with equiaxed grains. The size distribution of the powder was measured by a laser diffraction particle analyzer (Mastersizer 2000, Malvern Instruments, UK). The

powder diameter range was measured between 15 and 90 μm with a mean size of 40.33 μm and a median D10, D50, and D90 of 25.85, 38.65, and 57.23 μm respectively (Fig. 4.1c). The element compositions of the CoCrFeNi HEA powder were examined by energy-dispersive X-ray spectroscopy (EDS, Oxford Instruments INCA, UK) equipped on the SEM. As shown in Fig. 4.1d, the powder presents a uniform element distribution.

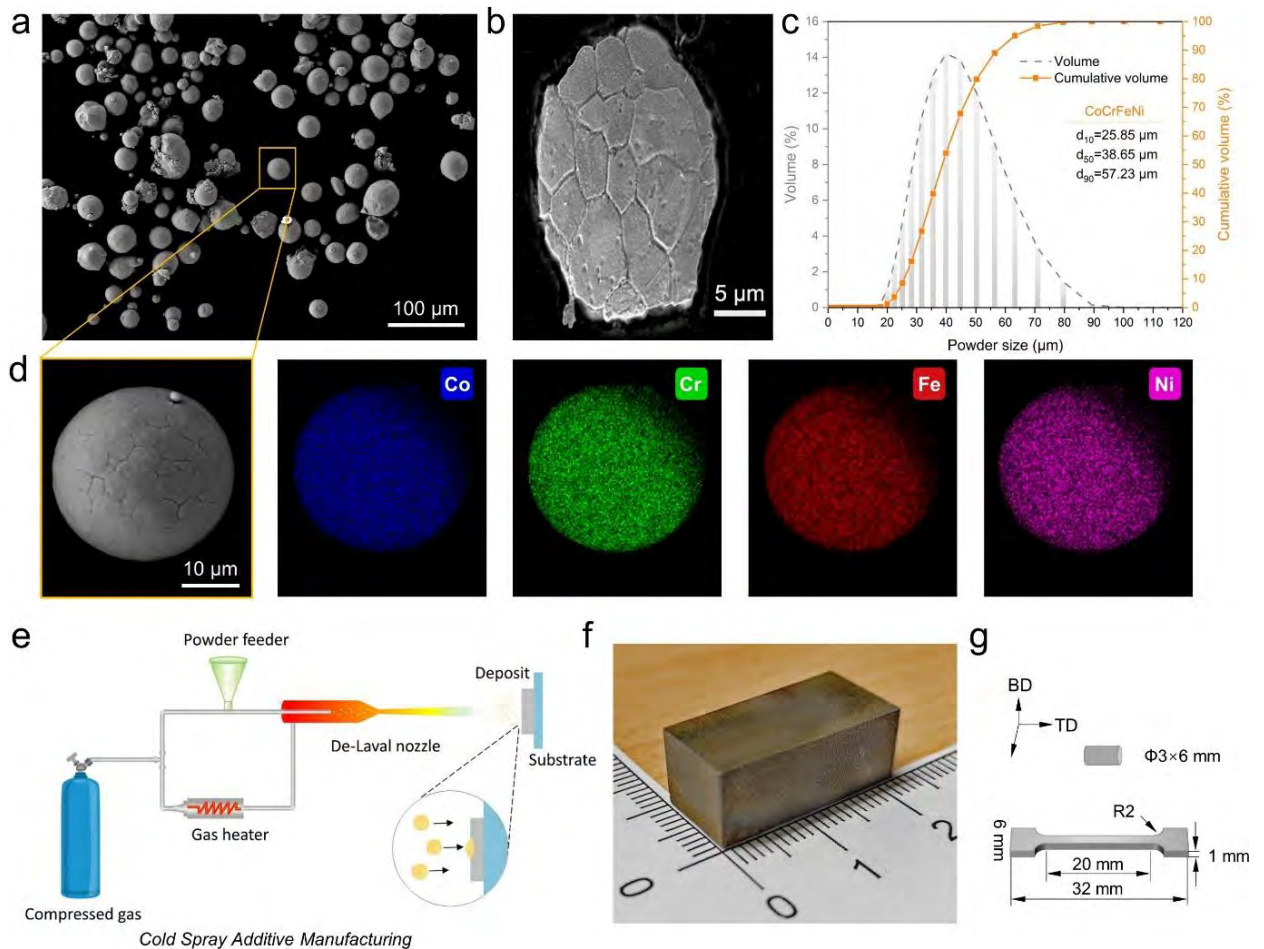


Fig. 4.1 Fabrication of CoCrFeNi HEA deposits via cold spray additive manufacturing process.

(a) Surface morphology of the gas-atomized powder, (b) Etched microstructure of individual powder with equiaxed grains, (c) Particle size distribution of the powder with D50 of 38.65 μm , (d) Uniform element distribution in the powder, (e) Schematic diagram of cold spray additive manufacturing, (f) Small bulk HEA (22 mm \times 10 mm \times 9 mm) machined from the deposit after cold spraying, (g) Schematic illustration of the extracted specimens from as-sprayed deposit for tension and compression tests. BD: Building direction, TD: Transverse direction.

The CoCrFeNi HEA deposit was manufactured using a commercial cold spray system (PCS-1000, Plasma Giken, Japan), as schematically shown in **Fig. 4.1e**. Compressed nitrogen was used as propelling gas, and the inlet pressure and temperature were kept at 5.0 MPa and 900 °C, respectively. The standoff distance from the exit of the nozzle to the Cu substrate surface remained 40 mm during the deposition. The nozzle moving trajectory followed a reciprocating zigzag strategy, and the space between two neighboring tracks was 1.0 mm. The deposits were subsequently removed from the Cu substrate and processed into cylinders and dog-bone-shaped specimens (see **Fig. 4.1f** and **g**) using a wire-cutting electrical discharge machine (EDM, V400G, Excetek V400G, China) for subsequent mechanical tests. To study the effect of annealing on the microstructure evolution and tensile/compressive properties of the as-sprayed deposits, the deposits were post-spray annealed in a Muffle furnace at 500 °C, 700 °C, 1000 °C (denoted by HT500, HT700, and HT1000 respectively) for two hours dwell time followed by furnace cooling to room temperature.

4.1.2 *Microstructure Characterization*

The cross-sectional samples were mechanically ground and polished following metallurgical procedures for microstructure analysis. To observe the microstructure evolution between feedstock powder and cold-sprayed deposits, the polished samples were electrochemically etched in an acid solution (69% wt. nitric acid and 31% wt. water) and then characterized by SEM. The density of the deposits was evaluated from optical microscopy (Leica DM LM, Germany) images using the image analysis method based on ASTM E2109-01 standard. The result was averaged from twelve different deposit regions to ensure data reliability. The phase structure of the deposits before and after annealing treatment were analyzed by X-ray diffraction (XRD, Bruker D8, Germany) equipped with Cu-K α radiation ($\lambda = 0.1542$ nm) from a range of 2θ values between 30° and 100° (40 kV, 40 mA) at a

scanning rate of 1.2 degree /min. To acquire grain size and grain crystallographic orientation information, the deposits (i.e., as-sprayed and HT1000) were further characterized by electron backscatter diffraction (EBSD). The EBSD data was achieved using a Symmetry detector (Oxford Instruments, UK). The step size for the EBSD test was set as 0.2 μm (for the as-sprayed deposit) and 0.3 μm (for the HT1000 deposit), respectively. The data was post-processed using the MTEX toolbox.

4.1.3 Mechanical Properties Measurement

The microhardness of the as-sprayed and post-spray annealed CoCrFeNi HEA deposits was measured using a Vickers hardness tester (ZHV30-M, ZwickRoell, UK) with an applied load of 500 g for 10s at ambient temperature. For comparison, the microhardness of the feedstock powder was also evaluated with a different hardness tester (MVK-H1, Mitutoyo, Japan) under a lower load of 50 g for 10s due to the limited size of the powder. To achieve data reliability, 10 indentations were conducted at randomized positions on the polished cross-sectional surface (for deposits) or different particles (for powder), and the result was averaged from all 10 indentations. The morphology of the indentations was characterized by optical microscopy. The compressive properties of both the as-sprayed and the annealed samples were evaluated using a universal mechanical testing machine (Instron 3366, UK) at a displacement rate of 1 mm/min. The specimens applied for compression testing were cylindrical in shape with a geometry of $\Phi 3 \text{ mm} \times 6 \text{ mm}$, and they were extracted from the as-sprayed deposits using EDM. The tensile properties of the samples were also evaluated using the same mechanical testing machine at a displacement rate of 1 mm/min. For uniaxial tensile tests, the dog-bone-shaped tensile specimens with a gauge dimension of 20 mm (length) \times 2 mm (width) \times 1 mm (thickness) were cut along the transverse direction and measured until a complete fracture. The fracture morphology of tensile specimens was characterized

by SEM to analyze the failure mechanism. For both tensile and compression tests, at least three specimens under each condition were evaluated to achieve data reliability, and the results were averaged.

4.2 Microstructure Evolution

Fig. 4.2 shows the cross-sectional microstructure of the cold-sprayed CoCrFeNi HEA deposits before and after annealing. Unsurprisingly, micropores and unbonded interfaces were visible in the as-sprayed deposit (**Fig. 4.2a**), which

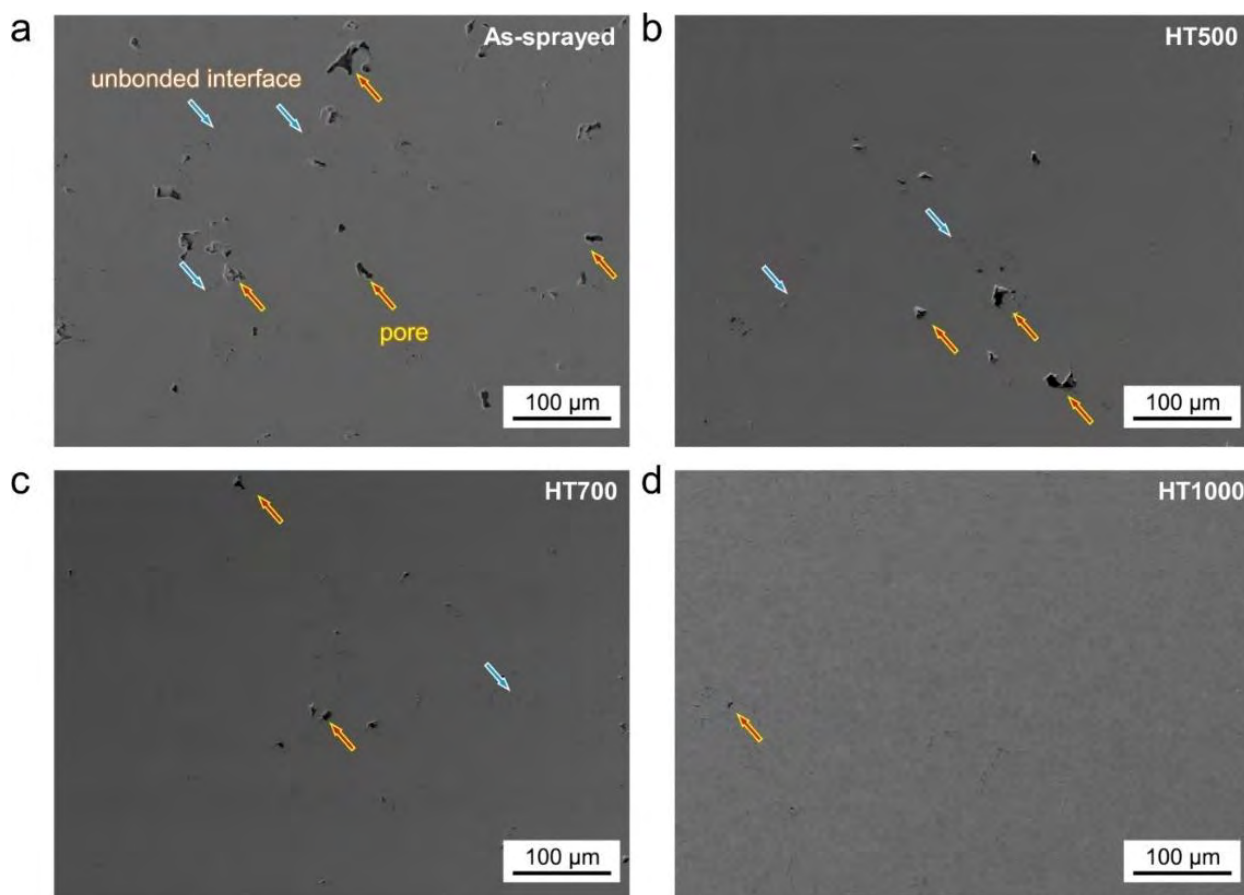


Fig. 4.2 Cross-sectional microstructure of the cold-sprayed CoCrFeNi HEA deposits under different annealing temperatures: (a) As-sprayed, (b) 500 °C, (c) 700 °C and (d) 1000 °C. The deposits exhibited gradually decreased micropores and interparticle boundaries with the increased temperatures.

indicates the insufficient plastic deformation of the feedstock powder during deposition despite the use of high processing parameters. Such a phenomenon was also reported during the deposition of other HEA powders due to the high deformation resistance of HEAs [203,225]. These microstructural defects were believed to become the sources of cracks and serve as a pathway for crack propagation when the deposits were under tension [263]. The relative density of the as-sprayed deposit is measured to be 97.57 ± 0.29 % based on the image analysis method (see Fig. 4.3). After annealing treatment, the deposit shows fewer voids and interparticle interfaces with the increase in annealing temperatures due to the improved interparticle diffusion and metallurgical bonding (Fig. 4.2b-d). The density of the deposit climbed to 98.14 ± 0.52 % (HT500), 98.44 ± 0.39 % (HT700), and 98.98 ± 0.43 % (HT1000) respectively, which was in accordance with the microstructure observations.

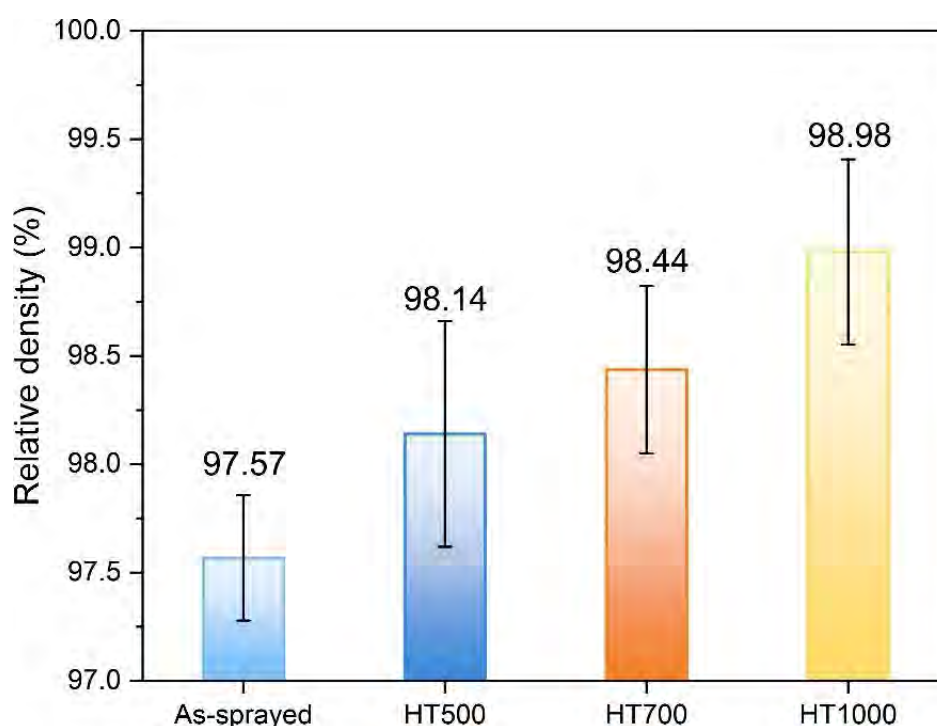


Fig. 4.3 Relative density of the cold-sprayed CoCrFeNi HEA deposits under different annealing temperatures.

Fig. 4.4 shows the XRD patterns of the CoCrFeNi HEA powder and the cold-

sprayed deposits in the as-fabricated and annealed states. The as-sprayed CoCrFeNi HEA deposit exhibited a single face centered cubic (FCC) solid solution structure as the original feedstock powder, which can be attributed to the solid-state deposition characteristics of cold spray. The annealed deposits also display FCC structures together with some weak peaks at around 56° , which can be identified as chromium oxides. As the annealing process was performed in the air atmosphere, the deposits were subjected to oxygen during the annealing process, particularly at higher temperatures. The oxide inclusion in the deposits may lead to the degradation of mechanical properties [101,264].

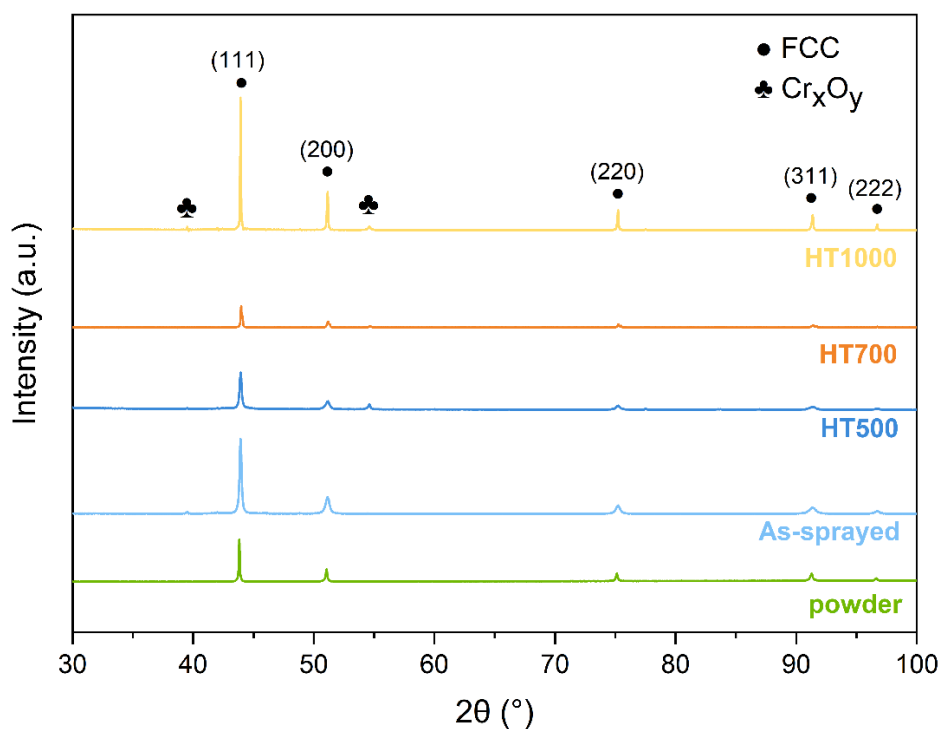


Fig. 4.4 X-ray diffraction (XRD) analysis of the feedstock powder and the cold-sprayed CoCrFeNi HEA deposits in the as-fabricated and annealed states.

To characterize the microstructure evolution of the deposits in as-sprayed and annealed states, the deposits were electrochemically etched, as shown in **Fig. 4.5**. After etching, the interparticle boundaries and grain boundaries of the deposits appeared, and it can be observed that the originally spherical CoCrFeNi HEA

powder was deformed and flattened after impact, as shown in **Fig. 4.5a** and **e**. The grains near interfacial regions were severely elongated, and ultra-fine grains were formed at the interparticle interfaces due to the dynamic recrystallization, while the grains in the particle interior had the original size. This is the typical bi-modal grain structure in the deformed particles in cold spray, and such heterogeneous microstructure can be attributed to the existence of temperature and strain gradients during the high-velocity impact process. For the HT500 deposit (**Fig. 4.5b** and **f**), the microstructural defects remained visible, and the bi-modal grain structure was retained in the deformed particle as the as-sprayed deposit, implying the HT500 deposit may only experience recovery at the current annealing temperature. This also corresponds to the previous report that remarkable recrystallization occurred in the highly deformed CoCrFeNi HEAs when the temperature was above 600 °C [265,266]. As the temperature increased to 700 °C, the interparticle boundaries were less visible due to the high-temperature diffusion at particle-particle interfaces (**Fig. 4.5c** and **g**), which led to partial defect annihilation and the resultant increase in density (see **Fig. 4.3**). The elongated grains near interfacial regions were substituted by new near-equiaxed grains, which indicated that the deposit partially recrystallized. The HT1000 deposit exhibited a rather different microstructure, as shown in **Fig. 4.5d** and **h**. The number of pores was significantly decreased, and the interparticle boundaries became indistinguishable. Moreover, a significant increase in grain size can be observed, suggesting that the HT1000 deposit had fully recrystallized and experienced grain growth.

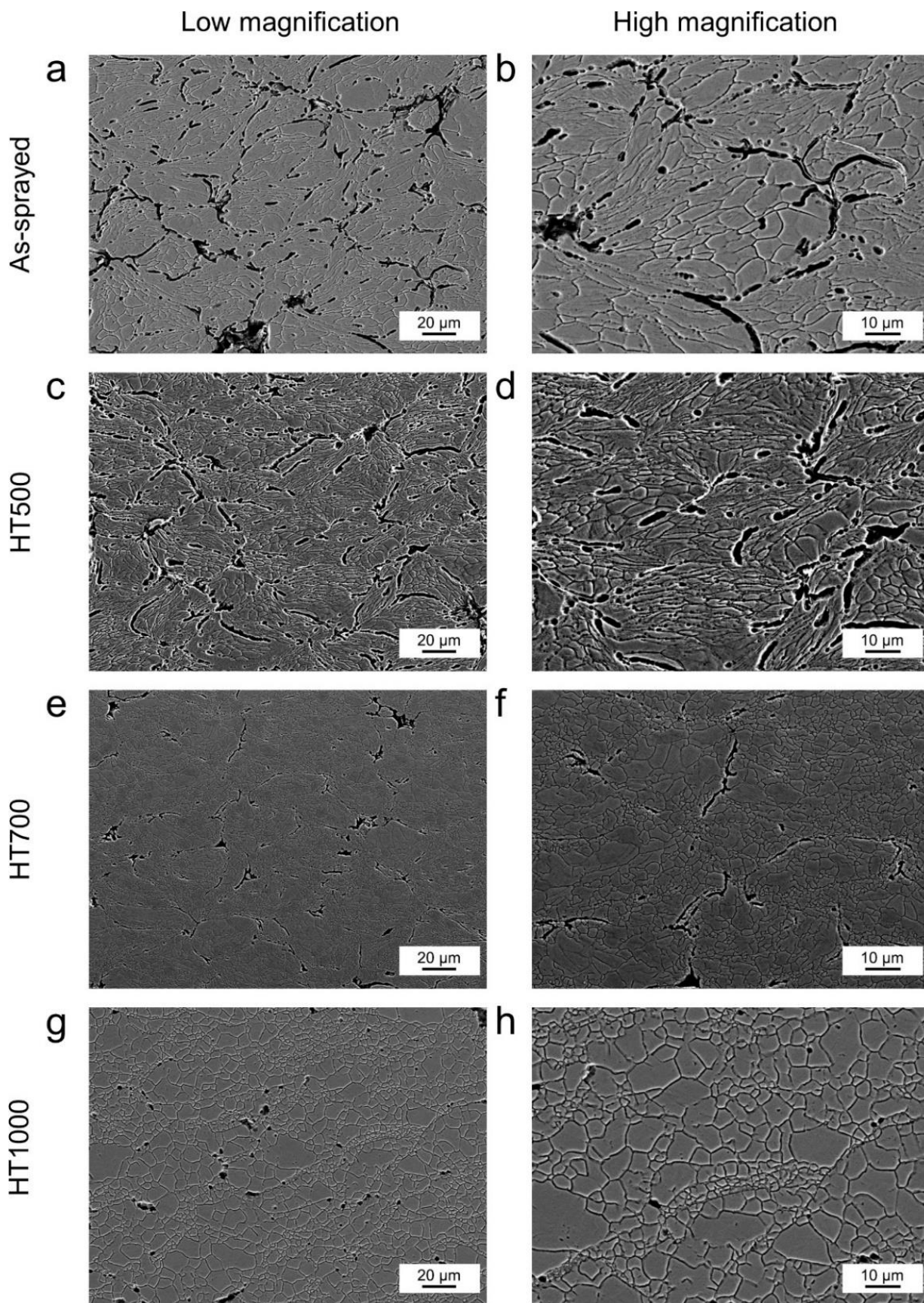


Fig. 4.5 Etched microstructure of the cold-sprayed CoCrFeNi HEA deposits under different

annealing temperatures: (a, e) As-sprayed, (b, f) 500 °C, (c, g) 700 °C, and (d, h) 1000 °C. The highly deformed particles experienced remarkable recrystallization and grain growth at 1000 °C, as evidenced by the increased grain size.

To further characterize the grain structure of the deposits in as-sprayed and fully recrystallized states, EBSD analysis was carried out on the cross-sectional surface of both deposits, as shown in **Fig. 4.6** and **Fig. 4.7** respectively. The inverse pole figure (IPF) of the as-sprayed deposit (see **Fig. 4.6a**) exhibited some unindexed zones due to the severe plastic deformation induced significant grain refinement and residual stress concentration, particularly at interfacial regions. The wide distribution of misorientation angles within the particles can be observed from the kernel average misorientation (KAM) map (see **Fig. 4.6b**), suggesting the different strain levels at each position. The high misorientation angles are associated with the high density of lattice defects, such as dislocation and stacking fault. The high frequency of low-angle grain boundary (LAGB, within the range of 2° and 10°), as shown in **Fig. 4.6d**, was also strong evidence of lattice defects. For the HT1000 deposit, a fully recrystallized grain structure containing strain-free grains with annealing twins inside was formed (see **Fig. 4.7a-b**). The annealing twins can also be demonstrated by the peak of misorientation angle at 60° (**Fig. 4.7d**), which was the feature of $\Sigma 3$ twin boundaries. The growth of annealing twins during recrystallization was associated with the low stacking fault energy (SFE) of CoCrFeNi (~ 32.5 mJ/m² [267]). Compared with the average grain size of the as-sprayed deposit (0.78 μm , see **Fig. 4.6c**), the grains experienced significant growth with an average size of 3.55 μm after annealing at 1000 °C (see **Fig. 4.7c**). The evolution of microstructure is expected to cause a significant difference in the mechanical behavior of the deposits.

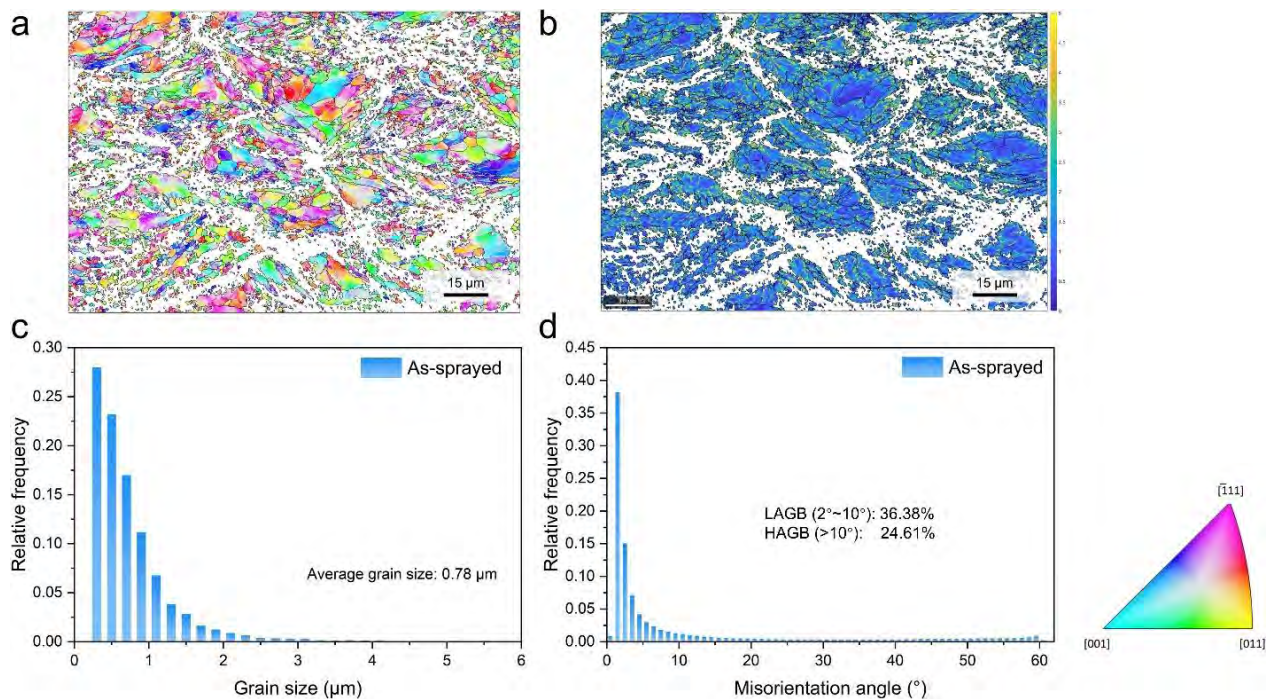


Fig. 4.6 EBSD characterization of the as-sprayed CoCrFeNi HEA deposit. (a) Inverse pole figure (IPF) map, (b) Kernel average misorientation (KAM) map, (c) Grain size distribution, and (d) Misorientation angle distribution.

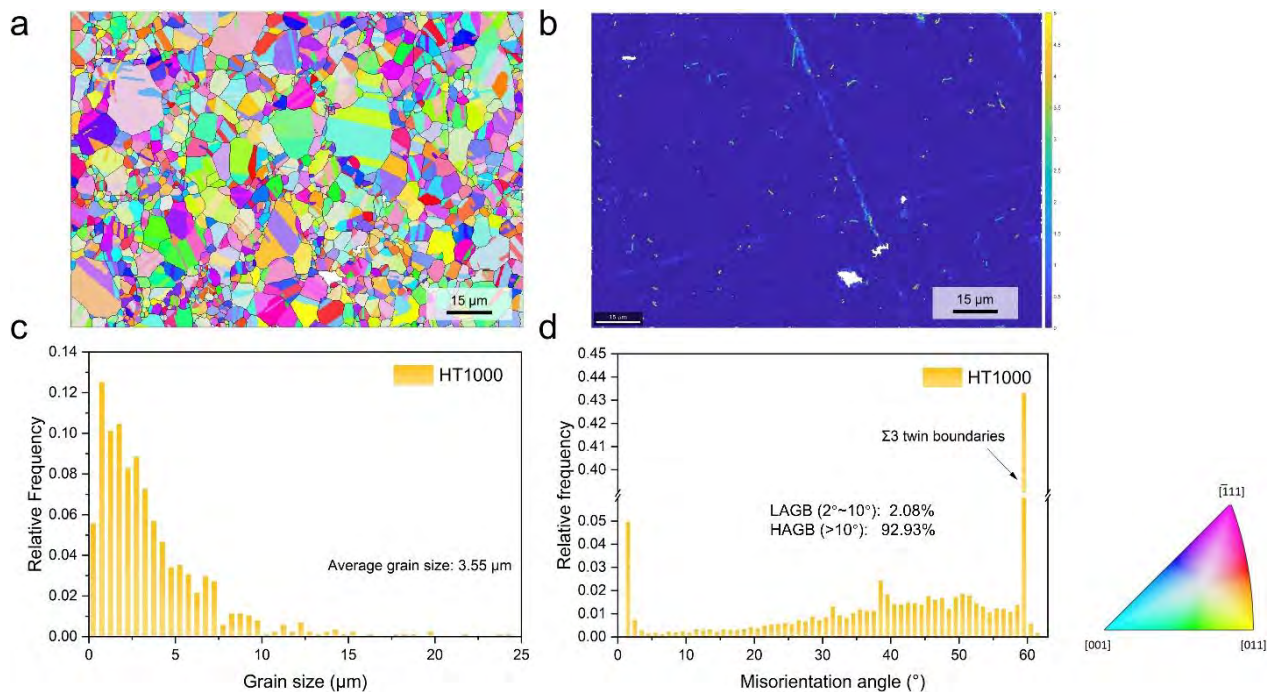


Fig. 4.7 EBSD characterization of the cold-sprayed CoCrFeNi HEA deposit annealed at 1000 °C (HT1000). (a) Inverse pole figure (IPF) map, (b) Kernel average misorientation (KAM) map, (c) Grain size distribution, and (d) Misorientation angle distribution.

4.3 Microhardness, Compressive and Tensile properties

Fig. 4.8 shows the Vickers hardness test results of the CoCrFeNi HEA feedstock powder and cold-sprayed deposits in both as-sprayed and annealed states. The as-sprayed deposit exhibited the highest microhardness of $430.7 \pm 21.10 \text{ HV}_{0.5}$ among all the deposits, which was in deep contrast with the feedstock powder (**Fig. 4.8a**) and its counterparts manufactured by other prevailing manufacturing routes (**Fig. 4.8d**). This is the result of significant work hardening induced by severe plastic deformation in cold spray. After annealing, the deposits show gradually downward microhardness with the increase in temperatures. It is notable that the microhardness of the HT500 deposit ($425.1 \pm 14.48 \text{ HV}_{0.5}$) is only a little lower than that of the as-sprayed one, as shown in **Fig. 4.8b**. Combined with the fact that the highly similar microstructure was retained in the HT500 deposit as the as-sprayed one (**Fig. 4.5b** and **f**), it is reasonable to infer that the HT500 deposit only experienced recovery. As the annealing temperature further increased to $700 \text{ }^\circ\text{C}$, the microhardness dramatically decreased to $273.4 \pm 11.71 \text{ HV}_{0.5}$. The deposit experienced partial recrystallization, and the dislocations and residual stress caused by working hardening were significantly reduced. For the fully recrystallized HT1000 deposit, the microhardness returned to the same level as the feedstock powder, implying ductility recovery. This can also be proved by the corresponding morphology of indentations, as shown in **Fig. 4.8c**. The localized deformation pile-up of the material around the indentations was observed in the as-sprayed, HT500, and HT700 deposits. However, this was invisible from the indentations on the feedstock powder and the HT1000 deposit, where the indentations remained in perfect diamond shapes without apparent pile-up behavior.

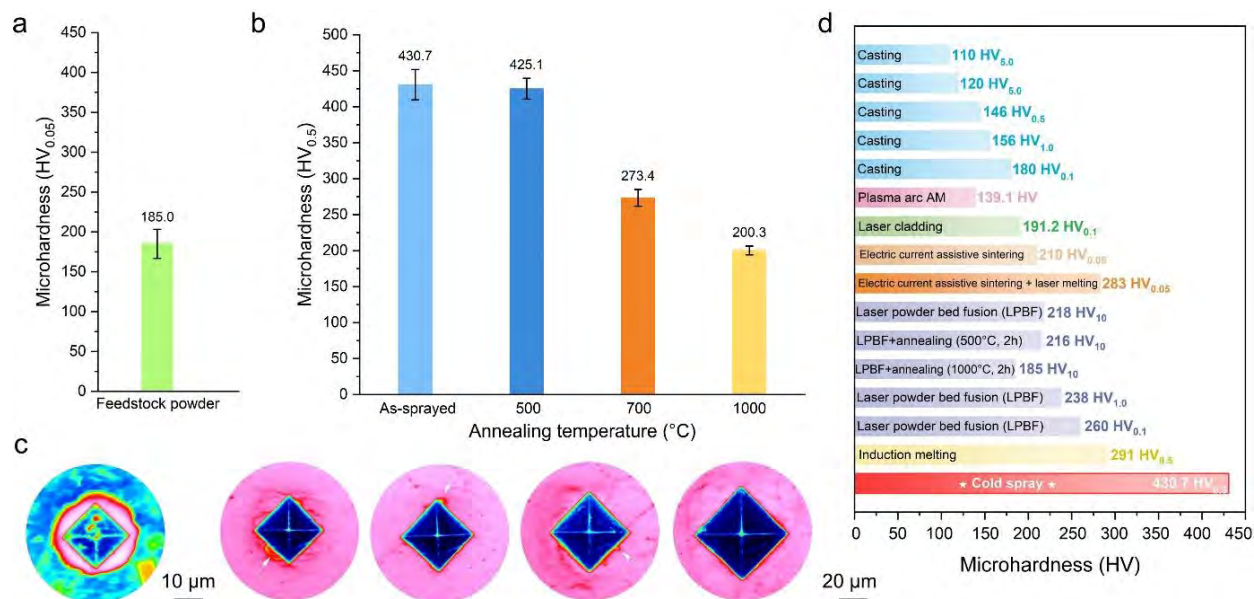


Fig. 4.8 Vickers hardness test results of the CoCrFeNi HEA feedstock powder and cold-sprayed deposits before and after annealing. (a) Feedstock powder and (b) Cold-sprayed deposits microhardness, (c) Corresponding morphology of indentations, and (d) A comparison with their counterparts fabricated through other prevailing manufacturing routes [196,268–277]. Note that the images of indents were displayed in the rainbow color scheme.

Fig. 4.9 shows the quasi-static uniaxial compressive properties of the cold-sprayed CoCrFeNi HEA specimens in as-sprayed and annealed conditions. The as-sprayed specimen exhibited linear elastic behavior followed by plastic flow and a sudden drop, as evidenced by the representative engineering stress-strain curve in **Fig. 4.9a**. The maximum compressive strength (σ_{\max}) and the fracture strain (ϵ_f) were 1144.27 ± 16.40 MPa and $29.38 \pm 1.24\%$, respectively. The HT500 deposit exhibited similar compressive behavior to the as-sprayed deposit with only 2.05 % higher σ_{\max} and a 15.93 % increase in ϵ_f . This is because stress relief annealing only reduced the residual stresses within the highly deformed deposit, and the microstructure and mechanical properties were not significantly altered. The deposits in both conditions show significantly higher yield strength (~ 900 MPa) than that of their counterparts manufactured by various processing routes, as shown in **Fig. 4.9c**. After annealing at higher temperatures, the deposits (i.e., HT700 and HT1000) presented a steady

increase of stress after elastic deformation and can be 50% height reduction without fracture (see Fig. 4.9a), exhibiting excellent compressive ductility of FCC materials. Compared with the HT1000 deposit, the deposit annealed at 700 °C shows 14.84 % higher compressive strength at 50% engineering strain (see Fig. 4.9a and b). This could be attributed to the smaller grain size of the HT700 deposit than that of the HT1000 deposit (see Fig. 4.5g and h), leading to a more significant grain boundary strengthening effect. Although the yield strength of the deposits annealed at elevated temperatures (i.e., HT700 and HT1000) dramatically decreased compared with that of the as-sprayed and the HT500 deposits, it is still much higher than that of their counterparts (see Fig. 4.9c). This shows the superiority of cold spray to manufacture high-strength materials. Besides, the compressive ductility was also recovered by the high-temperature annealing process, achieving a good combination of compressive strength and ductility. The strengthening and toughening mechanisms will be discussed in the forthcoming section.

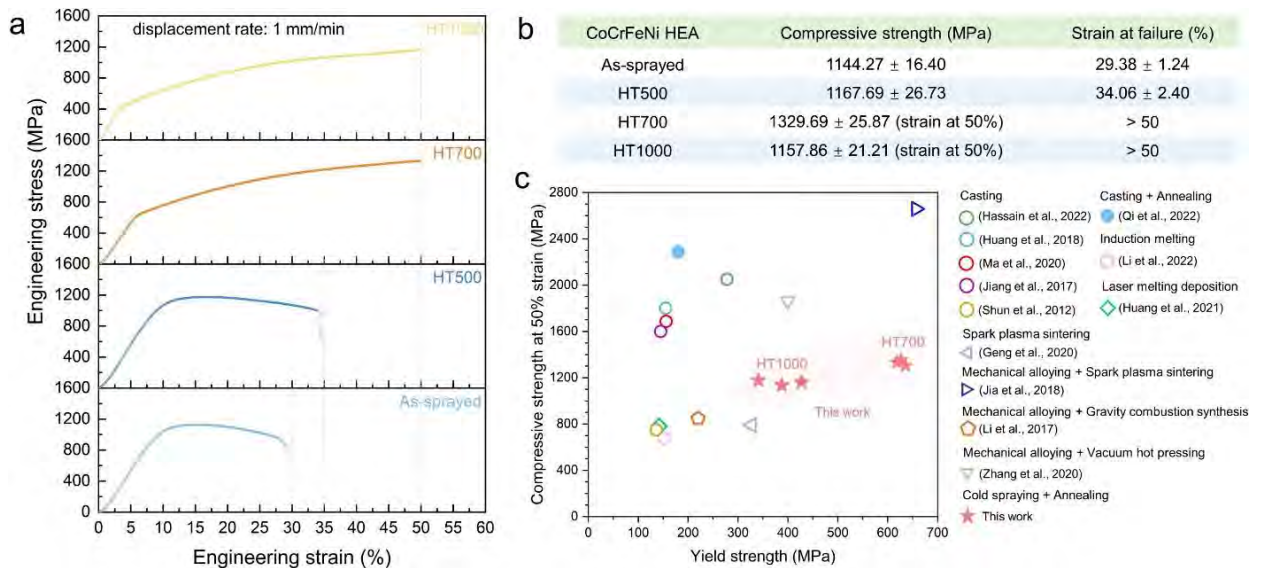


Fig. 4.9 Compressive properties of the cold-sprayed CoCrFeNi HEA deposits before and after annealing. (a) Representative engineering stress-strain curves, (b) Compressive strength and strain at failure, (c) Compressive strength at 50% strain versus yield strength of CoCrFeNi HEA parts manufactured by different techniques [271,278–288]. The yield strength of the deposits is determined by the 0.2% strain offset method.

Fig. 4.10 shows the tensile properties of the cold-sprayed CoCrFeNi HEA specimens before and after annealing. As depicted in the representative engineering stress-strain curves (see **Fig. 4.10a**), both the as-sprayed and the HT500 tensile samples fractured within the linear elastic regime and exhibited no macroscopical ductility. The cold-sprayed deposits generally exhibit a brittle feature due to imperfect particle bonding, leading to the premature failure initiated from particle-particle interfaces. The fracture strength of the HT500 deposit (410.15 ± 26.12 MPa) was higher than that of the as-sprayed one (372.49 ± 36.23 MPa), which could be attributed to the improved interparticle bonding and the released stress. When the deposit was subjected to a higher temperature at 700 °C, the samples performed similarly to the HT500 ones, but with 20.66% higher ultimate tensile strength (UTS) and improved elongation (EL) to $0.28 \pm 0.09\%$ (see **Fig. 4.10b**). This can be attributed to the interfacial diffusion induced by high temperature, leading to stronger interparticle metallurgical bonding and the decreased density of defects. With regards to the HT1000 deposit, the obvious plastic flow of the sample under tensile load can be observed, suggesting the partial recovery of ductility. The EL was improved to $2.48 \pm 0.29\%$ but at the expense of a reduction in UTS compared with the HT700 deposit. Although the HT1000 deposit shows the best recovery of tensile ductility among all the deposits, its EL is much lower than that of the as-cast bulk material and counterparts prepared by additive manufacturing routes (see **Table. 4.1**). The low tensile ductility was also in strong contrast with the excellent compressive ductility of the recrystallized samples, implying that the deposit may have a difference in sensitivity to interior defects under tensile and compressive loads.

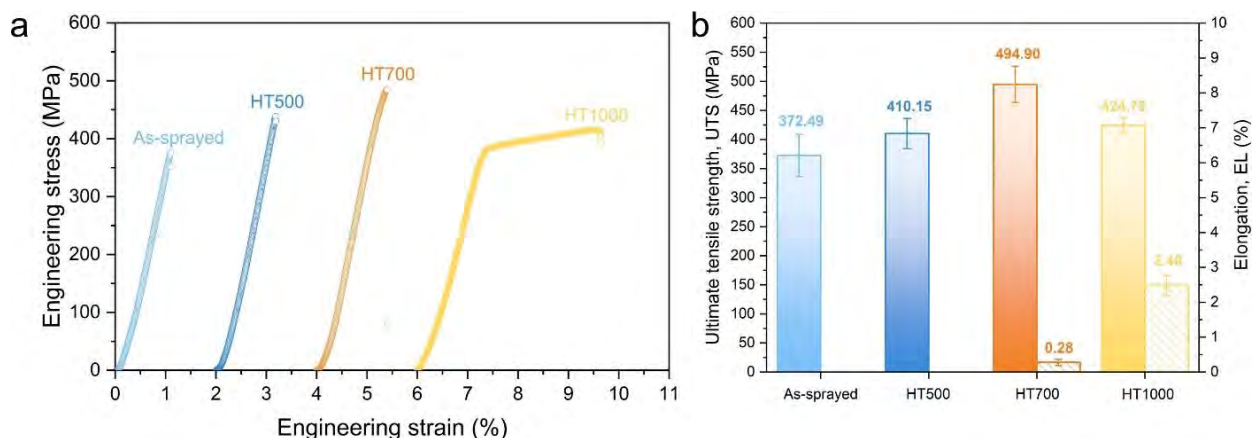


Fig. 4.10 Tensile properties of the cold-sprayed CoCrFeNi HEA deposits before and after annealing. (a) Representative engineering stress-strain curves, (b) The ultimate tensile strength (UTS) and elongation (EL).

Table 4.1 Summarization of room-temperature tensile properties of CoCrFeNi HEA fabricated by both traditional and additive manufacturing processes.

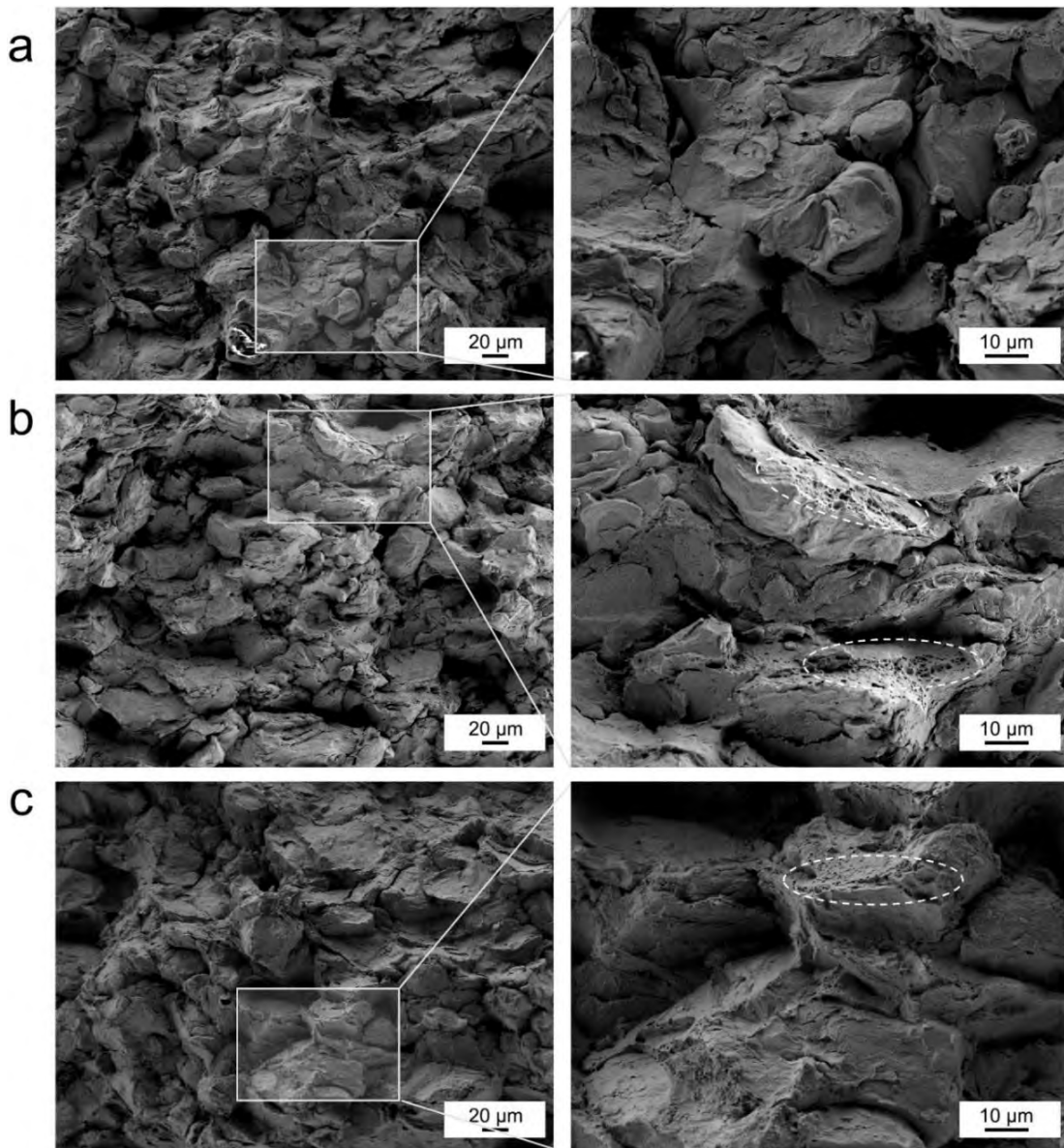
Starting material	Manufacturing routes	YS / MPa	UTS / MPa	EL / %	Ref.
pure metals	casting	140	488	83	[289]
pure metals	casting + homogenization (1100 °C/3h) + cold rolling + annealing (900 °C/1h) + water quenching	325	628	63	[290]
pure metals	casting + homogenization (1100 °C/3h) + cold rolling + annealing (900 °C/1h) + water quenching + friction stir welding	476	627	42	[290]
pure metals	casting + hot rolling (1050 °C) + annealing (1300 °C/40 min) + water quenching + cold rolling + annealing (1000 °C/2 min) + water quenching	285.3 ± 3.2	659.9 ± 3.2	73.1 ± 1.0	[291]

pure metals	casting + cold rolling + homogenization (1100 °C/6h) + cold rolling + homogenization (900 °C/1h) + laser welding	260	622	46.7	[292]
pure metal powder	mechanical alloying + die pressing (450 °C) + hot extrusion (1000 °C) + annealing (1150 °C/2h)	552 ± 1	856 ± 3	21.8 ± 2.4	[293]
pure metal powder	mechanical alloying + die pressing (450 °C) + hot extrusion (1000 °C) + liquid nitrogen (10 min) + forging + annealing (800 °C/15 min)	728 ± 13	1015 ± 2	24.7 ± 2.5	[293]
gas-atomized powder	laser powder bed fusion	600	745	32	[277]
gas-atomized powder	laser melting deposition	138	634	46	[286]
gas-atomized powder	powder hot extrusion	359	712.5	56	[294]
gas-atomized powder	high pressure torsion	1840 ± 30	2060 ± 20	~ 10	[295]
gas-atomized powder	high pressure torsion + annealing (700 °C/1h) + water quenching	990 ± 10	1060 ± 30	~ 45	[295]

YS: yield strength, UTS: ultimate tensile strength, EL: elongation

To uncover the failure mechanism of the cold-sprayed CoCrFeNi HEA deposits before and after annealing, the representative fracture surface of the tensile samples was analyzed. For the as-sprayed and the HT500 deposits, the stacking feature of the particles with visible boundaries can be recognized (see Fig. 4.11a-b). The less-bonded interfaces provided a pathway for the rapid crack propagation under tension and led to the fracture along the interparticle interfaces (inter-particle decohesion). Few to no dimples were observed from the fracture surface, implying the brittle fracture characteristic. This also corresponded to the mechanical behavior from the representative engineering stress-strain curves (see Fig. 4.10a). For the HT700

deposit, the interfaces between particles became less visible due to the high-temperature diffusion (see Fig. 4.11c), indicating stronger metallurgical bonding at interparticle interfaces. However, only localized dimple-like features were observed, which was in line with the negligible ductility in Fig. 4.10b. The HT1000 deposit exhibited more widely distributed dimples with larger sizes than the others (see Fig. 4.11d), which suggested that the fracture mode transformed into the coexistence of brittle fracture and ductile fracture. This was also in good agreement with the obvious plastic flow behavior of the HT1000 deposit, which exhibited the highest EL among all the deposits.



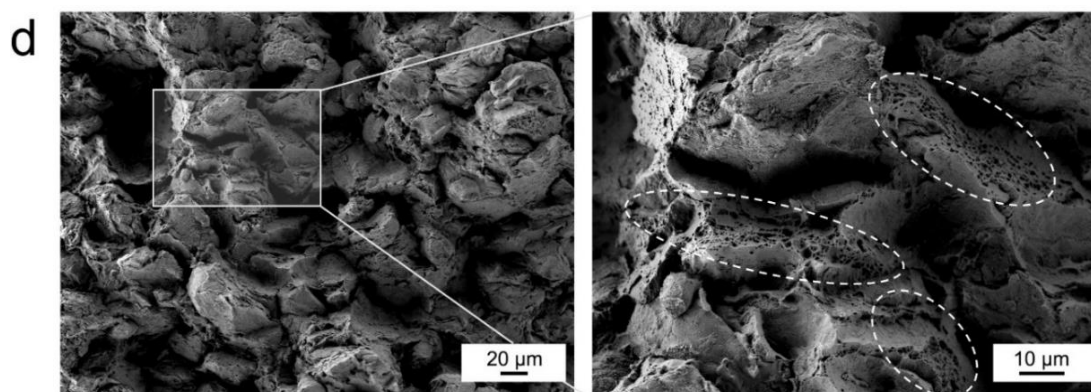


Fig. 4.11 Fractographic analysis of the fracture surface of the cold-sprayed CoCrFeNi HEA deposits under different annealing temperatures: (a) As-sprayed, (b) 500 °C, (c) 700 °C and (d) 1000 °C.

4.4 Strengthening and Toughening Mechanisms

The mechanical properties of materials are closely associated with their microstructure. In the cold spray process, the high-velocity impact of the originally spherical particle leads to significant strain, strain rate, and temperature gradients during particle deformation and the resultant heterostructure. To be specific, ultra-fine grains generally form near interfacial regions due to grain fragmentation and dynamic recrystallization, while elongated and flattened grains remain in the particle interior. The cross-scale grain structure from the interface to the particle inside (also known as bi-modal grain structure) remained in the deposit even after recrystallization annealing, as shown in [Fig. 4.5](#). It is reported that such heterostructure can lead to an excellent combination of strength and ductility [\[296,297\]](#). However, in the present work, the cold-sprayed CoCrFeNi HEA deposits exhibited excellent compressive but unsatisfied tensile properties. Given this, the compressive and tensile behaviors of the deposits before and after annealing will be further discussed in this section.

4.4.1 Origin of the High Strength in the Deposits

The strengthening mechanisms in polycrystalline materials mainly derive from solid-solution strengthening, grain boundary strengthening, dislocation strengthening, and precipitation strengthening. The yield strength can be given by a simple sum of the four individual contributions as follows:

$$\sigma_{0.2} = \sigma_0 + \Delta\sigma_s + \Delta\sigma_g + \Delta\sigma_d + \Delta\sigma_p \quad (\text{Eq. 4.1})$$

where σ_0 is the lattice friction strength (123 MPa for CoCrFeNi [298]), $\Delta\sigma_s$, $\Delta\sigma_g$, $\Delta\sigma_d$ and $\Delta\sigma_p$ are the contributions from solid-solution strengthening, grain boundary strengthening, dislocation strengthening, and precipitation strengthening respectively. For equiatomic CoCrFeNi HEA, the four principal elements have similar atomic radii, and therefore the solid solution strengthening effect is not that significant. Besides, the CoCrFeNi has a single-phase FCC structure, and there is no precipitation behavior before and after annealing based on the SEM image analysis. Therefore, the yield strength of the cold-sprayed CoCrFeNi HEA deposits can be simply expressed as follows (Herein, only the strengthening mechanism of the as-sprayed and the fully recrystallized (HT1000) deposits was analyzed),

$$\sigma_{0.2} = \sigma_0 + \Delta\sigma_d + \Delta\sigma_g \quad (\text{Eq. 4.2})$$

The contribution from dislocation strengthening ($\Delta\sigma_d$) can be approximated by the Taylor equation [299],

$$\Delta\sigma_d = M \times \alpha \times G \times b \times \rho^{1/2} \quad (\text{Eq. 4.3})$$

where M is the Taylor factor (3.06 for randomly textured FCC materials [300]), α is an empirical constant for polycrystalline FCC materials (0.2), G is the shear modulus (84.3 GPa [301]), b is the Burgers vector (0.2524 nm), ρ is the dislocation density, which can be roughly estimated based on the XRD results,

$$\rho = \frac{2\sqrt{3}\varepsilon}{Db} \quad (\text{Eq. 4.4})$$

where ε is the lattice micro-strain, D is the grain size, and b is the Burgers vector. The dislocation density of the as-sprayed deposit and the HT1000 deposit is $1.71 \times 10^{15} \text{ m}^{-2}$ and $1.16 \times 10^{14} \text{ m}^{-2}$, respectively. The calculated $\Delta\sigma_d$ were 523.78 MPa for the as-sprayed deposit and 136.42 MPa for the HT1000 deposit. The contribution of grain boundary strengthening ($\Delta\sigma_g$) can be estimated by the well-known Hall-Petch relationship:

$$\Delta\sigma_g = k \times d^{-1/2} \quad (\text{Eq. 4.5})$$

where k represents the grain boundary strengthening coefficient ($276 \text{ MPa} \cdot \mu\text{m}^{1/2}$ [298]), and d is the average grain size. The average grain size of the as-sprayed deposit and the HT1000 are $0.78 \mu\text{m}$ and $3.55 \mu\text{m}$, respectively (see Fig. 4.6c and Fig. 4.7c). Therefore, the calculated values of $\Delta\sigma_g$ were 312.51 MPa (for the as-sprayed deposit) and 146.49 MPa (for the HT1000 deposit), respectively. The theoretical yield strength of the cold-sprayed CoCrFeNi HEA deposits in the as-sprayed and fully recrystallized states was estimated to be 959.29 MPa and 405.91 MPa.

The cold-sprayed CoCrFeNi HEA deposits exhibited compressive yield strength ($901.83 \pm 61.14 \text{ MPa}$) close to the calculated theoretical value (959.29 MPa). Theoretically, it is reasonable that the yield strength obtained from the experiment was a little bit lower than the theoretical value due to the existence of microstructural defects. The high compressive yield strength of the as-sprayed deposit was the result of grain boundary strengthening and dislocation strengthening effects. For the HT1000 deposit, the high annealing temperature led to the dislocation annihilation in the highly deformed deposit, which weakened the dislocation strengthening effect. Besides, the increased grain size reduced the grain

boundary strengthening effect based on the Hall-Petch relationship, and therefore, the compressive yield strength decreased to 385.32 ± 43.15 MPa. It is notable that although the compressive yield strength decreased, it was still higher than their counterparts (see [Fig. 4.9c](#)). This can be attributed to the bi-modal heterostructure retained in the fully recrystallized deposit. Moreover, the widely distributed annealing twin boundaries can impede the motion of dislocations, which also contributed to the high strength of the deposit. The dislocation annihilation provided space for work hardening of the HT1000 deposit, which led to an excellent combination of strength and ductility.

When it comes to the tensile yield strength of the cold-sprayed CoCrFeNi HEA deposits, the vast discrepancy between the theoretical yield strength and the experimental yield strength obtained from the curve was found in the as-sprayed deposit but not in the HT1000 deposit. Technically, the so-called “experimental yield strength” is unattainable because the as-sprayed deposit fractured within the elastic deformation regime (see [Fig. 4.10a](#)). For convenience, the fracture strength of the as-sprayed deposit (372.49 ± 36.23 MPa) was taken as the tensile yield strength. The reason for the discrepancy is that the interior defects in the deposits, such as micro-pores and interparticle boundaries, are more sensitive to tensile loading, leading to poor tensile properties [302]. The defects in the deposit (see [Fig. 4.2a](#) and [Fig. 4.5e](#)) can promote crack propagation along the interparticle boundaries under tensile load, leading to premature failure. While for the HT1000 deposit, the tensile yield strength (395.29 ± 10.52 MPa) was close to the theoretical value (405.91 MPa) within the acceptable tolerances due to the residual defects in the deposit. The particle boundaries were the main sites for fracture propagation. The improved metallurgical bonding in these regions can increase the interparticle cohesion strength. Therefore, the tensile yield strength of the HT1000 deposit approached the theoretical value.

4.4.2 Tension-compression Asymmetry in the Deposits

Fig. 4.12 shows the yield strength of the cold-sprayed CoCrFeNi HEA deposits obtained from tensile and compression tests. It can be observed that the as-sprayed deposit had inferior strength in tension compared to compression, exhibiting remarkable tension-compression asymmetry like hard and brittle materials. Such tension-compression asymmetry hardly improved for the HT500 deposit due to the remaining pores and the lack of interparticle bonding. The reason for such asymmetry can be attributed to the fact that the deposit was high sensitivity to manufacturing defects under tension, leading to the failure within the elastic region. However, with the increase in annealing temperatures, the tension-compression asymmetry was gradually weakened, as evidenced by **Fig. 4.12**. The higher annealing temperatures helped to heal the interparticle boundaries and the part of

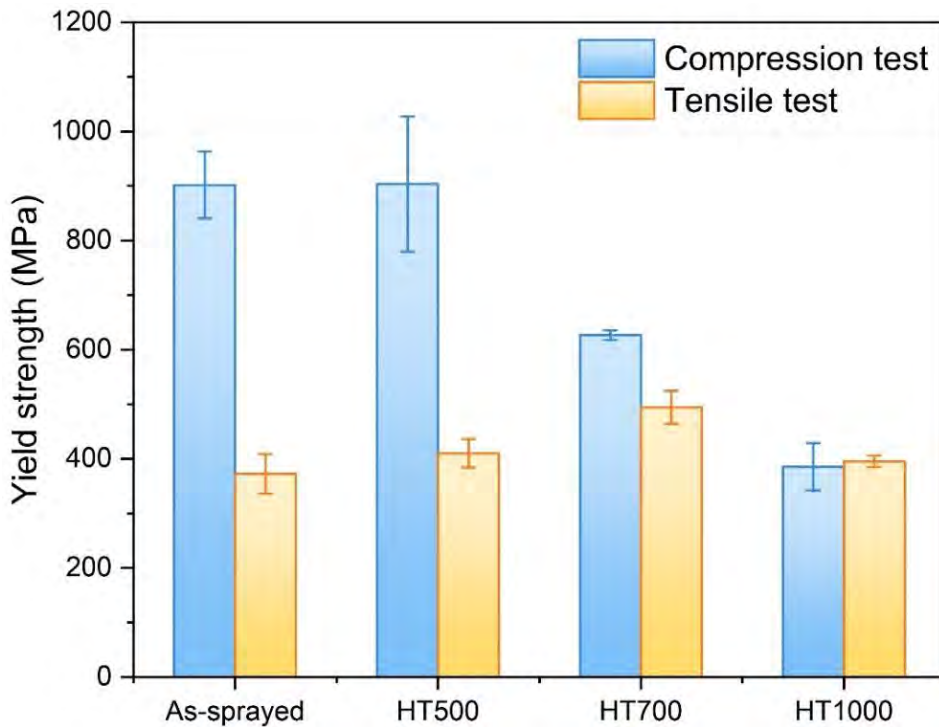


Fig. 4.12 The yield strength of the cold-sprayed CoCrFeNi deposits obtained from tensile and compression tests. Note that the as-sprayed and the HT500 deposits exhibited brittle failure without ductility under tension, and the strength at failure was taken as tensile yield strength.

micro-pores, leading to better particle bonding and increased cohesion strength. The deposit can transit to plastic flow after yielding rather than fracture within the elastic stage, which reduced the gap between the tensile yield strength and the theoretical value. This eventually led to the pretty close yield strength of the deposit under tension and compression.

The cold-sprayed CoCrFeNi HEA deposits show excellent compressive ductility after recrystallization annealing and can be 50% height reduction without fracture, which is in line with the previous report (see [Fig. 4.9c](#)). Compared with the as-sprayed deposit, the HT1000 deposit possessed the best recovery of tensile ductility ($2.48 \pm 0.29\%$). However, the tensile ductility of the deposit is significantly lower than that of their counterparts. Recrystallization annealing can promote interface diffusion and the resultant metallurgical bonding, but the pores in the deposit cannot be eliminated, as evidenced by the remaining $\sim 1\%$ of porosity. The optimization of post-spray annealing process parameters (e.g., annealing temperature, dwell time, and atmosphere) may further improve the tensile ductility of the deposit by increasing the particle cohesion strength through high-temperature diffusion. In addition, using higher cold spray processing parameters is expected to further reduce the unnecessary defects in the deposits by promoting the plastic deformation of particles and enhance the interparticle bonding by stronger mechanical interlocking and metallurgical consolidation. In brief, fewer interior defects and enhanced interparticle bonding are the keys to weakening the tension-compression asymmetry, and post-spray recrystallization annealing can be used as an effective strategy to approach the goal.

4.5 Summary

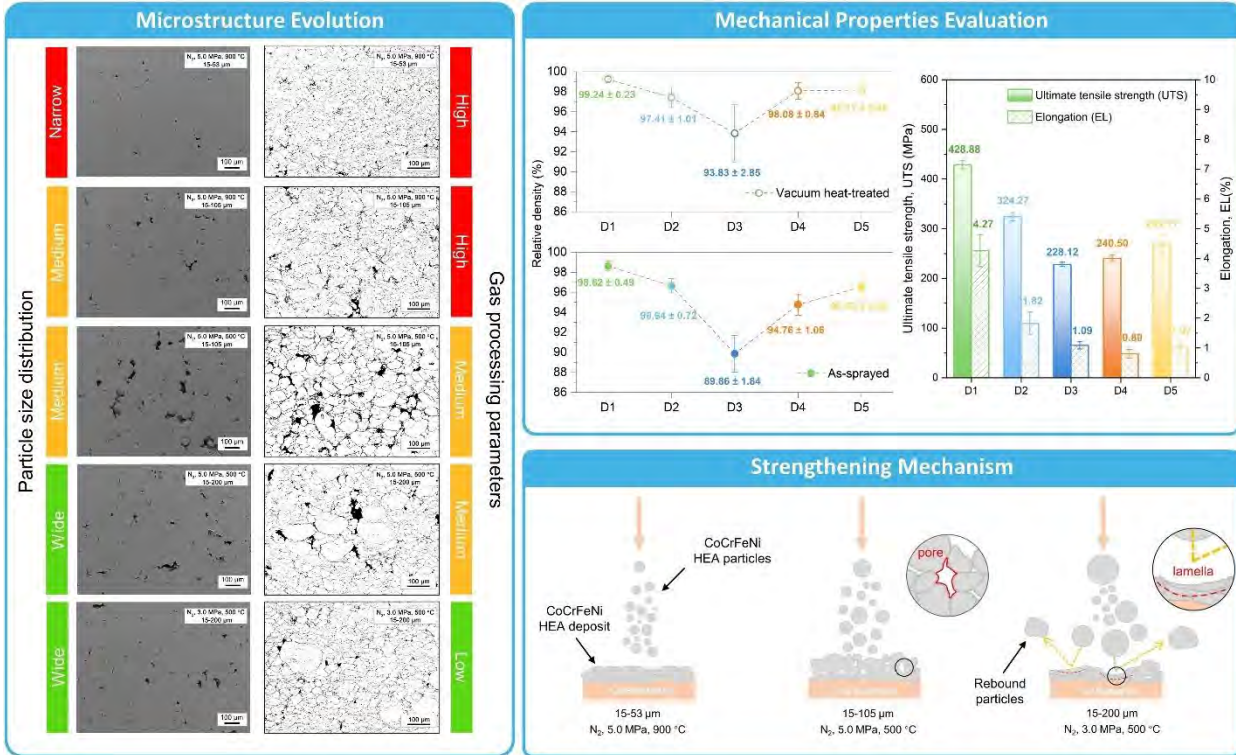
The equiatomic CoCrFeNi high-entropy alloy (HEA), serving as a basic system in the HEA family, was fabricated by cold spray additive manufacturing process, and

post-spray annealing treatment was carried out at various temperatures to intentionally adjust the microstructure and balance the strength and ductility. The as-sprayed deposit was composed of necessary heterostructure (i.e., bi-modal structure) and unnecessary interior defects (i.e., pores and interparticle boundaries). The deposit with such defects exhibited significantly different tensile and compressive performances due to the difference in sensitivity to interior defects under tensile and compressive loads. To be specific, the as-sprayed deposit exhibited high compressive yield strength due to the dislocation strengthening and grain boundary strengthening effects but fractured within the linear elastic regime in the tensile test. Recovery annealing had no remarkable influence on the microstructure and mechanical properties of the deposit. While recrystallization annealing led to enhanced interface diffusion and resultant metallurgical bonding, which can be demonstrated by the increased deposit density and indistinguishable particle boundaries. The fully recrystallized deposit possessed almost equal tensile and compressive yield strength and the best recovery of tensile ductility. The current study shows that recrystallization annealing is an effective post-treatment strategy to balance strength and ductility and weaken the tension-compression asymmetry of cold-sprayed deposits.

Chapter 5

Strengthening Cold Spray Additive Manufactured CoCrFeNi High-entropy Alloy by In-process Densification

In this chapter, the CoCrFeNi HEA deposits were fabricated using different combinations of particle size ranges and gas parameters. The microstructure evolution, deformation behavior, and mechanical properties of the deposits under different combinations were investigated. The results showed that a combination of a wide particle size range of the feedstock powder and low gas parameters could trigger in-process densification of the deposits, which is contrary to the common cognition that lower processing parameters lead to more manufacturing defects in the deposits. At such conditions, a proportion of the particles (particularly those with large sizes) fail to deposit and rebound after their impact instead. The rebound particles result in accumulative plastic deformation of the deposited particles and further reduction in porosity. With this novel strategy, the detrimental thermal effects encountered in cold spraying using high-temperature processing gas (such as oxidation, nitridation, and phase changes) can be effectively minimized. However, the strategy comes at the expense of the large-sized particles, implying low deposition efficiency. Moreover, the mismatch between the particle size ranges and the gas parameters will lead to the inclusion of less deformed large-sized particles, leading to the formation of large pores and deteriorated mechanical performance.



5.1 Material and Methodology

5.1.1 Feedstock Powder and Deposit Fabrication

Gas-atomized CoCrFeNi HEA powder (Vilory Advanced Materials Technology Ltd, China) with three different particle size ranges (i.e., 15–53 μm, 15–105 μm, and 15–200 μm, respectively) was used as feedstock. **Fig. 5.1** shows the surface morphology of the HEA powders characterized by scanning electron microscope (SEM, Carl Zeiss Ultra Plus, Germany). The majority of the feedstock powders exhibit spherical features. Some micro-satellite particles adhered to the surface of the powders typically with large sizes, which can be attributed to the different condensation rates during the gas atomization process. The size distribution of the powders was measured by a laser diffraction particle analyzer (Mastersizer 2000, Malvern Instruments, UK), as shown in **Fig. 5.1** b, d and f.

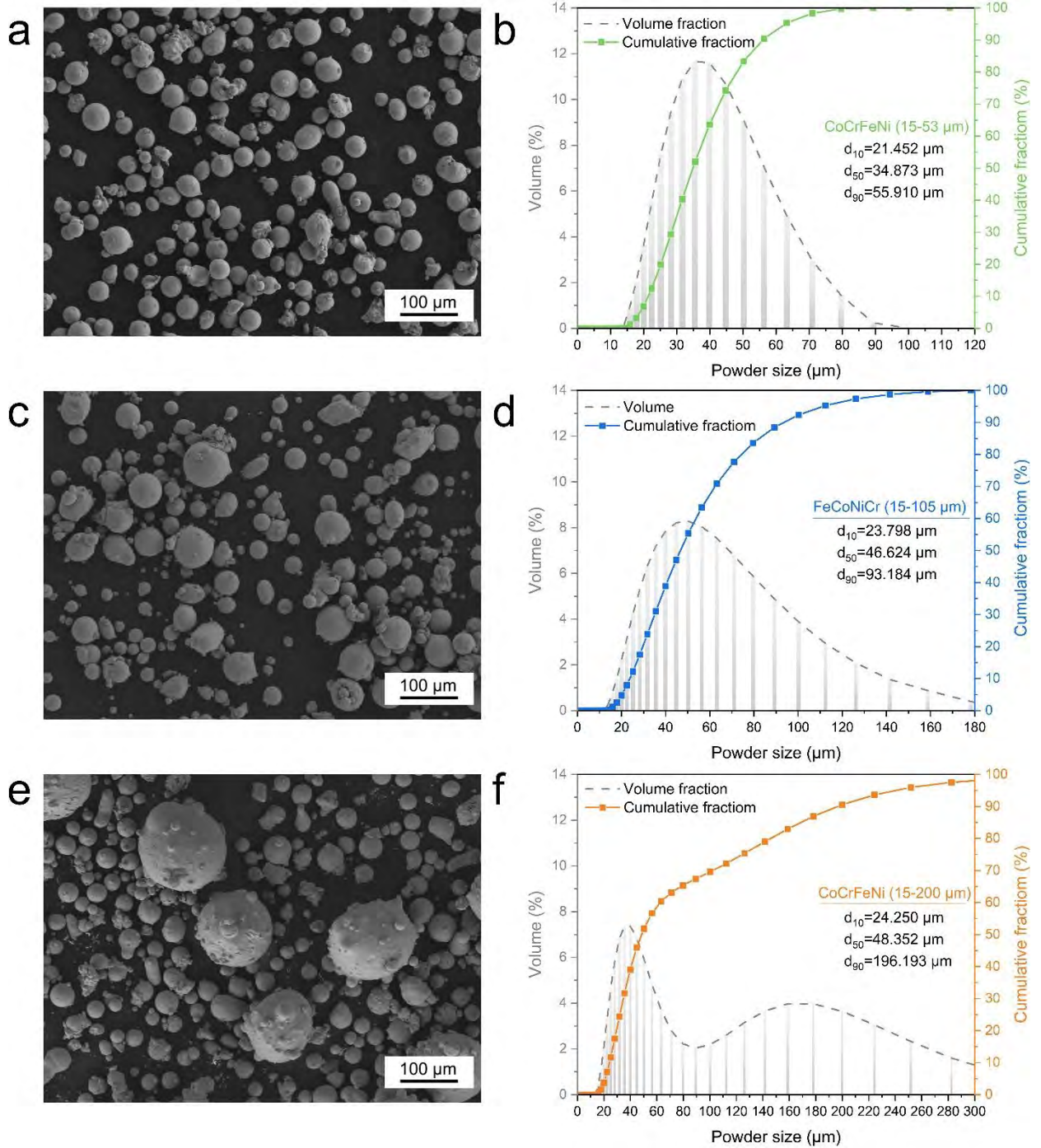


Fig. 5.1 Characterization of the gas-atomized CoCrFeNi HEA powders used for cold-sprayed deposits fabrication. (a, c, e) Particle surface morphology and (b, d, f) Particle size distribution.

A commercial high-pressure cold spray system (PCS-1000, Plasma Giken, Japan) was used for CoCrFeNi HEA deposits fabrication, and the particles were deposited onto a Cu plate with a thickness of 3.0 mm. The substrate surface was ground with

sandpaper prior to cold spraying to remove potential oxides and improve adhesion strength, followed by cleaning with anhydrous ethanol. The different combinations of particle size ranges and gas parameters used for the deposit fabrication are listed in Table. 5.1. The standoff distance from the exit of the nozzle to the Cu substrate surface remained 40 mm during the deposition. The nozzle moving trajectory followed a reciprocating zigzag strategy, and the space between two neighboring tracks was 1.0 mm. The produced deposits were subsequently removed from the substrate and processed into dog-bone-shaped specimens by a wire-cutting electrical discharge machine (EDM, V400G, Excetek V400G, China) for the following mechanical property evaluation. To heal the micro-pores and enhance interparticle metallurgical bonding, the specimens for tensile tests were post heat-treated in a vacuum sintering system at the temperature of 1000 °C for two hours dwell time, with a heating rate of 10°C/min, followed by furnace cooling to room temperature. The vacuum degree was kept at 1.0×10^{-3} Pa during the heat treatment process.

Table. 5.1 Cold spray processing parameters for the deposit fabrication

Set annotation	D1	D2	D3	D4	D5
Particle size range / μm	15-53	15-105	15-105	15-200	15-200
Propelling gas	N ₂				
Gas pressure /MPa	5.0	5.0	5.0	5.0	3.0
Gas temperature /°C	900	900	500	500	500
Relative particle impact velocity	High	High	Medium	Medium	Low

5.1.2 *Microstructure Characterization*

The cross-sectional samples were mechanically ground with silicon carbide grinding paper and polished with silica suspensions following metallurgical procedures for microstructure analysis. To reveal the interparticle boundary and

investigate the plastic deformation behavior of deposited particles, the polished samples were electrochemically etched in an acid solution (69% wt, nitric acid, and 31% wt. water) at a voltage of 10.0 V for 15 seconds. The cross-sectional morphology of the CoCrFeNi HEA deposits before and after etching was then characterized by SEM. The porosity of the deposits was measured using the ImageJ processing program (National Institute of Health, USA) based on the light microscope images. The result was averaged from ten different blocks to ensure the necessary data reliability.

5.1.3 Mechanical Properties Evaluation

The microhardness of the cold-sprayed CoCrFeNi HEA deposits was evaluated by a Vickers hardness tester (ZHV30-M, ZwickRoell, UK) with an applied load of 500g for 10s at room temperature. The morphology of the indentations was characterized by optical microscopy. To ensure data reliability, ten indentations were conducted at randomized positions on the polished cross-sectional surface, and the result was averaged. The tensile properties of the cold-sprayed CoCrFeNi deposits were evaluated using a universal mechanical testing machine (Instron 3366, UK) at a cross-head displacement rate of 1 mm/min. The specimens applied for uniaxial tensile tests were cut along the transverse direction using EDM into dog-bone shape with a gauge length of 20 mm, a width of 2 mm, and a thickness of 1 mm and measured until a complete fracture. The ultimate tensile strength (UTS) and elongation at break (EL) were calculated. To analyze the failure mechanisms, the morphology of the fracture surfaces was then characterized by SEM.

5.2 Microstructure Evolution

Fig. 5.2 shows the microstructure of the cold-sprayed CoCrFeNi HEA deposits fabricated under different combinations of particle size ranges and gas parameters

in the as-sprayed and vacuum heat-treated conditions. The D1 deposit (see [Fig. 5.2a](#)) exhibited a relatively dense structure with some micropores and partially visible interparticle boundaries, which can be attributed to the insufficient plastic deformation of the particles despite the high gas parameters. For the deposit (D2) fabricated with the same gas parameters as D1 but with a medium particle size range, more pores were generated as evidenced by the measured density, which decreased from $98.62 \pm 0.49\%$ (D1) to $96.64 \pm 0.72\%$ (D2). This is because the particle impact velocity decreased with the increase in particle size, and the medium-sized particles with lower in-flight velocities were less plastic-deformed during the deposition. Compared with the D2 deposit, the D3 deposit was manufactured using a lower gas temperature, and the weakened thermal softening effect was adverse to particle deformation. This can be confirmed by the widely distributed pores in the deposit (see [Fig. 5.2e](#)), and as a result, the D3 deposit exhibited a further decrease in density, which was measured to be $89.86 \pm 1.84\%$. The D4 deposit, which was fabricated using the same gas parameters as the D3 deposit but with a wider particle size range, exhibited fewer pores than D3 with an averaged density of $94.76 \pm 1.06\%$ (see [Fig. 5.2g](#) and [Fig. 5.3](#)). The increased density can be attributed to the in-process densification triggered by the large-sized particles, whose impact velocities were below their critical velocities under the current processing parameters. These particles rebounded from the deposit surface after impact, and the tamping effect during this process densified the deposit by promoting the secondary plastic deformation of deposited particles. The in-process densification was also achieved for the D5 deposit, which was manufactured under lower gas pressure compared to the D4 deposit. This helped to further reduce the particle impact velocities, and more particles can tamp the deposit rather than bond with the previously deposited layer. This can be demonstrated by the further increased density ($96.53 \pm 0.98\%$), which surpassed the D4 and D3 deposits and approached the D2 deposits. However, the density of the D5 deposit was still inferior to that of the D1 deposit.

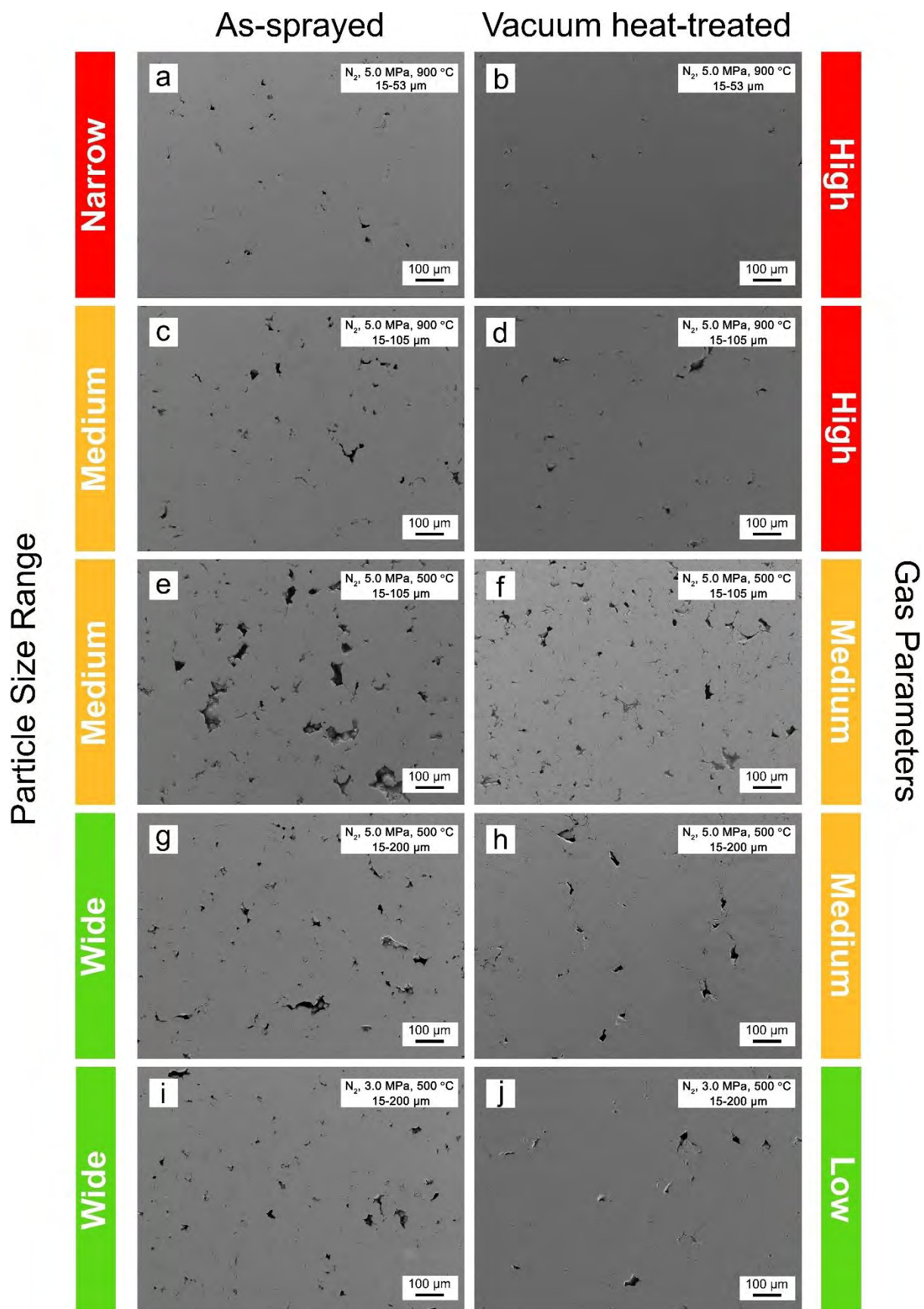


Fig. 5.2 Microstructure of the cold-sprayed CoCrFeNi HEA deposits fabricated using different

combinations of particle size ranges and gas parameters in as-sprayed (left column) and vacuum heat-treated (right column) conditions. (a, b) D1, (c, d) D2, (e, f) D3, (g, h) D4, (i, j) D5.

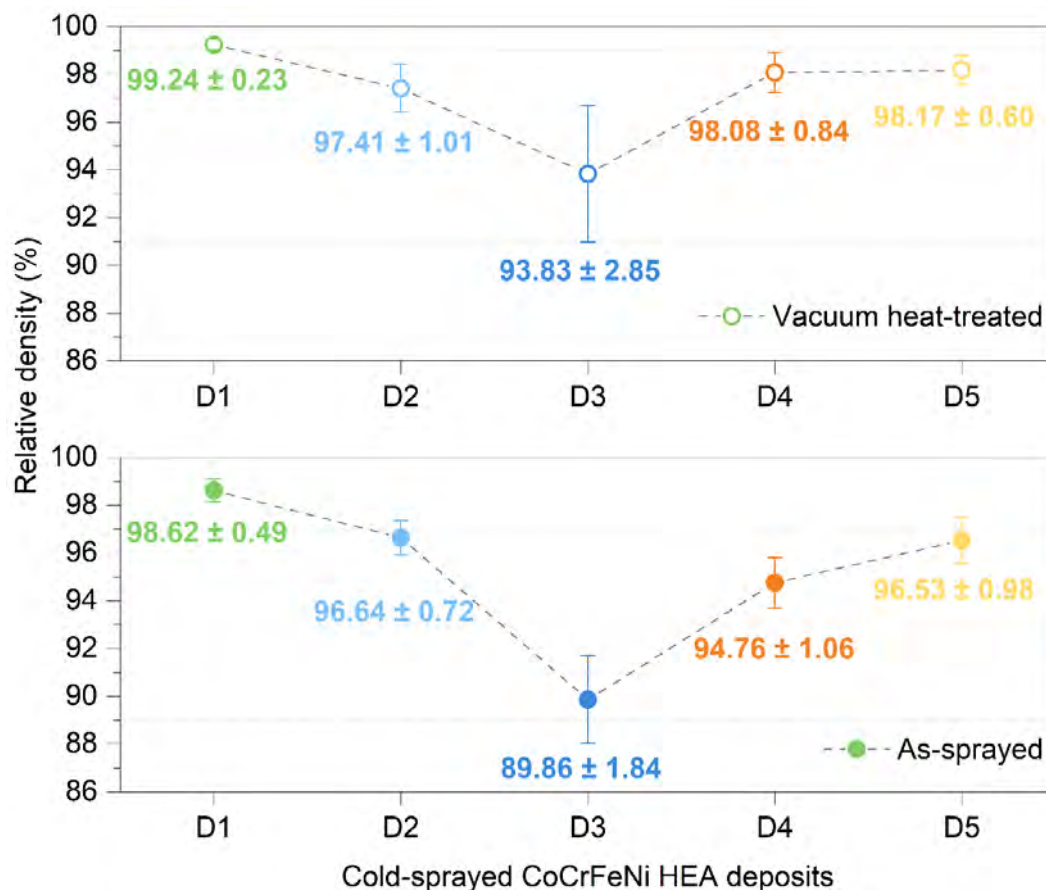
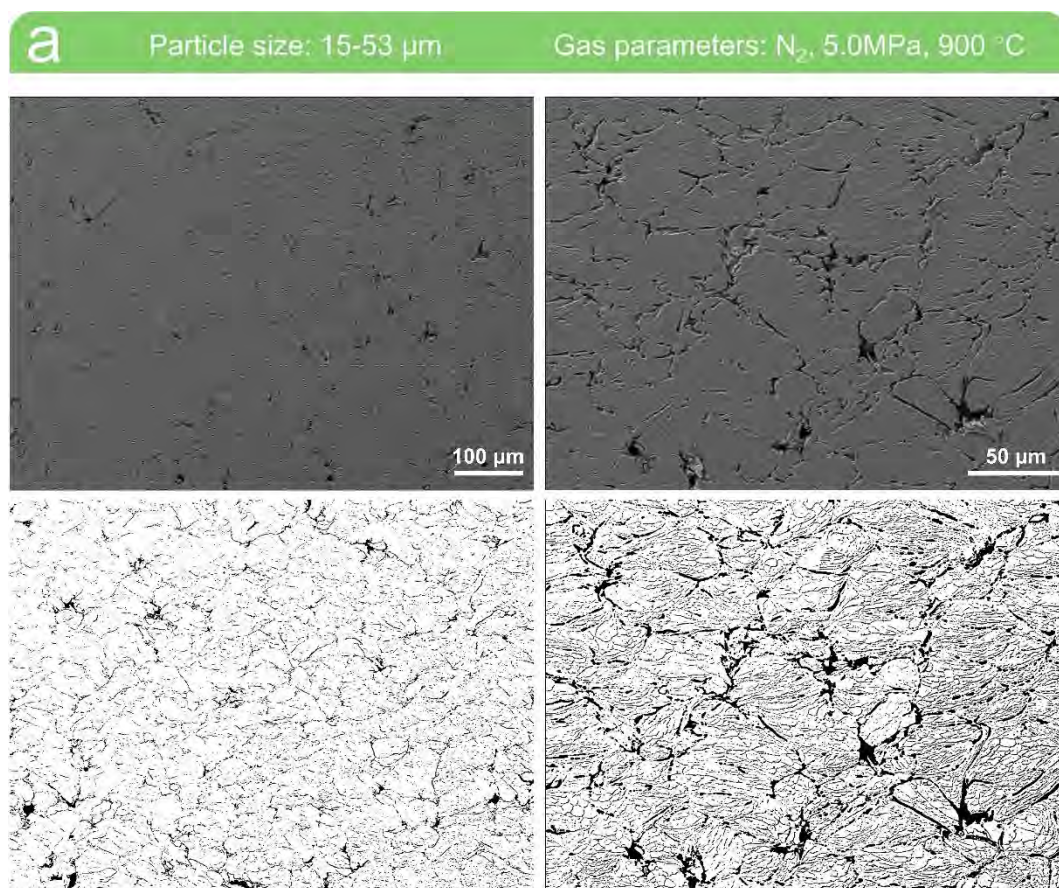


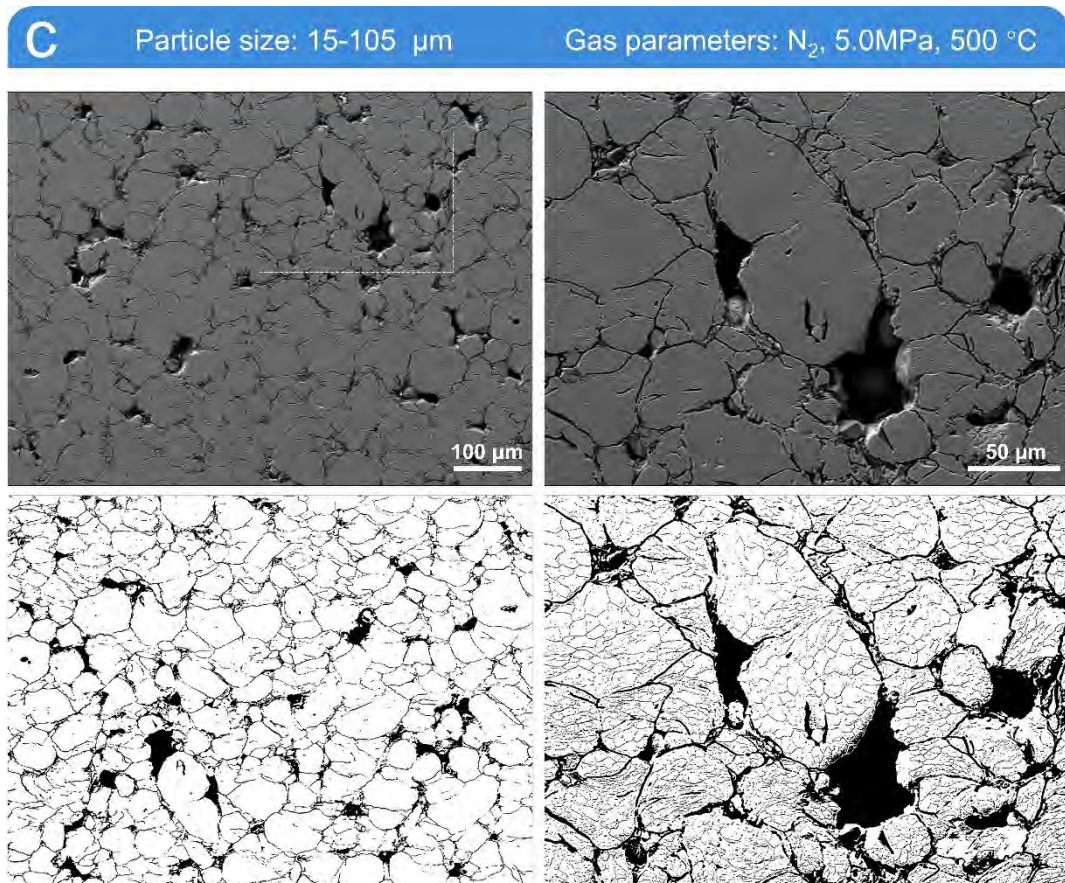
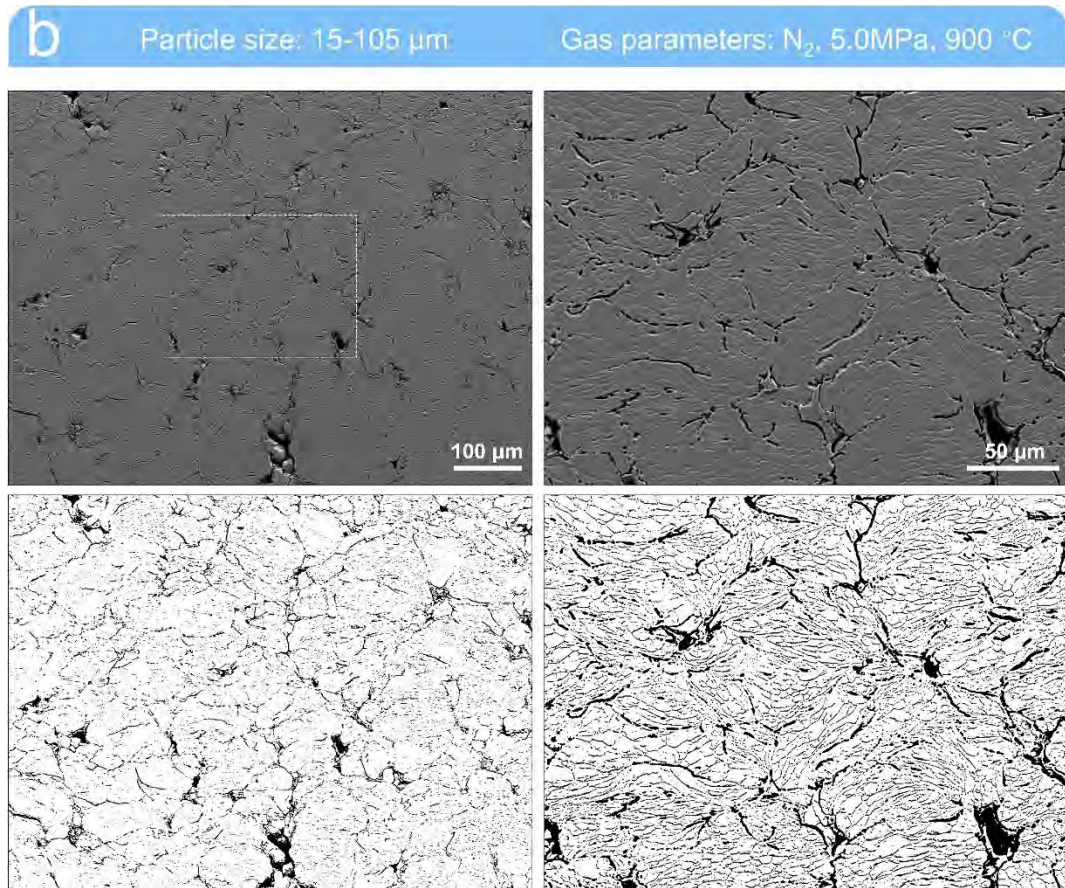
Fig. 5.3 Relative density of the cold-sprayed CoCrFeNi HEA deposits under different processing parameters in the as-fabricated and vacuum heat-treated status.

After the vacuum heat-treatment, all the deposits exhibited an increase in density (see **Fig. 5.3**) due to the improved interparticle diffusion and enhanced metallurgical bonding triggered by the high temperature. The measured density provided in **Fig. 5.3** was in good agreement with the microstructure observation, and both density curves (i.e., as-fabricated and vacuum heat-treated) followed the same trend. However, it is notable that it is rather difficult for the pores with large sizes to close up through the heat treatment process. These defects are likely to lead to premature failure of the deposits.

To investigate the particle deposition behavior under different combinations of particle size ranges and gas parameters, the etched microstructure and the corresponding binary images of the as-fabricated CoCrFeNi HEA deposits were displayed in **Fig. 5.4**. The interparticle boundaries and the grain boundaries were revealed after etching. It can be observed that the originally spherical CoCrFeNi were deformed to different extents after high-velocity impact. For the D1 deposit, the particles were severely deformed and flattened. The enlarged microstructure after etching shows that the grains near interfacial regions were significantly elongated, and ultra-fine grains were formed due to the grain fragmentation and dynamic recrystallization (see **Fig. 5.4a**), while the grains in the particle interior remained equiaxed or near-equiaxed. This is the typical bi-modal grain structure in the deformed particles in cold spray, and such heterogeneous microstructure can be attributed to the existence of temperature and strain gradients during the high-velocity impact process. The D2 deposit exhibited a highly similar microstructure as the D1 deposit apart from some less-deformed particles in medium sizes. Compared with the D1 and D2 deposits, the particles in the D3 deposits were significantly less deformed, particularly for the medium-sized particles, and the pores between the particles were clearly visible (see **Fig. 5.4c**). The grains in the less deformed particles were equiaxed or near-equiaxed. The insufficient plastic deformation of particles led to the porous structure, as shown in **Fig. 5.2e**. When using the particles with a wider size range but the same gas parameter as the D3 deposit, it can be found that the relatively small particles were more flattened than those in the D3 deposit. The tamping effect triggered by the large-sized particles promoted the secondary plastic deformation of small and even medium-sized particles, leading to the densification of the D4 deposit. However, some large-sized particles that remained in the deposit were less deformed, triggering the formation of large pores, as shown in **Fig. 5.4d**. This indicated that the impact velocities of these large-sized particles were probably above the corresponding critical velocities

under the current gas parameters, leading to the deposition of particles. To avoid the inclusion of large-sized particles in the deposit, the lower gas parameters were applied. As expected, the produced D5 deposit was mainly composed of smaller particles, which suggested that more large-sized particles rebounded from the deposit surface after impact and tamped the deposited layers. This can be verified by the increased density of the D5 deposit ($96.53 \pm 0.98\%$) as compared to the D4 deposit ($94.76 \pm 1.06\%$). Compared with the D4 deposit, the number of large-sized particles left in the deposit was significantly decreased. However, the inclusion of large-sized particles still existed in the deposit, which led to the formation of pores (see Fig. 5.4e). The unwanted inclusion is expected to influence the mechanical properties of the deposits.





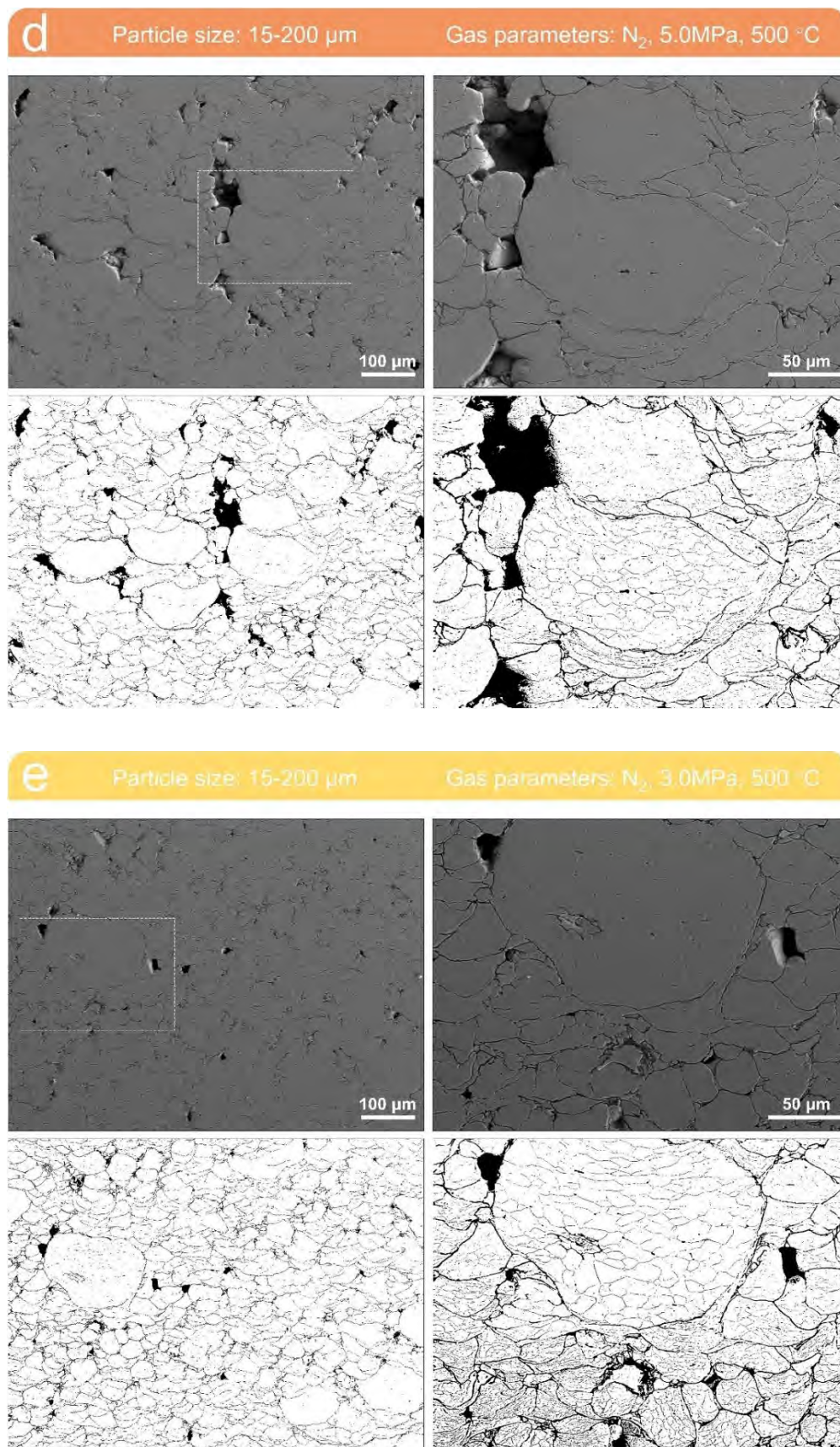
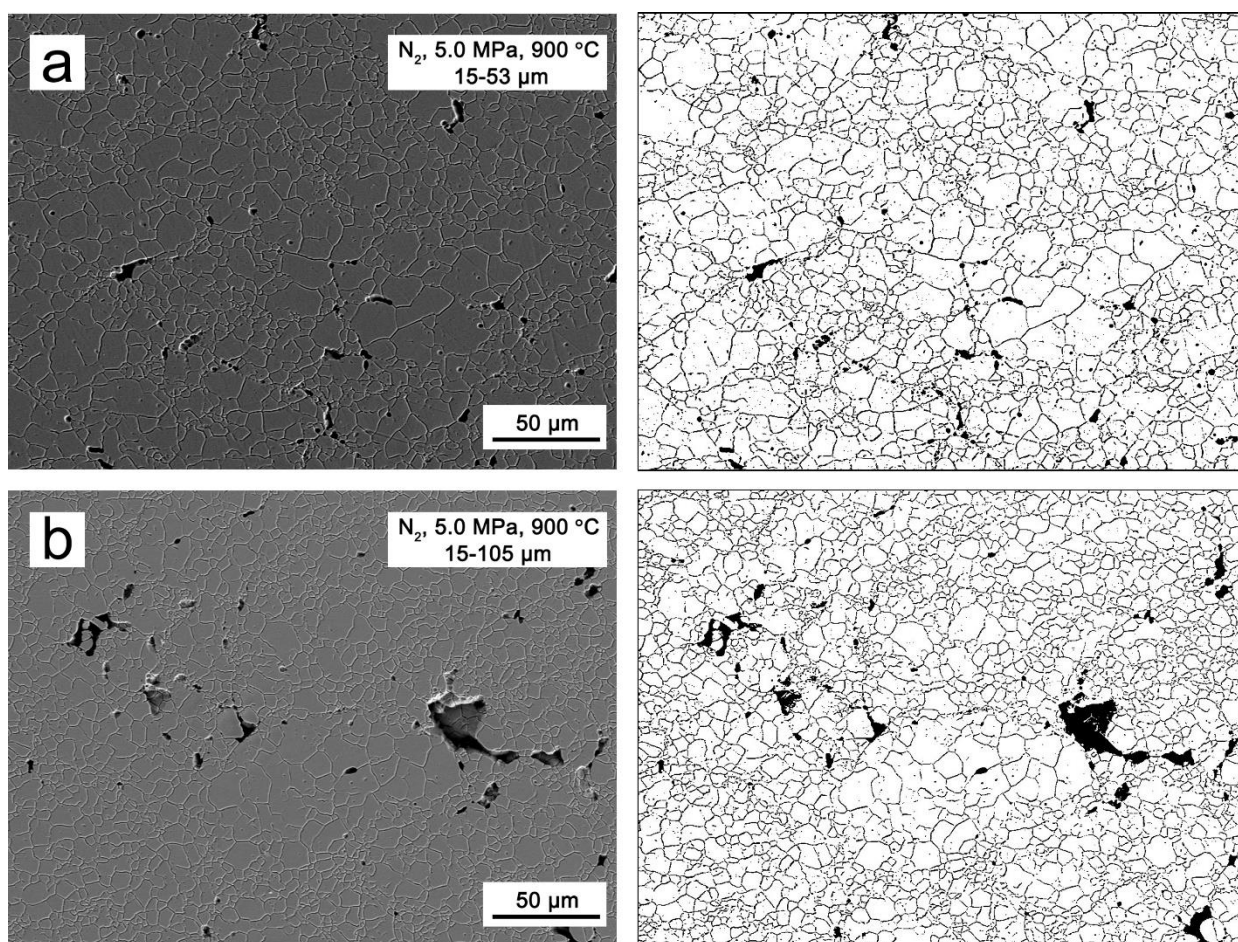


Fig. 5.4 Etched microstructure and the corresponding binary images of the as-fabricated

CoCrFeNi HEA deposits fabricated under different combinations of particle size ranges and gas parameters. (a) D1, (b) D2, (c) D3, (d) D4, (e) D5.

Fig. 5.5 shows the etched microstructure (left column) and the corresponding binary images (right column) of the vacuum heat-treated CoCrFeNi HEA deposits fabricated under different combinations of particle size ranges and gas parameters. The interparticle interfaces of the D1 and D2 deposits became indistinguishable due to the improved interparticle diffusion and enhanced metallurgical bonding. Moreover, the grains in both deposits experienced significant growth, suggesting the deposits were fully recrystallized. For the rest of the deposits, the interparticle diffusion induced by the high temperature was localized due to the existence of large-sized pores and poor particle-particle bonding.



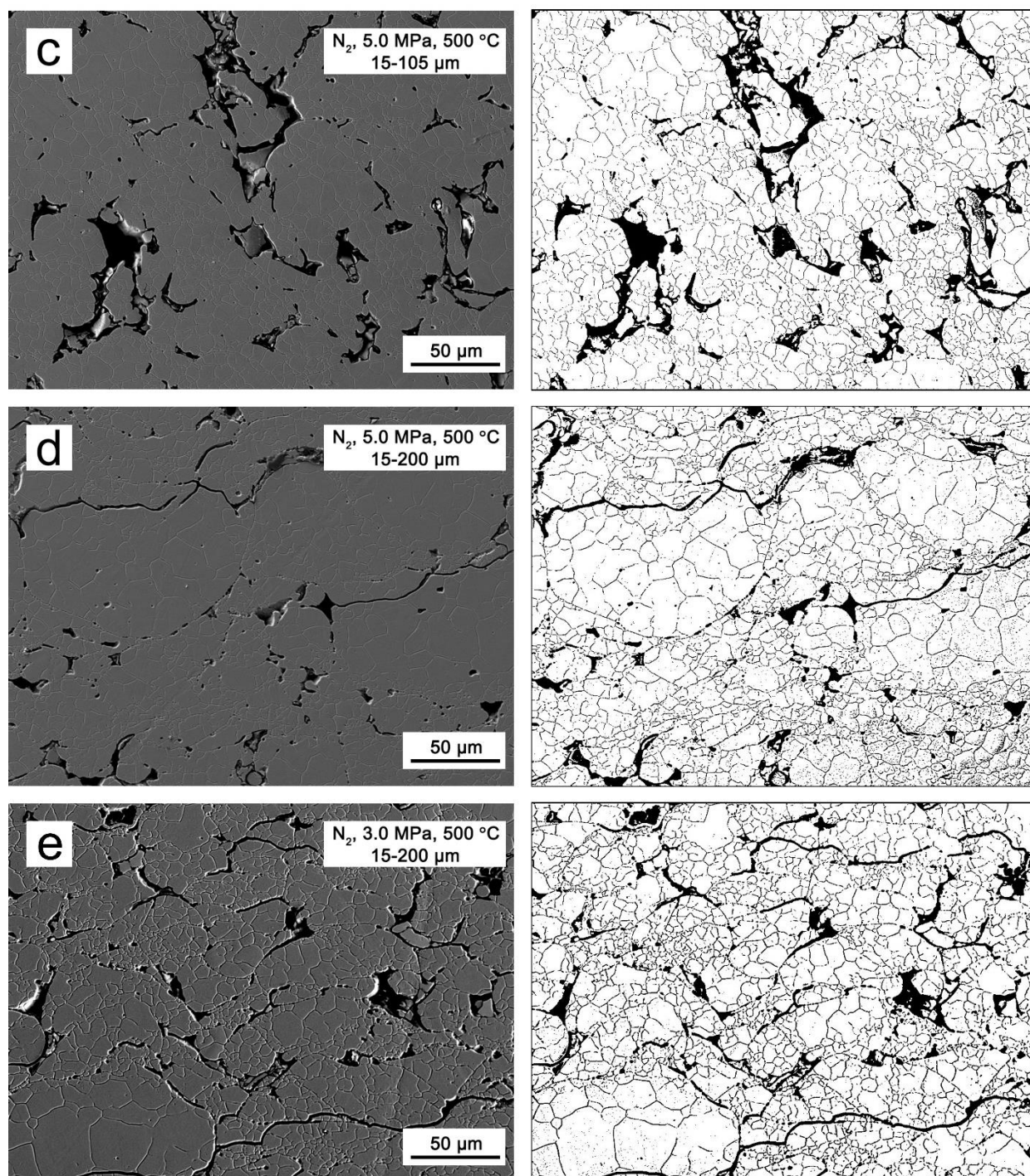


Fig. 5.5 Etched microstructure (left column) and the corresponding binary images (right column) of the vacuum heat-treated CoCrFeNi HEA deposits fabricated under different combinations of particle size ranges and gas parameters.

5.3 Mechanical Properties

Fig. 5.6 shows the Vickers hardness test results of the cold-sprayed CoCrFeNi HEA deposits fabricated under different combinations of particle size ranges and gas parameters in both as-fabricated and vacuum heat-treated states. The trend of the hardness variation is basically consistent with the trend of the measured density

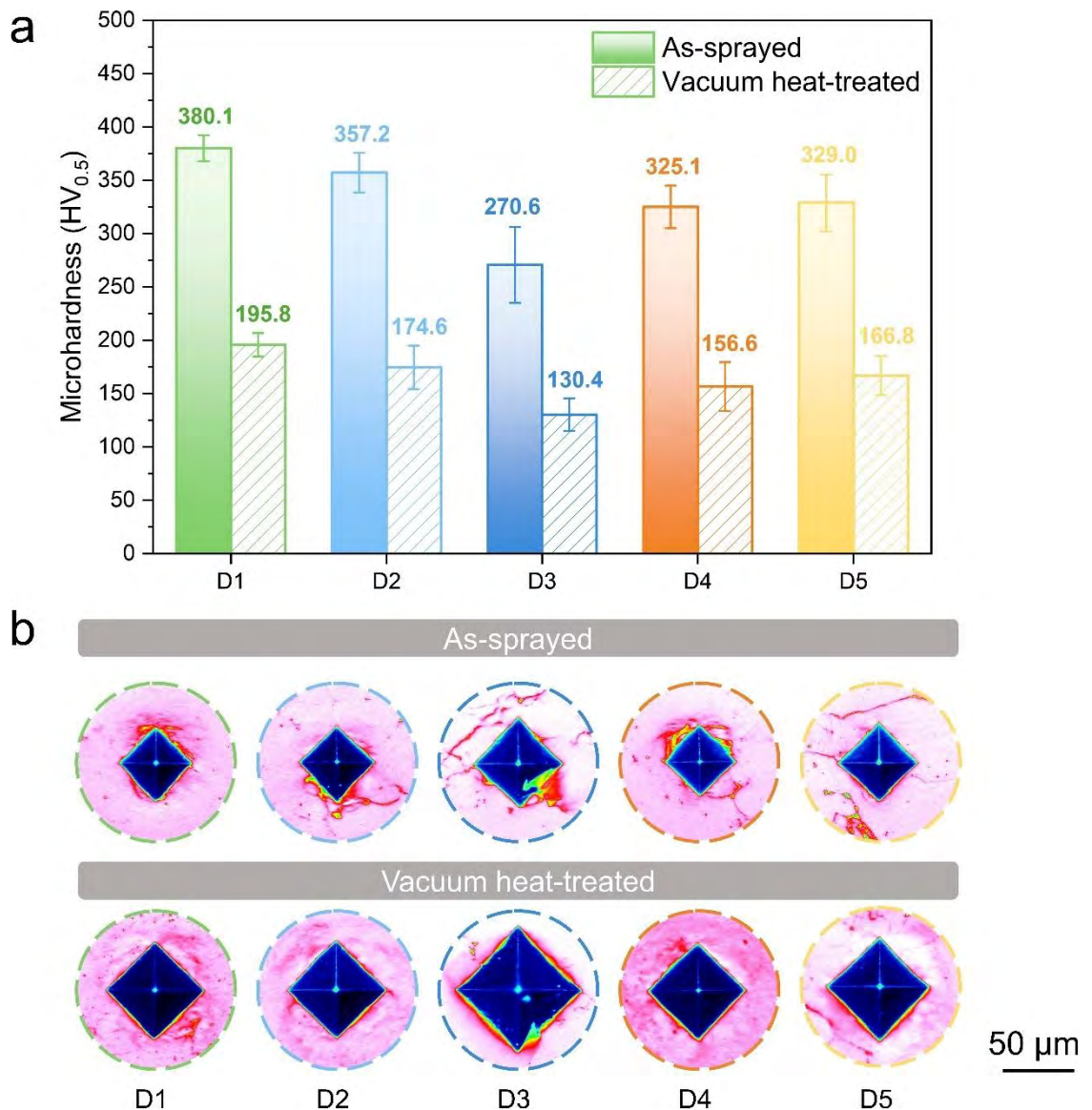


Fig. 5.6 Vickers hardness test results of the cold-sprayed CoCrFeNi HEA deposits fabricated under different combinations of particle size ranges and gas parameters in the as-fabricated and vacuum heat-treated states. (a) Microhardness and (b) Corresponding morphology of indentations.

variation (see [Fig. 5.6a](#)). The D1 deposit exhibited the highest microhardness of 380.1 HV_{0.5} among all the deposits, which is the result of significant work hardening induced by severe plastic deformation in cold spray. The less deformed particles and manufacturing defects in the D3 deposit led to the low microhardness value (270.6 HV_{0.5}), which is only 71.19% of that of the D1 deposit. This can be evidenced by the imperfect diamond shape of the indentation (D3), as shown in [Fig. 5.6b](#). When using particles with wide size ranges and lower gas parameters, the microhardness rose again to 325.1 HV_{0.5} for the D4 deposit and 329.0 HV_{0.5} for the D5 deposit, respectively. The improvement of the microhardness was the result of the tamping effect induced by large-sized particles, which can promote the secondary plastic deformation of previously deposited layers and the closure of the micropores. As expected, the microhardness of all the deposits significantly decreased after vacuum heat-treatment due to the suppression of the work-hardening effect. The corresponding indentation morphology also shows the perfect diamond shape with less visible localized deformation pile-up of the material, as compared to the indentations on the as-fabricated deposits, implying the recovery of ductility after vacuum heat treatment.

[Fig. 5.7](#) shows the uniaxial tensile properties of the cold-sprayed CoCrFeNi HEA deposits fabricated under different combinations of particle size ranges and gas parameters after vacuum heat treatment. As depicted in the representative engineering stress-strain curves (see [Fig. 5.7a](#)), the deposits exhibited more or less macroscopical ductility after vacuum heat treatment, which can be attributed to the interfacial diffusion induced by high temperature, leading to stronger interparticle metallurgical bonding, and the reduced manufacturing defects. The D1 deposit exhibits the highest ultimate tensile strength (UTS) and elongation (EL) among all the deposits, which are calculated to be 428.88 MPa and 4.27 %. However, compared with the tensile properties of the as-cast bulk material and counterparts prepared by additive manufacturing routes (see [Fig. 5.7c](#)), the UTS, particularly the

EL, of the D1 deposits are significantly inferior to them. This is associated with the solid-state deposition feature of cold spray, and the low tensile ductility is also a widely existing shortcoming for cold-sprayed deposits even in the heat-treated states [264]. Due to the increased defects induced by the less-deformed medium-sized particles and weakened interparticle bonding, the D2 deposit shows a 24.39% decrease in UTS and a 57.38% decrease in EL. For the D3 deposit exhibiting the lowest density after vacuum heat treatment, the tensile properties were also the worst among all the deposits, as evidenced by the lowest UTS (228.12 MPa) and EL (1.09%) in Fig. 5.7b. There is an upturn trend of UTS when using wider particle size ranges and lower gas parameters. The UTS of the D4 and D5 deposits was 240.50 MPa and 269.11 MPa, respectively, which were 5.43% and 17.97 % higher than that of the D3 deposit. This can be attributed to the tamping effect induced by the large-sized particles, leading to the densification of the deposits. However, the UTS was far inferior to the D1 deposit. Moreover, there was also no significant recovery of ductility for the D3 and D4 deposits.

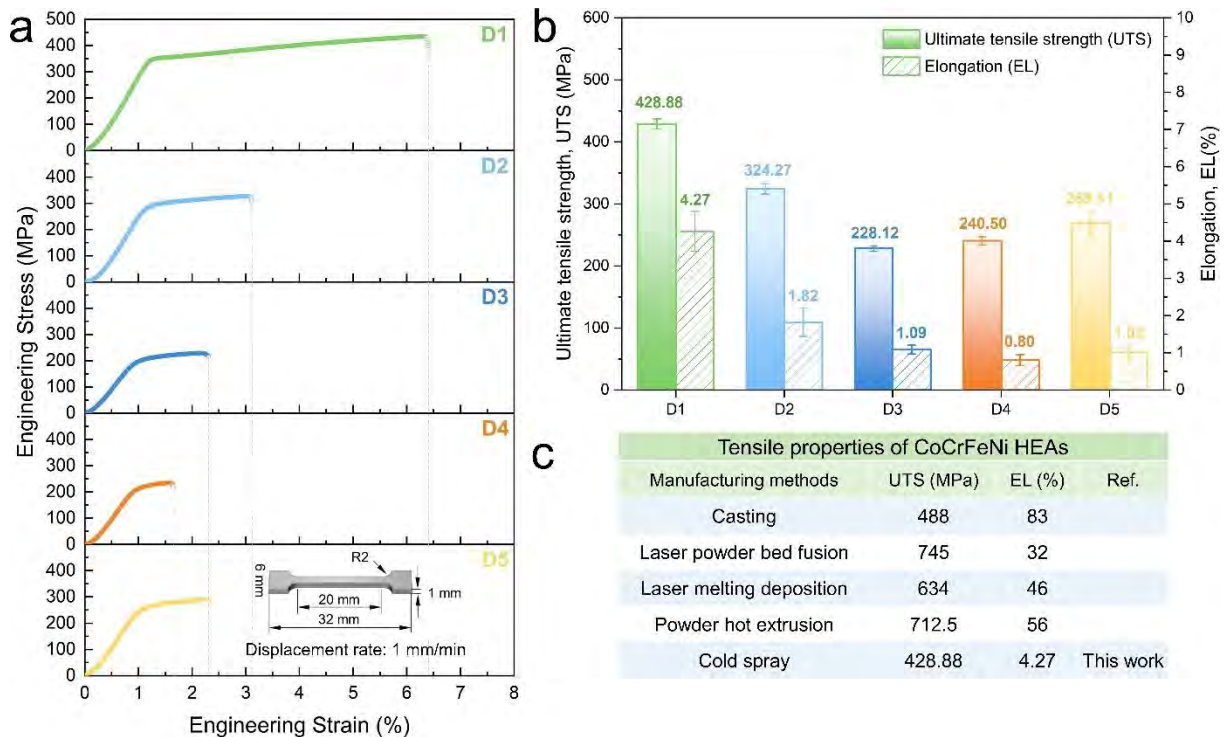
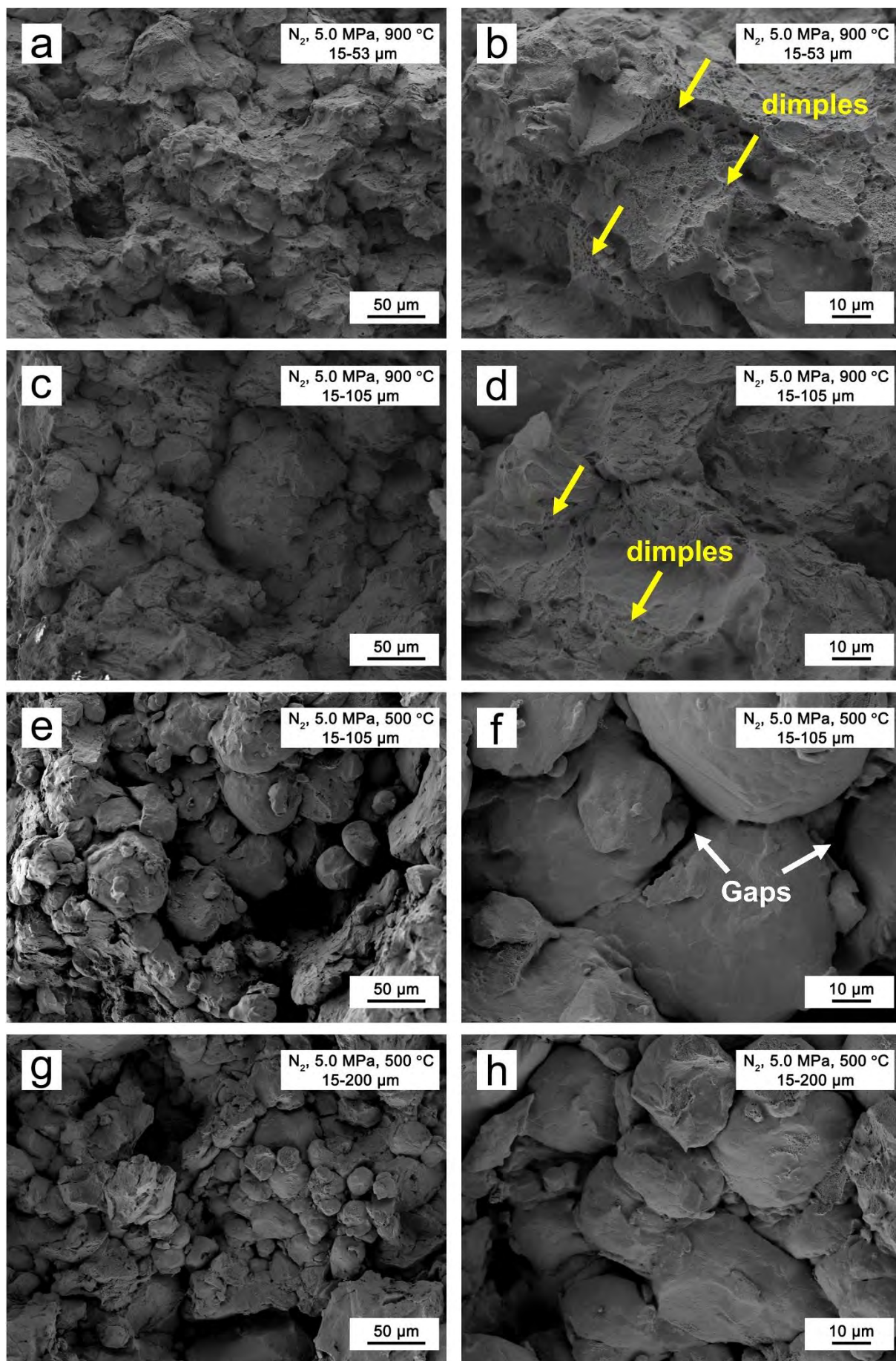


Fig. 5.7 Tensile properties of the cold-sprayed CoCrFeNi HEA deposits fabricated under

different combinations of particle size ranges and gas parameters. (a) Representative engineering stress-strain curves, (b) The ultimate tensile strength (UTS) and elongation (EL), (c) A comparison of room-temperature tensile properties of CoCrFeNi HEAs fabricated by other manufacturing processes and cold spray additive manufacture [289,303–305].

Fig. 5.8 shows the fracture surface of the cold-sprayed CoCrFeNi HEA deposits fabricated under different combinations of particle size ranges and gas parameters. The D1 deposit exhibited indistinguishable particle interfaces and dimple-like features on the fracture surface (see **Fig. 5.8a** and b), indicating the ductile fracture mode. The high-temperature diffusion can promote atomic diffusion at interfacial regions and enhance metallurgical bonding between adjacent particles. The D2 deposit shows less dimples than the D1 deposits, indicating the reduced ductility. The less-deformed particles in medium sizes led to the weak bonding between particles. For the D3 deposit, the loose accumulation of particles can be observed due to their insufficient plastic deformation under lower gas parameters, particularly for the particles with medium sizes. The pores and less-bonded interfaces, as evidenced by the gaps (see **Fig. 5.8e** and f), provided pathways for the rapid crack propagation under tension and led to the fracture along the interparticle interfaces (inter-particle decohesion), which resulted in a significant decrease in UTS and EL. The tamping effect achieved by the large-sized particles promoted the secondary plastic deformation of deposited particles and resulted in the improvement of particle bonding, which led to the increase in UTS for the D4 (240.50 MPa) and D5 (269.11 MPa) deposits. However, compared with the D1 and D2 deposits, few to no dimple features can be recognized from the fracture surface of the D3, D4, and D5 deposits, implying brittle fracture characteristics. This led to the negligible ductility of these deposits even in the vacuum heat-treated states, as shown in **Fig. 5.7b**.



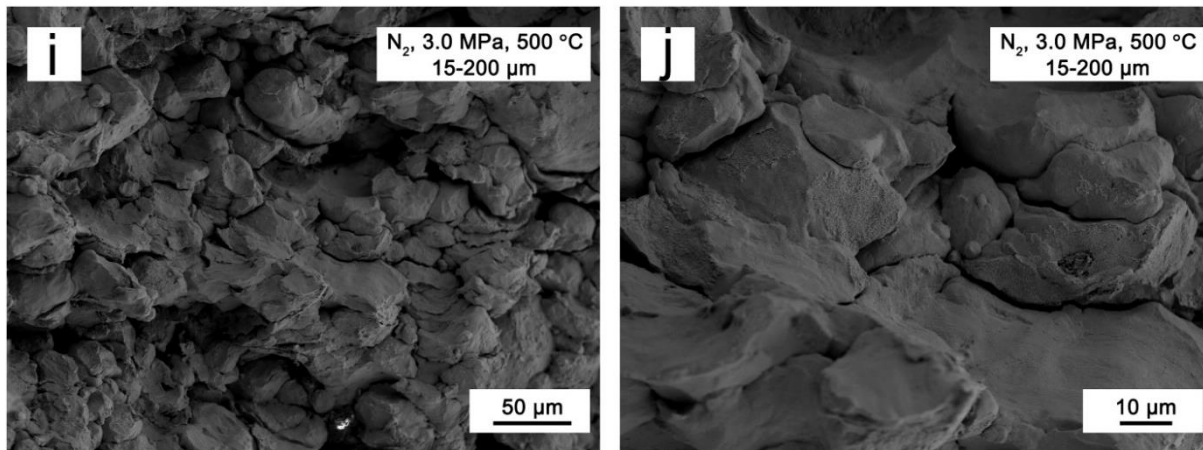


Fig. 5.8 Fractographic analysis of the fracture surface of the cold-sprayed CoCrFeNi HEA deposits fabricated under different combinations of particle size ranges and gas parameters. (a, b) D1, (c, d) D2, (e, f) D3, (g, h) D4, (i, j) D5.

5.4 Strengthening Mechanisms

In cold spray process, a general understanding between gas processing parameters and mechanical properties of the deposits is higher gas parameters lead to higher impact velocities and more sufficient plastic deformation of particles. At such conditions, cold-sprayed with dense structure and satisfactory mechanical properties can be manufactured. However, in this work, the densification can also be achieved at lower gas parameters when combined with the use of a wide particle size range. **Fig. 5.9** illustrates the strengthening mechanisms occurring under typical combinations of the particle size ranges and gas parameters. Generally, the typical particle size range of feedstock powder used for powder-based additive manufacturing techniques is 15-53 μm . As expected, the cold-sprayed CoCrFeNi HEA deposit (D1) exhibited a relatively dense structure when using nitrogen as the propelling gas at high temperature and high pressure. The particles sprayed under this condition experienced severe plastic deformation due to their high particle impact velocity, leading to satisfactory interparticle bonding, as shown in **Fig. 5.9a**.

When using particles with a medium size range (i.e., 15-105 μm) and simultaneously decreasing gas parameters, the particle impact velocities were decreased but for the majority of particles, the impact velocities of particles were beyond their critical velocities, as evidenced by the deposited particles in various sizes (see **Fig. 5.4c**). However, the decreased impact velocities and weakened thermal softening effect severely limited the plastic deformation of particles, leading to the formation of large pores between adjacent particles, as schematized in **Fig. 5.9b**. This resulted in the worst mechanical properties of the deposit (D3) among all the deposits. By further decreasing the gas processing parameters and using particles with a wider size range (i.e., 15-200 μm), the particle impact velocities were significantly decreased, particularly for the particles with large sizes. Consequently, these particles rebounded from the deposit surface after impacting instead of being deposited. The rebound particles continuously compacted the already formed deposit and densified it by inducing further plastic deformation, as schematized in **Fig. 5.9c**. The total plastic deformation of deposited particles was composed of two aspects: the high-velocity impact induced the primary plastic deformation and the tamping effect from rebounded particles induced secondary plastic deformation. Therefore, the D5 deposit exhibited a denser structure and better mechanical performance as compared to the D3 deposit.

Although the in-process densification was achieved for the D5 deposit, both the density and mechanical properties of the D5 deposit were inferior to those of the D1 deposit. This could be attributed to the total plastic deformation of deposited particles in the D5 deposit was smaller than that of the D1 deposit, leading to the weak interparticle bonding. In addition, the undesirable inclusion of large-sized particles in the D5 deposit also occurred, as shown in **Fig. 5.4e**. One possible solution to this problem is adjusting the proportion of large-sized particles in the feedstock powder and optimizing the gas parameters, such as using the combination of lower gas pressure but slightly higher gas temperature.

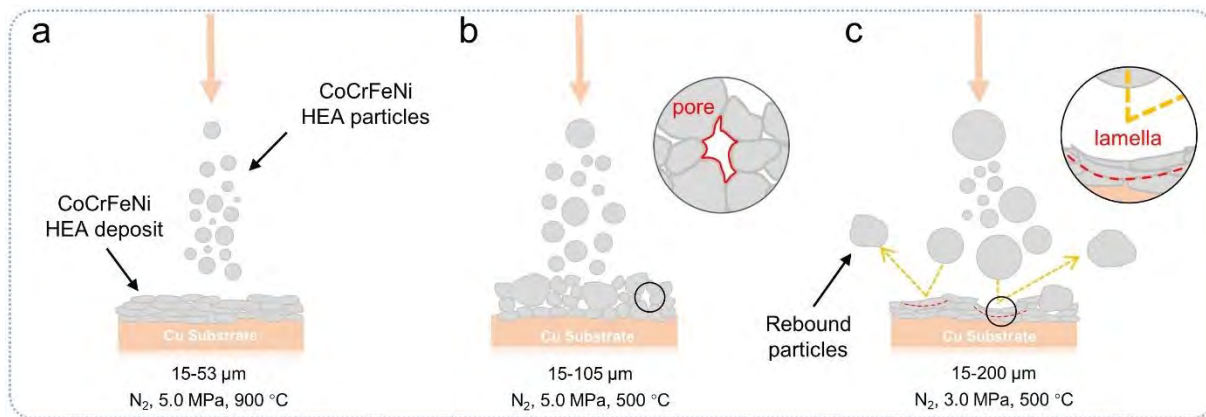


Fig. 5.9 Schematic illustration of strengthening mechanisms occurring under typical combinations of the particle size ranges and gas parameters. (a) D1 deposit, (b) D3 deposit, and (c) D5 deposit.

5.5 Advantages and Disadvantages of the in-process densification

5.5.1 Advantages

The fabrication of additively manufactured parts and components with fewer defects and excellent mechanical properties is always desirable. In cold spray process, the straightest way to intentionally fabricate high-performance deposits is by using higher gas parameters (i.e., increasing the gas pressure and/or the temperature of the propelling gas), particularly during the deposition of materials with high deformation-resistance, for example, the HEAs. However, the increased gas temperature may lead to increased oxidation, nitridation, phase changes, softening or even melting of particles, and the damage of the cold spray nozzle made of polymers [306,307]. These problems can be avoided to some extent when using helium (He) as the propelling gas. However, the high cost of He is economically unfavorable compared to the relatively cheap and sustainable N₂. Moreover, He, as a non-renewable resource, is becoming increasingly sparse on the earth. Hence, the

overall trend in the cold spray industry is to use N_2 rather than He. An alternative solution to densify the cold-sprayed deposits is adding peening particles into the feedstock to improve the mechanical properties of the deposits. The feasibility has been demonstrated in some paradigms including adding large stainless steel particles into Al and its alloys, Ni and Ni-based alloy, Ti and Ti-based alloy powders [90,93,95,97,308,309], adding Al_2O_3 particles into A380 alloy powder [310] or Cu_2O particles into Cu powders [311]. There are different names for this kind of strengthening process, such as “in-situ shot peening” [97,309,312], “in-situ forging” [93,95,308], “self-peening” [313,314]. In these processes, the peening effect was achieved through the impact and rebound of foreign powders, which are different from the feedstock powder for cold spraying process. These foreign particles may partially embed and lead to unnecessary stress concentrations, pores formation, and localized chemical heterogeneities. In addition, the heavy peening particles may increase the risk of nozzle wear or even nozzle clogging. For the in-process densification, which is realized through the combination of wide particle size ranges and low gas parameters, the peening effect is completely achieved through the impact and rebound of the coarse powders in the feedstock rather than the foreign powders. Therefore, this novel process is expected to avoid the aforementioned problems brought by foreign peening particles.

5.5.2 Disadvantages

Although in-process densification has its unique advantages, some drawbacks are equally worthy of attention. The in-process densification is achieved through the tamping effect of a portion of large-sized particles, and these particles will rebound after impact without participation in the cold spray deposition. This means that the deposition efficiency will be significantly reduced. In our previous research, the deposition efficiency of in-process densification assisted cold-sprayed Al deposits is only around 1.66% [307], which will increase the cost of feedstock powder and

gas consumption. The powders with a wider size range are typically less expensive than traditional metal or alloy powders. However, for HEAs, the price difference between powder with a narrow size range and powder with a wide size range is not that significant, which indicates the loss of price advantage.

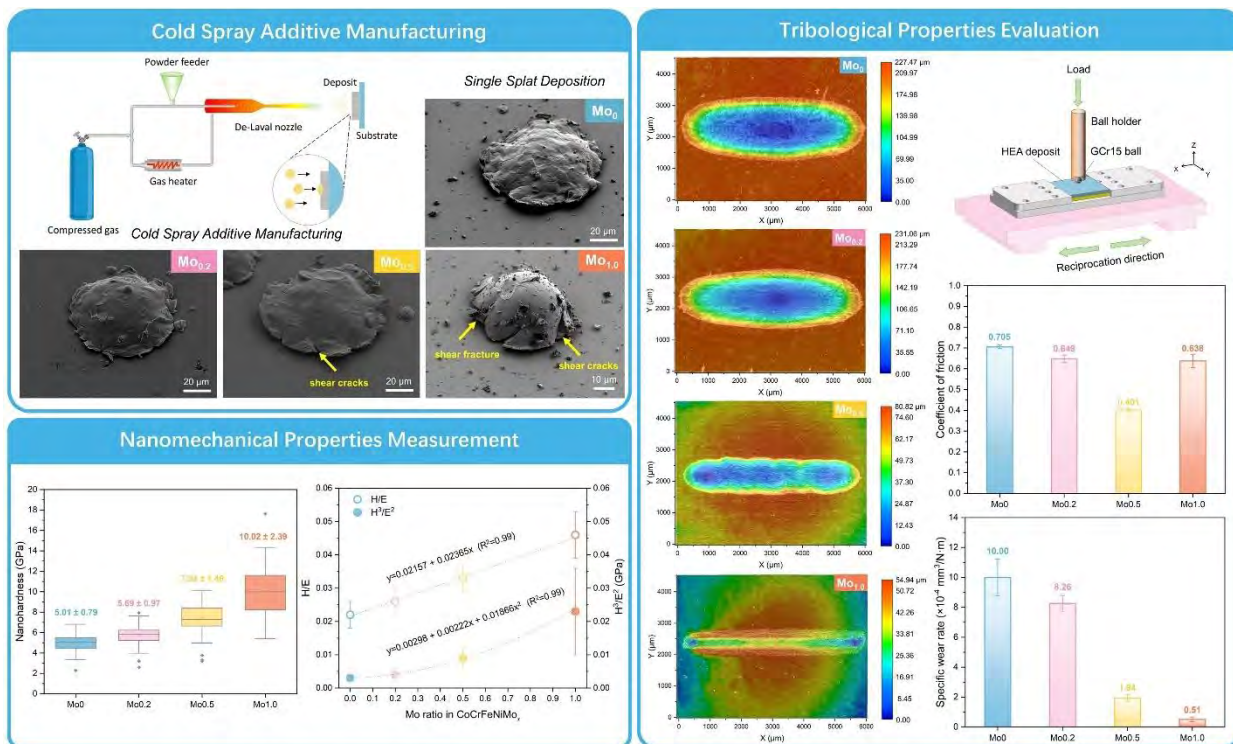
5.6 Summary

In this chapter, the CoCrFeNi high-entropy alloy (HEA) deposits were fabricated using different combinations of feedstock particle size ranges and gas parameters. It is found that the combination of a wide particle size range of the feedstock powder and low gas parameters can trigger in-process densification of the deposits. To be specific, the large-sized particles in the feedstock powder rebound from the deposit surface after impact due to their low impact velocity induced by low parameters, and these particles tamp the deposit and promote secondary plastic deformation of deposited particles, leading to the densification of the cold-sprayed deposits. Compared with the deposits fabricated using high processing parameters (i.e., using nitrogen at high pressure and high temperatures or using uneconomical and unrenewable helium as the propulsion gas), the associated detrimental effects such as increased oxidation, nitridation, phase changes, corrosion of the substrate or even damage to the expensive spray nozzle (when using gases at high temperatures) can be minimized as much as possible. The relative density and mechanical properties of the CoCrFeNi HEA deposits (D5) fabricated by using the combination of a wide particle size range and low gas parameters are inferior to the deposit manufactured by using particles with a narrow size range and high gas parameters (D1) at this stage, which can be attributed to the inclusion of some large-sized particles in the deposit. The further improvement of the density and mechanical properties of the deposits is expected to be achieved by adjusting the proportion and size of the large-sized particles and/or using lower gas parameters.

Chapter 6

Solid-state deposition of Mo-doped CoCrFeNi High-entropy Alloy with Excellent Wear Resistance via Cold Spray

The equiatomic CoCrFeNi high-entropy alloy (HEA), serving as a basic system in the HEA family, usually exhibits unsatisfactory wear resistance particularly in extreme environments (e.g., high loads and high temperatures). To improve the wear resistance of CoCrFeNi HEA alloy for a wider range of industrial applications, the alloying strategy was applied to CoCrFeNi HEA by doping Mo element in various ratios, and CoCrFeNiMo_x ($x=0, 0.2, 0.5, \text{ and } 1$) deposits were fabricated by cold spray additive manufacturing. The microstructure evolution, mechanical properties, and tribological properties of cold-sprayed CoCrFeNiMo_x deposits were systematically investigated. The results showed that Mo₀, Mo_{0.2}, and Mo_{0.5} deposits have a face-centered-cubic (FCC) single structure, while Mo_{1.0} deposits were composed of FCC matrix and hard brittle phases. The doping of Mo element into CoCrFeNi HEA deposits significantly increased the hardness due to the enhanced solid solution strengthening and precipitation strengthening. As a result, the anti-wear properties of Mo-doped CoCrFeNi HEA deposits were gradually improved with the increase in Mo ratios. To be specific, the Mo_{1.0} deposit exhibited the lowest specific wear rate of $0.51 \times 10^{-4} \text{ mm}^3/\text{N}\cdot\text{m}$, which was reduced by 94.9% in comparison to the Mo₀ deposit.



6.1 Feedstock Powder and Experimental Methodology

6.1.1 Feedstock Powder

Gas-atomized CoCrFeNiMo_x ($x = 0, 0.2, 0.5, 1.0$) HEA powder with a nominal particle size distribution of 15-53 μm was used as feedstock. **Fig. 6.1** shows the surface morphology and particle size distribution of the HEA powders. The particle surface morphology was characterized by scanning electron microscope (SEM, Carl Zeiss Ultra Plus, Germany). Most powders featured high sphericity. The size distribution of the powder was measured by a laser diffraction particle analyzer (Mastersizer 2000, Malvern Instruments, UK). The actual element composition of the CoCrFeNiMo_x HEA powders was examined by inductively coupled plasma optical emission spectroscopy (ICP-OES, Prodigy XP, Leeman, US), as listed in **Table. 6.1**.

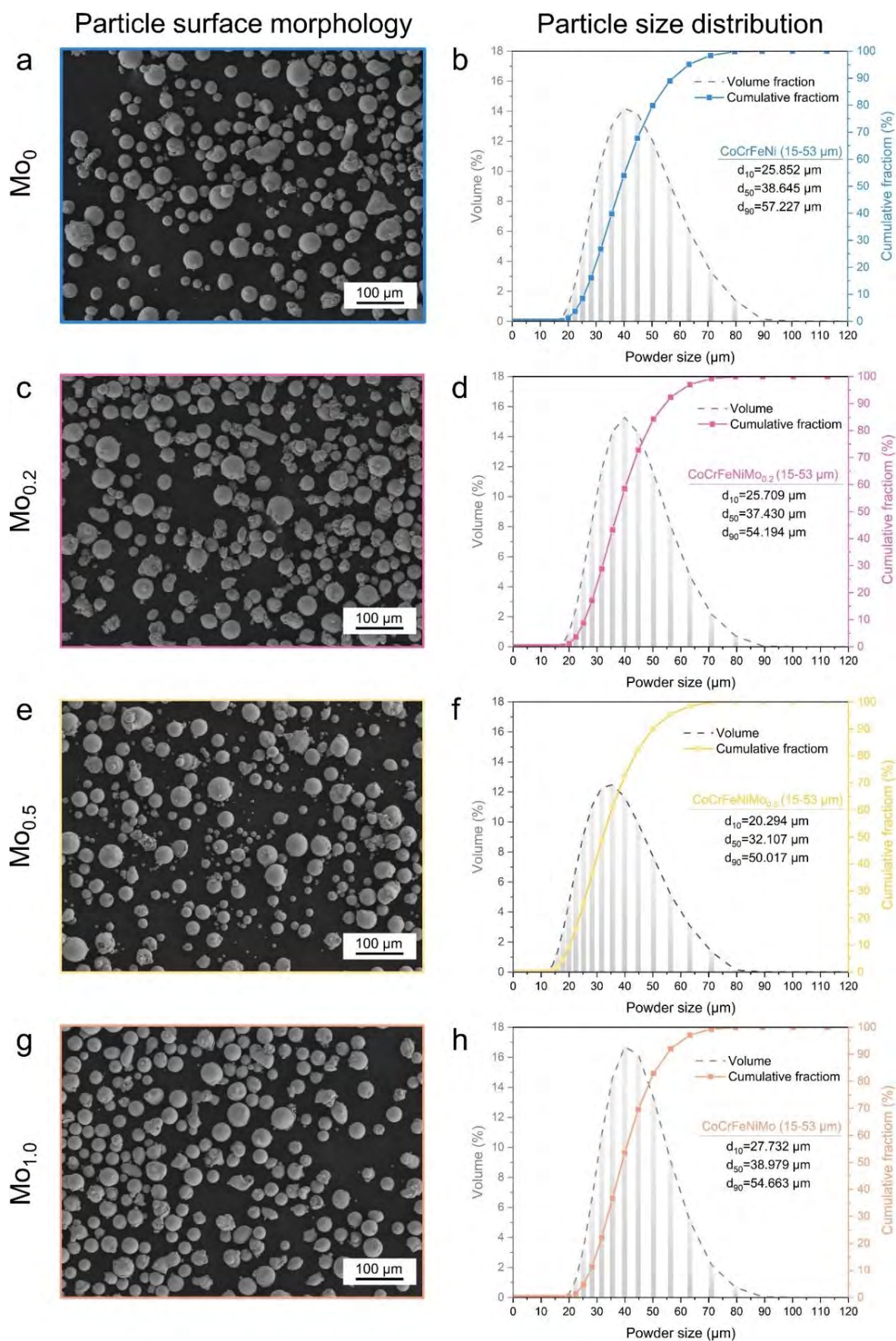


Fig. 6.1 Surface morphology (left side) and particle size distribution (right side) of the gas-

atomized CoCrFeNiMo_x HEA feedstock for deposits fabrication. (a, b) Mo₀, (c, d) Mo_{0.2}, (e, f) Mo_{0.5}, and (g, h) Mo_{1.0}.

Table. 6.1 Nominal and measured element composition of CoCrFeNiMo_x HEA feedstock.

Feedstock powder	Composition	Element / at %				
		Co	Cr	Fe	Ni	Mo
CoCrFeNi	Nominal	25.00	25.00	25.00	25.00	/
	Actual	24.25	25.08	25.60	25.06	/
CoCrFeNiMo _{0.2}	Nominal	23.81	23.81	23.81	23.81	4.76
	Actual	23.73	23.92	23.88	23.68	4.79
CoCrFeNiMo _{0.5}	Nominal	22.22	22.22	22.22	22.22	11.11
	Actual	21.96	22.19	22.58	22.08	11.19
CoCrFeNiMo _{1.0}	Nominal	20.00	20.00	20.00	20.00	20.00
	Actual	19.43	19.32	19.25	19.40	22.60

6.1.2 Cold Spray Process

A commercial high-pressure cold spray system (PCS-1000, Plasma Giken, Japan) was used for CoCrFeNiMo_x HEA deposits fabrication. Compressed nitrogen was used as propelling gas, and the inlet pressure and temperature were kept at 5.0 MPa and 900 °C, respectively. A square Cu plate with a size of 100 mm × 100 mm × 3.0 mm was used as the substrate, and the substrate surface was ground with sandpaper prior to cold spraying to remove oxide film and improve adhesion strength, followed by cleaning with anhydrous ethanol. The standoff distance from the exit of the nozzle to the Cu substrate surface remained 40 mm during the deposition. The nozzle moving trajectory followed a reciprocating zigzag strategy, and the space between two neighboring tracks was 1.0 mm. The deposits were subsequently processed into cubes (15 mm × 15 mm × 5mm) by a wire-cutting electrical discharge machine (EDM, V400G, Excetek V400G, China) for the following tribology

property evaluation. To investigate the deposition behavior of CoCrFeNiMo_x HEA particles, individual splat was deposited onto mirror-polished cold-sprayed CoCrFeNiMo_x HEA deposits under a nozzle traversal speed of 320 mm/s. The surface morphology of the single splat was characterized by SEM.

6.1.3 Microstructure Characterization

The cross-sectional samples were mechanically ground and polished following metallurgical procedures for microstructure analysis. The density of the deposits was evaluated from optical microscopy (Leica DM LM, Germany) images using an image analysis method based on ASTM E2109-01 standard. The result was averaged from ten different deposit regions to ensure data reliability. To identify phase composition, both the feedstock powders and deposits were analyzed by X-ray diffraction (XRD, X'pert Powder, PANalytical, Netherlands) equipped with Cu-K α radiation from a range of 2θ values between 20° and 100° (40 kV, 40 mA) with a scanning step size of 0.013.

6.1.4 Mechanical Properties Measurement

Depth sensing indentation test was carried out on the cross-section of the cold-sprayed CoCrFeNiMo_x deposits using a nanoindenter (MTS Nanoindenter XP, USA) equipped with a Berkovich triangular diamond tip at ambient temperature. The equipment has a high displacement resolution (< 0.01 nm) and load resolution (50 nN). A matrix of 10×6 indentations was conducted along the deposition direction with a depth limit of 1000 nm. The region without pores or cracks was selected for testing to avoid the effect of defects on the true indentation value of the deposits. The interval between each indentation in both horizontal and vertical directions was spaced at 20 μ m to avoid potential interactions between strain fields of adjacent indentations. The load on the sample and its corresponding displacement into the surface were recorded as a function of time during the nanoindentation test. The

hardness and elastic modulus of the deposit were obtained automatically from the system based on the Oliver-Pharr methodology [315]. The typical micrographs of indentations were then characterized by SEM.

The tribology properties of the cold-sprayed CoCrFeNiMo_x HEA deposits were evaluated by a ball-on-disk reciprocating tribometer (MFT-5000, RTEC, USA) at ambient temperature. The GCr15 steel ball (also known as AISI 52100 alloy steel) with a diameter of 4.0 mm was used as the counterpart. A constant normal load of 20 N was applied on the mirror-polished deposit surface during the test with an oscillating frequency of 4.0 Hz and a stroke length of 5.0 mm. The test lasted for 30 minutes, and at least three tests were run for each sample to ensure the data reliability. The coefficient of friction (COF) versus time was automatically recorded by the tribometer. The three-dimensional (3D) topography of the wear track was constructed using a 4K ultra-high accuracy digital microscope (VHX-7000N, Keyence, Japan), and the wear volume can be calculated automatically by the software. The specific wear rate was quantified according to Archard's wear law [223], which can be defined as

$$W = \frac{V}{F \cdot S} \quad (\text{Eq. 6.1})$$

where W is the wear rate ($\text{mm}^3/\text{N} \cdot \text{m}$), V is the wear volume (mm^3), F is the applied normal load (N), and S is the total sliding distance (m). The surface morphology, cross-sectional morphology, and chemical composition of the worn tracks were characterized by SEM and EDS to analyze the wear mechanisms.

6.2 Microstructure, Deposition behavior and Phase structure

6.2.1 General Microstructure

Fig. 6.2 shows the cross-sectional microstructure of the cold-sprayed CoCrFeNiMo_x HEA deposits. Micropores and incomplete particle bonding can be observed in the deposits, which are the typical manufacturing defects in cold-sprayed deposits. Such defects are generally associated with the insufficient plastic deformation of HEA particles during the deposition. The relative density of the CoCrFeNiMo_x HEA deposits was estimated to be $98.62 \pm 0.49\%$ (Mo₀), $98.05 \pm 0.23\%$ (Mo_{0.2}), $97.99 \pm 0.25\%$ (Mo_{0.5}) and $97.98 \pm 0.72\%$ (Mo_{1.0}) respectively. The relative density shows

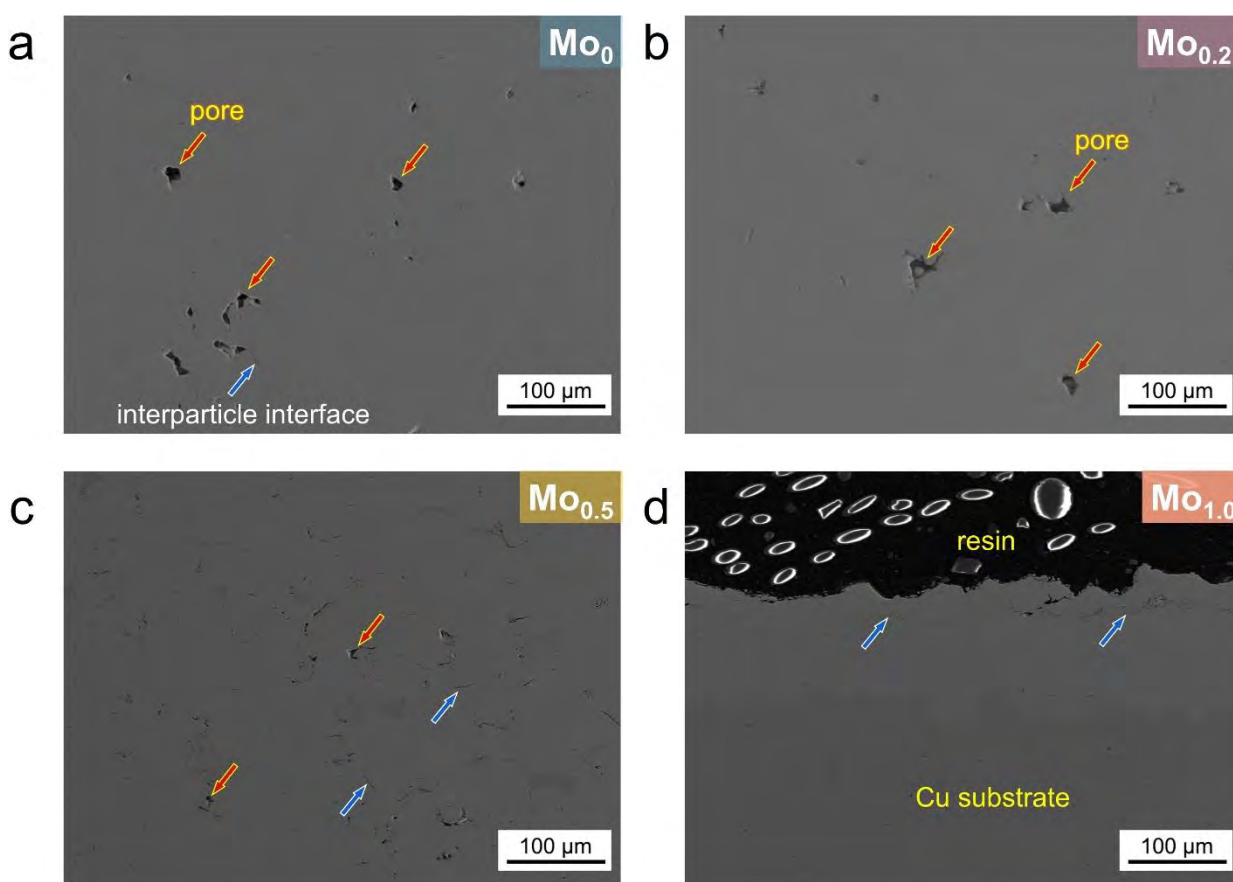


Fig. 6.2 Cross-sectional microstructure of the cold-sprayed CoCrFeNiMo_x HEA deposits. (a) Mo₀, (b) Mo_{0.2}, (c) Mo_{0.5}, (d) Mo_{1.0}.

a downward trend, which can be attributed to the increased plastic deformation resistance with the increase in the Mo ratio of CoCrFeNiMo_x HEAs. In addition, it is notable that the thickness of the Mo_{1.0} deposit is only around 0.1 mm in comparison to the thick Mo₀, Mo_{0.2}, and Mo_{0.5} deposits. This suggests that the deposition of Mo_{1.0} HEA powder is rather difficult, even though high processing parameters were used.

6.2.2 *Single Splat Deposition*

Fig. 6.3 shows the representative surface morphologies of individual CoCrFeNiMo_x HEA particles deposited onto polished cold-sprayed CoCrFeNiMo_x deposits. The spherical Mo₀ particle (see **Fig. 6.3a**) was flattened after high-velocity impact, suggesting the good ductility of the material. This also happened to Mo_{0.2} and Mo_{0.5} particles, as evidenced by the severely plastic deformed particles in **Fig. 6.3b** and **Fig. 6.3c**. The sufficient plastic deformation of particles contributes to the fabrication of deposits with fewer defects and better interparticle bonding. While for the Mo_{1.0} particles, the deposited particles were nearly hemispherical in shape, and shear cracks and fractures were visible, implying the brittle feature of the material. Such difference can be attributed to the increased deformation resistance with the increased Mo ratio in the CoCrFeNiMo_x HEA particles. It is reported that the as-casted Mo₀ HEA presented a compressive yield strength of 207 MPa and a 60% engineering strain without failure. While the compressive yield strength significantly increased to 825 MPa for Mo_{1.0} HEA due to the solid solution strengthening and precipitation strengthening, but the fracture strain was as low as 11.4% [316]. This is consistent with the brittle characteristics of the deposited Mo_{1.0} particles, as shown in **Fig. 6.3d-f**. The impact of subsequent particles onto the previous deposited layers or particles could lead to further particle fracture. The high deformation resistance and the brittle characteristics led to the low deposition efficiency of the Mo_{1.0} HEA deposit under the current processing parameters, and

the thickness of the deposit was limited to about 0.1 mm, as shown in Fig. 6.2d.

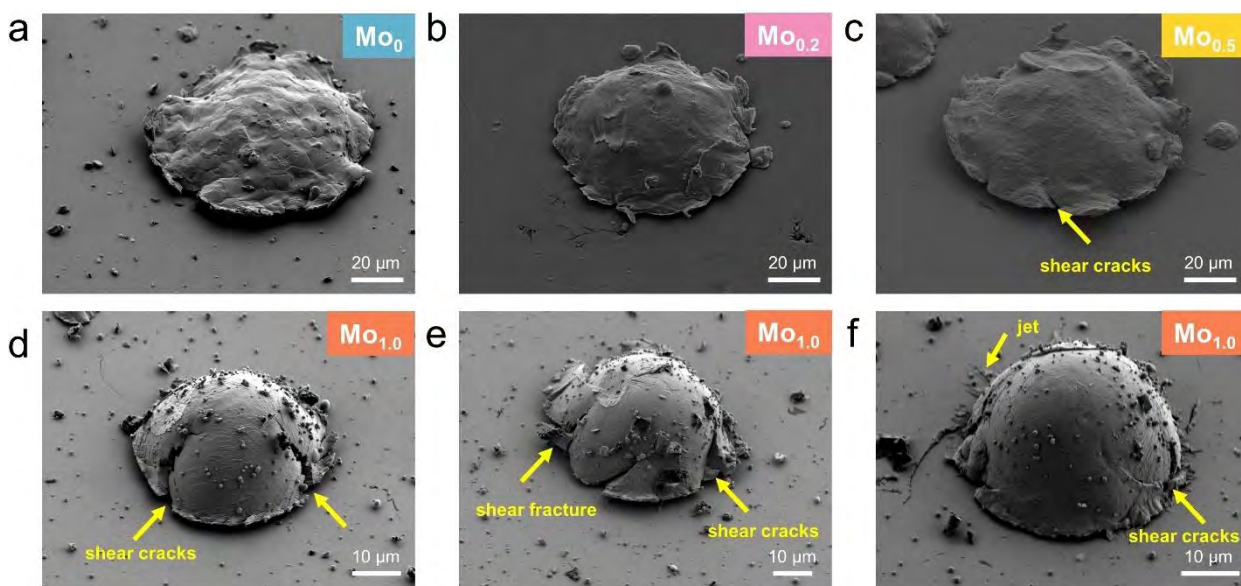


Fig. 6.3 Representative surface morphologies of individual deposited CoCrFeNiMo_x HEA particles. (a) Mo₀, (b) Mo_{0.2}, (c) Mo_{0.5}, (d-f) Mo_{1.0}. Note the substrate used in single particle deposition is the polished cold-sprayed CoCrFeNiMo_x deposits.

6.2.3 Phase Composition

Fig. 6.4 displays the XRD spectrum of the CoCrFeNiMo_x HEA feedstock powder and the cold-sprayed deposits. The Mo₀ deposit is identified as a single FCC solid solution structure as the original Mo₀ feedstock powder. However, the deposit shows a broadening in the peaks compared with the powder (see the enlarged XRD pattern in Fig. 6.4b), which can be attributed to the increased lattice defects and the refined grains induced by severe plastic deformation during the deposition process [317]. The Mo_{0.2} powder and corresponding deposit are also indexed as FCC phase, but the diffraction peaks shifted toward lower diffraction angles compared with Mo₀ powder and deposit, indicating the increase in lattice parameters. Due to the large atomic size difference between Mo and the other four elements (i.e., Co-0.125 nm, Cr-0.128 nm, Fe-0.126 nm, Ni-0.124 nm, and Mo-0.139 nm), the doping of Mo into CoCrFeNi HEA leads to lattice distortion [318]. This can also be demonstrated by

the lattice constant of Mo₀ and Mo_{0.2} deposits, which are determined to be 3.5577 Å and 3.5912 Å, respectively. The Mo_{0.5} and corresponding deposit were also identified as a single FCC solid solution structure, which was inconsistent with previous studies. It is reported that the as-casted CoCrFeNiMo_{0.5} was composed of FCC and hard brittle σ phase, and the σ phase appeared near the diffraction peak of the (111) plane [319,320]. Such difference is believed to be associated with the different manufacturing processes. Compared with the casting method, the microstructure of cold-sprayed deposits is more refined, and the size and content of the σ phase may exceed the detection limit of XRD. The increase in the Mo ratio resulted in more severe lattice distortion, as evidenced by the lattice parameter of Mo_{0.5} (3.6227 Å). The lattice distortion induced by the atomic size mismatch can lead to enhanced solid solution strengthening, which will hinder the movement of dislocation and lead to improved wear resistance. For the Mo_{1.0} feedstock powder and deposit, the hard and brittle sigma (σ) phase and mu (μ) phase were identified, as shown in Fig. 6.4a. The valence electron concentration (VEC) is regarded as a useful parameter to predict the stability of solid solution phases in HEAs, which can be expressed as:

$$VEC = \sum_i^n C_i VEC_i \quad (\text{Eq. 6.2})$$

where C_i is the atomic percentage of each element in HEA, and VEC_i is the VEC of each element. The VEC for CoCrFeNiMo_x HEA is calculated to be 8.25 (Mo₀), 8.14 (Mo_{0.2}), 8.00 (Mo_{0.5}), and 7.80 (Mo_{1.0}) respectively. It was reported that FCC is stable when $VEC \geq 8$, while BCC is stable when $VEC \leq 6.87$ [321,322]. Moreover, the formation of σ phase in Cr-containing HEAs is expected when the VEC is between 6.88 and 7.84 [323]. The formed σ and μ phases are believed to further improve the mechanical performance of the Mo_{1.0} deposit.

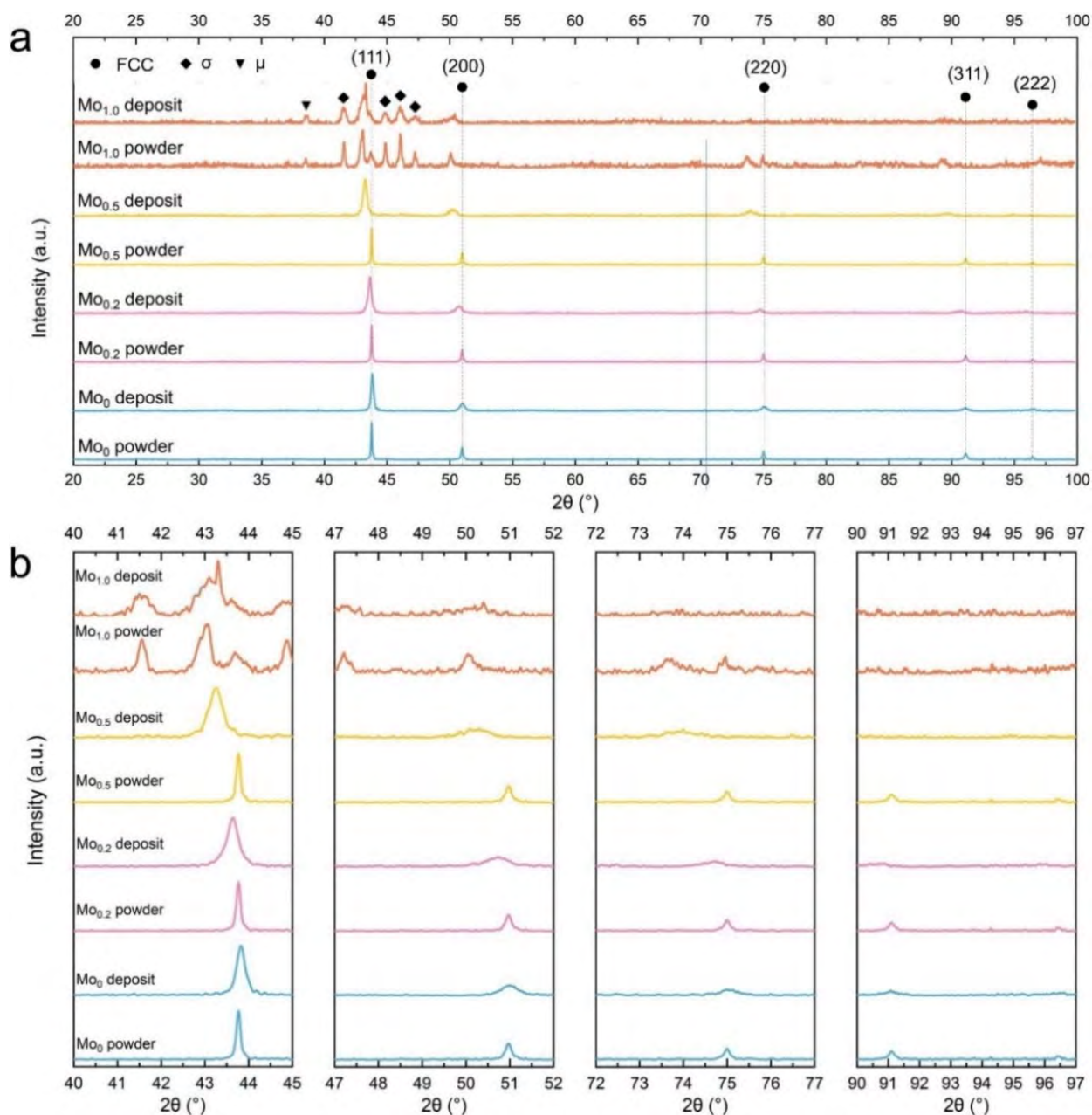
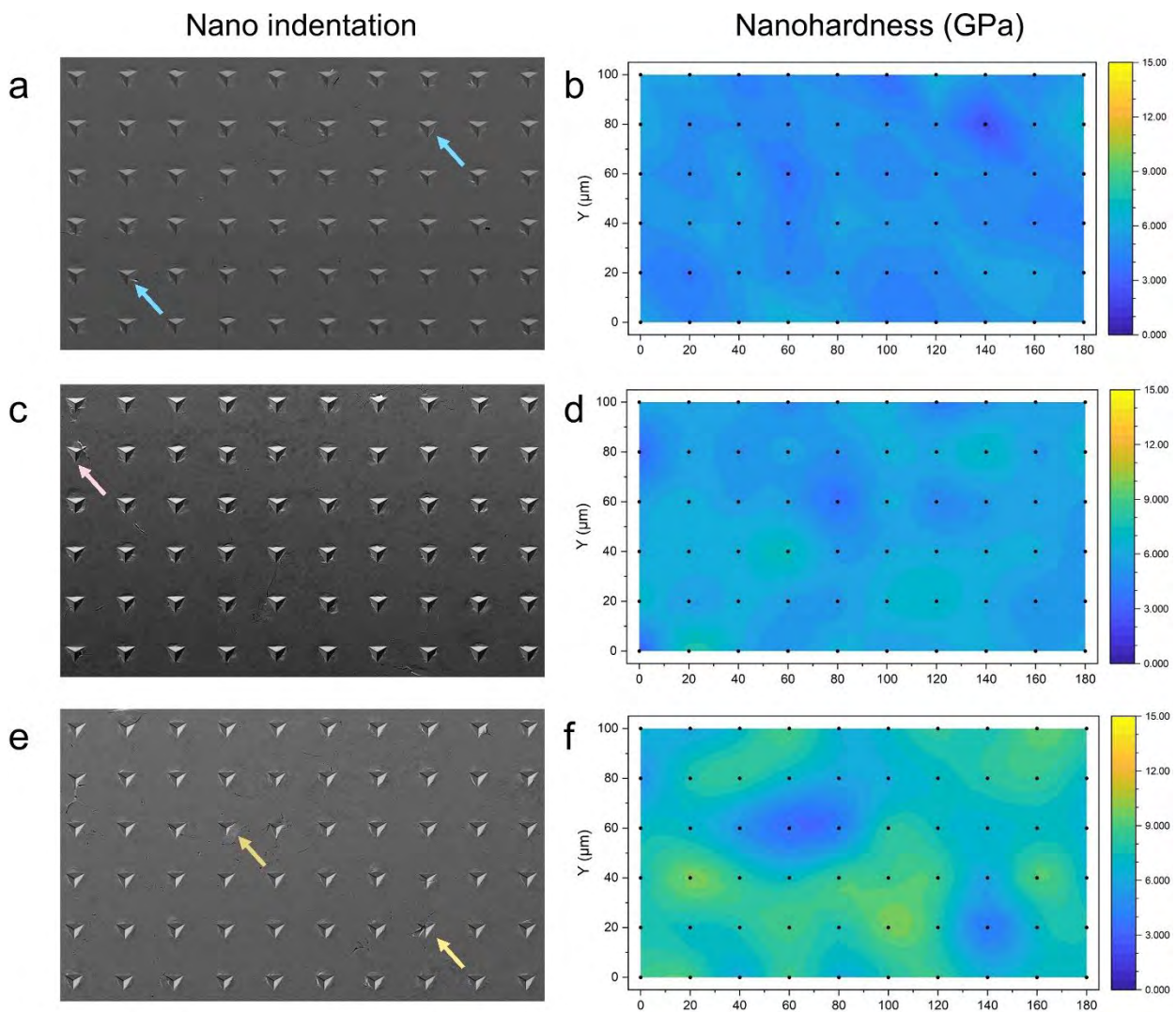


Fig. 6.4 X-ray diffraction (XRD) analysis of the CoCrFeNiMo_x HEA feedstock powder and the cold-sprayed deposits in the range of 20° to 100°. (a) XRD patterns, (b) Magnified patterns of main peaks.

6.3 Nanohardness

Fig. 6.5 and **Fig. 6.6** display the SEM images of the indentation matrix and corresponding contour maps of nanohardness and modulus versus position. It is

observed that all the deposits exhibited microscale heterogeneity, as indicated by the color variability in the hardness mapping. On the one hand, due to the existence of particle-particle boundaries and the micropores, the indentation near these defects (as indicated by the arrows) exhibited lower hardness and modulus. On the other hand, the high-velocity impact of the originally spherical particle led to significant strain, strain rate, and temperature gradients during severe plastic deformation and the resultant heterostructure. Specifically, ultra-fine grains usually form near interfacial regions due to grain fragmentation and dynamic recrystallization, while elongated and flattened grains remain in the particle interior. Such cross-scale grain structure led to the heterogeneous mechanical properties at different positions.



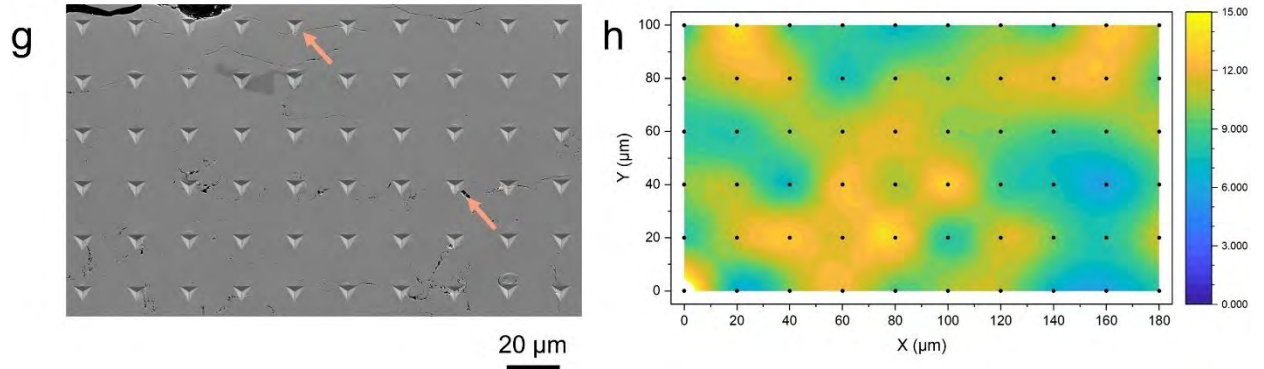


Fig. 6.5 Nanoindentation (left column) and nano-hardness (right column) mapping obtained from 10 x 6 nanoindentation grids on the polished cross-sectional CoCrFeNiMo_x HEA samples fabricated by cold spray. (a, b) Mo₀, (c, d) Mo_{0.2}, (e, f) Mo_{0.5}, (g, h) Mo_{1.0}.

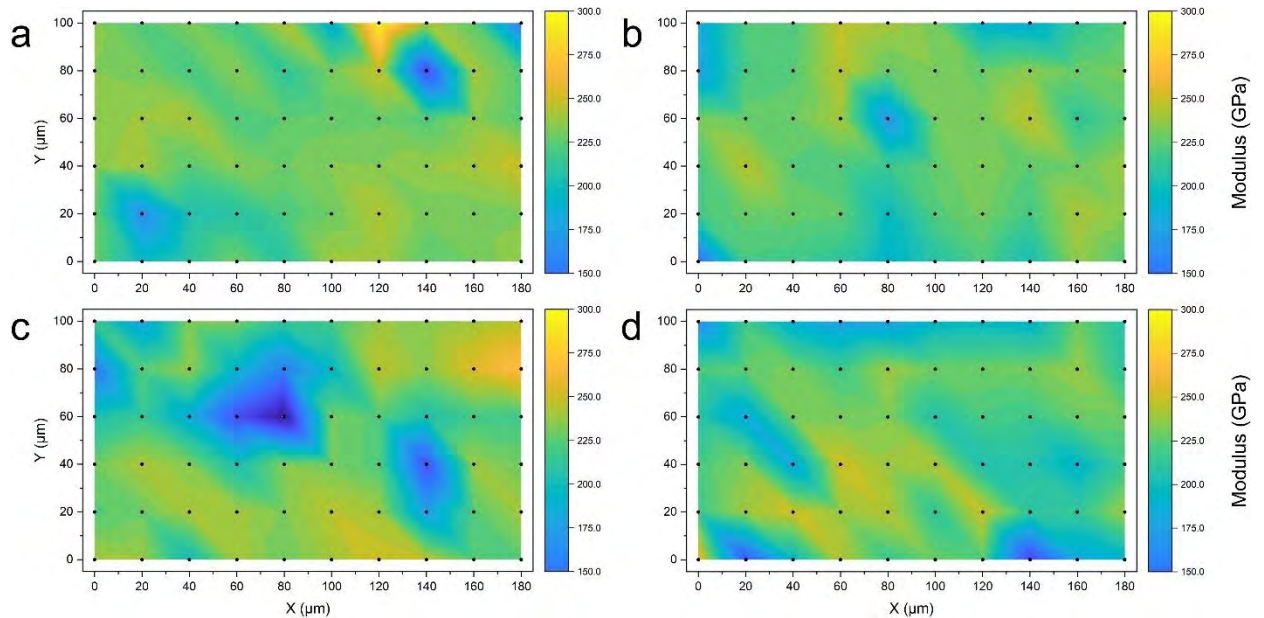


Fig. 6.6 Modulus mapping obtained from 10 x 6 nanoindentation grids on the polished cross-sectional CoCrFeNiMo_x HEA samples fabricated by cold spray. (a) Mo₀, (b) Mo_{0.2}, (c) Mo_{0.5}, (d) Mo_{1.0}.

Fig. 6.7 shows the average nanohardness, modulus, and representative load-displacement curves of the cold-sprayed CoCrFeNiMo_x HEA deposits during loading-unloading nanoindentation tests. The nanohardness increased from 5.01 ± 0.79 GPa to 10.2 ± 2.39 GPa with the increase in Mo ratio from 0 to 1.0 in

CoCrFeNiMo_x HEA deposits, as shown in [Fig. 6.7a](#). The nanohardness of the Mo_{0.2} and Mo_{0.5} deposits are 5.69 ± 0.97 GPa and 7.34 ± 1.47 GPa, respectively. Such a trend is in line with the previous study that the increase of Mo addition leads to the increased hardness in the CoCrFeNiMo_x HEAs [\[318,319\]](#). On the one hand, cold-sprayed deposits generally exhibited higher hardness than their counterparts due to the significant work hardening induced by severe plastic deformation. On the other hand, the doping of Mo into CoCrFeNi led to the lattice distortion of the FCC structure due to its larger atom size, which can be confirmed by the increased lattice constant calculated from the XRD data (see [Fig. 6.4](#)). Moreover, the hard σ and μ intermetallic precipitated in the FCC matrix further contributed to the high hardness of the Mo_{1.0} deposit. The modulus of Mo₀ reached 225.88 ± 23.32 GPa, and it slightly decreased to 220.79 ± 19.62 GPa (Mo_{0.2}), 219.30 ± 32.43 GPa (Mo_{0.5}) and 214.97 ± 27.09 GPa (Mo_{1.0}) respectively with the increase of Mo ratio in CoCrFeNiMo_x HEA deposits, as shown in [Fig. 6.7b](#).

It is reported that the ratio between hardness (H) and modulus (E) can be taken as a parameter to predict the wear resistance of a material (e.g., elastic strain to failure, the critical yield stress for plastic deformation, and the fracture toughness) [\[324\]](#). The ratio of hardness to elastic modulus (H/E) is related to the elastic strain to failure capability. The H/E of the cold-sprayed CoCrFeNiMo_x HEA deposits shows a near-linear increased trend with the increased ratio of Mo element. The H³/E² ratio, also known as the plasticity index, can be considered as a parameter to describe the resistance to plastic deformation [\[324\]](#). The H³/E² value of the Mo_{1.0} deposit reached 0.023 GPa, which is 86.96% higher than that of the Mo₀ deposit and 60.87% higher than that of the Mo_{0.5} deposit, respectively, as summarized in [Table. 6.2](#). This suggests that the Mo_{1.0} deposit exhibits high plastic deformation resistance and is expected to show superior wear resistance than the other deposits.

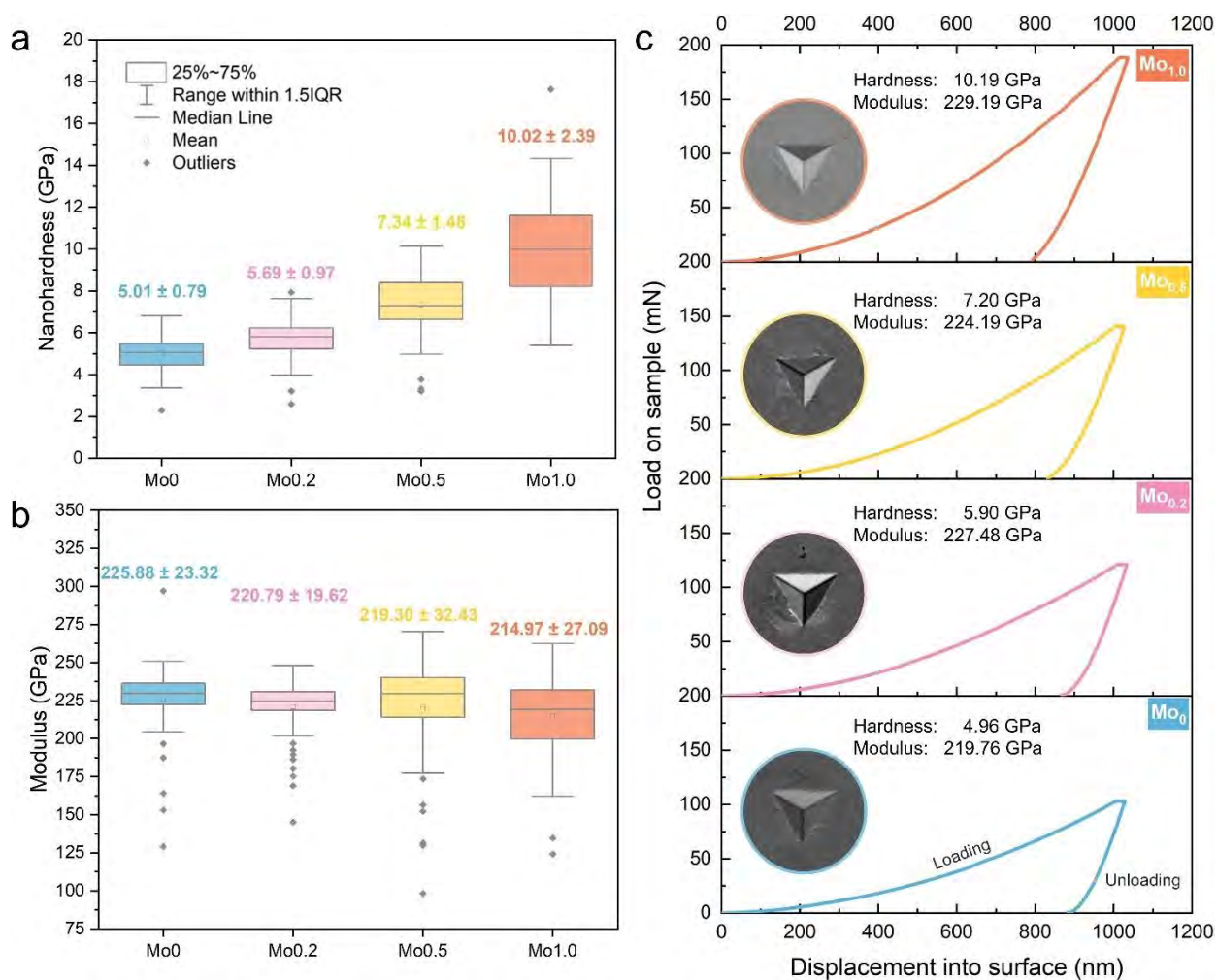


Fig. 6.7 (a) Nanohardness, (b) Modulus, and (c) Representative load-displacement curves of the cold-sprayed CoCrFeNiMo_x HEA deposits from the nanoindentation tests.

Table 6.2 Summary of Hardness (H), Modulus (E), H/E and H³/E² values of the cold-sprayed CoCrFeNiMo_x HEA deposits from the nanoindentation test.

Deposit	H (GPa)	E (GPa)	H/E	H ³ /E ² (GPa)
Mo ₀	5.01 ± 0.79	225.88 ± 23.32	0.022 ± 0.004	0.003 ± 0.001
Mo _{0.2}	5.69 ± 0.97	220.79 ± 19.62	0.026 ± 0.004	0.004 ± 0.002
Mo _{0.5}	7.34 ± 1.48	219.30 ± 32.43	0.033 ± 0.004	0.009 ± 0.003
Mo _{1.0}	10.02 ± 2.39	214.97 ± 27.09	0.046 ± 0.007	0.023 ± 0.013

6.4 Dry Sliding Wear Behavior

6.4.1 Coefficient of Friction

Fig. 6.8 shows the dry-sliding wear behavior of the cold-sprayed CoCrFeNiMo_x HEA deposits. The working principle of the tribometer used for dry-sliding wear behavior investigation was provided in **Fig. 6.8a**. The ball remains stationary while the platform together with the specimen reciprocates along the x-direction during the test. **Fig. 6.8b** plots the COF evolution history of the CoCrFeNiMo_x HEA deposits. All the deposits exhibit a running-in process (stage I) at the initial stage of the wear test, which is the result of contacting between micro-protrusions or asperities on the surface of the friction pair (i.e., GCr15 ball / CoCrFeNiMo_x HEA deposits). This two-body abrasion leads to a rapid increase in COF. In stage II, the COF fluctuated with time particularly for the Mo₀ and Mo_{0.2} specimens. This could be associated with the material removal from the friction pair, suggesting the poor wear resistance of the deposits. As the friction proceeded, wear debris was peeled off from the deposit surface and piled up between the two contacting surfaces, and the contact modes changed from two-body abrasion to three-body abrasion. For the Mo_{0.5} deposit, the fluctuation of COF was significantly weakened at stage II, exhibiting a slow upward trend in the range of 0.3 and 0.4. This could be attributed to the enhanced hardness of the deposit. The COF of the Mo_{1.0} deposit decreased after the running-in stage and steadily increased (stage II), with a higher COF level than that of the Mo_{0.5} deposit. In the late testing period (stage III), there is no obvious fluctuation of COF, particularly for Mo₀ and Mo_{1.0} deposits, which suggests the dynamic equilibrium of the wear. However, the steady-wear stage was not found for the Mo_{0.2} deposit. The sudden drop and rise of COF before the test end could be associated with the peeling off from the Mo_{0.2} deposit, and it was expected that the COF would tend towards stability at stage III for the Mo₀ deposit if the friction continued.

The average COF of the cold-sprayed CoCrFeNiMo_x HEA deposits based on the results of three tests was summarized in Fig. 6.8c. The Mo₀ deposit exhibits the highest coefficient of friction (COF) among all the deposits, and the average COF is 0.705 ± 0.009 . With the increase of Mo ratio in the CoCrFeNiMo_x HEA deposits, the COF decreased to 0.649 ± 0.017 (Mo_{0.2}) and 0.401 ± 0.008 (Mo_{0.5}), respectively. This suggests that less friction force is required for the sliding on the Mo-doped CoCrFeNi HEA deposit against the GCr15 ball. However, a further increase in Mo content led to the increased COF to 0.638 ± 0.032 (Mo_{1.0}). The decrease followed by the rebound of COF with the increasing Mo ratio in CoCrFeNiMo_x HEA was also found in previous studies [316,325].

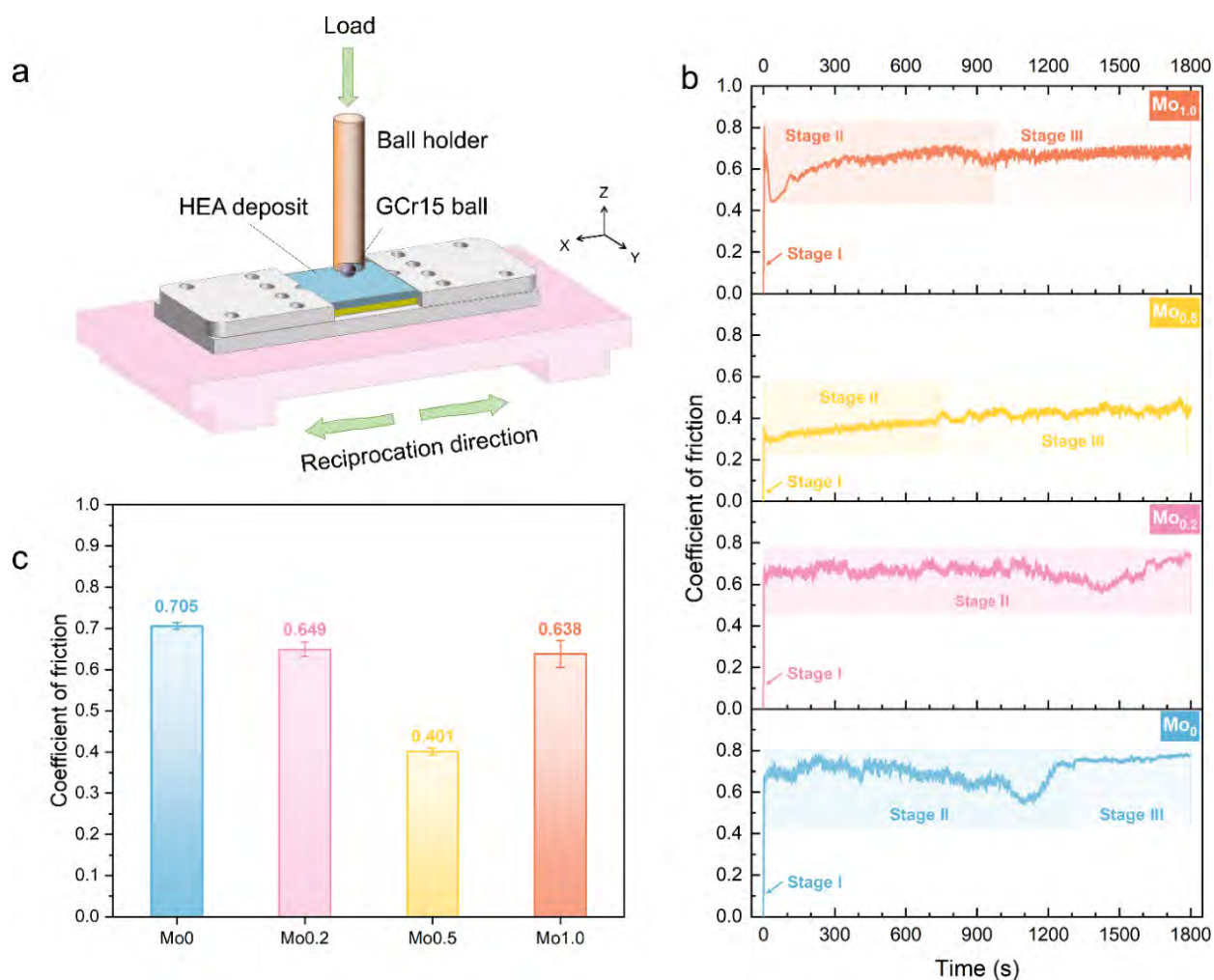


Fig. 6.8 Dry-sliding wear behavior of the cold-sprayed CoCrFeNiMo_x HEA deposits. (a) Schematic diagram of the reciprocating sliding friction and wear test, (b) Representative plots of

COF as a function of sliding time, (c) Coefficient of friction (COF) averaged from three tests.

The main parameters for the dry sliding wear test include normal load (20 N), oscillating frequency (4.0 Hz), stroke length (5.0 mm), and time of duration (30 mins).

6.4.2 2D & 3D Wear Track Morphology and Specific Wear Rate

Fig. 6.9 exhibits the 2D surface morphology and the 3D topography of the representative wear tracks of the cold-sprayed CoCrFeNiMo_x HEA specimens. The different colors indicate the depth change of the wear surface. The wear tracks of the Mo₀ and Mo_{0.2} deposits are nearly elliptical in shape, and the closer to the center of the elliptical, the deeper the wear track is. The maximum width and depth of the wear tracks were measured based on the optical images, as plotted in **Fig. 6.10a**. Compared with the Mo₀ deposit, the maximum width was decreased from 2.12 mm to 2.02 mm, and the maximum depth was also decreased from 0.267 mm to 0.246 mm, suggesting the reduced wear volume and the improved resistance to material removal for the Mo_{0.2} deposit. The wear track of the Mo_{0.5} deposit exhibited a “pill shape”, and the width and depth of the wear track further decreased to 1.18 mm and 0.083 mm, respectively. The Mo_{1.0} deposit exhibited the narrowest and shallowest wear track among all the deposits, and the average maximum width and depth were measured to be 0.89 mm and 0.052 mm, respectively. This implies that the doping of Mo element into CoCrFeNi HEA can significantly reduce the wear volume, which is associated with the increased hardness of the CoCrFeNiMo_x HEA deposits with the increased ratio of Mo element (see **Fig. 6.5**). According to Archard's law, the volume of the worn material is inversely proportional to the material hardness [223]. Moreover, the parameter H^3/E^2 (as listed in **Table. 6.2**) also shows an increasing trend with the increase in Mo ratio, indicating the increased plastic deformation resistance and the enhanced wear resistance of the cold-sprayed CoCrFeNiMo_x HEAs.

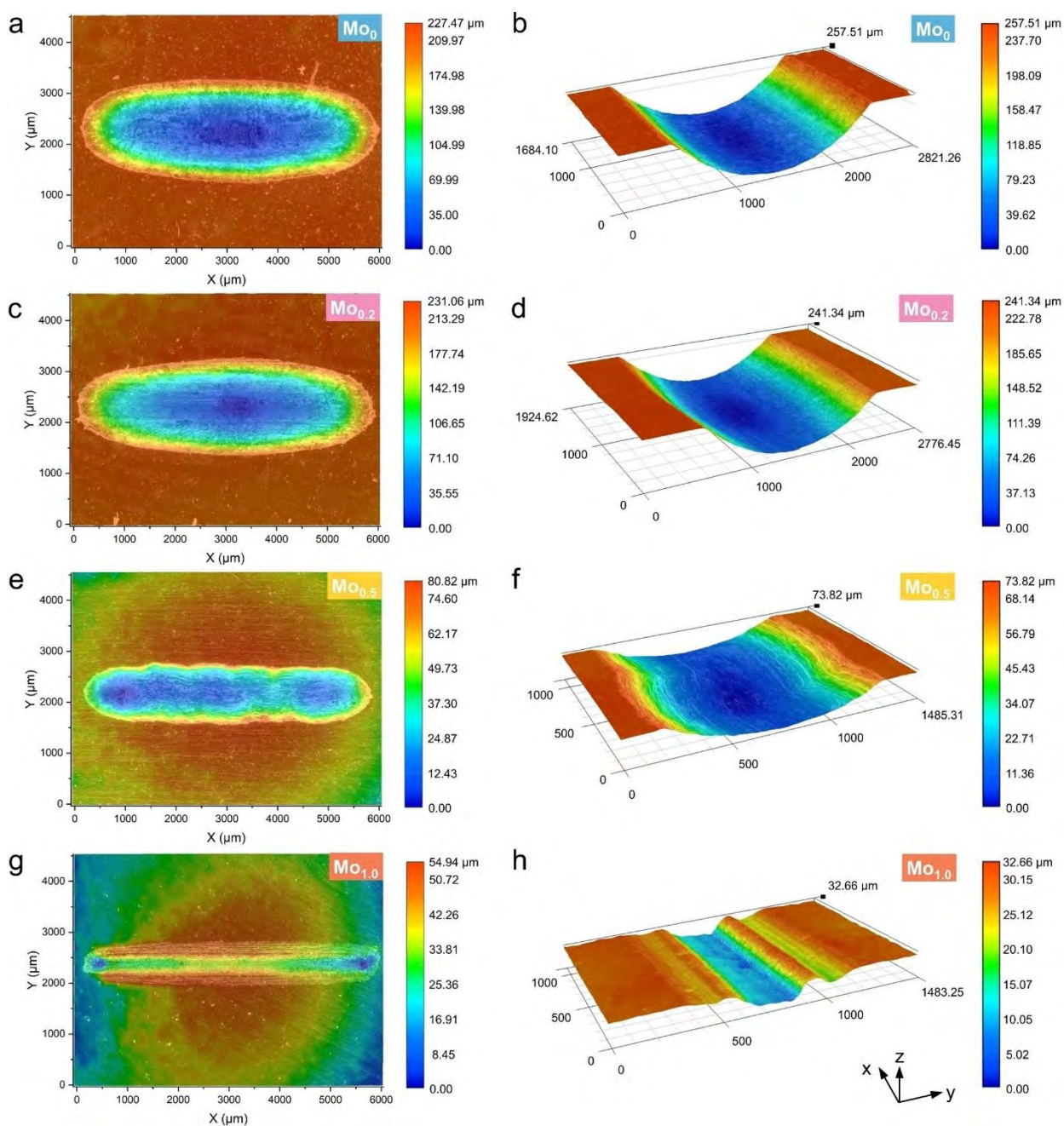


Fig. 6.9 2D surface morphology (left side) and 3D topography (right side) of the wear tracks on the cold-sprayed CoCrFeNiMo_x HEA deposits. (a, b) Mo_0 , (c, d) $\text{Mo}_{0.2}$, (e, f) $\text{Mo}_{0.5}$, (g, h) $\text{Mo}_{1.0}$.

For a more accurate description of the wear characteristic of the cold-sprayed CoCrFeNiMo_x HEA, the specific wear rate ($\text{mm}^3/\text{N}\cdot\text{m}$) was calculated, as shown in **Fig. 6.10b**. The Mo_0 deposit exhibits the worst wear resistance with a specific wear rate of $1.0 \times 10^{-3} \text{ mm}^3/\text{N}\cdot\text{m}$. The addition of Mo resulted in a gradual decrease in the

specific wear rate of the deposits, and the wear rate was down by 17.4%, 80.6%, and 94.9% for the Mo_{0.2}, Mo_{0.5}, and Mo_{1.0} deposits. **Table. 6.3** summarizes the specific wear rate of CoCrFeNiMo_x HEAs fabricated by different manufacturing methods. It can be found the specific wear rate exhibits a downward trend with the increase ratio of Mo element [316,318,325,326]. In addition, the wear resistance of the cold-sprayed CoCrFeNiMo_x HEA deposits is comparable or even superior to their counterparts. The significantly improved wear resistance can be attributed to the enhanced hardness induced by solid solution strengthening and the precipitation of hard phases [325].

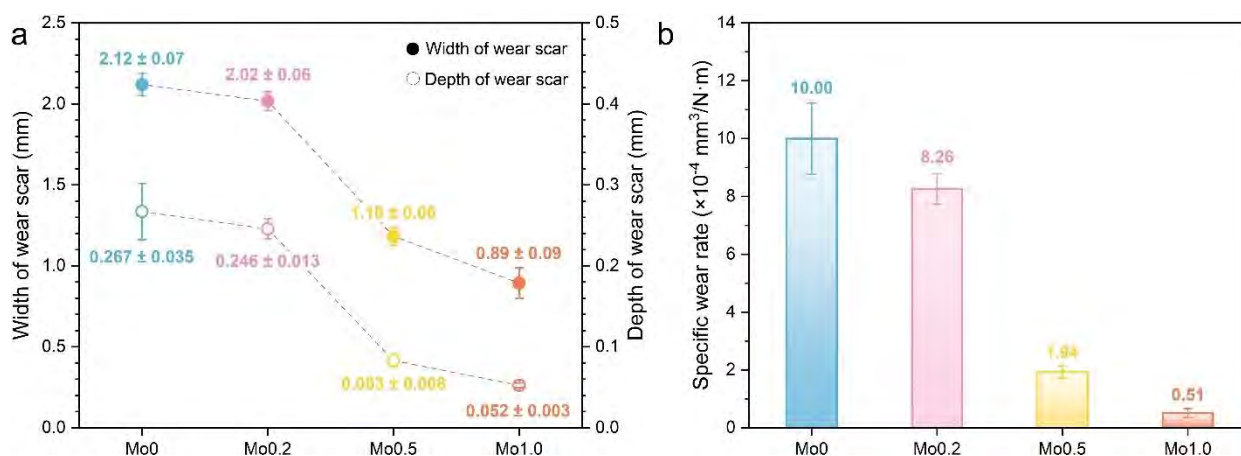


Fig. 6.10 (a) The maximum width and depth of the wear tracks and (b) The specific wear rate of the cold-sprayed CoCrFeNiMo_x HEA deposits.

Table. 6.3 Summarization of the specific wear rate of CoCrFeNiMo_x HEA samples fabricated by different manufacturing routes.

Raw material	Manufacturing routes	Specific wear rate (mm ³ /N·m)	Ref
Mo ₀		0.36	
Mo _{0.15}	FeCoNiCr and Mo powders Ball milling + Laser cladding	0.32	[326]
Mo _{0.2}		0.26	
Mo _{0.25}		0.22	
Mo ₀	Spherical HEA powders Spark plasma sintering + Cold rolling	0.42 × 10 ⁻³	[318]
Mo _{0.1}		0.36 × 10 ⁻³	
Mo _{0.3}		0.33 × 10 ⁻³	

Mo _{1.0}	Gas-atomized powder	Laser cladding	$\sim 3 \times 10^{-5}$	[327]
Mo _{0.2}	Pure metal powders	Casting + High-current pulsed electron beam	$0.92 \times 10^{-4} \sim 6.07 \times 10^{-4}$	[328]
Mo ₀	Pure metal powders	Casting	$\sim 8.50 \times 10^{-4}$	[316]
Mo _{0.3}			$\sim 5.85 \times 10^{-4}$	
Mo _{0.5}			$\sim 1.68 \times 10^{-4}$	
Mo ₁			$\sim 0.83 \times 10^{-4}$	
Mo _{1.5}			$\sim 1.30 \times 10^{-4}$	
Mo _{0.5}	Gas-atomized powder	Plasma spraying	1.27×10^{-4}	[329]
Mo _{0.2}	Pure metal powders	Ball milling + Laser cladding	1.33×10^{-3}	[330]
Mo ₀	Pure metal powders	Ball milling + Laser cladding	0.76	[325]
Mo _{0.3}			0.64	
Mo _{0.6}			0.44	
Mo _{0.9}			0.40	
Mo _{1.2}			0.29	

6.4.3 Worn Surface Morphology and Wear Mechanism

To unveil the wear mechanisms of the cold-sprayed CoCrFeNiMo_x HEA deposits, the morphology and chemical composition of the worn surface were examined by using SEM and EDS. **Fig. 6.11** shows the representative worn surface morphology of the Mo₀ HEA deposit. The worn surface exhibited scratches and furrows (see **Fig. 6.11a** and **b**) along the sliding direction, which were the typical features of abrasive wear. In addition, some dark-layered structures attached to the worn surface can be observed, as indicated by the white arrows in **Fig. 6.11b**. The EDS mapping (see **Fig. 6.11c**) shows that such a layered structure was oxygen-rich, suggesting that the layered structure was composed of oxides. Quantitatively, a high oxygen element content (17.47 wt%) was detected at position 1 on the oxidation layer, while the oxygen element content was only 1.28 wt% on the worn surface (see position 2). The formation of the oxidation layer on the worn surface can be attributed to the accumulation of heat generated by frictional interaction between the deposit surface and grinding ball and plastic deformation during the wear process [331]. The dark oxide layer was full of micro-cracks and nonuniformly distributed on the worn surface, which resulted in poor wear resistance [332]. Furthermore, the detection of

Mn, Si, and C elements on the worn surface indicated that the material from the GCr15 ball transferred to the worn surface of the Mo₀ deposit (see Fig. 6.11c and Fig. 6.11d), which exhibited adhesive wear characteristics.

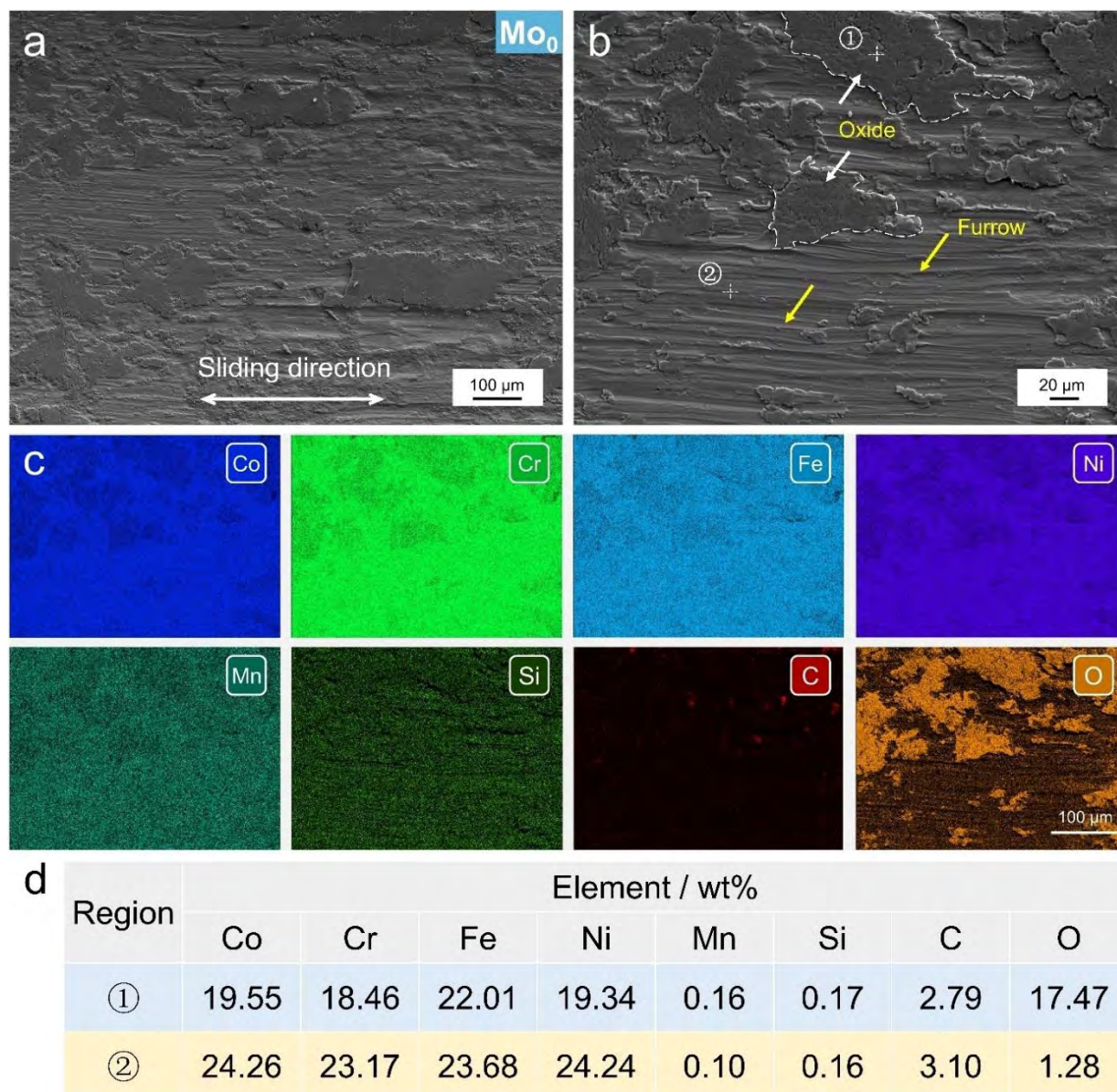


Fig. 6.11 Representative worn surface morphology and EDS results of the cold-sprayed CoCrFeNi HEA deposit. (a) and (b) SEM images, (c) EDS mapping and points analysis.

Fig. 6.12 shows the representative worn surface morphology of the cold-sprayed Mo_{0.2} HEA deposit. Compared to the worn surface of the Mo₀ deposit, the furrows became narrowed and shallowed, implying improved wear resistance. Moreover,

the shape of the oxide changed from large-sized lamellae to small fragments, and the number of oxides on the worn surface also dramatically decreased, as shown in Fig. 6.12a and b. The EDS results show that the oxygen element content at position 1 (oxide) and position 2 (worn surface) was 16.97 % and 4.25%, respectively. The elements of Mn, Si, and C can also be identified on the worn surface, which is the feature of adhesive wear. The wear mechanism of $\text{Mo}_{0.2}$ is dominated by abrasive wear, adhesive wear, and oxidative wear.

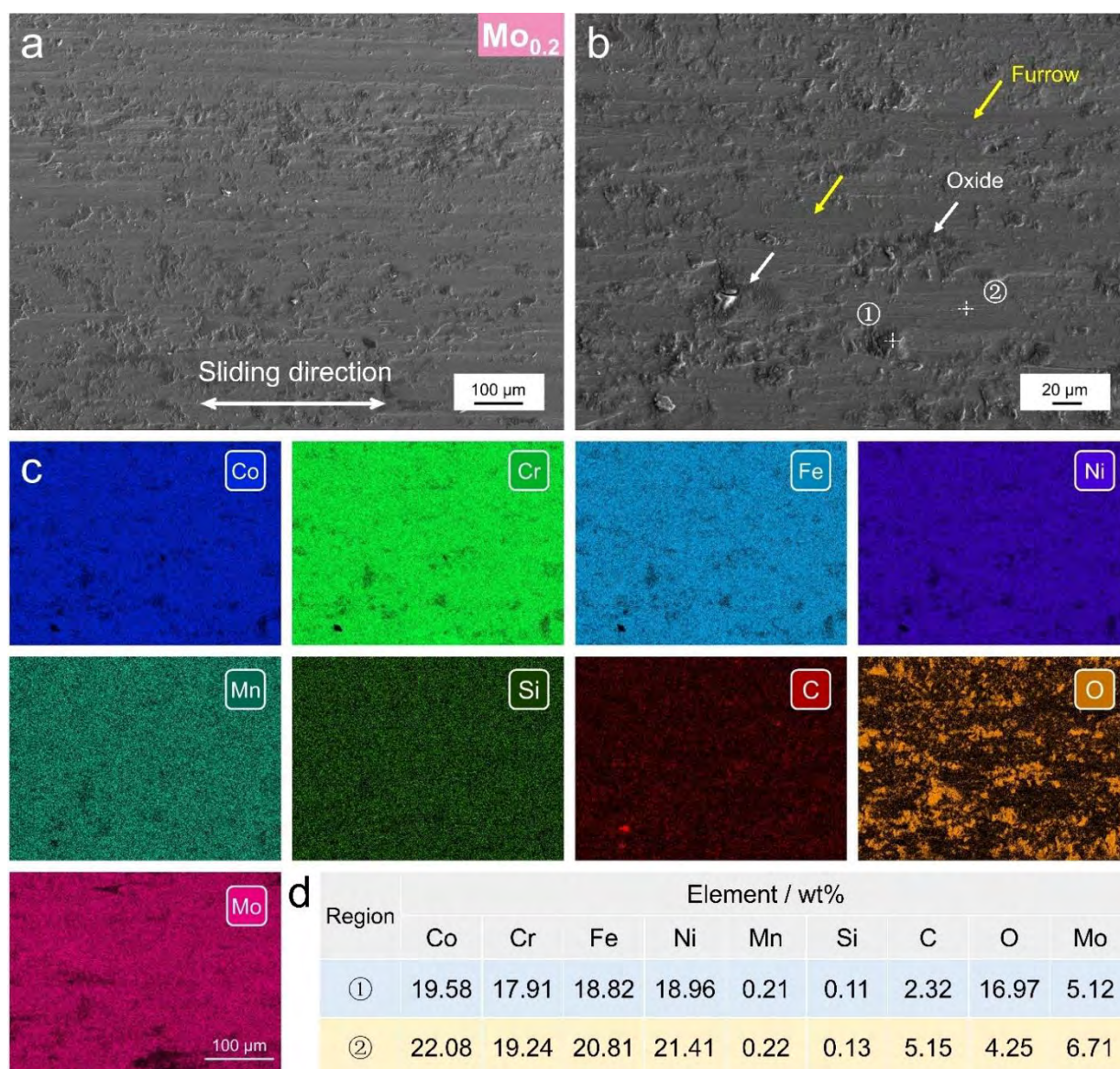


Fig. 6.12 Representative worn surface morphology and EDS results of the cold-sprayed $\text{CoCrFeNiMo}_{0.2}$ HEA deposit. (a) and (b) SEM images, (c) EDS mapping and points analysis.

From the representative worn surface morphology of the Mo_{0.5} HEA deposit (see Fig. 6.13), the worn surface became smooth, and the width and depth of the furrows were significantly reduced. This suggests the improvement of wear resistance of the Mo_{0.5} deposit, which can also be demonstrated by the dramatically decreased specific wear rate, as shown in Fig. 6.10b. Moreover, fewer oxides were visible although the oxygen element was widely distributed on the worn surface.

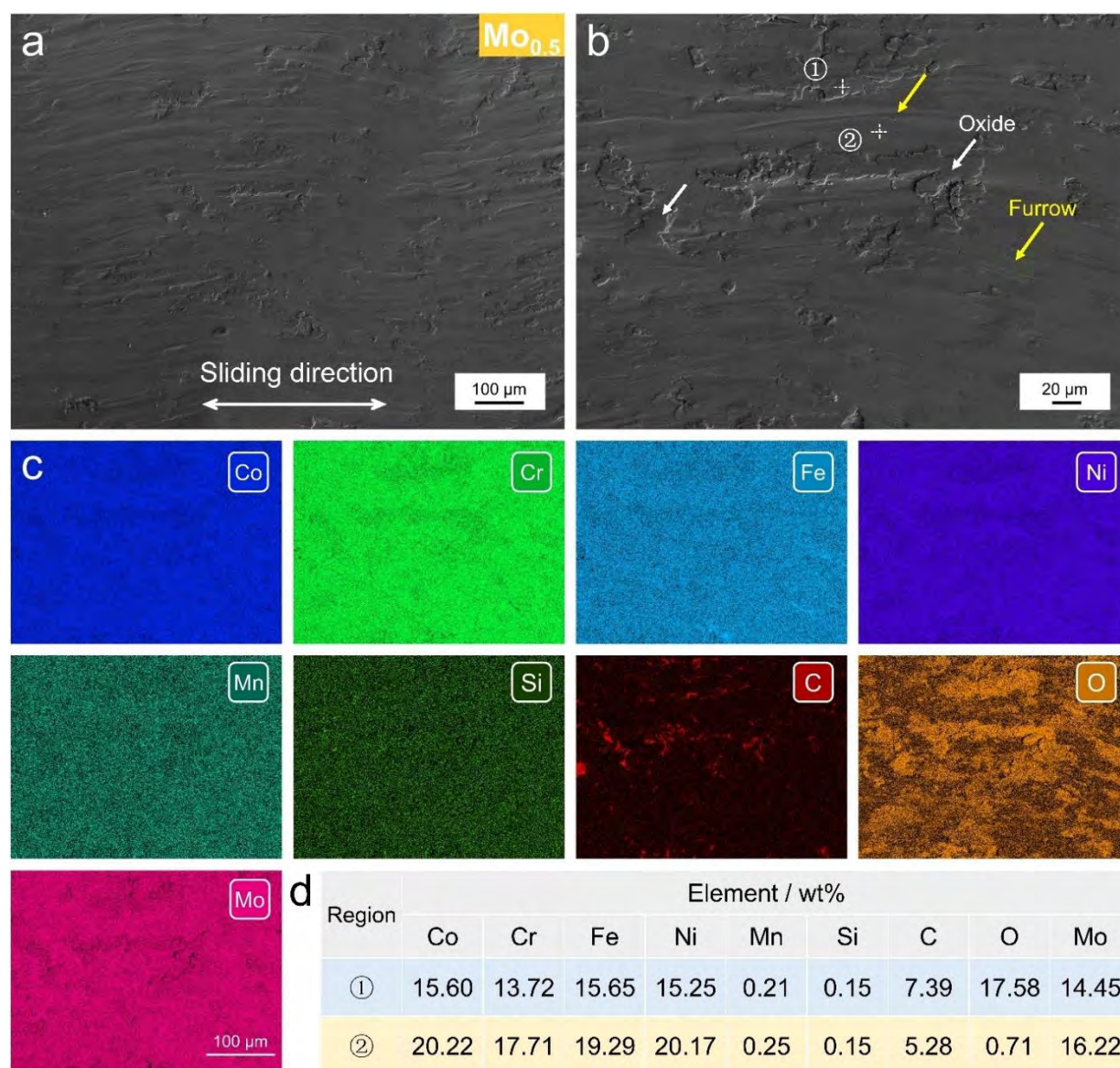


Fig. 6.13 Representative worn surface morphology and EDS results of the cold-sprayed CoCrFeNiMo_{0.5} HEA deposit. (a) and (b) SEM images, (c) EDS mapping and points analysis.

Fig. 6.14 exhibits the representative worn surface morphology of the cold-sprayed Mo_{1.0} HEA deposit. The furrows parallel to the sliding direction (as pointed by the yellow arrows in **Fig. 6.14b**) and the detection of elements from the GCR15 ball (see **Fig. 6.14c**) indicated the abrasive wear and adhesive wear characteristics. In addition, the particle-particle boundaries were clearly visible, which is dramatically different from the worn surfaces of the other deposits. It can be found that the majority of particles were near-spherical after deposition due to the high deformation resistance. Moreover, some particles were completely peeled off from the deposit surface, as shown in **Fig. 6.14b**. The detection of Cu element in the EDS mapping indicated localized base metal was exposed after the wear test despite the lowest specific wear rate of the deposit (see **Fig. 6.10b**). This can be attributed to the limited thickness of the Mo_{1.0} deposit (~0.1 mm). The increase in the Mo ratio in CoCrFeNiMo_x HEA powders can indeed enhance the wear resistance of the cold-sprayed deposits, but this also increases the difficulty of particle deposition at the same time due to the high deformation resistance and brittle characteristics.

Fig. 6.15 shows the cross-sectional morphology of the wear tracks of the cold-sprayed CoCrFeNiMo_x HEA deposits. A continuous oxide layer with a thickness of ~6.5 μm was formed on the worn surface of the Mo₀ deposit, as shown in **Fig. 6.15a**. The formation of oxide layers can be attributed to the increased temperature on the deposit surface over time. As the sliding friction proceeded, the oxide layers got worn due to fatigue on the surface, and the oxide layers were broken into small blocks with visible micro-cracks. The Mo_{0.2} deposit also shows the formed oxide layer, which was discontinuous and thinner as compared to that of the Mo₀ deposit (see **Fig. 6.15b**). For the Mo_{0.5} deposit, the oxide layer became indistinguishable from the SEM image, and only a thin oxide layer (~1 μm) was formed at the top of the deposit according to the EDS mapping (see **Fig. 6.15c**). With regard to the Mo_{1.0} deposit, no oxide layer was formed on the top layer of the deposit, as shown in **Fig. 6.15d**. Therefore, the wear mechanisms of the cold-sprayed CoCrFeNiMo_x HEA

deposits are abrasive wear, adhesive wear, and oxidative wear when the Mo ratio is relatively low (e.g., Mo₀ and Mo_{0.2}) and dominated by the abrasive wear and adhesive wear with the further increase in Mo ratio (e.g., Mo_{0.5} and Mo_{1.0}).

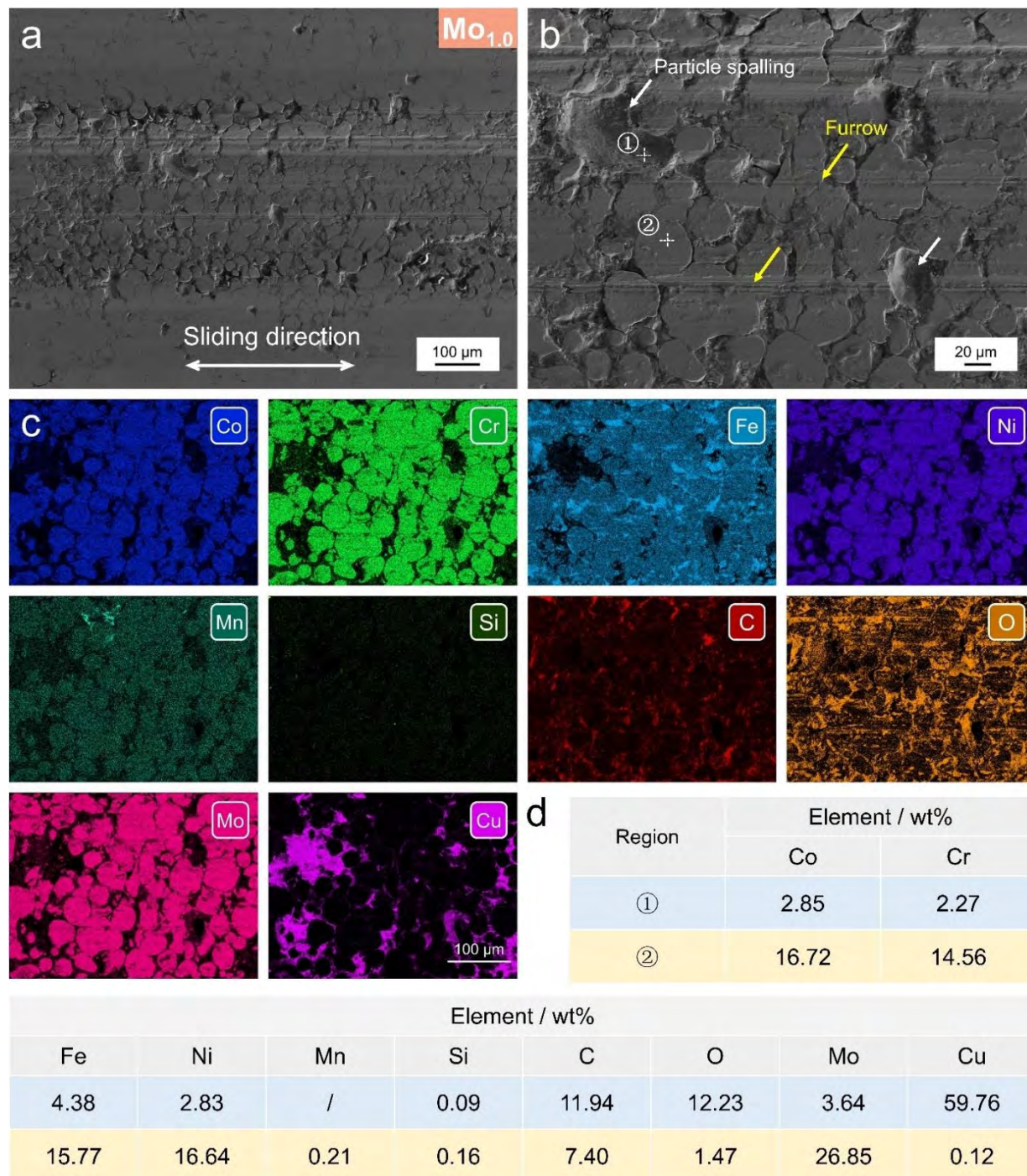


Fig. 6.14 Representative worn surface morphology and EDS results of the cold-sprayed CoCrFeNiMo_{1.0} HEA deposit. (a) and (b) SEM images, (c) EDS mapping and points analysis.

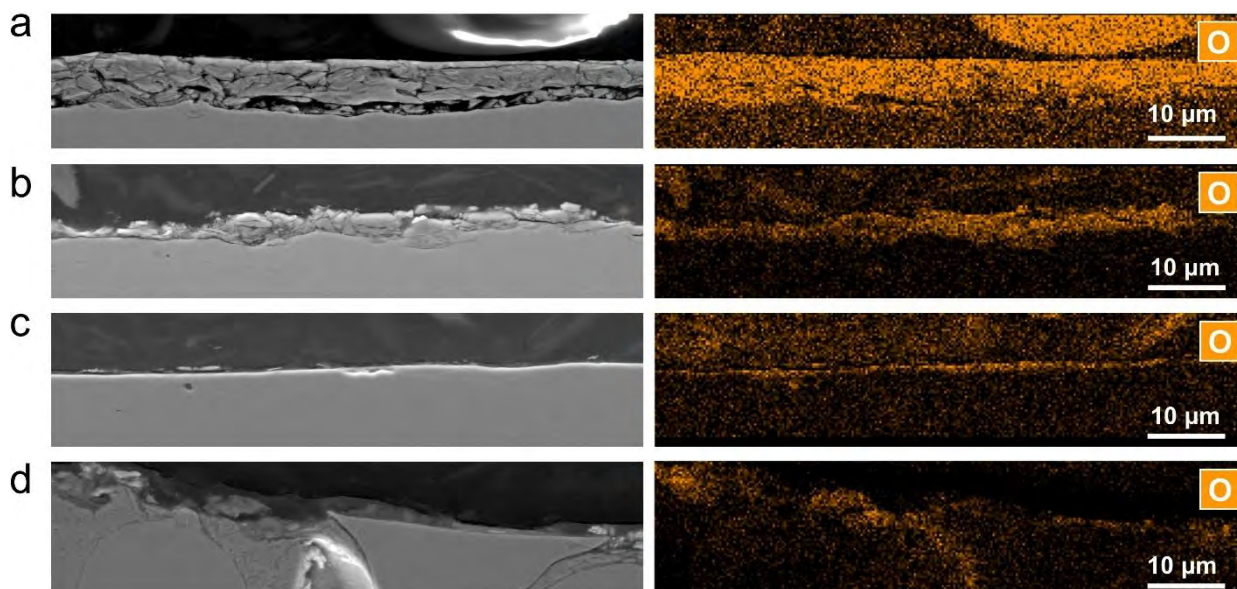


Fig. 6.15 Cross-sectional morphology of the wear tracks of the cold-sprayed CoCrFeNiMo_x HEA deposits. (a) Mo₀, (b) Mo_{0.2}, (c) Mo_{0.5}, (d) Mo_{1.0}.

6.5 Summary

In this chapter, Mo-doped CoCrFeNi high-entropy alloys (HEAs) were manufactured by solid-state cold spray deposition process to intentionally improve the wear resistance of CoCrFeNi HEA. The microstructural evolution, phase structure, nanomechanical property, and dry sliding wear behavior of the cold-sprayed CoCrFeNiMo_x HEA deposits were systematically investigated. The cold-sprayed CoCrFeNiMo_x HEA deposits presented microscale heterogeneity due to the unavoidable defects and heterostructure. The Mo_{0.2} and Mo_{0.5} deposits were identified as single FCC solid solution structures as Mo₀ deposit, while the sigma (σ) phase and mu (μ) phase were precipitated in the FCC matrix for the Mo_{1.0} deposit. The doping of Mo element into cold-sprayed CoCrFeNiMo_x HEAs significantly increased the global nanohardness from 5.01 GPa (Mo₀ deposit) to 10.02 GPa (Mo_{1.0} deposit) due to the synergistic effects of solid solution strengthening and precipitation strengthening. This makes the Mo_{1.0} deposit exhibit the lowest specific

wear rate of $0.51 \times 10^{-4} \text{ mm}^3/\text{N}\cdot\text{m}$, which decreased by 94.90% compared with that of the Mo_0 deposit. The wear mechanisms of Mo_0 and $\text{Mo}_{0.2}$ deposits were dominated by abrasive wear, adhesive wear, and oxidative wear, while for the $\text{Mo}_{0.5}$ and $\text{Mo}_{1.0}$ deposits, the wear mechanisms were mainly abrasive wear and adhesive wear. However, the increased Mo ratio in CoCrFeNiMo_x HEA powders significantly made it difficult to deposit due to the increased deformation resistance and brittle characteristics, particularly for $\text{Mo}_{1.0}$ powder. This was reflected in the extremely limited deposit thickness ($\sim 0.1 \text{ mm}$) even though high processing parameters were applied. This could lead to premature failure of the wear-resistance deposit under extreme working conditions. The current study has shown the doping of Mo element into CoCrFeNi can significantly enhance the wear resistance properties with the increase in Mo ratio. However, the trade-off between the Mo content and the depositability of material should be taken into consideration.

Chapter 7

Conclusion and Prospects

7.1 Conclusion

At the beginning of the dissertation, we investigated the bonding and nanocrystallization mechanisms of cold-sprayed metallic glass particles, which were two interesting scientific problems, by using $Zr_{55}Cu_{30}Ni_5Al_{10}$ metallic glass (MG) powder as feedstock. Based on the results and discussion, a number of important conclusions that can significantly enrich our knowledge and understanding of cold-sprayed bulk metallic glass (BMG) deposits were drawn and listed as follows:

In cold-sprayed BMG deposits, the interparticle bonding only occurred at the fringe area of the interface, which can be attributed to the high-velocity impact-induced localized metallurgical bonding. Moreover, a new interparticle bonding mechanism was first found. Some metallic glass particles impacted onto the substrate at temperatures in or above the supercooled liquid region, leading to a decrease in viscosity. The viscous fluid was forced to flow to the periphery upon impact and adhered with the substrate through an annular metallurgical bonding band. Ordered atomic structures at different levels were randomly dispersed in the amorphous matrix near the interparticle interface. The different amorphous/nanocrystal structures in cold-sprayed metallic glass particles can represent different evolution stages in the process of nanocrystallization. The formation of nanocrystals from an amorphous state can be divided into the following stages: composition segregation,

the formation of ordered 1D and 2D transition structures followed by the 3D nanocrystals.

In the latter part of this dissertation, according to the fact that the cold-sprayed CoCrFeNi high-entropy alloys (HEA) deposits generally exhibited undesirable manufacturing defects (e.g., pores and interparticle boundaries) even under high processing parameters, we combine various strengthening strategies (i.e., post heat-treatment, in-process densification, and microalloying) with the cold spray process to intentionally reduce manufacturing defects and enhance deposit properties. The microstructural evolution, plastic deformation behavior, and mechanical properties (e.g., tensile properties, compressive properties, or wear resistance) of the cold-sprayed CoCrFeNi HEA deposits with and without strengthening strategies were systematically investigated. The main conclusions are summarized as follows:

Post-spray annealing treatment was carried out at various temperatures (500 °C-1000 °C) to intentionally adjust the microstructure and balance the strength and ductility of the cold-sprayed CoCrFeNi HEA deposits. The as-sprayed deposit was composed of necessary heterostructure (i.e., bi-modal structure) and unnecessary interior defects (i.e., pores and interparticle boundaries). The deposit with such defects exhibited significantly different tensile and compressive performances due to the difference in sensitivity to interior defects under tensile and compressive loads. The as-sprayed deposit exhibited high compressive yield strength due to the dislocation strengthening and grain boundary strengthening effects but fractured within the linear elastic regime in the tensile test. Recovery annealing had no remarkable influence on the microstructure and mechanical properties of the deposit. While recrystallization annealing enhanced interface diffusion and resultant metallurgical bonding, resulting in increased deposit density and indistinguishable particle boundaries. The fully recrystallized deposit possessed almost equal tensile and compressive yield strength and the best recovery of tensile ductility.

Different combinations of powder size ranges and gas parameters were applied for the fabrication of the cold-sprayed CoCrFeNi HEA deposits. A combination of a wide particle size range of the powder and low gas parameters can trigger in-process densification of the deposits, which is contrary to the common cognition that lower processing parameters lead to more manufacturing defects in the deposits. At such conditions, a proportion of the particles (particularly those with large sizes) fail to deposit and rebound after their impact instead. The rebound particles result in accumulative plastic deformation of the deposited particles and further reduction in porosity. With this novel strategy, the detrimental thermal effects encountered in cold spraying using high-temperature processing gas (such as oxidation, nitridation, and phase changes) can be effectively minimized. However, the strategy comes at the expense of the large-sized particles, implying low deposition efficiency. Moreover, the mismatch between the particle size ranges and the gas parameters will lead to the inclusion of less deformed large-sized particles, leading to the formation of large pores and deteriorated mechanical performance.

Mo-doped CoCrFeNi HEA powders were used as feedstock for cold spraying to improve the wear resistance of the cold-sprayed CoCrFeNi HEA deposit. The cold-sprayed CoCrFeNiMo_x HEA deposits presented microscale heterogeneity due to the unavoidable defects and heterostructure. The Mo_{0.2} and Mo_{0.5} deposits were identified as single FCC solid solution structures as Mo₀ deposit, while the sigma (σ) phase and mu (μ) phase were precipitated in the FCC matrix for the Mo_{1.0} deposit. The doping of Mo element into cold-sprayed CoCrFeNiMo_x HEAs significantly increased the global nanohardness from 5.01 GPa (Mo₀ deposit) to 10.02 GPa (Mo_{1.0} deposit) due to the synergistic effects of solid solution strengthening and precipitation strengthening. This makes the Mo_{1.0} deposit exhibit the lowest specific wear rate of 0.51×10^{-4} mm³/N·m, which decreased by 94.90% compared with that of the Mo₀ deposit. The wear mechanisms of Mo₀ and Mo_{0.2} deposits were dominated by abrasive wear, adhesive wear, and oxidative wear, while for the Mo_{0.5}

and Mo_{1.0} deposits, the wear mechanisms were mainly abrasive wear and adhesive wear. However, the increased Mo ratio in CoCrFeNiMo_x HEA powders significantly made it difficult to deposit due to the increased deformation resistance and brittle characteristics, particularly for Mo_{1.0} powder. This led to premature failure of the wear-resistance deposit under extreme working conditions. The doping of Mo element into CoCrFeNi can significantly enhance the wear resistance properties with the increase in Mo ratio. However, the trade-off between the Mo content and the depositability of material should be taken into consideration.

7.2 Prospects

In this dissertation, metallic glasses and high-entropy alloys, which represent two emerging advanced alloys, are selected as research objects. The interparticle bonding and interfacial nanocrystallization mechanisms in the cold-sprayed metallic glass deposit were systematically investigated. In addition, various strengthening strategies (i.e., post heat-treatment, in-process densification, and microalloying) were combined with the cold spray process to intentionally modify the microstructure and improve the mechanical properties (e.g., tensile properties, compressive properties, and wear resistance) of the cold-sprayed CoCrFeNi HEA. There are still some issues to be further addressed in this dissertation, which can be summarized as follows:

(1) Analyzing the element distribution and composition at the nanocrystallization regions at the impacting interfaces of MG particles. Although the nanostructure at the interparticle interface was characterized by HRTEM in this work, and the amorphous/nanocrystal structures were found, the element composition of the nanocrystals was still unclear due to our limited characterization facilities. The nanocrystal structure is expected to be determined by electron energy loss spectroscopy (EELS) in the follow-on work.

(2) Optimization of feedstock powder properties and gas parameters for strengthening cold-sprayed HEA deposits through in-process densification. The current results show that individual particles with large sizes remained in the deposits rather than rebounding after impact when using the combination of wide particle size distribution and low gas parameters. The properties of the cold-sprayed HEA deposits strengthened by in-process densification are inferior to that of the conventional cold-sprayed HEA deposits (i.e., using the standard particle size of 15-53 μm and high gas processing parameters). These facts suggest that there is still room for the optimization of the matching between particle size distribution and gas processing parameters. The use of particles with larger sizes may enhance the tamping effects but will also increase the risk of nozzle wearing or even clogging at the same time. While using lower gas parameters may reduce the number of large-sized particles in the deposits, but this will also lead to the insufficient plastic deformation of small-sized particles even after the tamping by large-sized particles. The low gas processing parameters will also result in extremely low deposition efficiency, implying increased manufacturing costs. A balance should be considered between these factors before using this strengthening strategy.

(3) Exploring and developing novel strengthening strategies to assist cold spraying HEAs. In the future study, one or even more strengthening processes can be combined (e.g., powder heat treatment + in-situ micro forging, in-situ powder heating + in-process densification + post-annealing or other combinations) to modify the microstructure and enhance the material properties of cold-sprayed deposits. In addition, it is necessary to develop new strengthening processes, such as ultrasonic field- and magnetic field-assisted cold spray, to study the effect of these techniques on the microstructure evolution and materials properties.

Reference

- [1] D. Ouyang, N. Li, L. Liu, Structural heterogeneity in 3D printed Zr-based bulk metallic glass by selective laser melting, *J. Alloys Compd.* 740 (2018) 603–609. <https://doi.org/10.1016/j.jallcom.2018.01.037>.
- [2] R. Li, P. Niu, T. Yuan, P. Cao, C. Chen, K. Zhou, Selective laser melting of an equiatomic CoCrFeMnNi high-entropy alloy: Processability, non-equilibrium microstructure and mechanical property, *J. Alloys Compd.* 746 (2018) 125–134. <https://doi.org/10.1016/j.jallcom.2018.02.298>.
- [3] H.Z. Wang, Y.H. Cheng, J.Y. Yang, Q.Q. Wang, Microstructure and properties of laser clad Fe-based amorphous alloy coatings containing Nb powder, *J. Non. Cryst. Solids.* 550 (2020) 120351. <https://doi.org/10.1016/j.jnoncrsol.2020.120351>.
- [4] H. Zhang, Y. Pan, Y.Z. He, Synthesis and characterization of FeCoNiCrCu high-entropy alloy coating by laser cladding, *Mater. Des.* 32 (2011) 1910–1915. <https://doi.org/10.1016/j.matdes.2010.12.001>.
- [5] C. Zhang, W. Wang, Y.C. Li, Y.G. Yang, Y. Wu, L. Liu, 3D printing of Fe-based bulk metallic glasses and composites with large dimensions and enhanced toughness by thermal spraying, *J. Mater. Chem. A.* 6 (2018) 6800–6805. <https://doi.org/10.1039/c8ta00405f>.
- [6] G. Wang, Z. Huang, P. Xiao, X. Zhu, Spraying of Fe-based amorphous coating with high corrosion resistance by HVAF, *J. Manuf. Process.* 22 (2016) 34–38. <https://doi.org/10.1016/j.jmapro.2016.01.009>.
- [7] J. Kim, K. Kang, S. Yoon, S. Kumar, H. Na, C. Lee, Oxidation and crystallization mechanisms in plasma-sprayed Cu-based bulk metallic glass coatings, *Acta Mater.* 58 (2010) 952–962. <https://doi.org/10.1016/j.actamat.2009.10.011>.
- [8] K.C. Cheng, J.H. Chen, S. Stadler, S.H. Chen, Properties of atomized AlCoCrFeNi high-entropy alloy powders and their phase-adjustable coatings prepared via plasma spray process, *Appl. Surf. Sci.* 478 (2019) 478–486. <https://doi.org/10.1016/j.apsusc.2019.01.203>.
- [9] W. Guo, J. Zhang, Y. Wu, S. Hong, Y. Qin, Fabrication and characterization of Fe-based amorphous coatings prepared by high-velocity arc spraying, *Mater. Des.* 78 (2015) 118–124. <https://doi.org/10.1016/j.matdes.2015.04.027>.
- [10] A. Meghwal, A. Anupam, B.S. Murty, C.C. Berndt, R.S. Kottada, A.S.M. Ang, *Thermal Spray High-Entropy Alloy Coatings: A Review*, Springer US, 2020. <https://doi.org/10.1007/s11666-020-01047-0>.
- [11] S. Yin, P. Cavaliere, B. Aldwell, R. Jenkins, H. Liao, W. Li, R. Lupoi, Cold spray additive manufacturing and repair: Fundamentals and applications, *Addit. Manuf.* 21 (2018) 628–650. <https://doi.org/10.1016/j.addma.2018.04.017>.

- [12] A.P. Alkhimov, V.F. Kosarev, N.I. Nesterovich, A.N. Papyrin., Method of applying coatings (SU 1618778), 1980.
- [13] A.P. Alkhimov, V.F. Kosareve, A.N. Papyrin, A Method of Cold Gas-Dynamic Spray Deposition, *Dokl. Akad. Nauk SSSR*. 315 (1990) 1062–1065.
- [14] T. Suhonen, T. Varis, S. Dosta, M. Torrell, J.M. Guilemany, Residual stress development in cold sprayed Al, Cu and Ti coatings, *Acta Mater.* 61 (2013) 6329–6337. <https://doi.org/10.1016/j.actamat.2013.06.033>.
- [15] S. Bagherifard, A. Heydari Astaraee, M. Locati, A. Nawaz, S. Monti, J. Kondás, R. Singh, M. Guagliano, Design and analysis of additive manufactured bimodal structures obtained by cold spray deposition, *Addit. Manuf.* 33 (2020) 101131. <https://doi.org/10.1016/j.addma.2020.101131>.
- [16] S. Yin, W. Li, B. Song, X. Yan, M. Kuang, Y. Xu, K. Wen, R. Lupoi, Deposition of FeCoNiCrMn high entropy alloy (HEA) coating via cold spraying, *J. Mater. Sci. Technol.* 35 (2019) 1003–1007. <https://doi.org/10.1016/j.jmst.2018.12.015>.
- [17] J. Henao, A. Concustell, I. G.Cano, S. Dosta, N. Cinca, J.M. Guilemany, T. Suhonen, Novel Al-based metallic glass coatings by Cold Gas Spray, *Mater. Des.* 94 (2016) 253–261. <https://doi.org/10.1016/j.matdes.2016.01.040>.
- [18] S. Yin, J. Cizek, C. Chen, R. Jenkins, G. O'Donnell, R. Lupoi, Metallurgical bonding between metal matrix and core-shelled reinforcements in cold sprayed composite coating, *Scr. Mater.* 177 (2020) 49–53. <https://doi.org/10.1016/j.scriptamat.2019.09.023>.
- [19] S. Yin, Y. Xie, J. Cizek, E.J. Ekoi, T. Hussain, D.P. Dowling, R. Lupoi, Advanced diamond-reinforced metal matrix composites via cold spray: Properties and deposition mechanism, *Compos. Part B Eng.* 113 (2017) 44–54. <https://doi.org/10.1016/j.compositesb.2017.01.009>.
- [20] Y. Zou, Cold Spray Additive Manufacturing: Microstructure Evolution and Bonding Features, *Accounts Mater. Res.* 2 (2021) 1071–1081. <https://doi.org/10.1021/accountsmr.1c00138>.
- [21] K. Spencer, D.M. Fabijanic, M.X. Zhang, The use of Al-Al₂O₃ cold spray coatings to improve the surface properties of magnesium alloys, *Surf. Coatings Technol.* 204 (2009) 336–344. <https://doi.org/10.1016/j.surfcoat.2009.07.032>.
- [22] N.W. Khun, A.W.Y. Tan, W. Sun, E. Liu, Wear and Corrosion Resistance of Thick Ti-6Al-4V Coating Deposited on Ti-6Al-4V Substrate via High-Pressure Cold Spray, *J. Therm. Spray Technol.* 26 (2017) 1393–1407. <https://doi.org/10.1007/S11666-017-0588-8>.
- [23] C.S. Witharamage, M.A. Alrizqi, J. Chirstudasjustus, A.A. Darwish, T. Ansell, A. Nieto, R.K. Gupta, Corrosion-resistant metallic coatings for aluminum alloys by cold spray, *Corros. Sci.* 209 (2022) 110720. <https://doi.org/10.1016/j.corsci.2022.110720>.
- [24] Y.K. Wei, Y.J. Li, Y. Zhang, X.T. Luo, C.J. Li, Corrosion resistant nickel coating with strong adhesion on AZ31B magnesium alloy prepared by an in-situ shot-peening-assisted

- cold spray, *Corros. Sci.* 138 (2018) 105–115.
<https://doi.org/10.1016/j.corsci.2018.04.018>.
- [25] N. Kaur, M. Kumar, S.K. Sharma, D.Y. Kim, S. Kumar, N.M. Chavan, S. V. Joshi, N. Singh, H. Singh, Study of mechanical properties and high temperature oxidation behavior of a novel cold-spray Ni-20Cr coating on boiler steels, *Appl. Surf. Sci.* 328 (2015) 13–25.
<https://doi.org/10.1016/j.apsusc.2014.12.033>.
- [26] T.-Y. Liao, A. Biesiekierski, C.C. Berndt, P.C. King, E.P. Ivanova, H. Thissen, P. Kingshott, Multifunctional cold spray coatings for biological and biomedical applications: A review, *Prog. Surf. Sci.* 97 (2022) 100654.
<https://doi.org/10.1016/j.progsurf.2022.100654>.
- [27] N. Sanpo, M.L. Tan, P. Cheang, K.A. Khor, Antibacterial property of cold-sprayed HA-Ag/PEEK coating, *J. Therm. Spray Technol.* 18 (2009) 10–15.
<https://doi.org/10.1007/s11666-008-9283-0>.
- [28] S. Zhou, C.A. Bernard, K. Ravi, H. Saito, Y. Ichikawa, K. Ogawa, S. Yin, Development and Characterization of Photocatalytic GaN Coatings by Cold Spray Process, *J. Therm. Spray Technol.* 30 (2021) 1294–1309. <https://doi.org/10.1007/s11666-021-01207-w>.
- [29] M. Yamada, H. Isago, H. Nakano, M. Fukumoto, Cold Spraying of TiO₂ Photocatalyst Coating With Nitrogen Process Gas, *J. Therm. Spray Technol.* 19 (2010) 1218–1223.
<https://doi.org/10.1007/s11666-010-9520-1>.
- [30] K. Ravi, W.L. Sulen, C. Bernard, Y. Ichikawa, K. Ogawa, Fabrication of micro-/nano-structured super-hydrophobic fluorinated polymer coatings by cold-spray, *Surf. Coatings Technol.* 373 (2019) 17–24. <https://doi.org/10.1016/j.surfcoat.2019.05.078>.
- [31] Z. Wang, X. Chen, Y. Gong, B. Zhang, H. Li, Superhydrophobic nanocoatings prepared by a novel vacuum cold spray process, *Surf. Coatings Technol.* 325 (2017) 52–57.
<https://doi.org/10.1016/j.surfcoat.2017.06.044>.
- [32] D. Seo, K. Ogawa, K. Sakaguchi, N. Miyamoto, Y. Tsuzuki, Parameter study influencing thermal conductivity of annealed pure copper coatings deposited by selective cold spray processes, *Surf. Coatings Technol.* 206 (2012) 2316–2324.
<https://doi.org/10.1016/j.surfcoat.2011.10.010>.
- [33] <https://impact-innovations.com/en>, (n.d.).
- [34] A. Astarita, F. Coticelli, U. Prisco, Repairing of an engine block through the cold gas dynamic spray technology, *Mater. Res.* 19 (2016) 1226–1231.
<https://doi.org/10.1590/1980-5373-MR-2016-0109>.
- [35] V.K. Champagne, D. Helfritch, P.F. Leyman, Magnesium repair by cold spray, *Annu. Int. Tech. Conf. Natl. Assoc. Surf. Finish. SUR/FIN 2007.* 3 (2007) 150–176.
- [36] C.A. Widener, M.J. Carter, O.C. Ozdemir, R.H. Hrabe, B. Hoiland, T.E. Stamey, V.K. Champagne, T.J. Eden, Application of High-Pressure Cold Spray for an Internal Bore Repair of a Navy Valve Actuator, *J. Therm. Spray Technol.* 25 (2016) 193–201.
<https://doi.org/10.1007/s11666-015-0366-4>.

- [37] S. Yin, P. Cavaliere, B. Aldwell, R. Jenkins, H. Liao, W. Li, R. Lupoi, Cold spray additive manufacturing and repair: Fundamentals and applications, *Addit. Manuf.* 21 (2018) 628–650. <https://doi.org/10.1016/j.addma.2018.04.017>.
- [38] J. Lee, S. Shin, H.J. Kim, C. Lee, Effect of gas temperature on critical velocity and deposition characteristics in kinetic spraying, *Appl. Surf. Sci.* 253 (2007) 3512–3520. <https://doi.org/10.1016/j.apsusc.2006.07.061>.
- [39] S. Yin, X. Suo, H. Liao, Z. Guo, X. Wang, Significant influence of carrier gas temperature during the cold spray process, *Surf. Eng.* 30 (2014) 443–450. <https://doi.org/10.1179/1743294414Y.0000000276>.
- [40] A. Candel, R. Gadow, Trajectory Generation and Coupled Numerical Simulation for Thermal Spraying Applications on Complex Geometries, *J. Therm. Spray Technol.* 18 (2009) 981–987. <https://doi.org/10.1007/s11666-009-9338-x>.
- [41] D. Kotoban, S. Grigoriev, A. Okunkova, A. Sova, Influence of a shape of single track on deposition efficiency of 316L stainless steel powder in cold spray, *Surf. Coatings Technol.* 309 (2017) 951–958. <https://doi.org/10.1016/j.surfcoat.2016.10.052>.
- [42] J. Pattison, S. Celotto, A. Khan, W. O'Neill, Standoff distance and bow shock phenomena in the Cold Spray process, *Surf. Coatings Technol.* 202 (2008) 1443–1454. <https://doi.org/10.1016/j.surfcoat.2007.06.065>.
- [43] W.-Y. Li, C. Zhang, X.P. Guo, G. Zhang, H.L. Liao, C.-J. Li, C. Coddet, Effect of standoff distance on coating deposition characteristics in cold spraying, *Mater. Des.* 29 (2008) 297–304. <https://doi.org/10.1016/j.matdes.2007.02.005>.
- [44] K. Binder, J. Gottschalk, M. Kollenda, F. Gärtner, T. Klassen, Influence of Impact Angle and Gas Temperature on Mechanical Properties of Titanium Cold Spray Deposits, *J. Therm. Spray Technol.* 20 (2011) 234–242. <https://doi.org/10.1007/s11666-010-9557-1>.
- [45] S. Yin, X. Suo, J. Su, Z. Guo, H. Liao, X. Wang, Effects of Substrate Hardness and Spray Angle on the Deposition Behavior of Cold-Sprayed Ti Particles, *J. Therm. Spray Technol.* 23 (2014) 76–83. <https://doi.org/10.1007/s11666-013-0039-0>.
- [46] D.L. Gilmore, R.C. Dykhuizen, R.A. Neiser, T.J. Roemer, M.F. Smith, Particle Velocity and Deposition Efficiency in the Cold Spray Process, *J. Therm. Spray Technol.* 8 (1999) 576–582. <https://doi.org/10.1361/105996399770350278>.
- [47] X.-T. Luo, Y.-J. Li, C.-X. Li, G.-J. Yang, C.-J. Li, Effect of spray conditions on deposition behavior and microstructure of cold sprayed Ni coatings sprayed with a porous electrolytic Ni powder, *Surf. Coatings Technol.* 289 (2016) 85–93. <https://doi.org/10.1016/j.surfcoat.2016.01.058>.
- [48] H.-T. Wang, C.-J. Li, G.-J. Yang, C.-X. Li, Effect of heat treatment on the microstructure and property of cold-sprayed nanostructured FeAl/Al₂O₃ intermetallic composite coating, *Vacuum.* 83 (2008) 146–152. <https://doi.org/10.1016/j.vacuum.2008.03.094>.
- [49] J. Henao, G. Bolelli, A. Concustell, L. Lusvardi, S. Dosta, I.G. Cano, J.M. Guilemany, Deposition behavior of cold-sprayed metallic glass particles onto different substrates,

- Surf. Coatings Technol. 349 (2018) 13–23.
<https://doi.org/10.1016/j.surfcoat.2018.05.047>.
- [50] K.H. Ko, J.O. Choi, H. Lee, Pretreatment effect of Cu feedstock on cold-sprayed coatings, *J. Mater. Process. Technol.* 214 (2014) 1530–1535.
<https://doi.org/10.1016/j.jmatprotec.2014.02.020>.
- [51] D. Rafaja, T. Schucknecht, V. Klemm, A. Paul, H. Berek, Microstructural characterisation of titanium coatings deposited using cold gas spraying on Al₂O₃ substrates, *Surf. Coatings Technol.* 203 (2009) 3206–3213.
<https://doi.org/10.1016/j.surfcoat.2009.03.054>.
- [52] S. Yin, X. Yan, C. Chen, R. Jenkins, M. Liu, R. Lupoi, Hybrid additive manufacturing of Al-Ti6Al4V functionally graded materials with selective laser melting and cold spraying, *J. Mater. Process. Technol.* 255 (2018) 650–655.
<https://doi.org/10.1016/j.jmatprotec.2018.01.015>.
- [53] S. Yin, E.J. Ekoi, T.L. Lupton, D.P. Dowling, R. Lupoi, Cold spraying of WC-Co-Ni coatings using porous WC-17Co powders: Formation mechanism, microstructure characterization and tribological performance, *Mater. Des.* 126 (2017) 305–313.
<https://doi.org/10.1016/j.matdes.2017.04.040>.
- [54] B. Jodoin, L. Ajdelsztajn, E. Sansoucy, A. Zúñiga, P. Richer, E.J. Lavernia, Effect of particle size, morphology, and hardness on cold gas dynamic sprayed aluminum alloy coatings, *Surf. Coatings Technol.* 201 (2006) 3422–3429.
<https://doi.org/10.1016/j.surfcoat.2006.07.232>.
- [55] T. Schmidt, F. Gärtner, H. Assadi, H. Kreye, Development of a generalized parameter window for cold spray deposition, *Acta Mater.* 54 (2006) 729–742.
<https://doi.org/10.1016/j.actamat.2005.10.005>.
- [56] O.C. Ozdemir, C.A. Widener, M.J. Carter, K.W. Johnson, Predicting the Effects of Powder Feeding Rates on Particle Impact Conditions and Cold Spray Deposited Coatings, *J. Therm. Spray Technol.* 26 (2017) 1598–1615. <https://doi.org/10.1007/s11666-017-0611-0>.
- [57] H. Assadi, F. Gärtner, T. Stoltenhoff, H. Kreye, Bonding mechanism in cold gas spraying, *Acta Mater.* 51 (2003) 4379–4394. [https://doi.org/10.1016/S1359-6454\(03\)00274-X](https://doi.org/10.1016/S1359-6454(03)00274-X).
- [58] F. Raletz, M. Vardelle, G. Ezo'o, Critical particle velocity under cold spray conditions, *Surf. Coatings Technol.* 201 (2006) 1942–1947.
<https://doi.org/10.1016/j.surfcoat.2006.04.061>.
- [59] C.-J. Li, W.-Y. Li, H. Liao, Examination of the Critical Velocity for Deposition of Particles in Cold Spraying, *J. Therm. Spray Technol.* 15 (2006) 212–222.
<https://doi.org/10.1361/105996306X108093>.

- [60] T. Schmidt, H. Assadi, F. Gärtner, H. Richter, T. Stoltenhoff, H. Kreye, T. Klassen, From Particle Acceleration to Impact and Bonding in Cold Spraying, *J. Therm. Spray Technol.* 18 (2009) 794–808. <https://doi.org/10.1007/s11666-009-9357-7>.
- [61] M. Grujicic, C.. Zhao, W.. DeRosset, D. Helfrich, Adiabatic shear instability based mechanism for particles/substrate bonding in the cold-gas dynamic-spray process, *Mater. Des.* 25 (2004) 681–688. <https://doi.org/10.1016/j.matdes.2004.03.008>.
- [62] G. Bae, Y. Xiong, S. Kumar, K. Kang, C. Lee, General aspects of interface bonding in kinetic sprayed coatings, *Acta Mater.* 56 (2008) 4858–4868. <https://doi.org/10.1016/j.actamat.2008.06.003>.
- [63] W.Y. Li, C.J. Li, H. Liao, Significant influence of particle surface oxidation on deposition efficiency, interface microstructure and adhesive strength of cold-sprayed copper coatings, *Appl. Surf. Sci.* 256 (2010) 4953–4958. <https://doi.org/10.1016/j.apsusc.2010.03.008>.
- [64] G. Bae, S. Kumar, S. Yoon, K. Kang, H. Na, H.J. Kim, C. Lee, Bonding features and associated mechanisms in kinetic sprayed titanium coatings, *Acta Mater.* 57 (2009) 5654–5666. <https://doi.org/10.1016/j.actamat.2009.07.061>.
- [65] M. Grujicic, J.R. Saylor, D.E. Beasley, W.S. DeRosset, D. Helfrich, Computational analysis of the interfacial bonding between feed-powder particles and the substrate in the cold-gas dynamic-spray process, *Appl. Surf. Sci.* 219 (2003) 211–227. [https://doi.org/10.1016/S0169-4332\(03\)00643-3](https://doi.org/10.1016/S0169-4332(03)00643-3).
- [66] W.Y. Li, C. Zhang, X. Guo, C.J. Li, H. Liao, C. Coddet, Study on impact fusion at particle interfaces and its effect on coating microstructure in cold spraying, *Appl. Surf. Sci.* 254 (2007) 517–526. <https://doi.org/10.1016/j.apsusc.2007.06.026>.
- [67] C.J. Li, W.Y. Li, Y.Y. Wang, Formation of metastable phases in cold-sprayed soft metallic deposit, *Surf. Coatings Technol.* 198 (2005) 469–473. <https://doi.org/10.1016/j.surfcoat.2004.10.063>.
- [68] S. Guetta, M.H. Berger, F. Borit, V. Guipont, M. Jeandin, M. Boustie, Y. Ichikawa, K. Sakaguchi, K. Ogawa, Influence of particle velocity on adhesion of cold-sprayed splats, *J. Therm. Spray Technol.* 18 (2009) 331–342. <https://doi.org/10.1007/s11666-009-9327-0>.
- [69] K.H. Ko, J.O. Choi, H. Lee, The interfacial restructuring to amorphous: A new adhesion mechanism of cold-sprayed coatings, *Mater. Lett.* 175 (2016) 13–15. <https://doi.org/10.1016/j.matlet.2016.03.132>.
- [70] V.K. Champagne, M.K. West, M. Reza Rokni, T. Curtis, V. Champagne, B. McNally, Joining of Cast ZE41A Mg to Wrought 6061 Al by the Cold Spray Process and Friction Stir Welding, *J. Therm. Spray Technol.* 25 (2016) 143–159. <https://doi.org/10.1007/s11666-015-0301-8>.
- [71] T. Hussain, Cold Spraying of Titanium: A Review of Bonding Mechanisms, Microstructure and Properties, *Key Eng. Mater.* 533 (2012) 53–90. <https://doi.org/10.4028/www.scientific.net/kem.533.53>.

- [72] P.C. King, C. Busch, T. Kittel-Sherri, M. Jahedi, S. Gulizia, Interface melting in cold spray titanium particle impact, *Surf. Coatings Technol.* 239 (2014) 191–199. <https://doi.org/10.1016/j.surfcoat.2013.11.039>.
- [73] S. Yoon, Y. Xiong, H. Kim, C. Lee, Dependence of initial powder temperature on impact behaviour of bulk metallic glass in a kinetic spray process, *J. Phys. D. Appl. Phys.* 42 (2009). <https://doi.org/10.1088/0022-3727/42/8/082004>.
- [74] M. Hassani-Gangaraj, D. Veysset, K.A. Nelson, C.A. Schuh, In-situ observations of single micro-particle impact bonding, *Scr. Mater.* 145 (2018) 9–13. <https://doi.org/10.1016/j.scriptamat.2017.09.042>.
- [75] M. Hassani-Gangaraj, D. Veysset, V.K. Champagne, K.A. Nelson, C.A. Schuh, Adiabatic shear instability is not necessary for adhesion in cold spray, *Acta Mater.* 158 (2018) 430–439. <https://doi.org/10.1016/j.actamat.2018.07.065>.
- [76] C.J. Li, H.T. Wang, Q. Zhang, G.J. Yang, W.Y. Li, H.L. Liao, Influence of spray materials and their surface oxidation on the critical velocity in cold spraying, *J. Therm. Spray Technol.* 19 (2010) 95–101. <https://doi.org/10.1007/s11666-009-9427-x>.
- [77] Y. Ichikawa, R. Tokoro, M. Tanno, K. Ogawa, Elucidation of cold-spray deposition mechanism by auger electron spectroscopic evaluation of bonding interface oxide film, *Acta Mater.* 164 (2019) 39–49. <https://doi.org/10.1016/j.actamat.2018.09.041>.
- [78] Y. Li, Y. Wei, X. Luo, C. Li, N. Ma, Correlating particle impact condition with microstructure and properties of the cold-sprayed metallic deposits, *J. Mater. Sci. Technol.* 40 (2020) 185–195. <https://doi.org/10.1016/j.jmst.2019.09.023>.
- [79] W.Y. Li, W. Gao, Some aspects on 3D numerical modeling of high velocity impact of particles in cold spraying by explicit finite element analysis, *Appl. Surf. Sci.* 255 (2009) 7878–7892. <https://doi.org/10.1016/j.apsusc.2009.04.135>.
- [80] H. Yeom, T. Dabney, G. Johnson, B. Maier, M. Lenling, K. Sridharan, Improving deposition efficiency in cold spraying chromium coatings by powder annealing, *Int. J. Adv. Manuf. Technol.* 100 (2019) 1373–1382. <https://doi.org/10.1007/s00170-018-2784-1>.
- [81] B.A. Bedard, T.J. Flanagan, A.T. Ernst, A. Nardi, A.M. Dongare, H.D. Brody, V.K. Champagne, S.-W. Lee, M. Aindow, Microstructure and Micromechanical Response in Gas-Atomized Al 6061 Alloy Powder and Cold-Sprayed Splats, *J. Therm. Spray Technol.* (2018). <https://doi.org/10.1007/s11666-018-0785-0>.
- [82] T. Liu, W.A. Story, L.N. Brewer, Effect of Heat Treatment on the Al-Cu Feedstock Powders for Cold Spray Deposition, *Metall. Mater. Trans. A Phys. Metall. Mater. Sci.* 50 (2019) 3373–3387. <https://doi.org/10.1007/s11661-019-05230-z>.
- [83] A. Sabard, T. Hussain, Inter-particle bonding in cold spray deposition of a gas-atomised and a solution heat-treated Al 6061 powder, *J. Mater. Sci.* 54 (2019) 12061–12078. <https://doi.org/10.1007/s10853-019-03736-w>.

- [84] S. Krebs, F. Gärtner, T. Klassen, Cold Spraying of Cu-Al-Bronze for Cavitation Protection in Marine Environments, *J. Therm. Spray Technol.* 24 (2014) 126–135. <https://doi.org/10.1007/s11666-014-0161-7>.
- [85] A. Sabard, H.L. de Villiers Lovelock, T. Hussain, Microstructural Evolution in Solution Heat Treatment of Gas-Atomized Al Alloy (7075) Powder for Cold Spray, *J. Therm. Spray Technol.* 27 (2017) 145–158. <https://doi.org/10.1007/s11666-017-0662-2>.
- [86] C. Huang, A. List, J. Shen, B. Fu, S. Yin, T. Chen, B. Klusemann, F. Gärtner, T. Klassen, Tailoring powder strengths for enhanced quality of cold sprayed Al6061 deposits, *Mater. Des.* 215 (2022) 110494. <https://doi.org/10.1016/j.matdes.2022.110494>.
- [87] W.A. Story, L.N. Brewer, Heat Treatment of Gas-Atomized Powders for Cold Spray Deposition, *Metall. Mater. Trans. A Phys. Metall. Mater. Sci.* 49 (2018) 446–449. <https://doi.org/10.1007/s11661-017-4428-8>.
- [88] S. Yin, X. Wang, X. Suo, H. Liao, Z. Guo, W. Li, C. Coddet, Deposition behavior of thermally softened copper particles in cold spraying, *Acta Mater.* 61 (2013) 5105–5118. <https://doi.org/10.1016/j.actamat.2013.04.041>.
- [89] S. Yoon, H.J. Kim, C. Lee, Deposition behavior of bulk amorphous NiTiZrSiSn according to the kinetic and thermal energy levels in the kinetic spraying process, *Surf. Coatings Technol.* 200 (2006) 6022–6029. <https://doi.org/10.1016/j.surfcoat.2005.09.022>.
- [90] X.T. Luo, Y.K. Wei, Y. Wang, C.J. Li, Microstructure and mechanical property of Ti and Ti6Al4V prepared by an in-situ shot peening assisted cold spraying, *Mater. Des.* 85 (2015) 527–533. <https://doi.org/10.1016/j.matdes.2015.07.015>.
- [91] H. Zhou, C. Li, G. Ji, S. Fu, H. Yang, X. Luo, G. Yang, C. Li, Local microstructure inhomogeneity and gas temperature effect in in-situ shot-peening assisted cold-sprayed Ti-6Al-4V coating, *J. Alloys Compd.* 766 (2018) 694–704. <https://doi.org/10.1016/j.jallcom.2018.07.009>.
- [92] Y.-K. Wei, X.-T. Luo, Y. Ge, X. Chu, G.-S. Huang, C.-J. Li, Deposition of fully dense Al-based coatings via in-situ micro-forging assisted cold spray for excellent corrosion protection of AZ31B magnesium alloy, *J. Alloys Compd.* 806 (2019) 1116–1126. <https://doi.org/10.1016/j.jallcom.2019.07.279>.
- [93] Y.K. Wei, X.T. Luo, X. Chu, G.S. Huang, C.J. Li, Solid-state additive manufacturing high performance aluminum alloy 6061 enabled by an in-situ micro-forging assisted cold spray, *Mater. Sci. Eng. A.* 776 (2020) 139024. <https://doi.org/10.1016/j.msea.2020.139024>.
- [94] F.F. Lu, K. Ma, C.X. Li, M. Yasir, X.T. Luo, C. jiu Li, Enhanced corrosion resistance of cold-sprayed and shot-peened aluminum coatings on LA43M magnesium alloy, *Surf. Coatings Technol.* 394 (2020) 125865. <https://doi.org/10.1016/j.surfcoat.2020.125865>.
- [95] X.T. Luo, M.L. Yao, N. Ma, M. Takahashi, C.J. Li, Deposition behavior, microstructure and mechanical properties of an in-situ micro-forging assisted cold spray enabled

- additively manufactured Inconel 718 alloy, *Mater. Des.* 155 (2018) 384–395. <https://doi.org/10.1016/j.matdes.2018.06.024>.
- [96] H. Zhou, C. Li, X. Luo, G. Yang, T. Hussain, C. Li, Microstructure of Cross-Linked High Densification Network and Strengthening Mechanism in Cold-Sprayed Ti-6Al-4V Coating After Heat Treatment, *J. Therm. Spray Technol.* 29 (2020) 1054–1069. <https://doi.org/10.1007/s11666-020-01042-5>.
- [97] Y.K. Wei, X.T. Luo, C.X. Li, C.J. Li, Optimization of In-Situ Shot-Peening-Assisted Cold Spraying Parameters for Full Corrosion Protection of Mg Alloy by Fully Dense Al-Based Alloy Coating, *J. Therm. Spray Technol.* 26 (2017) 173–183. <https://doi.org/10.1007/s11666-016-0492-7>.
- [98] M. Kulmala, P. Vuoristo, Influence of process conditions in laser-assisted low-pressure cold spraying, *Surf. Coatings Technol.* 202 (2008) 4503–4508. <https://doi.org/10.1016/j.surfcoat.2008.04.034>.
- [99] F. Gärtner, T. Stoltenhoff, J. Voyer, H. Kreye, S. Riekehr, M. Koçak, Mechanical properties of cold-sprayed and thermally sprayed copper coatings, *Surf. Coatings Technol.* 200 (2006) 6770–6782. <https://doi.org/10.1016/j.surfcoat.2005.10.007>.
- [100] N. Fan, A. Rafferty, R. Lupoi, W. Li, Y. Xie, S. Yin, Microstructure evolution and mechanical behavior of additively manufactured CoCrFeNi high-entropy alloy fabricated via cold spraying and post-annealing, *Mater. Sci. Eng. A.* 873 (2023) 144748. <https://doi.org/10.1016/j.msea.2023.144748>.
- [101] S. Yin, J. Cizek, X. Yan, R. Lupoi, Annealing strategies for enhancing mechanical properties of additively manufactured 316L stainless steel deposited by cold spray, *Surf. Coatings Technol.* 370 (2019) 353–361. <https://doi.org/10.1016/j.surfcoat.2019.04.012>.
- [102] N.H. Tariq, L. Gyansah, X. Qiu, H. Du, J.Q. Wang, B. Feng, D.S. Yan, T.Y. Xiong, Thermo-mechanical post-treatment: A strategic approach to improve microstructure and mechanical properties of cold spray additively manufactured composites, *Mater. Des.* 156 (2018) 287–299. <https://doi.org/10.1016/j.matdes.2018.06.062>.
- [103] H. Zhao, C. Tan, X. Yu, X. Ning, Z. Nie, H. Cai, F. Wang, Y. Cui, Enhanced reactivity of Ni-Al reactive material formed by cold spraying combined with cold-pack rolling, *J. Alloys Compd.* 741 (2018) 883–894. <https://doi.org/10.1016/j.jallcom.2018.01.170>.
- [104] N. ul H. Tariq, L. Gyansah, X. Qiu, C. Jia, H. Bin Awais, C. Zheng, H. Du, J. Wang, T. Xiong, Achieving strength-ductility synergy in cold spray additively manufactured Al/B 4 C composites through a hybrid post-deposition treatment, *J. Mater. Sci. Technol.* 35 (2019) 1053–1063. <https://doi.org/10.1016/j.jmst.2018.12.022>.
- [105] Z. Zhao, N. ul H. Tariq, J. Tang, C. Jia, X. Qiu, Y. Ren, H. Liu, Y. Shen, H. Du, X. Cui, J. Wang, T. Xiong, Microstructural evolutions and mechanical characteristics of Ti/steel clad plates fabricated through cold spray additive manufacturing followed by hot-rolling and annealing, *Mater. Des.* 185 (2020) 108249. <https://doi.org/10.1016/j.matdes.2019.108249>.

- [106] Z. Zhao, N. ul H. Tariq, J. Tang, Y. Ren, H. Liu, M. Tong, L. Yin, H. Du, J. Wang, T. Xiong, Influence of annealing on the microstructure and mechanical properties of Ti/steel clad plates fabricated via cold spray additive manufacturing and hot-rolling, *Mater. Sci. Eng. A*. 775 (2020) 138968. <https://doi.org/10.1016/j.msea.2020.138968>.
- [107] Z. Zhao, J. Tang, N. ul H. Tariq, H. Liu, H. Liu, Y. Ren, M. Tong, L. Yin, H. Du, J. Wang, T. Xiong, Effect of rolling temperature on microstructure and mechanical properties of Ti/steel clad plates fabricated by cold spraying and hot-rolling, *Mater. Sci. Eng. A*. 795 (2020) 139982. <https://doi.org/10.1016/j.msea.2020.139982>.
- [108] X. Qiu, N. ul H. Tariq, L. Qi, Y. ning Zan, Y. jiang Wang, J. qiang Wang, H. Du, T. ying Xiong, In-situ Sip/A380 alloy nano/micro composite formation through cold spray additive manufacturing and subsequent hot rolling treatment: Microstructure and mechanical properties, *J. Alloys Compd.* 780 (2019) 597–606. <https://doi.org/10.1016/j.jallcom.2018.11.399>.
- [109] W. Wang, P. Han, Y. Wang, T. Zhang, P. Peng, K. Qiao, Z. Wang, Z. Liu, K. Wang, High-performance bulk pure Al prepared through cold spray-friction stir processing composite additive manufacturing, *J. Mater. Res. Technol.* 9 (2020) 9073–9079. <https://doi.org/10.1016/j.jmrt.2020.06.034>.
- [110] C. Huang, W. Li, Y. Feng, M.-P.P. Planche, H. Liao, G. Montavon, Y. Xie, M.-P.P. Planche, H. Liao, G. Montavon, Microstructural evolution and mechanical properties enhancement of a cold-sprayed Cu[sbn]Zn alloy coating with friction stir processing, *Mater. Charact.* 125 (2017) 76–82. <https://doi.org/10.1016/j.matchar.2017.01.027>.
- [111] K. Yang, W. Li, Y. Xu, X. Yang, Using friction stir processing to augment corrosion resistance of cold sprayed AA2024/Al 2 O 3 composite coatings, *J. Alloys Compd.* 774 (2019) 1223–1232. <https://doi.org/10.1016/j.jallcom.2018.09.386>.
- [112] X. Xie, C. Chen, Z. Chen, W. Wang, S. Yin, G. Ji, H. Liao, Achieving simultaneously improved tensile strength and ductility of a nano-TiB₂/AlSi10Mg composite produced by cold spray additive manufacturing, *Compos. Part B Eng.* 202 (2020) 108404. <https://doi.org/10.1016/j.compositesb.2020.108404>.
- [113] W. Li, D. Wu, K. Hu, Y. Xu, X. Yang, Y. Zhang, A comparative study on the employment of heat treatment, electric pulse processing and friction stir processing to enhance mechanical properties of cold-spray-additive-manufactured copper, *Surf. Coatings Technol.* 409 (2021) 126887. <https://doi.org/10.1016/j.surfcoat.2021.126887>.
- [114] C.J. Huang, X.C. Yan, W.Y. Li, W.B. Wang, C. Verdy, M.P. Planche, H.L. Liao, G. Montavon, Post-spray modification of cold-sprayed Ni-Ti coatings by high-temperature vacuum annealing and friction stir processing, *Appl. Surf. Sci.* 451 (2018) 56–66. <https://doi.org/10.1016/j.apsusc.2018.04.257>.
- [115] C. Huang, W. Li, Z. Zhang, M. Fu, M.P. Planche, H. Liao, G. Montavon, Modification of a cold sprayed SiCp/Al5056 composite coating by friction stir processing, *Surf. Coatings Technol.* 296 (2016) 69–75. <https://doi.org/10.1016/j.surfcoat.2016.04.016>.

- [116] W. KLEMENT, R.H. WILLENS, P. DUWEZ, Non-crystalline Structure in Solidified Gold–Silicon Alloys, *Nature*. 187 (1960) 869–870. <https://doi.org/10.1038/187869b0>.
- [117] W.H. Wang, Bulk metallic glasses with functional physical properties, *Adv. Mater.* 21 (2009) 4524–4544. <https://doi.org/10.1002/adma.200901053>.
- [118] J.J. Kruzic, Bulk Metallic Glasses as Structural Materials: A Review, *Adv. Eng. Mater.* 18 (2016) 1308–1331. <https://doi.org/10.1002/adem.201600066>.
- [119] M.M. Trexler, N.N. Thadhani, Mechanical properties of bulk metallic glasses, *Prog. Mater. Sci.* 55 (2010) 759–839. <https://doi.org/10.1016/j.pmatsci.2010.04.002>.
- [120] W.H. Wang, C. Dong, C.H. Shek, Bulk metallic glasses, *Mater. Sci. Eng. R Reports*. 44 (2004) 45–89. <https://doi.org/10.1016/j.mser.2004.03.001>.
- [121] M. Telford, The case for bulk metallic glass, *Mater. Today*. 7 (2004) 36–43. [https://doi.org/10.1016/S1369-7021\(04\)00124-5](https://doi.org/10.1016/S1369-7021(04)00124-5).
- [122] J. Schroers, Processing of Bulk Metallic Glass, *Adv. Mater.* 22 (2010) 1566–1597. <https://doi.org/10.1002/adma.200902776>.
- [123] S. Pauly, L. Löber, R. Petters, M. Stoica, S. Scudino, U. Kühn, J. Eckert, Processing metallic glasses by selective laser melting, *Mater. Today*. 16 (2013) 37–41. <https://doi.org/10.1016/j.mattod.2013.01.018>.
- [124] Y. Shen, Y. Li, C. Chen, H.L. Tsai, 3D printing of large, complex metallic glass structures, *Mater. Des.* 117 (2017) 213–222. <https://doi.org/10.1016/j.matdes.2016.12.087>.
- [125] H. Li, Z. Li, J. Yang, H.B. Ke, B. Sun, C.C. Yuan, J. Ma, J. Shen, W.H. Wang, Interface design enabled manufacture of giant metallic glasses, *Sci. China Mater.* 64 (2021) 964–972. <https://doi.org/10.1007/s40843-020-1561-x>.
- [126] C. Zhang, D. Ouyang, S. Pauly, L. Liu, 3D printing of bulk metallic glasses, *Mater. Sci. Eng. R Reports*. 145 (2021) 100625. <https://doi.org/10.1016/j.mser.2021.100625>.
- [127] H.W. Kui, A.L. Greer, D. Turnbull, Formation of bulk metallic glass by fluxing, *Appl. Phys. Lett.* 45 (1984) 615–616. <https://doi.org/10.1063/1.95330>.
- [128] W.L. Johnson, Bulk Glass-Forming Metallic Alloys: Science and Technology, *MRS Bull.* 24 (1999) 42–56. <https://doi.org/10.1557/S0883769400053252>.
- [129] A. Inoue, Stabilization of metallic supercooled liquid and bulk amorphous alloys, *Acta Mater.* 48 (2000) 279–306. [https://doi.org/10.1016/S1359-6454\(99\)00300-6](https://doi.org/10.1016/S1359-6454(99)00300-6).
- [130] A. Inoue, High Strength Bulk Amorphous Alloys with Low Critical Cooling Rates (Overview), *Mater. Trans. JIM*. 36 (1995) 866–875. <https://doi.org/10.2320/matertrans1989.36.866>.

- [131] W. WANG, Roles of minor additions in formation and properties of bulk metallic glasses, *Prog. Mater. Sci.* 52 (2007) 540–596. <https://doi.org/10.1016/j.pmatsci.2006.07.003>.
- [132] A. Peker, W.L. Johnson, A highly processable metallic glass: Zr 41.2 Ti 13.8 Cu 12.5 Ni 10.0 Be 22.5, *Appl. Phys. Lett.* 63 (1993) 2342–2344. <https://doi.org/10.1063/1.110520>.
- [133] N. Nishiyama, K. Takenaka, H. Miura, N. Saidoh, Y. Zeng, A. Inoue, The world's biggest glassy alloy ever made, *Intermetallics*. 30 (2012) 19–24. <https://doi.org/10.1016/j.intermet.2012.03.020>.
- [134] N. Nishiyama, A. Inoue, Glass-forming ability of Pd_{42.5}Cu₃₀Ni_{7.5}P₂₀ alloy with a low critical cooling rate of 0.067 K/s, *Appl. Phys. Lett.* 80 (2002) 568–570. <https://doi.org/10.1063/1.1445475>.
- [135] M. Bakkal, U. Karagüzel, A.T. Kuzu, Manufacturing Techniques of Bulk Metallic Glasses, in: *Mod. Manuf. Process.*, John Wiley & Sons, Inc., Hoboken, NJ, USA, 2019: pp. 137–148. <https://doi.org/10.1002/9781119120384.ch6>.
- [136] Y. Li, Y. Shen, M.C. Leu, H.L. Tsai, Building Zr-based metallic glass part on Ti-6Al-4V substrate by laser-foil-printing additive manufacturing, *Acta Mater.* 144 (2018) 810–821. <https://doi.org/10.1016/j.actamat.2017.11.046>.
- [137] X. Lin, Y. Zhang, G. Yang, X. Gao, Q. Hu, J. Yu, L. Wei, W. Huang, Microstructure and compressive/tensile characteristic of large size Zr-based bulk metallic glass prepared by laser solid forming, *J. Mater. Sci. Technol.* 35 (2019) 328–335. <https://doi.org/10.1016/j.jmst.2018.10.033>.
- [138] I.D. Kuchumova, I.S. Batraev, V.Y. Ulianitsky, A.A. Shtertser, K.B. Gerasimov, A. V. Ukhina, N. V. Bulina, I.A. Bataev, G.Y. Koga, Y. Guo, W.J. Botta, H. Kato, T. Wada, B.B. Bokhonov, D. V. Dudina, A. Moreira Jorge, Formation of Metallic Glass Coatings by Detonation Spraying of a Fe₆₆Cr₁₀Nb₅B₁₉ Powder, *Metals (Basel)*. 9 (2019) 846. <https://doi.org/10.3390/met9080846>.
- [139] C. SCHUH, T. HUFNAGEL, U. RAMAMURTY, Mechanical behavior of amorphous alloys, *Acta Mater.* 55 (2007) 4067–4109. <https://doi.org/10.1016/j.actamat.2007.01.052>.
- [140] J. Lu, G. Ravichandran, W.L. Johnson, Deformation behavior of the Zr_{41.2}Ti_{13.8}Cu_{12.5}Ni₁₀Be_{22.5} bulk metallic glass over a wide range of strain-rates and temperatures, *Acta Mater.* 51 (2003) 3429–3443. [https://doi.org/10.1016/S1359-6454\(03\)00164-2](https://doi.org/10.1016/S1359-6454(03)00164-2).
- [141] H. Choi, S. Yoon, G. Kim, H. Jo, C. Lee, Phase evolutions of bulk amorphous NiTiZrSiSn feedstock during thermal and kinetic spraying processes, *Scr. Mater.* 53 (2005) 125–130. <https://doi.org/10.1016/j.scriptamat.2005.01.046>.
- [142] S. Yoon, C. Lee, H. Choi, H. Jo, Kinetic spraying deposition behavior of bulk amorphous NiTiZrSiSn feedstock, *Mater. Sci. Eng. A*. 415 (2006) 45–52. <https://doi.org/10.1016/j.msea.2005.08.132>.

- [143] S. Yoon, C. Lee, H. Choi, H. Kim, J. Bae, Impacting behavior of bulk metallic glass powder at an abnormally high strain rate during kinetic spraying, *Mater. Sci. Eng. A.* 448–451 (2007) 911–915. <https://doi.org/10.1016/j.msea.2006.02.433>.
- [144] L. Ajdelsztajn, B. Jodoin, P. Richer, E. Sansoucy, E.J. Lavernia, Cold Gas Dynamic Spraying of Iron-Base Amorphous Alloy, *J. Therm. Spray Technol.* 15 (2006) 495–500. <https://doi.org/10.1361/105996306X146857>.
- [145] S. Yoon, C. Lee, H. Choi, Evaluation of the effects of the crystallinity of kinetically sprayed Ni-Ti-Zr-Si-Sn bulk metallic glass on the scratch response, *Mater. Sci. Eng. A.* 448–451 (2007) 285–289. <https://doi.org/10.1016/j.msea.2006.02.434>.
- [146] J.H. Choi, C. Lee, D.B. Lee, Oxidation behavior of bulk amorphous Ni₅₇Ti₁₈Zr₂₀Si₃Sn₂ coatings between 473 and 973 K in air, *J. Alloys Compd.* 449 (2008) 384–388. <https://doi.org/10.1016/j.jallcom.2006.02.106>.
- [147] Y.H. Yoo, S.H. Lee, J.G. Kim, J.S. Kim, C. Lee, Effect of heat treatment on the corrosion resistance of Ni-based and Cu-based amorphous alloy coatings, *J. Alloys Compd.* 461 (2008) 304–311. <https://doi.org/10.1016/j.jallcom.2007.06.118>.
- [148] S. Yoon, G. Bae, Y. Xiong, S. Kumar, K. Kang, J.J. Kim, C. Lee, Strain-enhanced nanocrystallization of a CuNiTiZr bulk metallic glass coating by a kinetic spraying process, *Acta Mater.* 57 (2009) 6191–6199. <https://doi.org/10.1016/j.actamat.2009.08.045>.
- [149] S. Yoon, Y. Xiong, K. Kang, G. Bae, C. Lee, Phase separation in kinetic sprayed bulk metallic glasses, *J. Phys. D. Appl. Phys.* 42 (2009) 182007. <https://doi.org/10.1088/0022-3727/42/18/182007>.
- [150] S. Yoon, J. Kim, G. Bae, B. Kim, C. Lee, Formation of coating and tribological behavior of kinetic sprayed Fe-based bulk metallic glass, *J. Alloys Compd.* 509 (2011) 347–353. <https://doi.org/10.1016/j.jallcom.2010.09.024>.
- [151] A. List, F. Gärtner, T. Schmidt, T. Klassen, Impact conditions for cold spraying of hard metallic glasses, *J. Therm. Spray Technol.* 21 (2012) 531–540. <https://doi.org/10.1007/s11666-012-9750-5>.
- [152] D. Lahiri, P.K. Gill, S. Scudino, C. Zhang, V. Singh, J. Karthikeyan, N. Munroe, S. Seal, A. Agarwal, Cold sprayed aluminum based glassy coating: Synthesis, wear and corrosion properties, *Surf. Coatings Technol.* 232 (2013) 33–40. <https://doi.org/10.1016/j.surfcoat.2013.04.049>.
- [153] P.S. Babu, R. Jha, M. Guzman, G. Sundararajan, A. Agarwal, Indentation creep behavior of cold sprayed aluminum amorphous/nano-crystalline coatings, *Mater. Sci. Eng. A.* 658 (2016) 415–421. <https://doi.org/10.1016/j.msea.2016.02.030>.
- [154] S.J. Choi, H.S. Lee, J.W. Jang, S. Yi, Corrosion behavior in a 3.5 wt% NaCl solution of amorphous coatings prepared through plasma-spray and cold-spray coating processes, *Met. Mater. Int.* 20 (2014) 1053–1057. <https://doi.org/10.1007/s12540-014-6008-4>.

- [155] R. Nikbakht, M. Saadati, T.-S. Kim, M. Jahazi, H.S. Kim, B. Jodoin, Cold spray deposition characteristic and bonding of CrMnCoFeNi high entropy alloy, *Surf. Coatings Technol.* 425 (2021) 127748. <https://doi.org/10.1016/j.surfcoat.2021.127748>.
- [156] A. List, F. Gärtner, T. Mori, M. Schulze, H. Assadi, S. Kuroda, T. Klassen, Cold Spraying of Amorphous Cu₅₀Zr₅₀ Alloys, *J. Therm. Spray Technol.* 24 (2014) 108–118. <https://doi.org/10.1007/s11666-014-0187-x>.
- [157] J. Henao, A. Concustell, I.G. Cano, N. Cinca, S. Dosta, J.M. Guilemany, Influence of Cold Gas Spray process conditions on the microstructure of Fe-based amorphous coatings, *J. Alloys Compd.* 622 (2015) 995–999. <https://doi.org/10.1016/j.jallcom.2014.11.037>.
- [158] A. Concustell, J. Henao, S. Dosta, N. Cinca, I.G. Cano, J.M. Guilemany, On the formation of metallic glass coatings by means of Cold Gas Spray technology, *J. Alloys Compd.* 651 (2015) 764–772. <https://doi.org/10.1016/j.jallcom.2015.07.270>.
- [159] J. Henao, A. Concustell, S. Dosta, G. Bolelli, I.G. Cano, L. Lusvarghi, J.M. Guilemany, Deposition mechanisms of metallic glass particles by Cold Gas Spraying, *Acta Mater.* 125 (2017) 327–339. <https://doi.org/10.1016/j.actamat.2016.12.007>.
- [160] J. Henao, A. Concustell, S. Dosta, N. Cinca, I.G. Cano, J.M. Guilemany, Influence of the Substrate on the Formation of Metallic Glass Coatings by Cold Gas Spraying, *J. Therm. Spray Technol.* 25 (2016) 992–1008. <https://doi.org/10.1007/s11666-016-0419-3>.
- [161] M.S. El-Eskandrany, A. Al-Azmi, Potential applications of cold sprayed Cu₅₀Ti₂₀Ni₃₀ metallic glassy alloy powders for antibacterial protective coating in medical and food sectors, *J. Mech. Behav. Biomed. Mater.* 56 (2016) 183–194. <https://doi.org/10.1016/j.jmbbm.2015.11.030>.
- [162] J. Henao, A. Concustell, I. G.Cano, S. Dosta, N. Cinca, J.M. Guilemany, T. Suhonen, Novel Al-based metallic glass coatings by Cold Gas Spray, *Mater. Des.* 94 (2016) 253–261. <https://doi.org/10.1016/j.matdes.2016.01.040>.
- [163] C.W. Ziemian, W.J. Wright, D.E. Cipoletti, Influence of Impact Conditions on Feedstock Deposition Behavior of Cold-Sprayed Fe-Based Metallic Glass, *J. Therm. Spray Technol.* 27 (2018) 843–856. <https://doi.org/10.1007/s11666-018-0720-4>.
- [164] C. Sun, X. Zhou, C. Xie, Effect of processing conditions on Al-based amorphous/nanocrystalline coating by cold-spraying, *Surf. Coatings Technol.* 362 (2019) 97–104. <https://doi.org/10.1016/j.surfcoat.2019.01.096>.
- [165] M. Tului, C. Bartuli, A. Bezzon, A.L. Marino, F. Marra, S. Matera, G. Pulci, Amorphous Steel Coatings Deposited by Cold-Gas Spraying, *Metals (Basel)*. 9 (2019) 678. <https://doi.org/10.3390/met9060678>.
- [166] J. Su, J. Kang, W. Yue, G. Ma, Z. Fu, L. Zhu, D. She, H. Wang, C. Wang, Comparison of tribological behavior of Fe-based metallic glass coatings fabricated by cold spraying and high velocity air fuel spraying, *J. Non. Cryst. Solids.* 522 (2019) 119582. <https://doi.org/10.1016/j.jnoncrsol.2019.119582>.

- [167] Q. Cao, G. Huang, L. Ma, L. Xing, Comparison of a cold-sprayed and plasma-sprayed Fe₂₅Cr₂₀Mo₁Si amorphous alloy coatings on 40Cr substrates, *Mater. Corros.* (2020). <https://doi.org/10.1002/maco.202011558>.
- [168] L. Jin, Z. Che, L. Zhang, B. Zhang, Z. Fan, Y. Chen, The composition design and properties investigation of Al-based amorphous powder, *Int. J. Light. Mater. Manuf.* 3 (2020) 198–203. <https://doi.org/10.1016/j.ijlmm.2019.12.001>.
- [169] L. Jin, L. Zhang, K. Liu, Z. Che, K. Li, M. Zhang, B. Zhang, Preparation of Al-based amorphous coatings and their properties, *J. Rare Earths.* (2020) 2–9. <https://doi.org/10.1016/j.jre.2020.04.018>.
- [170] Z. Wang, L. Ma, B. Han, G. Huang, Q. Cao, M. Sun, Influence of parameters on the cold spraying FeCoCrMoBCY amorphous coatings, *Surf. Eng.* (2020) 1–13. <https://doi.org/10.1080/02670844.2020.1805716>.
- [171] K. Georgarakis, M. Aljerf, Y. Li, A. Lemoulec, F. Charlot, A.R. Yavari, K. Chornokhvostenko, E. Tabachnikova, G.A. Evangelakis, D.B. Miracle, A.L. Greer, T. Zhang, Shear band melting and serrated flow in metallic glasses, *Appl. Phys. Lett.* 93 (2008) 93–96. <https://doi.org/10.1063/1.2956666>.
- [172] R. Busch, Thermophysical properties of bulk metallic glass-forming liquids, *Jom.* 52 (2000) 39–42. <https://doi.org/10.1007/s11837-000-0160-7>.
- [173] Q.P. Cao, J.F. Li, Y.H. Zhou, A. Horsewell, J.Z. Jiang, Effect of rolling deformation on the microstructure of bulk Cu₆₀Zr₂₀Ti₂₀ metallic glass and its crystallization, *Acta Mater.* 54 (2006) 4373–4383. <https://doi.org/10.1016/j.actamat.2006.05.030>.
- [174] A.J. Kim, Y. Choi, S. Suresh, A.S. Argon, Nanocrystallization during Nanoindentation of a Bulk Amorphous Metal Alloy at Room Temperature Published by : American Association for the Advancement of Science Stable URL : <http://www.jstor.org/stable/3075692> Linked references are available on JSTOR for, *Science* (80-.). 295 (2002) 654–657.
- [175] E. Pekarskaya, J.F. Löffler, W.L. Johnson, Microstructural studies of crystallization of a Zr-based bulk metallic glass, *Acta Mater.* 51 (2003) 4045–4057. [https://doi.org/10.1016/S1359-6454\(03\)00225-8](https://doi.org/10.1016/S1359-6454(03)00225-8).
- [176] Q. Wang, C.T. Liu, Y. Yang, Y.D. Dong, J. Lu, Atomic-scale structural evolution and stability of supercooled liquid of a Zr-based bulk metallic glass, *Phys. Rev. Lett.* 106 (2011) 1–4. <https://doi.org/10.1103/PhysRevLett.106.215505>.
- [177] T. Nagase, Y. Umakoshi, Electron irradiation induced crystallization of the amorphous phase in Zr-Cu based metallic glasses with various thermal stability, *Mater. Trans.* 45 (2004) 13–23. <https://doi.org/10.2320/matertrans.45.13>.
- [178] T. Nagase, Y. Umakoshi, Electron irradiation induced crystallization behavior in Zr_{66.7}Cu_{33.3} and Zr_{65.0}Al_{7.5}Cu_{27.5} amorphous alloys, *Mater. Sci. Eng. A.* 352 (2003) 251–260. [https://doi.org/10.1016/S0921-5093\(02\)00896-1](https://doi.org/10.1016/S0921-5093(02)00896-1).

- [179] Z.X. Wang, D.Q. Zhao, M.X. Pan, P. Wen, W.H. Wang, T. Okada, W. Utsumi, Crystallization mechanism of Cu-based supercooled liquid under ambient and high pressure, *Phys. Rev. B - Condens. Matter Mater. Phys.* 69 (2004) 1–4. <https://doi.org/10.1103/PhysRevB.69.092202>.
- [180] L. Xia, Y.D. Dong, Crystallization-melting behaviors and crystallization kinetics of Nd₆₀Al₁₀Fe₂₀Co₁₀ bulk metallic glass, *Int. J. Mod. Phys. B.* 18 (2004) 911–917. <https://doi.org/10.1142/S0217979204024422>.
- [181] A.L. Greer, Confusion by design, *Nature.* 366 (1993) 303–304. <https://doi.org/10.1038/366303a0>.
- [182] B. Cantor, I.T.H. Chang, P. Knight, A.J.B. Vincent, Microstructural development in equiatomic multicomponent alloys, *Mater. Sci. Eng. A.* 375–377 (2004) 213–218. <https://doi.org/10.1016/j.msea.2003.10.257>.
- [183] Y.F. Ye, Q. Wang, J. Lu, C.T. Liu, Y. Yang, High-entropy alloy: challenges and prospects, *Mater. Today.* 19 (2016) 349–362. <https://doi.org/10.1016/j.mattod.2015.11.026>.
- [184] Y. Zhang, T.T. Zuo, Z. Tang, M.C. Gao, K.A. Dahmen, P.K. Liaw, Z.P. Lu, Microstructures and properties of high-entropy alloys, *Prog. Mater. Sci.* 61 (2014) 1–93. <https://doi.org/10.1016/j.pmatsci.2013.10.001>.
- [185] Y. Zhang, T.T. Zuo, Z. Tang, M.C. Gao, K.A. Dahmen, P.K. Liaw, Z.P. Lu, Microstructures and properties of high-entropy alloys, *Prog. Mater. Sci.* 61 (2014) 1–93. <https://doi.org/10.1016/j.pmatsci.2013.10.001>.
- [186] W. Li, D. Xie, D. Li, Y. Zhang, Y. Gao, P.K. Liaw, Mechanical behavior of high-entropy alloys, *Prog. Mater. Sci.* 118 (2021) 100777. <https://doi.org/10.1016/j.pmatsci.2021.100777>.
- [187] Q.F. He, Z.Y. Ding, Y.F. Ye, Y. Yang, Design of High-Entropy Alloy: A Perspective from Nonideal Mixing, *JOM.* 69 (2017) 2092–2098. <https://doi.org/10.1007/s11837-017-2452-1>.
- [188] A. Kumar, A. Singh, A. Suhane, Mechanically alloyed high entropy alloys: existing challenges and opportunities, *J. Mater. Res. Technol.* 17 (2022) 2431–2456. <https://doi.org/10.1016/j.jmrt.2022.01.141>.
- [189] Y. Zhang, Z.P. Lu, S.G. Ma, P.K. Liaw, Z. Tang, Y.Q. Cheng, M.C. Gao, Guidelines in predicting phase formation of high-entropy alloys, *MRS Commun.* 4 (2014) 57–62. <https://doi.org/10.1557/mrc.2014.11>.
- [190] B. Gludovatz, A. Hohenwarter, D. Catoor, E.H. Chang, E.P. George, R.O. Ritchie, A fracture-resistant high-entropy alloy for cryogenic applications, *Science (80-.)*. 345 (2014) 1153–1158. <https://doi.org/10.1126/science.1254581>.
- [191] J.-W. Yeh, S.-Y. Chang, Y.-D. Hong, S.-K. Chen, S.-J. Lin, Anomalous decrease in X-ray diffraction intensities of Cu–Ni–Al–Co–Cr–Fe–Si alloy systems with multi-principal

- elements, *Mater. Chem. Phys.* 103 (2007) 41–46.
<https://doi.org/10.1016/j.matchemphys.2007.01.003>.
- [192] K.-Y. Tsai, M.-H. Tsai, J.-W. Yeh, Sluggish diffusion in Co–Cr–Fe–Mn–Ni high-entropy alloys, *Acta Mater.* 61 (2013) 4887–4897. <https://doi.org/10.1016/j.actamat.2013.04.058>.
- [193] J.-W. Yeh, S.-K. Chen, S.-J. Lin, J.-Y. Gan, T.-S. Chin, T.-T. Shun, C.-H. Tsau, S.-Y. Chang, Nanostructured High-Entropy Alloys with Multiple Principal Elements: Novel Alloy Design Concepts and Outcomes, *Adv. Eng. Mater.* 6 (2004) 299–303.
<https://doi.org/10.1002/adem.200300567>.
- [194] S. Ranganathan, Alloyed pleasures: Multimetalllic cocktails, *Curr. Sci.* 85 (2003) 1404–1406. <http://eprints.iisc.ac.in/id/eprint/6189>.
- [195] J.-W. Yeh, S.-K. Chen, S.-J. Lin, J.-Y. Gan, T.-S. Chin, T.-T. Shun, C.-H. Tsau, S.-Y. Chang, Nanostructured High-Entropy Alloys with Multiple Principal Elements: Novel Alloy Design Concepts and Outcomes, *Adv. Eng. Mater.* 6 (2004) 299–303.
<https://doi.org/10.1002/ADEM.200300567>.
- [196] W.-R. Wang, W.-L. Wang, S.-C. Wang, Y.-C. Tsai, C.-H. Lai, J.-W. Yeh, Effects of Al addition on the microstructure and mechanical property of Al_xCoCrFeNi high-entropy alloys, *Intermetallics*. 26 (2012) 44–51. <https://doi.org/10.1016/j.intermet.2012.03.005>.
- [197] A. Ostovari Moghaddam, N.A. Shaburova, M.N. Samodurova, A. Abdollahzadeh, E.A. Trofimov, Additive manufacturing of high entropy alloys: A practical review, *J. Mater. Sci. Technol.* 77 (2021) 131–162. <https://doi.org/10.1016/j.jmst.2020.11.029>.
- [198] P. Cavaliere, A. Perrone, A. Silvello, A. Laska, G. Blasi, I.G. Cano, B. Sadeghi, S. Nagy, Cyclic behavior of FeCoCrNiMn high entropy alloy coatings produced through cold spray, *J. Alloys Compd.* 931 (2023) 167550.
<https://doi.org/10.1016/j.jallcom.2022.167550>.
- [199] R. Supekar, R.B. Nair, A. McDonald, P. Stoyanov, Sliding wear behavior of high entropy alloy coatings deposited through cold spraying and flame spraying: A comparative assessment, *Wear*. 516–517 (2023) 204596. <https://doi.org/10.1016/j.wear.2022.204596>.
- [200] R.B. Nair, S. Ngan, A. McDonald, Dry abrasive wear and solid particle erosion assessments of high entropy alloy coatings fabricated by cold spraying, *Mater. Today Commun.* 34 (2023). <https://doi.org/10.1016/j.mtcomm.2023.105527>.
- [201] R.S. Kiplangat, T.T. Lin, N.G. Kipkirui, S.H. Chen, Microstructure and Mechanical Properties of the Plasma-Sprayed and Cold-Sprayed Al_{0.5}CoCrFeNi₂Ti_{0.5} High-Entropy Alloy Coatings, *J. Therm. Spray Technol.* 31 (2022) 1207–1221.
<https://doi.org/10.1007/s11666-022-01356-6>.
- [202] Y. Zou, Z. Qiu, C. Huang, D. Zeng, R. Lupoi, N. Zhang, S. Yin, Microstructure and tribological properties of Al₂O₃ reinforced FeCoNiCrMn high entropy alloy composite coatings by cold spray, *Surf. Coatings Technol.* 434 (2022) 128205.
<https://doi.org/10.1016/j.surfcoat.2022.128205>.

- [203] S. Feng, S. Guan, W.A. Story, J. Ren, S. Zhang, A. Te, M.A. Gleason, J. Heelan, C. Walde, A. Birt, K.L. Tsaknopoulos, D.L. Cote, W. Kapalczynski, A.T. Naardi, V.K. Champagne, M.J. Siopis, W. Chen, Cold Spray Additive Manufacturing of CoCrFeNiMn High-Entropy Alloy: Process Development, Microstructure, and Mechanical Properties, *J. Therm. Spray Technol.* 31 (2022) 1222–1231. <https://doi.org/10.1007/s11666-022-01374-4>.
- [204] P. Cavaliere, A. Perrone, A. Silvello, A. Laska, G. Blasi, I.G. Cano, Fatigue Bending of V-Notched Cold-Sprayed FeCoCrNiMn Coatings, *Metals (Basel)*. 12 (2022) 780. <https://doi.org/10.3390/met12050780>.
- [205] A.I. Yurkova, D. V. Hushchyk, A. V. Minitsky, Synthesis of High-Entropy AlNiCoFeCrTi Coating by Cold Spraying, *Powder Metall. Met. Ceram.* 59 (2021) 681–694. <https://doi.org/10.1007/s11106-021-00203-7>.
- [206] R. Nikbakht, C. V. Cojocar, M. Aghasibeig, É. Irissou, T.S. Kim, H.S. Kim, B. Jodoin, Cold Spray and Laser-Assisted Cold Spray of CrMnCoFeNi High Entropy Alloy Using Nitrogen as the Propelling Gas, *J. Therm. Spray Technol.* (2022) 1129–1142. <https://doi.org/10.1007/s11666-022-01361-9>.
- [207] J. Zhu, X. Cheng, L. Zhang, X. Hui, Y. Wu, H. Zheng, Z. Ren, Y. Zhao, W. Wang, S. Zhu, X. Wang, Microstructures, wear resistance and corrosion resistance of CoCrFeNi high entropy alloys coating on AZ91 Mg alloy prepared by cold spray, *J. Alloys Compd.* 925 (2022) 166698. <https://doi.org/10.1016/j.jallcom.2022.166698>.
- [208] J. Mahaffey, A. Vackel, S. Whetten, M. Melia, A.B. Kustas, Structure Evolution and Corrosion Performance of CoCrFeMnNi High Entropy Alloy Coatings Produced Via Plasma Spray and Cold Spray, *J. Therm. Spray Technol.* 31 (2022) 1143–1154. <https://doi.org/10.1007/s11666-022-01373-5>.
- [209] H. Wang, J. Kang, W. Yue, G. Jin, R. Li, Y. Zhou, J. Liang, Y. Yang, Microstructure and Corrosive Wear Properties of CoCrFeNiMn High-Entropy Alloy Coatings, *Materials (Basel)*. 16 (2023). <https://doi.org/10.3390/ma16010055>.
- [210] A. Anupam, S. Kumar, N.M. Chavan, B.S. Murty, R.S. Kottada, First report on cold-sprayed AlCoCrFeNi high-entropy alloy and its isothermal oxidation, *J. Mater. Res.* 34 (2019) 796–806. <https://doi.org/10.1557/jmr.2019.38>.
- [211] J. Lehtonen, H. Koivuluoto, Y. Ge, A. Juselius, S.-P. Hannula, Cold Gas Spraying of a High-Entropy CrFeNiMn Equiatomic Alloy, *Coatings*. 10 (2020) 53. <https://doi.org/10.3390/coatings10010053>.
- [212] J.-E. Ahn, Y.-K. Kim, S.-H. Yoon, K.-A. Lee, Tuning the Microstructure and Mechanical Properties of Cold Sprayed Equiatomic CoCrFeMnNi High-Entropy Alloy Coating Layer, *Met. Mater. Int.* 27 (2021) 2406–2415. <https://doi.org/10.1007/s12540-020-00886-4>.
- [213] Y. Xu, W. Li, L. Qu, X. Yang, B. Song, R. Lupoi, S. Yin, Solid-state cold spraying of FeCoCrNiMn high-entropy alloy: an insight into microstructure evolution and oxidation

- behavior at 700-900 °C, *J. Mater. Sci. Technol.* 68 (2020) 172–183. <https://doi.org/10.1016/j.jmst.2020.06.041>.
- [214] D. V. Hushchyk, A.I. Yurkova, V. V. Cherniavsky, I.I. Bilyk, S.O. Nakonechnyy, Nanostructured AlNiCoFeCrTi high-entropy coating performed by cold spray, *Appl. Nanosci.* 10 (2020) 4879–4890. <https://doi.org/10.1007/s13204-020-01364-4>.
- [215] A. Silvello, P. Cavaliere, S. Yin, R. Lupoi, I. Garcia Cano, S. Dosta, Microstructural, Mechanical and Wear Behavior of HVOF and Cold-Sprayed High-Entropy Alloys (HEAs) Coatings, *J. Therm. Spray Technol.* (2022). <https://doi.org/10.1007/s11666-021-01293-w>.
- [216] D.F. Rojas, H. Li, O.K. Orhan, C. Shao, J.D. Hogan, M. Ponga, Mechanical and microstructural properties of a CoCrFe_{0.75}NiMo_{0.3}Nb_{0.125} high-entropy alloy additively manufactured via cold-spray, *J. Alloys Compd.* 893 (2022) 162309. <https://doi.org/10.1016/j.jallcom.2021.162309>.
- [217] D. Wu, Y. Xu, W. Li, Y. Yang, K. Liu, W. Wan, Z. Qi, Process optimisation of cold spray additive manufacturing of FeCoNiCrMn high-entropy alloy, *Sci. Technol. Weld. Join.* 28 (2023) 540–547. <https://doi.org/10.1080/13621718.2023.2190264>.
- [218] C.J. Akisin, B. Dovggy, C.J. Bennett, M.-S. Pham, F. Venturi, T. Hussain, Microstructural Study of Cold-Sprayed CoCrFeNiMn High Entropy Alloy, *J. Therm. Spray Technol.* (2023). <https://doi.org/10.1007/s11666-023-01646-7>.
- [219] Y. Zhang, B. Qin, K.C. Chan, R. Lupoi, S. Yin, Y. Xie, S. Ye, P. Yu, H. Ke, W. Wang, Enhancement on mechanical properties of CoCrNi medium entropy alloy via cold spray additive manufacturing associated with sintering, *J. Manuf. Process.* 94 (2023) 413–423. <https://doi.org/10.1016/j.jmapro.2023.03.017>.
- [220] Z. Yao, G. Xiao, K. Ma, L. Feng, Microstructure and Properties of AlCrCoFe_xNiCu High-Entropy Alloy Coating Synthesized via Cold Spraying-Assisted Induction Remelting Method, *Trans. Indian Inst. Met.* 76 (2023) 2063–2072. <https://doi.org/10.1007/s12666-023-02877-6>.
- [221] A. Sova, M. Doubenskaia, E. Trofimov, M. Samodurova, Deposition of High-Entropy Alloy Coating by Cold Spray Combined with Laser Melting: Feasibility Tests, *J. Therm. Spray Technol.* 31 (2022) 1112–1128. <https://doi.org/10.1007/s11666-021-01300-0>.
- [222] C. Suryanarayana, Mechanical Alloying: A Novel Technique to Synthesize Advanced Materials, *Research.* 2019 (2019) 1–17. <https://doi.org/10.34133/2019/4219812>.
- [223] J.F. Archard, Contact and rubbing of flat surfaces, *J. Appl. Phys.* 24 (1953) 981–988. <https://doi.org/10.1063/1.1721448>.
- [224] Y. Qiu, S. Thomas, M.A. Gibson, H.L. Fraser, N. Birbilis, Corrosion of high entropy alloys, *Npj Mater. Degrad.* 1 (2017) 15. <https://doi.org/10.1038/s41529-017-0009-y>.
- [225] Y. Xu, W. Li, L. Qu, X. Yang, B. Song, R. Lupoi, S. Yin, Solid-state cold spraying of FeCoCrNiMn high-entropy alloy: an insight into microstructure evolution and oxidation

- behavior at 700–900 °C, *J. Mater. Sci. Technol.* 68 (2021) 172–183.
<https://doi.org/10.1016/j.jmst.2020.06.041>.
- [226] T. Stoltenhoff, H. Kreye, H.J. Richter, An Analysis of the Cold Spray Process and Its Coatings, *J. Therm. Spray Technol.* 11 (2002) 542–550.
<https://doi.org/10.1361/105996302770348682>.
- [227] M. Grujicic, C.L. Zhao, C. Tong, W.S. DeRosset, D. Helfritsch, Analysis of the impact velocity of powder particles in the cold-gas dynamic-spray process, *Mater. Sci. Eng. A.* 368 (2004) 222–230. <https://doi.org/10.1016/j.msea.2003.10.312>.
- [228] L. Wu, G. Zhang, B. Li, W. Wang, X. Huang, Z. Chen, G. Dong, Q. Zhang, J. Yao, Study on microstructure and tribological performance of diamond/cu composite coating via supersonic laser deposition, *Coatings.* 10 (2020).
<https://doi.org/https://doi.org/10.3390/coatings10030276>.
- [229] H. Bingyuan, B. Shaoyi, D. Wenbo, H. Weixing, Y. Xue, C. Fangfang, C. Jiajie, G. Xianghan, Z. Sheng, Laser-irradiation-induced dynamically recrystallized microstructure and properties of supersonic-particle-deposited Ni-Fe-Cr-Nb-Ti-Al high-entropy alloy coating, *Mater. Charact.* 183 (2022) 111600.
<https://doi.org/10.1016/j.matchar.2021.111600>.
- [230] M. Yandouzi, P. Richer, B. Jodoin, SiC particulate reinforced Al-12Si alloy composite coatings produced by the pulsed gas dynamic spray process: Microstructure and properties, *Surf. Coatings Technol.* 203 (2009) 3260–3270.
<https://doi.org/10.1016/j.surfcoat.2009.04.001>.
- [231] W.-Y. Li, G. Zhang, C. Zhang, O. Elkedim, H. Liao, C. Coddet, Effect of Ball Milling of Feedstock Powder on Microstructure and Properties of TiN Particle-Reinforced Al Alloy-Based Composites Fabricated by Cold Spraying, *J. Therm. Spray Technol.* 17 (2008) 316–322. <https://doi.org/10.1007/s11666-008-9182-4>.
- [232] H.K. Kang, S.B. Kang, Tungsten/copper composite deposits produced by a cold spray, *Scr. Mater.* 49 (2003) 1169–1174. <https://doi.org/10.1016/j.scriptamat.2003.08.023>.
- [233] K.S. Al-Hamdani, J.W. Murray, T. Hussain, A.T. Clare, Heat-treatment and mechanical properties of cold-sprayed high strength Al alloys from satellited feedstocks, *Surf. Coatings Technol.* 374 (2019) 21–31. <https://doi.org/10.1016/j.surfcoat.2019.05.043>.
- [234] L. He, M. Hassani, A Review of the Mechanical and Tribological Behavior of Cold Spray Metal Matrix Composites, *J. Therm. Spray Technol.* 29 (2020) 1565–1608.
<https://doi.org/10.1007/s11666-020-01091-w>.
- [235] X.T. Luo, G.J. Yang, C.J. Li, Multiple strengthening mechanisms of cold-sprayed cBNp/NiCrAl composite coating, *Surf. Coatings Technol.* 205 (2011) 4808–4813.
<https://doi.org/10.1016/j.surfcoat.2011.04.065>.
- [236] D.B. Miracle, O.N. Senkov, A critical review of high entropy alloys and related concepts, *Acta Mater.* 122 (2017) 448–511. <https://doi.org/10.1016/j.actamat.2016.08.081>.

- [237] H. Assadi, H. Kreye, F. Gärtner, T. Klassen, Cold spraying – A materials perspective, *Acta Mater.* 116 (2016) 382–407. <https://doi.org/10.1016/j.actamat.2016.06.034>.
- [238] D. Ouyang, Q. Zheng, L. Wang, H. Wang, C. Yang, P. Zhang, N. Li, The brittleness of post-treatment of 3D printed Zr-based metallic glasses in supercooled liquid state, *Mater. Sci. Eng. A.* 782 (2020) 139259. <https://doi.org/10.1016/j.msea.2020.139259>.
- [239] A.L. Greer, Y.Q. Cheng, E. Ma, Shear bands in metallic glasses, *Mater. Sci. Eng. R Reports.* 74 (2013) 71–132. <https://doi.org/10.1016/j.mser.2013.04.001>.
- [240] O. Haruyama, Y. Nakayama, R. Wada, H. Tokunaga, J. Okada, T. Ishikawa, Y. Yokoyama, Volume and enthalpy relaxation in Zr₅₅Cu₃₀Ni₅Al₁₀ bulk metallic glass, *Acta Mater.* 58 (2010) 1829–1836. <https://doi.org/10.1016/j.actamat.2009.11.025>.
- [241] J.J. Lewandowski, A.L. Greer, Temperature rise at shear bands in metallic glasses, *Nat. Mater.* 5 (2006) 15–18. <https://doi.org/10.1038/nmat1536>.
- [242] B. Zheng, Y. Lin, Y. Zhou, E.J. Lavernia, Gas atomization of amorphous aluminum: Part I. thermal behavior calculations, *Metall. Mater. Trans. B Process Metall. Mater. Process. Sci.* 40 (2009) 768–778. <https://doi.org/10.1007/s11663-009-9276-5>.
- [243] M. Zhang, Z. Zhang, Numerical simulation study on cooling of metal droplet in atomizing gas, *Mater. Today Commun.* 25 (2020) 101423. <https://doi.org/10.1016/j.mtcomm.2020.101423>.
- [244] Z. Kovács, P. Henits, A.P. Zhilyaev, Á. Révész, Deformation induced primary crystallization in a thermally non-primary crystallizing amorphous Al₈₅Ce₈Ni₅Co₂ alloy, *Scr. Mater.* 54 (2006) 1733–1737. <https://doi.org/10.1016/j.scriptamat.2006.02.004>.
- [245] J.J. Kim, Y. Choi, S. Suresh, A.S. Argon, Nanocrystallization during nanoindentation of a bulk amorphous metal alloy at room temperature, *Science* (80-.). 295 (2002) 654–657. <https://doi.org/10.1126/science.1067453>.
- [246] S.H. Joo, D.H. Pi, A.D.H. Setyawan, H. Kato, M. Janecek, Y.C. Kim, S. Lee, H.S. Kim, Work-Hardening Induced Tensile Ductility of Bulk Metallic Glasses via High-Pressure Torsion, *Sci. Rep.* 5 (2015) 1–9. <https://doi.org/10.1038/srep09660>.
- [247] G.J. Fan, M.X. Quan, Z.Q. Hu, W. Löser, J. Eckert, Deformation-induced microstructural changes in Fe₄₀Ni₄₀P₁₄B₆ metallic glass, *J. Mater. Res.* 14 (1999) 3765–3774. <https://doi.org/10.1557/JMR.1999.0510>.
- [248] S.W. Lee, M.Y. Huh, S.W. Chae, J.C. Lee, Mechanism of the deformation-induced nanocrystallization in a Cu-based bulk amorphous alloy under uniaxial compression, *Scr. Mater.* 54 (2006) 1439–1444. <https://doi.org/10.1016/j.scriptamat.2006.01.002>.
- [249] Y.X. Zhuang, J.Z. Jiang, T.J. Zhou, H. Rasmussen, L. Gerward, M. Mezouar, W. Crichton, A. Inoue, Pressure effects on Al₈₉La₆Ni₅ amorphous alloy crystallization, *Appl. Phys. Lett.* 77 (2000) 4133–4135. <https://doi.org/10.1063/1.1332409>.

- [250] S.W. Lee, M.Y. Huh, E. Fleury, J.C. Lee, Crystallization-induced plasticity of Cu-Zr containing bulk amorphous alloys, *Acta Mater.* 54 (2006) 349–355. <https://doi.org/10.1016/j.actamat.2005.09.007>.
- [251] A. Argon, Plastic deformation in metallic glasses, *Acta Metall.* 27 (1979) 47–58. [https://doi.org/10.1016/0001-6160\(79\)90055-5](https://doi.org/10.1016/0001-6160(79)90055-5).
- [252] F. Spaepen, A microscopic mechanism for steady state inhomogeneous flow in metallic glasses, *Acta Metall.* 25 (1977) 407–415. [https://doi.org/10.1016/0001-6160\(77\)90232-2](https://doi.org/10.1016/0001-6160(77)90232-2).
- [253] Q.P. Cao, J.F. Li, Y.H. Zhou, A. Horsewell, J.Z. Jiang, Free-volume evolution and its temperature dependence during rolling of Cu₆₀Zr₂₀Ti₂₀ bulk metallic glass, *Appl. Phys. Lett.* 87 (2005) 101901. <https://doi.org/10.1063/1.2037858>.
- [254] W.H. Jiang, M. Atzmon, Mechanically-assisted nanocrystallization and defects in amorphous alloys: A high-resolution transmission electron microscopy study, *Scr. Mater.* 54 (2006) 333–336. <https://doi.org/10.1016/j.scriptamat.2005.09.052>.
- [255] B.J. Park, H.J. Chang, D.H. Kim, W.T. Kim, In situ formation of two amorphous phases by liquid phase separation in Y-Ti-Al-Co alloy, *Appl. Phys. Lett.* 85 (2004) 6353–6355. <https://doi.org/10.1063/1.1842360>.
- [256] A. Takeuchi, A. Inoue, Classification of Bulk Metallic Glasses by Atomic Size Difference, Heat of Mixing and Period of Constituent Elements and Its Application to Characterization of the Main Alloying Element, *Mater. Trans.* 46 (2005) 2817–2829. <https://doi.org/10.2320/matertrans.46.2817>.
- [257] G.L. Chen, X.J. Liu, X.D. Hui, H.Y. Hou, K.F. Yao, C.T. Liu, J. Wadsworth, Molecular dynamic simulations and atomic structures of amorphous materials, *Appl. Phys. Lett.* 88 (2006) 20–23. <https://doi.org/10.1063/1.2198015>.
- [258] X.J. Liu, G.L. Chen, H.Y. Hou, X. Hui, K.F. Yao, Z.P. Lu, C.T. Liu, Atomistic mechanism for nanocrystallization of metallic glasses, *Acta Mater.* 56 (2008) 2760–2769. <https://doi.org/10.1016/j.actamat.2008.02.019>.
- [259] S.-T. Yau, P.G. Vekilov, Quasi-planar nucleus structure in apoferritin crystallization, *Nature.* 406 (2000) 494–497. <https://doi.org/10.1038/35020035>.
- [260] J. Wu, H. Fang, H.J. Kim, C. Lee, High speed impact behaviors of Al alloy particle onto mild steel substrate during kinetic deposition, *Mater. Sci. Eng. A.* 417 (2006) 114–119. <https://doi.org/10.1016/j.msea.2005.11.011>.
- [261] X.J. Liu, X.D. Hui, G.L. Chen, M.H. Sun, In situ synchrotron SAXS study of nanocrystallization in Zr₆₅Ni₂₅Ti₁₀ metallic glass, *Intermetallics.* 16 (2008) 10–15. <https://doi.org/10.1016/j.intermet.2007.06.014>.
- [262] X.J. Liu, G.L. Chen, F. Li, X.D. Hui, Z.P. Lu, F. Ye, C.T. Liu, Evolution of atomic ordering in metallic glasses, *Intermetallics.* 18 (2010) 2333–2337. <https://doi.org/10.1016/j.intermet.2010.08.004>.

- [263] W. Sun, A.W.Y. Tan, N.W. Khun, I. Marinescu, E. Liu, Effect of substrate surface condition on fatigue behavior of cold sprayed Ti6Al4V coatings, *Surf. Coatings Technol.* 320 (2017) 452–457. <https://doi.org/10.1016/j.surfcoat.2016.11.093>.
- [264] S. Yin, N. Fan, C. Huang, Y. Xie, C. Zhang, R. Lupoi, W. Li, Towards high-strength cold spray additive manufactured metals: Methods, mechanisms, and properties, *J. Mater. Sci. Technol.* 170 (2024) 47–64. <https://doi.org/10.1016/j.jmst.2023.05.047>.
- [265] G. Chen, Q. Zhu, S.R. Chen, S.J. Yao, H. Wang, L. Zhao, P. Zhang, C.J. Wang, Influence of heat treatment on the texture, microstructure and tensile deformation behaviours of cold rolled FeCoNiCr sheets, *Mater. Sci. Eng. A.* 848 (2022) 143412. <https://doi.org/10.1016/j.msea.2022.143412>.
- [266] Z. Wu, H. Bei, F. Otto, G.M. Pharr, E.P. George, Recovery, recrystallization, grain growth and phase stability of a family of FCC-structured multi-component equiatomic solid solution alloys, *Intermetallics.* 46 (2014) 131–140. <https://doi.org/10.1016/j.intermet.2013.10.024>.
- [267] Y. Wang, B. Liu, K. Yan, M. Wang, S. Kabra, Y.-L. Chiu, D. Dye, P.D. Lee, Y. Liu, B. Cai, Probing deformation mechanisms of a FeCoCrNi high-entropy alloy at 293 and 77 K using in situ neutron diffraction, *Acta Mater.* 154 (2018) 79–89. <https://doi.org/10.1016/j.actamat.2018.05.013>.
- [268] H.-C. Liu, C.-W. Tsai, Effect of Ge addition on the microstructure, mechanical properties, and corrosion behavior of CoCrFeNi high-entropy alloys, *Intermetallics.* 132 (2021) 107167. <https://doi.org/10.1016/j.intermet.2021.107167>.
- [269] W. Zhao, J.-K. Han, Y.O. Kuzminova, S.A. Evlashin, A.P. Zhilyaev, A.M. Pesin, J. Jang, K.-D. Liss, M. Kawasaki, Significance of grain refinement on micro-mechanical properties and structures of additively-manufactured CoCrFeNi high-entropy alloy, *Mater. Sci. Eng. A.* 807 (2021) 140898. <https://doi.org/10.1016/j.msea.2021.140898>.
- [270] L.J. Zhang, M.D. Zhang, Z. Zhou, J.T. Fan, P. Cui, P.F. Yu, Q. Jing, M.Z. Ma, P.K. Liaw, G. Li, R.P. Liu, Effects of rare-earth element, Y, additions on the microstructure and mechanical properties of CoCrFeNi high entropy alloy, *Mater. Sci. Eng. A.* 725 (2018) 437–446. <https://doi.org/10.1016/j.msea.2018.04.058>.
- [271] H. Ma, C.H. Shek, Effects of Hf on the microstructure and mechanical properties of CoCrFeNi high entropy alloy, *J. Alloys Compd.* 827 (2020) 154159. <https://doi.org/10.1016/j.jallcom.2020.154159>.
- [272] J.L. Dong, X.Q. Wu, C.G. Huang, Mechanical behavior of thin CoCrFeNi high-entropy alloy sheet under laser shock peening, *Intermetallics.* 144 (2022) 107529. <https://doi.org/10.1016/j.intermet.2022.107529>.
- [273] Q. Shen, X. Kong, X. Chen, X. Yao, V.B. Deev, E.S. Prusov, Powder plasma arc additive manufactured CoCrFeNi(SiC)_x high-entropy alloys: Microstructure and mechanical properties, *Mater. Lett.* 282 (2021) 128736. <https://doi.org/10.1016/j.matlet.2020.128736>.

- [274] B. Han, Y. Chen, C. Tan, M. Jiang, J. Bi, J. Feng, X. Chen, L. Chen, L. Zhang, X. Liu, L. Cao, G. Bi, Microstructure and wear behavior of laser clad interstitial CoCrFeNi high entropy alloy coating reinforced by carbon nanotubes, *Surf. Coatings Technol.* 434 (2022) 128241. <https://doi.org/10.1016/j.surfcoat.2022.128241>.
- [275] A. Erdogan, K.M. Döleker, S. Zeytin, Effect of laser re-melting on electric current assistive sintered CoCrFeNiAlxTiy high entropy alloys: Formation, micro-hardness and wear behaviors, *Surf. Coatings Technol.* 399 (2020) 126179. <https://doi.org/10.1016/j.surfcoat.2020.126179>.
- [276] D. Lin, L. Xu, H. Jing, Y. Han, L. Zhao, F. Minami, Effects of annealing on the structure and mechanical properties of FeCoCrNi high-entropy alloy fabricated via selective laser melting, *Addit. Manuf.* 32 (2020) 101058. <https://doi.org/10.1016/j.addma.2020.101058>.
- [277] Y. Brif, M. Thomas, I. Todd, The use of high-entropy alloys in additive manufacturing, *Scr. Mater.* 99 (2015) 93–96. <https://doi.org/10.1016/j.scriptamat.2014.11.037>.
- [278] S.W. Hussain, M.A. Mehmood, M.R.A. Karim, A. Godfrey, K. Yaqoob, Microstructural evolution and mechanical characterization of a WC-reinforced CoCrFeNi HEA matrix composite, *Sci. Rep.* 12 (2022) 9822. <https://doi.org/10.1038/s41598-022-13649-5>.
- [279] R.X. Li, P.K. Liaw, Y. Zhang, Synthesis of AlxCoCrFeNi high-entropy alloys by high-gravity combustion from oxides, *Mater. Sci. Eng. A.* 707 (2017) 668–673. <https://doi.org/10.1016/j.msea.2017.09.101>.
- [280] G. Zhang, G. Wang, T. Yang, Z. Liu, Synthesis and characterisation of TiC reinforced CoCrFeNi composite by hot-pressing sintering, *Mater. Sci. Technol.* 36 (2020) 409–416. <https://doi.org/10.1080/02670836.2019.1706815>.
- [281] T. Huang, L. Jiang, C. Zhang, H. Jiang, Y. Lu, T. Li, Effect of carbon addition on the microstructure and mechanical properties of CoCrFeNi high entropy alloy, *Sci. China Technol. Sci.* 61 (2018) 117–123. <https://doi.org/10.1007/s11431-017-9134-6>.
- [282] H. Jiang, L. Jiang, D. Qiao, Y. Lu, T. Wang, Z. Cao, T. Li, Effect of Niobium on Microstructure and Properties of the CoCrFeNb x Ni High Entropy Alloys, *J. Mater. Sci. Technol.* 33 (2017) 712–717. <https://doi.org/10.1016/j.jmst.2016.09.016>.
- [283] T.-T. Shun, L.-Y. Chang, M.-H. Shiu, Microstructures and mechanical properties of multiprincipal component CoCrFeNiTix alloys, *Mater. Sci. Eng. A.* 556 (2012) 170–174. <https://doi.org/10.1016/j.msea.2012.06.075>.
- [284] W. Qi, W. Wang, X. Yang, L. Xie, J. Zhang, D. Li, Y. Zhang, Effect of Zr on phase separation, mechanical and corrosion behavior of heterogeneous CoCrFeNiZrx high-entropy alloy, *J. Mater. Sci. Technol.* 109 (2022) 76–85. <https://doi.org/10.1016/j.jmst.2021.08.062>.
- [285] J. Li, K. Yamanaka, A. Chiba, Significant lattice-distortion effect on compressive deformation in Mo-added CoCrFeNi-based high-entropy alloys, *Mater. Sci. Eng. A.* 830 (2022) 142295. <https://doi.org/10.1016/j.msea.2021.142295>.

- [286] L. Huang, Y. Sun, A. Amar, C. Wu, X. Liu, G. Le, X. Wang, J. Wu, K. Li, C. Jiang, J. Li, Microstructure evolution and mechanical properties of Al CoCrFeNi high-entropy alloys by laser melting deposition, *Vacuum*. 183 (2021) 109875. <https://doi.org/10.1016/j.vacuum.2020.109875>.
- [287] Y. Geng, J. Chen, H. Tan, J. Cheng, J. Yang, W. Liu, Vacuum tribological behaviors of CoCrFeNi high entropy alloy at elevated temperatures, *Wear*. 456–457 (2020) 203368. <https://doi.org/10.1016/j.wear.2020.203368>.
- [288] B. Jia, X. Liu, H. Wang, Y. Wu, Z. Lu, Microstructure and mechanical properties of FeCoNiCr high-entropy alloy strengthened by nano-Y₂O₃ dispersion, *Sci. China Technol. Sci.* 61 (2018) 179–183. <https://doi.org/10.1007/s11431-017-9115-5>.
- [289] G.A. Salishchev, M.A. Tikhonovsky, D.G. Shaysultanov, N.D. Stepanov, A. V. Kuznetsov, I. V. Kolodiy, A.S. Tortika, O.N. Senkov, Effect of Mn and v on structure and mechanical properties of high-entropy alloys based on CoCrFeNi system, *J. Alloys Compd.* 591 (2014) 11–21. <https://doi.org/10.1016/j.jallcom.2013.12.210>.
- [290] X. Qin, Y. Xu, Y. Sun, H. Fujii, Z. Zhu, C.H. Shek, Effect of process parameters on microstructure and mechanical properties of friction stir welded CoCrFeNi high entropy alloy, *Mater. Sci. Eng. A*. 782 (2020) 1–11. <https://doi.org/10.1016/j.msea.2020.139277>.
- [291] H. Chen, Y. Ma, C. Li, Q. Zhao, Y. Huang, H. Luo, H. Ma, X. Li, A nano-sized NbC precipitation strengthened FeCoCrNi high entropy alloy with superior hydrogen embrittlement resistance, *Corros. Sci.* 208 (2022) 110636. <https://doi.org/10.1016/j.corsci.2022.110636>.
- [292] Z.G. Zhu, F.L. Ng, J.W. Qiao, P.K. Liaw, H.C. Chen, S.M.L. Nai, J. Wei, G.J. Bi, Interplay between microstructure and deformation behavior of a laser-welded CoCrFeNi high entropy alloy, *Mater. Res. Express*. 6 (2019). <https://doi.org/10.1088/2053-1591/aafabe>.
- [293] Z. Zhang, Z. Jiang, Y. Xie, S.L.I. Chan, J. Liang, J. Wang, Multiple deformation mechanisms induced by pre-twinning in CoCrFeNi high entropy alloy, *Scr. Mater.* 207 (2022) 114266. <https://doi.org/10.1016/j.scriptamat.2021.114266>.
- [294] B. Liu, J. Wang, Y. Liu, Q. Fang, Y. Wu, S. Chen, C.T. Liu, Microstructure and mechanical properties of equimolar FeCoCrNi high entropy alloy prepared via powder extrusion, *Intermetallics*. 75 (2016) 25–30. <https://doi.org/10.1016/j.intermet.2016.05.006>.
- [295] S. Son, P. Asghari-Rad, A. Zargaran, W. Chen, H.S. Kim, Superlative room temperature and cryogenic tensile properties of nanostructured CoCrFeNi medium-entropy alloy fabricated by powder high-pressure torsion, *Scr. Mater.* 213 (2022) 114631. <https://doi.org/10.1016/j.scriptamat.2022.114631>.
- [296] Y. Zhu, X. Wu, Heterostructured materials, *Prog. Mater. Sci.* 131 (2023) 101019. <https://doi.org/10.1016/j.pmatsci.2022.101019>.

- [297] C. Chen, Y. Xie, S. Yin, W. Li, X. Luo, X. Xie, R. Zhao, C. Deng, J. Wang, H. Liao, M. Liu, Z. Ren, Ductile and high strength Cu fabricated by solid-state cold spray additive manufacturing, *J. Mater. Sci. Technol.* 134 (2023) 234–243. <https://doi.org/10.1016/j.jmst.2022.07.003>.
- [298] S. Yoshida, T. Ikeuchi, T. Bhattacharjee, Y. Bai, A. Shibata, N. Tsuji, Effect of elemental combination on friction stress and Hall-Petch relationship in face-centered cubic high / medium entropy alloys, *Acta Mater.* 171 (2019) 201–215. <https://doi.org/10.1016/j.actamat.2019.04.017>.
- [299] N. Hansen, Hall-etch relation and boundary strengthening, *Scr. Mater.* 51 (2004) 801–806. <https://doi.org/10.1016/j.scriptamat.2004.06.002>.
- [300] F. Otto, A. Dlouhý, C. Somsen, H. Bei, G. Eggeler, E.P. George, The influences of temperature and microstructure on the tensile properties of a CoCrFeMnNi high-entropy alloy, *Acta Mater.* 61 (2013) 5743–5755. <https://doi.org/10.1016/j.actamat.2013.06.018>.
- [301] M. Naeem, H. He, S. Harjo, T. Kawasaki, W. Lin, J.J. Kai, Z. Wu, S. Lan, X.L. Wang, Temperature-dependent hardening contributions in CrFeCoNi high-entropy alloy, *Acta Mater.* 221 (2021) 117371. <https://doi.org/10.1016/j.actamat.2021.117371>.
- [302] Y. Wang, J. Ding, Z. Fan, L. Tian, M. Li, H. Lu, Y. Zhang, E. Ma, J. Li, Z. Shan, Tension–compression asymmetry in amorphous silicon, *Nat. Mater.* 20 (2021) 1371–1377. <https://doi.org/10.1038/s41563-021-01017-z>.
- [303] Y. Brif, M. Thomas, I. Todd, The use of high-entropy alloys in additive manufacturing, *Scr. Mater.* 99 (2015) 93–96. <https://doi.org/10.1016/j.scriptamat.2014.11.037>.
- [304] L. Huang, Y. Sun, A. Amar, C. Wu, X. Liu, G. Le, X. Wang, J. Wu, K. Li, C. Jiang, J. Li, Microstructure evolution and mechanical properties of Al_xCoCrFeNi high-entropy alloys by laser melting deposition, *Vacuum.* 183 (2021) 109875. <https://doi.org/10.1016/j.vacuum.2020.109875>.
- [305] B. Liu, J. Wang, Y. Liu, Q. Fang, Y. Wu, S. Chen, C.T. Liu, Microstructure and mechanical properties of equimolar FeCoCrNi high entropy alloy prepared via powder extrusion, *Intermetallics.* 75 (2016) 25–30. <https://doi.org/10.1016/j.intermet.2016.05.006>.
- [306] A.N. Papyrin, The development of the cold spray process, in: V.K. Champagne (Ed.), *Cold Spray Mater. Depos. Process Fundam. Appl.*, Woodhead Publishing Limited, Cambridge, 2007: pp. 43–61. <https://doi.org/10.1533/9781845693787>.
- [307] N. Fan, J. Cizek, C. Huang, X. Xie, Z. Chlup, R. Jenkins, R. Lupoi, S. Yin, A new strategy for strengthening additively manufactured cold spray deposits through in-process densification, *Addit. Manuf.* 36 (2020) 101626. <https://doi.org/10.1016/j.addma.2020.101626>.
- [308] Y.K. Wei, X.T. Luo, Y. Ge, X. Chu, G.S. Huang, C.J. Li, Deposition of fully dense Al-based coatings via in-situ micro-forging assisted cold spray for excellent corrosion

- protection of AZ31B magnesium alloy, *J. Alloys Compd.* 806 (2019) 1116–1126. <https://doi.org/10.1016/j.jallcom.2019.07.279>.
- [309] Y.K. Wei, Y.J. Li, Y. Zhang, X.T. Luo, C.J. Li, Corrosion resistant nickel coating with strong adhesion on AZ31B magnesium alloy prepared by an in-situ shot-peening-assisted cold spray, *Corros. Sci.* 138 (2018) 105–115. <https://doi.org/10.1016/j.corsci.2018.04.018>.
- [310] X. Qiu, N. ul H. Tariq, L. Qi, J.Q. Wang, T.Y. Xiong, A hybrid approach to improve microstructure and mechanical properties of cold spray additively manufactured A380 aluminum composites, *Mater. Sci. Eng. A.* 772 (2020). <https://doi.org/10.1016/j.msea.2019.138828>.
- [311] D. Rui, X. Li, W. Jia, W. Li, W. Xiao, T. Gui, Releasing kinetics of dissolved copper and antifouling mechanism of cold sprayed copper composite coatings for submarine screen doors of ships, *J. Alloys Compd.* 763 (2018) 525–537. <https://doi.org/10.1016/j.jallcom.2018.05.355>.
- [312] Aaron T.Nardi, Tahany Ibrahim El-Wardany, William Werkheiser, Michael A.Klecka, Method for enhancing bond strength through in-situ peening, US9938624B2, 2018.
- [313] Y. Xie, C. Chen, M.P. Planche, S. Deng, R. Huang, Z. Ren, H. Liao, Strengthened Peening Effect on Metallurgical Bonding Formation in Cold Spray Additive Manufacturing, *J. Therm. Spray Technol.* 28 (2019) 769–779. <https://doi.org/10.1007/s11666-019-00854-4>.
- [314] A.T.N. Michael A. Klecka, Self-peening feedstock materials for cold spray deposition, US9890460B2, 2018.
- [315] W.C. Oliver, G.M. Pharr, An improved technique for determining hardness and elastic modulus using load and displacement sensing indentation experiments, *J. Mater. Res.* 7 (1992) 1564–1583. <https://doi.org/10.1557/JMR.1992.1564>.
- [316] Y. Liu, Y. Xie, S. Cui, Y. Yi, X. Xing, X. Wang, W. Li, Effect of Mo element on the mechanical properties and tribological responses of CoCrFeNiMo high-entropy alloys, *Metals (Basel)*. 11 (2021) 1–18. <https://doi.org/10.3390/met11030486>.
- [317] T. Ungár, Microstructural parameters from X-ray diffraction peak broadening, *Scr. Mater.* 51 (2004) 777–781. <https://doi.org/10.1016/j.scriptamat.2004.05.007>.
- [318] G. Deng, A.K. Tieu, L. Su, P. Wang, L. Wang, X. Lan, S. Cui, H. Zhu, Investigation into reciprocating dry sliding friction and wear properties of bulk CoCrFeNiMo high entropy alloys fabricated by spark plasma sintering and subsequent cold rolling processes: Role of Mo element concentration, *Wear.* 460–461 (2020). <https://doi.org/10.1016/j.wear.2020.203440>.
- [319] T.-T. Shun, L.-Y. Chang, M.-H. Shiu, Microstructure and mechanical properties of multiprincipal component CoCrFeNiMox alloys, *Mater. Charact.* 70 (2012) 63–67. <https://doi.org/10.1016/j.matchar.2012.05.005>.

- [320] M. Mukarram, M.A. Munir, M. Mujahid, K. Yaqoob, Systematic development of eutectic high entropy alloys by thermodynamic modeling and experimentation: An example of the CoCrFeNi-Mo system, *Metals (Basel)*. 11 (2021). <https://doi.org/10.3390/met11091484>.
- [321] S. Guo, C. Ng, J. Lu, C.T. Liu, Effect of valence electron concentration on stability of fcc or bcc phase in high entropy alloys, *J. Appl. Phys.* 109 (2011) 103505. <https://doi.org/10.1063/1.3587228>.
- [322] S. GUO, C.T. LIU, Phase stability in high entropy alloys: Formation of solid-solution phase or amorphous phase, *Prog. Nat. Sci. Mater. Int.* 21 (2011) 433–446. [https://doi.org/10.1016/S1002-0071\(12\)60080-X](https://doi.org/10.1016/S1002-0071(12)60080-X).
- [323] M.-H. Tsai, K.-Y. Tsai, C.-W. Tsai, C. Lee, C.-C. Juan, J.-W. Yeh, Criterion for Sigma Phase Formation in Cr- and V-Containing High-Entropy Alloys, *Mater. Res. Lett.* 1 (2013) 207–212. <https://doi.org/10.1080/21663831.2013.831382>.
- [324] A. Leyland, A. Matthews, On the significance of the H/E ratio in wear control: a nanocomposite coating approach to optimised tribological behaviour, *Wear*. 246 (2000) 1–11. [https://doi.org/10.1016/S0043-1648\(00\)00488-9](https://doi.org/10.1016/S0043-1648(00)00488-9).
- [325] C. Zhou, S. Wang, G. Wang, J. Zhang, W. Liu, Investigation on the microstructure, wear and corrosion resistance of FeCoNiCrMox high-entropy alloy coatings deposited on 40Cr by laser cladding, *J. Mater. Sci.* 57 (2022) 18615–18639. <https://doi.org/10.1007/s10853-022-07684-w>.
- [326] H. Wu, S. Zhang, Z.Y. Wang, C.H. Zhang, H.T. Chen, J. Chen, New studies on wear and corrosion behavior of laser cladding FeNiCoCrMox high entropy alloy coating: The role of Mo, *Int. J. Refract. Met. Hard Mater.* 102 (2022) 105721. <https://doi.org/10.1016/j.ijrmhm.2021.105721>.
- [327] K. Li, J. Liang, J. Zhou, Microstructure and elevated temperature tribological performance of the CoCrFeNiMo high entropy alloy coatings, *Surf. Coatings Technol.* 449 (2022) 128978. <https://doi.org/10.1016/j.surfcoat.2022.128978>.
- [328] P. Lyu, T. Peng, Y. Miao, Z. Liu, Q. Gao, C. Zhang, Y. Jin, Q. Guan, J. Cai, Microstructure and properties of $\text{CoCrFeNiMo}_{0.2}$ high-entropy alloy enhanced by high-current pulsed electron beam, *Surf. Coatings Technol.* 410 (2021) 126911. <https://doi.org/10.1016/j.surfcoat.2021.126911>.
- [329] J.K. Xiao, T.T. Li, Y.Q. Wu, J. Chen, C. Zhang, Microstructure and Tribological Properties of Plasma-Sprayed CoCrFeNi -based High-Entropy Alloy Coatings Under Dry and Oil-Lubricated Sliding Conditions, *J. Therm. Spray Technol.* 30 (2021) 926–936. <https://doi.org/10.1007/s11666-021-01175-1>.
- [330] C. Deng, C. Wang, L. Chai, T. Wang, J. Luo, Mechanical and chemical properties of $\text{CoCrFeNiMo}_{0.2}$ high entropy alloy coating fabricated on Ti6Al4V by laser cladding, *Intermetallics*. 144 (2022) 107504. <https://doi.org/10.1016/j.intermet.2022.107504>.
- [331] G. Sutter, N. Ranc, Flash temperature measurement during dry friction process at high sliding speed, *Wear*. 268 (2010) 1237–1242. <https://doi.org/10.1016/j.wear.2010.01.019>.

- [332] H. Li, X. Li, C. Jin, Q. Li, Q. Ma, K. Hua, H. Wang, W. Liu, Mechanical and tribological performance of $\text{AlCr}_{0.5}\text{NbTaTi}_4-x$ ($x = 0, 0.5, 1$) refractory high-entropy alloys, *J. Mater. Sci. Technol.* 156 (2023) 241–253. <https://doi.org/10.1016/j.jmst.2023.02.016>.

